Chair of Materials Physics

Doctoral Thesis

Locally resolved deformation and fracture processes near interfaces

Dipl.-Ing. Markus Alfreider, BSc

December 2021

This doctoral thesis was composed at the Department Materials Science, Montanuniversität Leoben under the scope of the COMET program within the K2 Center "Integrated Computational Material, Process and Product Engineering, IC-MPPE" (Project 859480, A2.12). This program is supported by the Austrian Federal Ministries for Transport, Innovation and Technology (BMVIT) and for Digital and Economic Affairs (BMDW), represented by the Österreichische Forschungsförderungsgesellschaft (Funder ID: 10.13039/501100004955), and the federal states of Styria, Upper Austria, and Tyrol. Furthermore, part of this thesis was conducted during a research stay at UCSB financed by an Austrian Marshall Plan Scholarship, which is gratefully acknowledged.

Department Materials Science
Montanuniversität Leoben
Jahnstrasse 12
8700 Leoben Austria

MONTANUNIVERSITÄT LEOBEN
www.unileoben.ac.at

AFFIDAVIT

I declare on oath that I wrote this thesis independently, did not use other than the specified sources and aids, and did not otherwise use any unauthorized aids.

I declare that I have read, understood, and complied with the guidelines of the senate of the Montanuniversität Leoben for "Good Scientific Practice".

Furthermore, I declare that the electronic and printed version of the submitted thesis are identical, both, formally and with regard to content.

Date 20.12.2021

Signature Author
Markus Alfreider

Acknowledgements

Firstly, I want to thank my supervisor Daniel Kiener for the balance between guidance and academic freedom he provided for me since I started working in the field of micromechanics.

Furthermore, a big thank you to Daniel S. Gianola for taking me in at UCSB and giving me the opportunity to work/play around on some of the world's top micromechanical equipment.

I would also like to mention Anton Hohenwarter and Stefan Wurster for taking care of, and helping me with the SEM/FIB equipment at Montanuniversität Leoben as well as Fulin Wang, Jean-Charles Stinville, Glenn Balbus, Aidan Taylor and Eric Yao for doing the same at UCSB. None of these findings would have been possible without their help. Thank you for sharing your experience with me.

A special thanks also to Otmar Kolednik, Darjan Kozic, Stefan Kolitsch for providing various finite element simulations and input with regards to general fracture mechanics as well as Rishi Bodlos and Lorenz Romaner for the conduction of detailed *ab-initio* simulations. All of these contributions and the thereof emerging discussions helped deepen my understanding of interface fracture.

Furthermore, I'd like to thank Johannes Zechner and Roland Brunner for taking care of organizational part of the project and for keeping things running smoothly.

I am also very grateful to all my office colleagues over the years for many chats about work and/or just life in general and for creating a happy and friendly atmosphere all the time I was around.

Finally, sincere thanks to my family - to my kids Emma and Noah, for being highly energetic bundles of joy (but still sleeping enough to let me finish this thesis) and to Andrea for taking such good care of the three of us.

Abstract

With the building blocks of modern technological devices ever decreasing in size, *e.g.* microelectronic components, the investigation of lifetime and durability becomes more and more challenging due to considerably higher stresses given day-to-day mechanical or thermal loads. Especially interfaces between two different materials are oftentimes the source for device failure, due to *e.g.* loss of conductive properties or spallation of protective layers. Therefore, a general approach to determine interfacial fracture properties of such very confined systems would be highly desired. Various methodologies have already been developed for macroscopic testing, *e.g.* brazil nut specimen or four-point bending specimen. However, down-scaling such techniques to the micron or even sub-micron regime proves challenging. Therefore, specific techniques based on nowadays widely spread nanoindentation devices have been developed. However, these techniques as well as the associated evaluation schemes are commonly only applicable to specific material combinations, with the prevalent restriction that only linear elastic deformation takes place. Given that many industrially relevant material combinations contain at least one constituent which is prone to plastic deformation, *e.g.* Cu, Al or various polymers, a new methodological approach, incorporating plasticity is highly demanded.

This work presents a study on the interface fracture behaviour of a Si-SiO_x-WTi-Cu model material system, as commonly found in the microelectronics industry, utilizing novel micro mechanical approaches to take plasticity of the Cu phase into account. The methodology is based on the notched microcantilever bending specimen geometry in conjunction with a transducer equipment capable of continuous stiffness measurement for the steady determination of crack length, mounted inside a scanning electron microscope (SEM) for *in situ* observation during the test. This thesis covers the investigation of the mechanical testing setup inside the vacuum chamber of an SEM, the development of a mathematical framework for evaluation based on elastic-plastic fracture mechanical considerations, and finally successfully conducts experiments on the model material system.

Experiments with the focus on determining the fracture properties of the

SiO_x/WTi interface as well as the WTi/Cu interface revealed a distinct difference from purely brittle interface cleavage to extensive crack tip plasticity without any crack extension. This confirmed for the first time the applicability of the technique for the determination of fracture mechanical parameters in spatially confined heterogeneous structures. Further investigations on interfaces with intentional exposition to atmosphere showed a transition from crack tip plasticity to interface cleavage, which proves a weakening of interface cohesion from oxygen accumulation. In conjunction with analytical dislocation plasticity models a shift in local mode mixity was conjectured, leading to a final study focusing on the different deformation behaviour upon pure normal- or shear loading on the interface utilizing transmission scanning electron microscopy. While normal loading led to pure ductile failure in the Cu phase, shear loading reveled the nucleation and extension of an interface crack.

In summary, this thesis presents a detailed picture of the interface deformation and fracture behaviour of a model material system, with the caveat that the local microstructure, especially in the Cu phase remains oftentimes unknown. However, the obtained results showed that the developed methodologies were able to resolve previously inaccessible information with regards to interface failure and can act as a basis for further studies and improvements on similar materials systems.

Kurzfassung

Mit den immer kleiner werdenden Bausteinen moderner technischer Geräte, *z.B.* mikroelektronische Komponenten, wird die Untersuchung von Lebensdauer und Haltbarkeit durch die wesentlich höheren Spannungen bei tagtäglicher mechanischer oder thermischer Belastung immer anspruchsvoller. Insbesondere Grenzflächen zwischen zwei unterschiedlichen Materialien sind oft die Quelle für Geräteausfälle, *z.B.* aufgrund von Verlust der leitfähigen Eigenschaften oder durch Abplatzen von Schutzschichten. Daher wäre ein allgemeiner Ansatz zur Bestimmung der Grenzflächenbrucheigenschaften solcher miniaturisierten Systeme erstrebenswert. Für makroskopische Prüfungen wurden bereits verschiedene Methoden entwickelt, *z.B.* 'Brasil-nut' Proben oder Vierpunktbiegeproben. Das Herunterskalieren solcher Techniken auf den Mikrometer- oder sogar Submikrometerbereich erweist sich jedoch als eine Herausforderung. Daher wurden spezielle Techniken entwickelt, die auf heute weit verbreiteten Nanoindentierungsgeräten basieren. Diese Techniken sowie die dazugehörigen Bewertungsschemata sind jedoch üblicherweise nur auf bestimmte Materialkombinationen anwendbar, mit der vorherrschenden Einschränkung, dass nur linear-elastische Verformung stattfindet. Da viele industriell relevante Materialkombinationen mindestens einen zur plastischen Verformung neigenden Bestandteil besitzen, *z.B.* Cu, Al oder verschiedene Polymere, ist ein neuer methodischer Ansatz, der Plastizität miteinbezieht, von großem Interesse.

Diese Doktorarbeit präsentiert eine Studie zum Grenzflächenbruchverhalten eines Si-SiO_x-WTi-Cu-Modellmaterialsystems, wie es üblicherweise in der Mikroelektronikindustrie zu finden ist, unter Verwendung neuartiger mikromechanischer Ansätze zur Berücksichtigung der Plastizität der Cu-Phase. Die Methodik basiert auf der gekerbten Mikro-Biegeprobengeometrie in Verbindung mit einer Signalgeber, der durch kontinuierlichen Steifigkeitsmessung zur stationären Bestimmung der Risslänge geeignet ist und in einem Rasterelektronenmikroskop (REM) zur *in situ*-Beobachtung während des Tests montiert ist. Die Arbeit umfasst die Untersuchung des mechanischen Versuchsaufbaus in der Vakuumkammer eines REM, die Entwicklung eines mathematischen Bewertungsrahmens auf Basis elastisch-plastischer

bruchmechanischer Betrachtungen und schließlich die erfolgreiche Durchführung von Experimenten am Modellmaterialsystem.

Experimente mit dem Fokus auf der Bestimmung der Brucheigenschaften der SiO_x/WTi sowie der WTi/Cu Grenzfläche zeigten einen deutlichen Unterschied von rein spröder Grenzflächenspaltung bis hin zu ausgedehnter Rissspitzenplastizität ohne Rissausdehnung. Damit wurde erstmals die Anwendbarkeit der Technik zur Bestimmung bruchmechanischer Parameter in räumlich begrenzten heterogenen Strukturen bestätigt. Weitere Untersuchungen an Grenzflächen mit absichtlichem Kontakt zur Atmosphäre zeigten einen Übergang von der Rissspitzenplastizität zur Grenzflächenspaltung, was eine Schwächung der Grenzflächenkohäsion durch Sauerstoffanreicherung beweist. Weitere Untersuchungen an Grenzflächen mit absichtlichem Kontakt zur Atmosphäre zeigten einen Übergang von der Rissspitzenplastizität zur Grenzflächenspaltung, was eine Schwächung der Grenzflächenkohäsion durch Sauerstoffanreicherung beweist. In Verbindung mit analytischen Versetzungsplastizitätsmodellen wurde eine Verschiebung der lokalen Spannungskonzentrationsmoden vermutet, was zu einer abschließenden Studie führte, die sich auf das unterschiedliche Deformationsverhalten bei reiner Normal- oder Scherbelastung an der Grenzfläche, unter Verwendung von Transmissionsrasterelektronenmikroskopie, konzentrierte. Während normale Belastung zu rein duktilem Versagen in der Cu-Phase führte, offenbarte Scherbelastung die Entstehung und Ausdehnung eines Grenzflächenrisses.

Zusammenfassend präsentiert diese Doktorarbeit ein detailliertes Bild der Grenzflächendeformation und des Bruchverhaltens eines Modellmaterialsystems, mit dem Vorbehalt, dass die lokale Mikrostruktur, insbesondere in der Cu-Phase, oft unbekannt bleibt. Die erhaltenen Ergebnisse zeigten jedoch, dass die entwickelten Methoden in der Lage waren, bisher unzugängliche Informationen in Bezug auf Grenzflächenversagen aufzulösen und als Grundlage für weitere Studien und Verbesserungen an ähnlichen Materialsystemen dienen können.

Contents

Chapter 1

Introduction

A vast majority of modern materials systems is built on the concept of fairly confined individual constituents taking over rather specific application relevant tasks, *e.g.* electrical- [1, 2] or thermal- [3–5] conduction/isolation, semiconducting [6] or optical [7, 8] properties, diffusion [9] or wear [10] resistance, or even drug delivery [11, 12]. Most of these systems are built up by individual layered structures ranging from a few hundred nm to tens of µm with strong variations of elastic and plastic mechanical properties between the individual layers. Given the oftentimes non-negligible mechanical encumbrance during service, local interface decohesion between the constituents is more often than not the origin of final device failure. For example, during the life cycle of coated turbine blades the cyclic thermal load in conjunction with mismatch in thermal expansion coefficient (CTE) between the thermal barrier coating (TBC) and the underlying structural material can lead to local buckling or even full spallation of the TBC [13, 14]. In microelectronic devices the epitaxial growth of single crystalline layers for semiconducting or optical purposes is now at a point where only very few threading dislocations remain [15], which leads to considerable interface mismatch stresses upon cooldown and subsequently can lead to debonding and fracture even before usage [8]. Thermal overload due to short circuits or other error conditions in small power devices can lead to the occurrence of interface cracks, preceding device failure as the CTE mismatch can be quite considerable [16–18]. In vascular medicine, drug-eluting stents [19] consist of a metallic base material coated with a polymer-organic drug composite, which need to withstand an extreme amount of non-reversible deformation during their application by *in vivo* ballon expansion [20]. This leads to very high strains at the interface between polymer and base material and therefore a chance for interface failure while being inside a patient.

All of these applications have in common that the source for final failure

lies at an interface with at least one constituent exhibiting plastic deformation, raising the question on whether these localized fracture properties can somehow be understood and quantified. However, the very limited size of the constituents and the fact that oftentimes other, similarly brittle, phases are close to the interface in question pose considerable experimental challenges to address such problems.

1.1 Aim of the Thesis

In a first step this thesis focuses on implementing and refining the quasi-continuous elastic-plastic fracture mechanics (EPFM) evaluation methodology by Ast *et al.* [21] within an SEM for the first time to obtain visual *in situ* information of the occurring fracture processes in conjunction with sustainable mechanical data. The challenge there lies with the non-existent air damping of the system, which can lead to vibration and resonance phenomena during the test. Once realized, this technique amongst others was used in a second step to shed light on the interfacial fracture behavior of a Cu-WTi-SiO_x-Si model multilayer system. There the focus lies on understanding the interaction between occurring dislocation plasticity in the ductile Cu phase and possible fracture processes along the Cu/WTi interface.

1.2 State of the Art

While interfaces are very confined structures by definition, various research groups have been successful in testing their fracture characteristics by cleverly designed macroscopic testing approaches. For example using a commonly available four-point bending setup, one can construct a specimen where a crack initiates from an initial notch and deflects along an interface with lower resistance to crack extension than either of the bulk layers (see Fig. 1.1a). This has been shown to work for various material combinations, *e.g.* Al/PMMA [22], NiAl/Steel [23], ZrO_2/Steel [24], thermally grown oxide (TGO)/NiCoCrAlY bond coat [25] or borophosphosilicate glass (BPSG)/W-base metallizations [26], to name a few. However, this approach just works if the involved materials fulfill the above mentioned conditions.

Furthermore, analogous to the classical double cantilever bending (DCB) experiment in fracture mechanics of homogeneous materials [27], a sandwich type specimen [28–30], as shown in Fig. 1.1b can be constructed. Here, the challenge lies in actual synthesis and/or fabrication of the specimen as it should be very long in comparison to the individual constituent thick-

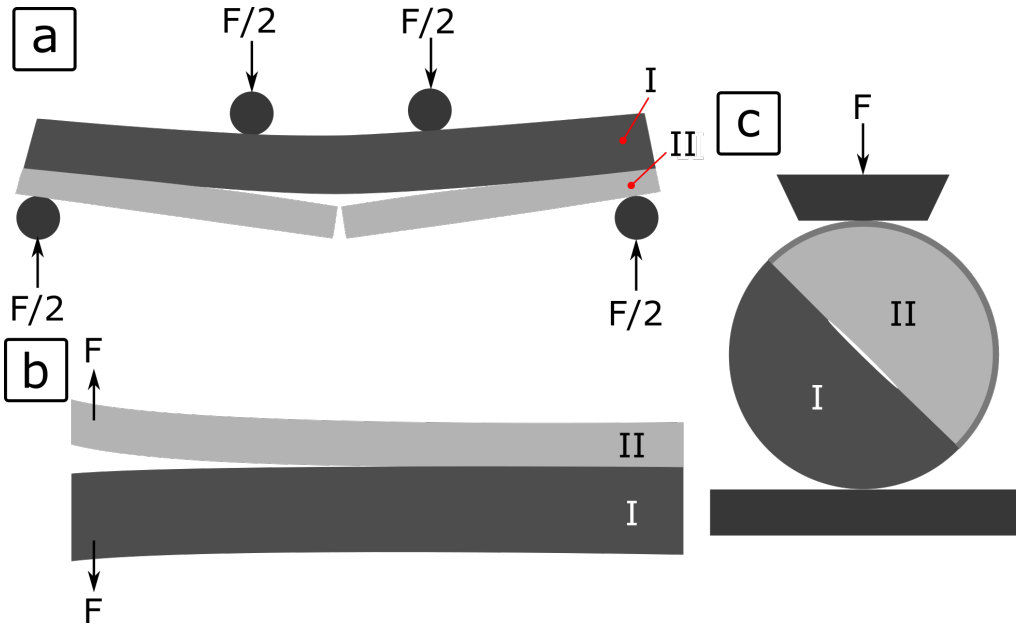

Figure 1.1: Schematic of macroscopic (a) Four point bending, (b) Double-cantilever bending and (c) Brazilian disk specimens for interface fracture measurements.

ness to utilize simple evaluation schemes. Another specimen geometry, commonly encountered when investigating the influence of loading mode on interface fracture toughness is the Brazilian disk specimen schematically shown in Fig. 1.1c. This geometry was initially developed in the 1940s for the determination of failure characteristics in concrete [31, 32], but was adapted by Wang and Suo [33] for a variety of metal/epoxy interfaces. Despite representing somewhat more of an academic specimen geometry it's strength lies in the easily changeable external loading conditions, facilitating fracture investigations with respect to mode mixity [34].

While all of these macroscopic approaches have their useful applications and can act as inspiration for miniaturized interface fracture testing, downscaling them to the µm-sized regime of functional thin films or protective coatings is most of the time not feasible. However, with the recent rise of micromechanical testing setups [35–37], able to resolve loads in the µN- and displacements in the nm-range, a complementary set of investigation techniques focusing on interface toughness evaluation has been developed, which are frequently capable of addressing the very confined volumes of nowadays material systems.

One general approach is based on the fact that high compressive stresses in thin enough films can lead to decohesion as the film minimizes the stored strain energy by plastic deformation, resulting in separation and the forma-

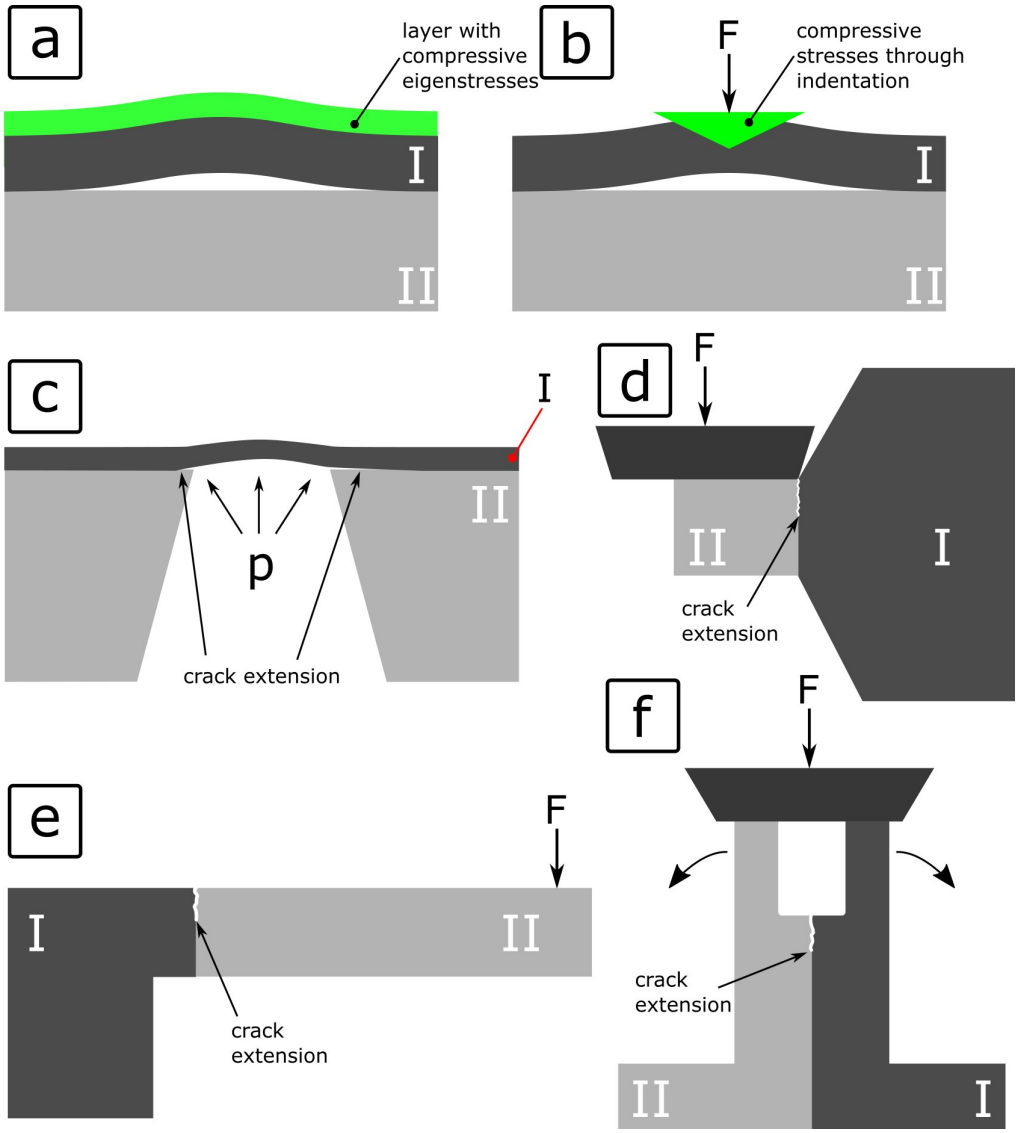

Figure 1.2: Schematic of interface decohesion or fracture testing through (a) a stressed surface layer, (b) nanoindentation, (c) bulge testing, (d) layer shearing, (e) cantilever bending and (f) double cantilever splitting.

tion of so called buckles. This phenomenon can occur naturally (most often in the form of telephone cord buckles), given a specific configuration of film stress, thickness and adhesion [38, 39], and is reasonably understood, to the point where the external measurement of buckle geometry through, *e.g.* atomic force microscopy (AFM) [39] or interferometry [40] in conjunction with known film thickness is sufficient to calculate adhesion properties [41]. If a film does not inherently exhibit high enough compressive eigenstresses, one can facilitate debonding of the interface via deposition of a layer with high compressive eigenstresses and a higher adhesion to the film than the

interface in question [42, 43] (see Fig. 1.2a). Similarly, decohesion can be promoted by the increase of in-plane compressive stresses through external means,*e.g.* nanoindentation [44, 45] or scratch testing [46–48], as shown schematically in Fig. 1.2b. While easier accessible than the following techniques the drawback of this method is that it is not generally applicable but restricted to systems that exhibit a fitting combination of weak interface adhesion and compressive stress buildup. Furthermore, if individual interfaces in a multilayer stack are to be probed, only the weakest one will be prone to decohesion, while all other remain inaccessible.

Another general concept to promote interface fracture is the generation of high local stresses through external forces. One type of experiment to achieve this would be the bulge (or blister) test, where a free standing film is forced to bend upwards due to a pressurized region underneath [49, 50], see schematically in Fig. 1.2c. However, the drawback of this method is that it requires free volume underneath the film, *e.g.* chemical removal, restricting it to a given set of substrate/film combinations.

In an effort to counteract such stringent restrictions micromechanical techniques have been developed that are based on specific focused ion beam (FIB) milled geometries such as stump shear testing (see Fig. 1.2d) or double cantilever bending through compression (see Fig. 1.2f) [51]. While these are successful in probing interfaces selectively, the high mode II contribution and elastic mismatch in bilayer systems makes mechanical evaluation rather challenging. By far the most promising geometry is based on the cantilever shaped geometry depicted schematically in Fig. 1.2e. This geometry is easily machinable via FIB, easily testable with common nanoindentation devices, and quite well understood with respect to evaluation schemes and general mechanical behavior.

1.3 A short history of microcantilever fracture testing

While FIB machined microcantilever specimens can be found as far back as 1999 [52], the start of active research in this field is most often associated with the work of DiMaio and Roberts [53] in 2005. Their cantilever was fabricated using angled cuts into the surface of a Si wafer, leading to a pentagonal cross section. The initial notch was also fabricated via FIB, which they argued led to a slight increase in fracture toughness compared to macroscopic data, but the overall agreement was proven and subsequent experiments on 10 µm thick chemical vapor deposited WC on steel demonstrated the applicability of this technique for fracture mechanical testing of coatings, without the influence of the substrate. Armstrong *et al.* [54]

used the same geometry to investigate stress corrosion cracking on a single grain boundary (GB) in 304 stainless steel by exposing the specimen to potassium tetrathionate [55] inside the nanoindenter, emphasizing for the first time the possibility of this method to probe individual microstructural features. This further inspired multiple research groups to apply and refine this technique to investigate various interfaces, *e.g.* SiO_x/W, SiO_x/WTi or SiO_x/Cu interfaces [56], Li doped Al GBs [57] or amorphous C:H on steel [58], to name a few. While the majority of microcantilever experiments up to 2012 utilized only linear elastic fracture mechanic (LEFM) concepts, Wurster *et al.* [59] developed a framework to include EPFM via sequential unloading steps, analogous to macrocopic testing schemes. In fracture mechanics one of the main aims is to obtain geometry independent material parameters, which is only possible for specimen sizes considerably larger than any plastic zone size [60]. Incorporating EPFM reduces this threshold for specimen dimensions to some extend, which makes this a major step, especially for microscopic specimens. Furthermore, Wurster *et al.*'s [59] work was conducted *in situ* inside a scanning electron microscope (SEM), opening up the possibility to investigate crack extension during the experiment and study the interplay between deformation and crack extension features. Research continued with the focus on stable crack growth and sharp initial notches via down scaling the chevron notch geometry to fit within microcantilevers [61, 62]. In 2016 Ast *et al.* [21] refined the elastic-plastic evaluation scheme by utilizing a nanoindenter with a small sinusoidal signal imposed on the load signal, commonly referred to as continuous stiffness measurement (CSM) [63], to determine the cantilever compliance and henceforth the crack extension quasi-continuously. Nowadays multiple research groups are focusing on microcantilever bending experiments to determine various fracture related properties, with research directions ranging from *in situ* combination with other techniques, *e.g.* high-resolution electron backscatter diffraction (HR-EBSD) [64], over mixed mode testing [65] to size effects in fracture toughness [66], to name a few.

1.4 The Si-SiO_x-WTi-Cu model material system

The selected model material system consists of a ∼725 µm (001)-oriented single crystalline Si wafer with a 50–70 nm thick thermally grown oxide, on which a 270–300 nm thick WTi layer (nominal composition W-22 %Ti [67]) was deposited through magnetron sputter deposition. On top of that a 300 nm thick Cu film was deposited using the same technique, which subsequently acted as a seed layer for further galvanical deposition of Cu to

a final thickness of 5 µm, as shown schematically in Fig. 1.3a. To homogenize the Cu phase and remove residual stresses, the stack was annealed at 400 °C for 30 min (see Fig. 1.3b). A cross section of the final microstructure is shown in Fig. 1.3c using transmission electron microscopy (TEM). Similar system stacks are commonly encountered in microelectronic devices, where the Cu metallization layer serves as a heat sink [5] and the WTi layer acts as a diffusion barrier [9] against Cu-Si inter-diffusion, as this would lead to deep-level traps in the bandgap of silicon [68], resulting in loss of semiconducting properties.

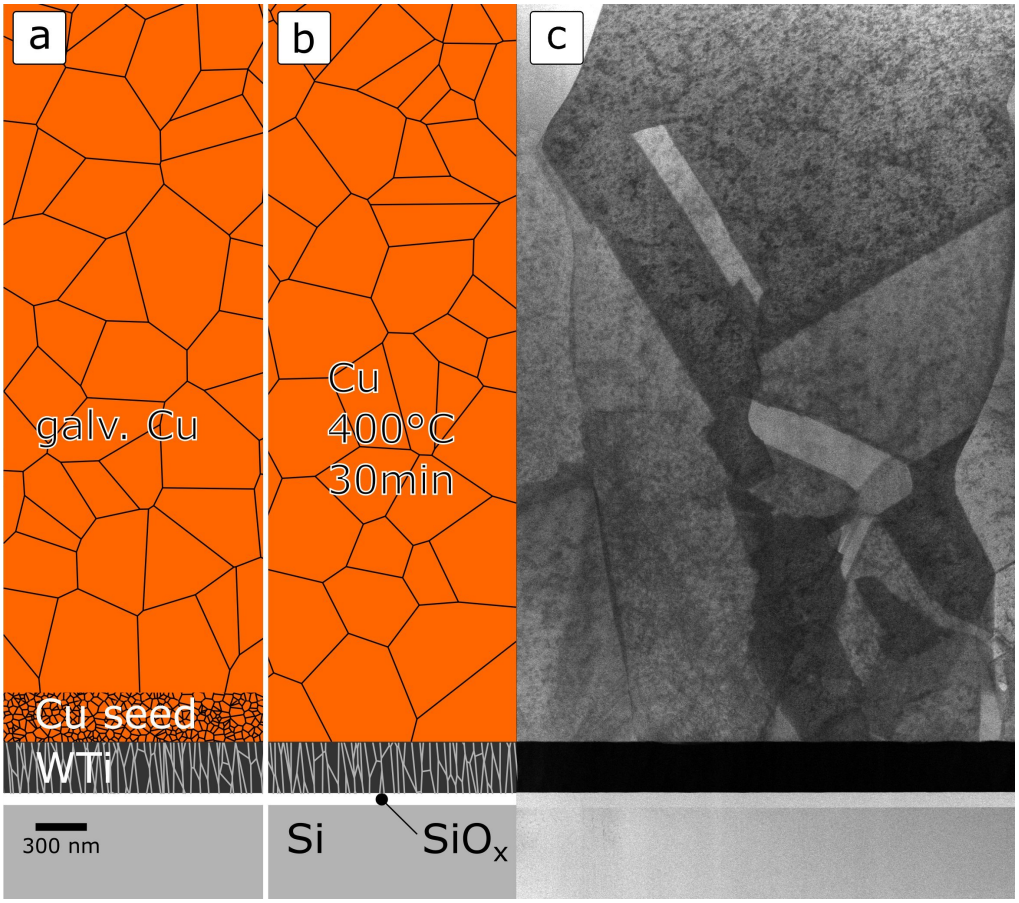

Figure 1.3: Schematic of multilayer stack (a) after fabrication (b) after annealing at 400 °C for 30 min as well as (c) corresponding TEM image of the structure.

The individual components of this configuration have been studied extensively by previous researchers. Wimmer *et al.* [69] investigated microstructural parameters and tensile properties of a Cu film with the same processing parameters as herein (Film A) and found an average grain size of (2.7 ± 0.6) µm and a 0.2 % yield strength of $\sigma_{0.2\%} = (142 \pm 5)$ MPa. While the actual grain size of the WTi layer is not determined due to challeng-

ing experimental conditions, but rather estimated as $\sim$15 nm [70] using Scherrer's equation [71], it is known that the structure is single phase body centered cubic (bcc) with a slightly increased unit cell due to incorporation of Ti into the W crystal structure [72, 73].

Chapter 2

Theoretical Principles

The mechanics of plastic deformation and fracture are by themselves large areas of still ongoing research activities, with the theoretical basis dating back as early as 1907 for Volterra's first description of dislocation theory [74] or 1921 for Griffith's energy criterion for brittle fracture [75]. Therefore, finding an easily comprehensible common ground for their interaction remains rather challenging, and addressing all of the nuances of both fields is not feasible for the present work. The following should therefore only give an overview of the theoretical background necessary to rationalize the general statements and conclusions in the appended publications, while more detailed calculations and considerations will be drawn on the basis of the WTi-Cu model interface.

2.1 Plasticity

Plastic deformation is the result of nucleation of defects or the mobility of inherent defect structures in a material, leading to an irreversible change of the overall geometric shape. While 0-dimensional point defects (vacancies, interstitial/substitutional atoms) can lead to such deformation via diffusion processes, *i.e.* creep [76], the vast majority of deformation in metals is rather carried by 1-dimensional defects called dislocations [77–79]. These features are line-like defects, resulting from a distortion in the crystal lattice, and are commonly described by the Burger's vector $\vec{b}$, which is the mismatch between a closed circuit in a dislocation-free lattice and a dislocation-containing lattice. Depending on the direction of $\vec{b}$ with respect to the line segment of the dislocation $\vec{s}$, it is generally distinguished between edge ($\vec{b} \perp \vec{s}$), screw ($\vec{b} \parallel \vec{s}$) or mixed character [77–79]. However, independent of the exact character a dislocation exhibits an elastic stress field that decays with distance from the core as r^{-1} and the interaction

between this elastic field, other inherent defects' stress fields and externally applied stresses leads to movement of the dislocations to minimize the overall potential energy of the system. The elastic energy of a single dislocation cannot be defined precisely, as it depends on the actual atomistic structure in the core region and the extent of the crystal [78]. However, it is proportional to [79]:

$$E_{elastic} \sim \mu \mathbf{b}^2 \tag{2.1}$$

where μ is the shear modulus and $\mathbf{b} = |\vec{b}|$ is the magnitude of the Burger's vector. Considering the trend towards energy minimization this leads to the fact that the most common dislocations are ones with low magnitudes of $\vec{b}$, which in an fcc crystal such as Cu lie on a $\{111\}$ plane with $\langle 110 \rangle$ direction. For Cu with a unit cell spacing of 361 pm [80] the magnitude of $\vec{b}$ along such a $\{111\}\langle 110 \rangle$ dislocation is $\mathbf{b} = 255\,\text{pm}$. However, further energy minimization can be achieved by splitting such a $\{111\}\langle 110 \rangle$ dislocation into two $\{111\}\langle 112 \rangle$ partial dislocations separated by a stacking fault [78, 79], which leads to the fact that such an extended dislocation is somewhat restricted to a given slip plane as movement out of the plane, *i.e.* cross-slip would require an energetically less favorable contraction of the spread-out dislocation by, *e.g.* a high enough backstress.

The resistance against dislocation glide in a perfect crystal can be considered based on the movement through a sinusoidal potential well, commonly referred to as the Peierls-Nabarro model [81, 82] and results in a threshold shear stress τ_{PN}, which can be considered as lattice friction. As there are twelve independent $\{111\}\langle 110 \rangle$ systems in an fcc crystal [79] and the lattice friction is rather low in Cu ($\tau_{PN} \approx 0.28\,\text{MPa}$ [83]) mobility of dislocations is rather easy to activate in a Cu crystal independent of the loading direction.

2.1.1 Dislocations and interfaces

The interaction of dislocations with two-dimensional interfaces is dependent on the type of the interface, *i.e.* GB or phase boundary, as well as crystallographic relationships between the interface and the slip planes of both involved crystals. While for certain low misorientation angles the transfer of dislocations from one grain to another is possible [84–86], as shown schematically in Fig. 2.1a, it is far more common that a dislocation interacts with the GB, changing the local atomic structure of both, dislocation and boundary. A GB is considered to consist of individual dislocations in an arrangement that accommodates the crystallographic mismatch of both

grains. For low tilt angles up to $\sim 15°$ the arrangement can be described by the well know Read-Shockley construction [87], where edge dislocations are stacked on top of each other with a certain spacing. While this construction breaks down at higher misorientation angles, periodicity is still observed in these GBs [88], leading to the conclusion that it still consists of an intrinsic arrangement of dislocations, with the caveat that these do not have a precisely defined core position in their elastic field, but rather a vague position within the GB [89]. Additional dislocations from the grain interior that are moved towards the GB by mechanical stresses can now interact with such a GB by formation of an extrinsic GB dislocation [89], which means that it exhibits a locally higher stress field than the rest of the GB. Given enough time and/or temperature an extrinsic GB dislocation can be incorporated into the GB network, eliminating the local stress concentration. However, most often there is not a single dislocation but rather multiple dislocations, *e.g.* nucleating from a single source, which are pushed towards a GB in a time too short to enable removal of dislocations through incorporation. This leads to a pile-up behavior at the GB, which exerts a back stress on the source and thus a higher threshold for further nucleation [78], as shown schematically in Fig. 2.1b. Consequently, this results in a hardening phenomenon commonly referred to as Hall-Petch behaviour [90, 91], where a higher content of GBs, *i.e.* smaller grain size, leads to higher onset stresses of plastic deformation.

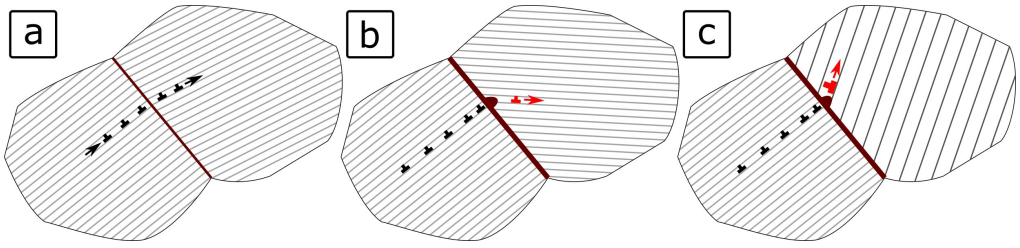

Figure 2.1: Schematic of (a) a low angle GB which allows dislocation transmission, (b) a higher angle GB and (c) a heterogeneous interface. The latter two promote a pile-up behaviour.

The same is true for interfaces between dissimilar materials, *e.g.* Cu and WTi, where a transmission of dislocations is even less likely (see Fig. 2.1c). Furthermore, considering not the interface but the free surface, *e.g.* at a crack tip, also the occurrence of image forces can play a role. Commonly, image forces are considered as the forces pulling a dislocation towards a free surface when it is in close proximity to it. This would lead to annihilation of the dislocation and thus a lower state of potential energy [78, 79]. However, dynamic effects can alter the magnitude or direction of the image force [92].

2.2 General fracture mechanics

Fracture mechanics in general treats the nucleation and propagation of cracks in materials originating from a preexisting defect or inhomogeneity. While seemingly a simple premise, no single universal treatment of the problem can be considered, as the influence of nonlinear material behavior, *e.g.* plasticity or phase transformation, can have a considerable impact, leading to the distinction between linear-elastic (LEFM) and nonlinear elastic (EPFM) fracture mechanics concepts. LEFM can be described quite well in consideration of either stress-intensity [27, 93, 94] or energy criteria [27, 75, 94], whereas EPFM raises the need for different frameworks, such as the J-Integral [27, 94, 95] or the crack tip opening displacement (CTOD) [27, 94, 96] evaluation schemes. Regardless of the chosen method, the criterion for crack extension is similar for all approaches and can be generalized as [97]:

$$D_{gen} < R_{gen} \qquad \text{no crack extension} \tag{2.2}$$

$$D_{gen} = R_{gen} \qquad \text{stable crack extension} \tag{2.3}$$

$$D_{gen} > R_{gen} \qquad \text{unstable crack extension} \tag{2.4}$$

where D_{gen} is a generalized crack driving force, *i.e.* energy release rate G, applied stress intensity K, applied J-Integral J or occurring crack tip opening displacement δ and R_{gen} is a generalized resistance to crack growth, *i.e.* energy dissipation rate R, critical stress intensity K_c, critical J-Integral J_c or critical crack tip opening displacement δ_c. Hence, independent of the chosen criterion a crack will only extend if the applied crack driving force is at least equal to the local resistance to crack growth. While the plastic deformation in the model material system chosen for this thesis raises the necessity for EPFM, *e.g.* J-Integral, the mathematics of heterogeneous interfaces is based on complex stress intensity factors, *i.e.* LEFM. Therefore, a short overview of both branches of fracture mechanics will be presented in the following.

2.2.1 Linear elastic fracture mechanics

The core ideas of potential energy based LEFM were first formulated in 1921 by Griffith building on the elastic solution of an elliptical hole by Inglis [98]. He observed that the resistance to rupture of pre-cracked glass is equivalent to twice the surface tension, *i.e.* the work to create two free surfaces [75]. While glass was used as an ideally isotropic and brittle material, the concept was picked up also for other relevant material systems,

e.g. steels, which lead to theoretical incorporation of energy dissipating elements such as plastic deformation and the well known Orowan modification to Griffith's criterion [99]:

$$G_c = 2\gamma + \gamma_p \tag{2.5}$$

where γ is the surface tension and γ_p denotes dissipated work by plastic deformation. This plastic part is generally unknown, as it depends on the occurring deformation during the fracture process, and can be orders of magnitude larger than the surface tension, which lead to the development of EPFM. However, for brittle materials and interfaces the concept still remains useful due to it's easily understandable derivation and boundary conditions. In 1957, Irwin derived a link between potential energy and local stress considerations by introducing the stress intensity factor K [93]. Considering the elastic modulus E and Poisson's ratio ν the resistances against crack extension G_c and K_c are related as [27, 93, 97]:

$$G_c = \frac{K_c^2}{E'} \qquad \text{with} \qquad E' = \begin{cases} E & \text{for plane stress} \\ E/(1-\nu^2) & \text{for plane strain} \end{cases} \tag{2.6}$$

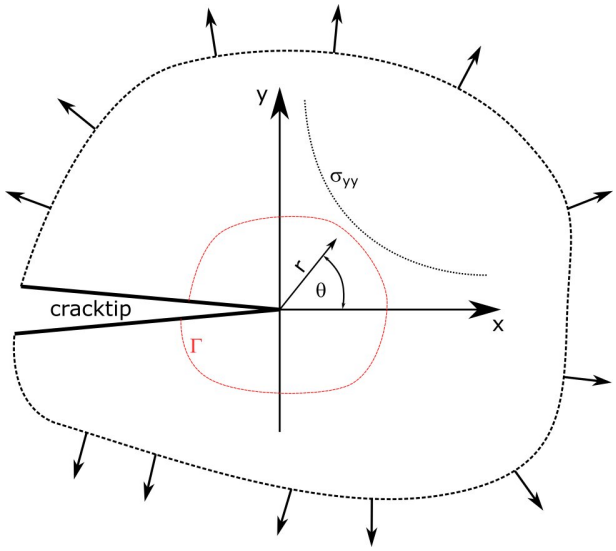

Figure 2.2: Cracktip within an arbitrarily loaded body, showing the Cartesian (x,y) and polar (r,θ) coordinate systems as well as the decay of the normal stress in y-direction as r increases.

On the example of an arbitrarily loaded body as shown in Fig. 2.2 the

stresses around the cracktip can be described as [93]:

$$\sigma_{ij} = \frac{K}{\sqrt{2\pi r}} f_{ij}(\theta) + \text{nonsingular terms} \tag{2.7}$$

where, σ_{ij} are the components of a full stress tensor, r is the radial distance from the crack tip and $f_{ij}(\theta)$ is a function of the crack plane angle. As schematically depicted for the yy-stress component in Fig. 2.2, close to the cracktip a $r^{-0.5}$ singularity dominates, which leads to the fact that the scalar stress intensity parameter has a major impact on the magnitude of the stresses in the vicinity of the tip. Therefore, K was found to act as a loading parameter, under the assumption that a cracked material can sustain an certain critical stress intensity before further crack extension occurs. However, this singularity is of purely mathematical nature as any real material would accommodate these incredibly high stresses by another mechanism, *e.g.* plastic yielding, which results in a plastic zone around the crack tip. Nevertheless, using K as a failure criterion remains valid for as long as a $r^{-0.5}$ singularity (commonly referred to as K-dominated zone) is present. This can be achieved for a wide range of materials given the specimen size is large enough. Standardized testing protocols such as ASTM E399 [100] suggest specimens geometries where:

$$a, W - a, B \geq 2.5 \left(\frac{K_c}{\sigma_{0.2\,\%}} \right)^2 \tag{2.8}$$

with crack length a, ligament size $W-a$ and specimen thickness B. Considering Cu as model material with $\sigma_{0.2\,\%} \approx 150\,\text{MPa}$ and $K_c \approx 88\,\text{MPa}\sqrt{\text{m}}$ [101] leads to 860 cm, which is far outside any feasible macroscopic specimen dimensions and orders of magnitude away from the microscopic experiments as considered herein. Nevertheless, while K_c will not be a geometry independent crack extension resistance parameter, at small loads, where majorly elastic deformation takes place, K can still be considered as a loading parameter and is effectively valid until the onset of plasticity.

2.2.2 Elastic-plastic fracture mechanics

EPFM, or more generally non-linear elastic fracture mechanics, for cases where other mechanisms than plastic deformation contribute to the fracture process, *e.g.* phase transformation, extends fracture mechanical evaluation by incorporating respective dissipating elements in the framework.

The most widely applied EPFM criterion is based on the J-integral concept around a crack tip, which was developed by Rice [95], based on Eshelby's

conserved energy integrals around elastic inhomogeneities [102] in a two-dimensional case as:

$$J = \int_{\Gamma} \phi dy - T_i \frac{\partial u_i}{\partial x} ds \tag{2.9}$$

with Γ being an arbitrary integration path around the crack tip (see Fig. 2.2), $\phi = \int_0^{\epsilon_{ij}} \sigma_{ij} d\epsilon_{ij}$ being the strain energy density, $T_i = \sigma_{ij} n_j$ being a traction vector perpendicular to the integration path, u_i being the displacement vector, and ds being a length increment on the integration path. The stress σ_{ij} and strain tensors ϵ_{ij} as well as the displacement vectors u_i are functions of the individual positions x, y. The J-integral is path independent as long as the integration path encircles only one defect, i.e. the cracktip. While Eq. 2.9 is the original mathematical description for the J-integral another interpretation is that the J-integral is the change of the stored potential energy P upon crack extension in a loaded body as [97, 103]:

$$J = -\frac{1}{B} \frac{dP}{da} \tag{2.10}$$

whereby B is the specimen thickness. Finding the actual value of P for a given cracked body would require knowledge of all boundary conditions and material parameters in conjunction with simulations. However, the change in stored elastic potential energy dP is easier to address, as it is the area between two load-displacement $(F-u)$ curves, independent of the specimen type, as long as the experimental equipment is reasonably stiff in comparison to the specimen, as shown in Fig. 2.3.

Measurements of $P-u$ data can be achieved with any mechanical testing device suitable for, *e.g.* tensile testing, which makes this approach an easy basis for the determination of experimental J-integral values. In general, there are two approaches to determine the $J-da$ behavior using these considerations. The first one is based on measuring multiple specimens with the same external geometry but differing initial crack lengths a_0 (multiple specimen measurement) [104], while the second one is based on measuring the crack extension during one single experiment (single specimen measurement) [104], either by optical or electrical means or by sequential unloading steps to measure the change in stiffness of the specimen. Nowadays the standard shifts towards using a single specimen approach, as it reduces preparation time, as well as measurement uncertainties originating from mechanical specimen fabrication and deviations in the microstructure between different specimens. However, the measurement of crack extension during an experiment brings its own challenges, specifically if standardized geometries, *e.g.* compact-tension specimens need to be used due to a re-

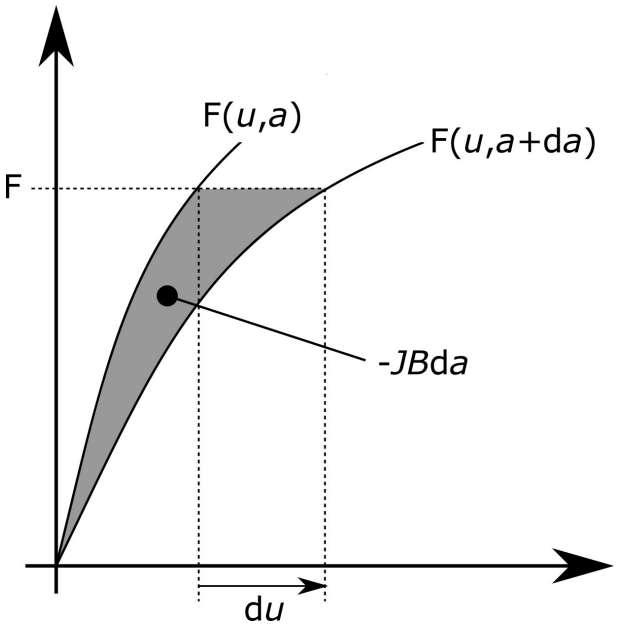

Figure 2.3: Schematic load-displacement ($F-u$) data for a crack containing body at crack lengths a and $a+da$, respectively. The gray area depicts the change in stored potential energy upon crack extension by da. (reproduced after [97])

stricting initial sample shape or volume. Nevertheless, independent of the crack extension measurement, the experimental J-integral value is calculated by splitting it into an elastic and plastic part, whereby the plastic part is calculated in an iterative manner at n points as [105]:

$$J_n = J_n^{el} + J_n^{pl} \tag{2.11}$$

$$J_n^{el} = \frac{K_n^2(1-\nu^2)}{E} \tag{2.12}$$

$$J_n^{pl} = \left\{ J_{n-1}^{pl} + \frac{\eta_{n-1}}{W-a_{n-1}} \frac{A_n^{pl} - A_{n-1}^{pl}}{B} \right\} \left\{ 1 - \gamma_{n-1} \frac{a_n - a_{n-1}}{W-a_{n-1}} \right\} \tag{2.13}$$

where K_n is calculated linear elastically [100], A_n^{pl} is the area under the $P-u$ curve minus the elastic contribution, $W-a_n$ is the remaining ligament of the specimen and η_n, γ_n are correction factors based on the specimen geometry. While these equations might seem abstruse and raise the need for correction factors, they still have the benefit of consisting only of experimentally measured values and geometries. In comparison with K evaluation schemes, the necessary specimen dimensions using J-integral calculations is also significantly less restricting with:

$$a, W - a, B \geq 10 \frac{J_c}{\sigma_{0.2\,\%}} \tag{2.14}$$

Considering again Cu as a model material with $E = 123.5\,\mathrm{GPa}$ and $\nu = 0.35$ [106] and the fact that in the linear elastic case $G_c = J_c = K_c^2/E'$ one can calculate the ratio between Eq. 2.8 and Eq. 2.14 to be 938, which means that instead of a 860 cm thick specimen, a less than 1 cm thick specimen would suffice if the J-integral evaluation scheme is to be employed.

Furthermore, similar to K, the J-Integral can be used to describe the stress state around a crack tip, but for nonlinear materials, which exhibit a hardening behavior following a Ramberg-Osgood type hardening law [107]. This is known as the HRR-field (after Hutchinson [108], Rice and Rosengren [109]) and states:

$$\sigma_{ij} = \sigma_0 \left(\frac{EJ}{\alpha \sigma_0^2 I_N r} \right)^{1/(N+1)} \tilde{\sigma}_{ij}(N, \theta) \tag{2.15}$$

where, α, σ_0 and N are Ramberg-Osgood model fit parameters for a yield offset, yield strength and hardening, respectively, I_N is a parameter depending on the hardening N and on whether plane strain or plane stress condition are assumed, and $\tilde{\sigma}_{ij}(N, \theta)$ is a function of the hardening and of the angle, describing the shape of the stress field. However, these shape functions $\tilde{\sigma}_{ij}(N, \theta)$ cannot be found analytically, but have to be calculated numerically by, *e.g.* multiple shooting method for each N, θ combination individually and are therefore tabulated [110].

Diverging from all previous fracture mechanical parameters, which where based on energy- or stress considerations, the CTOD evaluation scheme is based purely on the occurring deformation at the crack tip prior to and during the fracture process. The nucleation and movement of dislocations away from the crack tip leads to a deformation profile which can be considerably less sharp than the initial crack tip (depending on the machining method) and thus to a so called blunting of the crack tip [27]. This blunting is defined somewhat arbitrary as the rigid deformation of a point in the specimen continues after the crack has extended further but one of the most often shown constructions stems from finite element modeling and is based on a symmetric 90° intersect from the current crack tip to take this continuing deformation into account [111, 112]. In a homogeneous solid with isotropic elasticity and deformation parameters, a previously sharp crack tip would deform to a semicircle, which leads to the fact that this 90° construction yields the opening at exactly the position where the previously sharp crack tip was, as shown in Fig. 2.4.

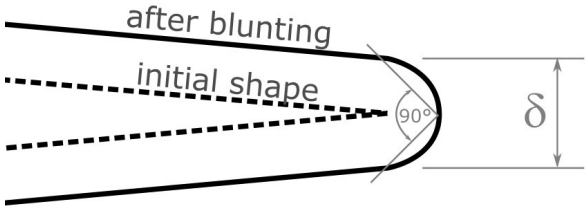

Figure 2.4: Definition of the crack tip opening displacement δ in an isotropic and homogeneous but deforming solid after Tracey [111] and Shih [112].

Based on the HRR-field solution [108, 109] for the J-integral one can calculate also the opening δ in an isotropic material following the Ramberg-Osgood [107] law and correlate it with the solution for the J-integral, which leads to the simplified relationship [112]

$$\delta = d_N \frac{J}{\sigma_0} \tag{2.16}$$

with d_N being a parameter to account for hardening N and the ratio between plasticity and elasticity σ_0/E in a given material. In the HRR model the maximum value of d_N occurs for a perfect elastic plastic transition without any hardening ($N \to \infty$) and equals d_N=0.78 for the plane strain and d_N=1 for the plane stress state, respectively. Using finite element calculations it was found that by incorporating different plasticity theories the discrepancy of this value can be up to ≈30 %, but reasonable values for common engineering materials are likely to lie between 0.4 and 0.8 [112].

2.2.3 Fracture mechanical considerations in the vicinity of heterogeneous interfaces

Independent on whether LEFM or EPFM are to be considered, all basic methodology is developed with a homogeneous material at the crack tip in mind. Therefore, the incorporation of a heterogeneous interface with differing elastic (E, ν) or plastic (σ_0) properties close-to or at the crack tip adds an additional layer of complexity to the problem, which makes any kind of experimental quantification approach rather intricate. Commonly in fracture mechanics the specimens are tested predominately in a configuration that enables opening of the crack flanks perpendicular to each other (mode I), as it is the most critical for crack extension. However, also in-plane (mode II) and out-of-plane (mode III) shearing modes as shown

on the schematic crack tip element in Fig. 2.5 can be considered based on the occurring external loading of a device during service.

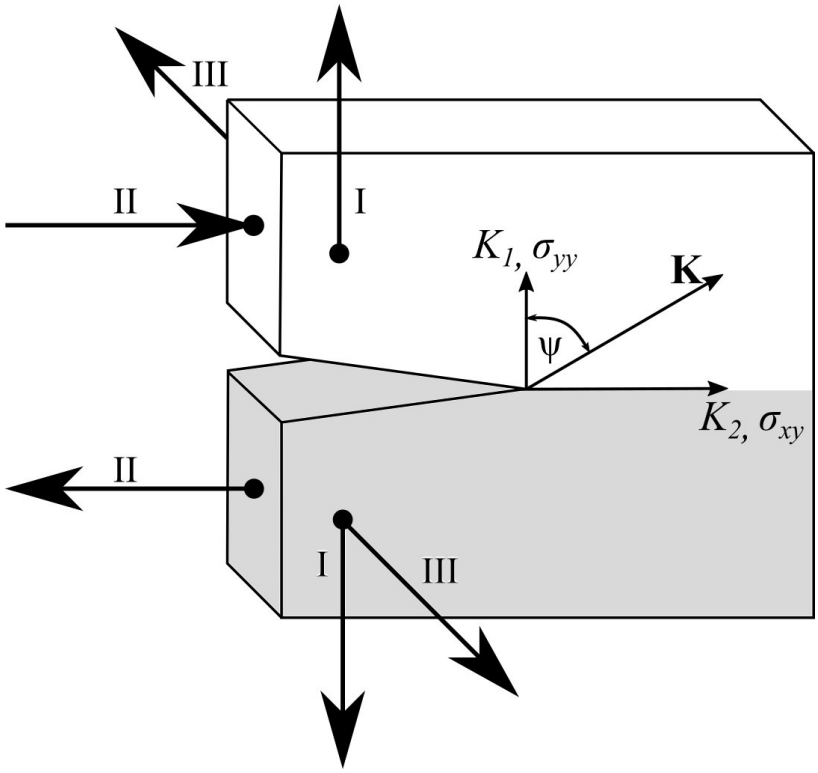

Figure 2.5: Schematic crack tip element of a bimaterial system with the interface along the crack plane depicting the three fracture mechanical loading modes (I,II,III) and the complex stress intensity factor **K** with its real (K_1, σ_{yy}) and imaginary (K_2, σ_{xy}) components as well as the mode mixity angle ψ.

In heterogeneous systems with the interface lying in the crack plane the stress state as originating from the applied external loading condition is not translated uniform down to the crack tip, but the stress state is changing due to the elastic mismatch between the two constituents. Thus, externally applying a pure mode I condition as would be the case in a homogeneous material using *e.g.* a three-point bend specimen does not lead to a pure mode I condition at the crack tip but rather a mixed mode loading. For simplification it is common to consider a plane problem (plane stress, plane strain), neglecting mode III components. Thus, two majorly acting stress components in such a setup would be σ_{yy} and σ_{xy} (see Fig. 2.2), with the respective stress intensity factors K_I and K_{II} in Eq. 2.7. As quantification criterion for the mode mixity in homogeneous solids containing a crack, usually the mode mixity angle ψ is calculated as:

$$\psi = arctan\frac{\sigma_{xy}^{\infty}}{\sigma_{yy}^{\infty}} = arctan\frac{K_{II}}{K_I} \tag{2.17}$$

based on the far field stresses σ_{yy}^{∞}, σ_{xy}^{∞}, which results in quasi-constant K_I, K_{II} stress intensities in the vicinity of the crack tip. Considering the same parameter for a heterogeneous interface proves not as trivial, due to the additional complication given by the elastic mismatch. In 1969 Dundurs found that a wide variety of two dimensional bimaterial problems depend on only two non dimensional parameters α and β [113]:

$$\alpha = \frac{\mu_1(\kappa_2+1) - \mu_2(\kappa_1+1)}{\mu_1(\kappa_2+1) + \mu_2(\kappa_1+1)} \tag{2.18}$$

$$\beta = \frac{\mu_1(\kappa_2-1) - \mu_2(\kappa_1-1)}{\mu_1(\kappa_2+1) + \mu_2(\kappa_1+1)} \tag{2.19}$$

where

$$\kappa_i = \begin{cases} (3-4\nu_i) & \text{for plane strain} \\ (3-\nu_i)/(1+\nu_i) & \text{for plane stress} \end{cases} \tag{2.20}$$

and the subscripts 1,2 correspond to the specific materials on each side of the interface. For better understanding α can be considered as the mismatch in linear elastic modulus and β can be considered as the mismatch in bulk modulus of the two materials [41]. Based on these parameters and complex potential methods for plane problems [114] one can derive a relationship for the stresses in front of the crack tip in a bimaterial as [115, 116]:

$$\sigma_{yy} + i\sigma_{xy} = \frac{\mathbf{K}}{\sqrt{2\pi r}} r^{i\epsilon} \tag{2.21}$$

where $\mathbf{K} = K_1 + iK_2$ is the complex stress intensity and

$$\epsilon = \frac{1}{2\pi} ln\left(\frac{1-\beta}{1+\beta}\right) \tag{2.22}$$

is the oscillatory index. The components of $\mathbf{K}$ (K_1, K_2) are generally not equal to the global stress intensities K_I, K_{II}, but are dependent on the

loading geometry and shape of the specimen, with the exception of the case where $\beta = 0$.

To obtain an estimate of the mode mixity for the structure of interest, concrete numbers and boundary conditions are necessary. Therefore, elastic parameters for Cu and W are assumed (as a substitute for the missing WTi values) [106, 117], as summarized in Tab. 2.1 and the geometry for a pure Cu cantilever standing out of the wafer surface, *i.e.* a length of 5 µm (see Fig. 1.3) is assumed.

Table 2.1: Elastic parameters for Cu and W, as well as calculated Dundurs' paramter α, β and oscillatory index ϵ.

	μ [GPa]	ν [-]
Cu [106]	45	0.34
W [117]	157	0.28

	α	β	ϵ
plane strain	-0.518	-0.103	0.0324
plane stress	-0.536	-0.166	0.0533

The geometry and loading dependent part of the mode mixity is commonly denoted as $\omega(\alpha, \beta, \eta)$, where η is the ratio of the heights on both sides of the crack. This value needs to be calculated numerically. Suo and Hutchinson [118] derived a general form for mixed loading conditions using the arguments of a bimaterial semi-infinite DCB specimen. Arguing that in the present case $\eta \to 0$ as the Cu layer is considerably thinner than the rest of the wafer, one can look up the solution for the given system (roughly independent of plane strain/stress conditions) as $\omega \approx 53°$. Furthermore, one can assume that in a properly designed cantilever bending situation shear forces are negligible and only loading moments exhibit a major contribution, which leads to $\psi_h = \arctan \frac{\sqrt{1/12}\sin\omega - \cos\omega}{\sqrt{1/12}\cos\omega + \sin\omega} \approx -21°$ [118]. However, this value is only valid for a set length scale (in our case the height of the Cu layer h) and if one is to translate it to any other length scale r it follows:

$$\psi_r = \psi_h + \epsilon \ln \frac{r}{h} \tag{2.23}$$

Fig. 2.6 shows the increase of ψ as well as the ratio between opening and shear stresses with distance from the crack tip. Even given the fact that this train of thought is based on various simplifications and the absolute quantities should be taken with care, it is clear that the evident change in mode mixity makes any kind of comparative quantification rather challenging.

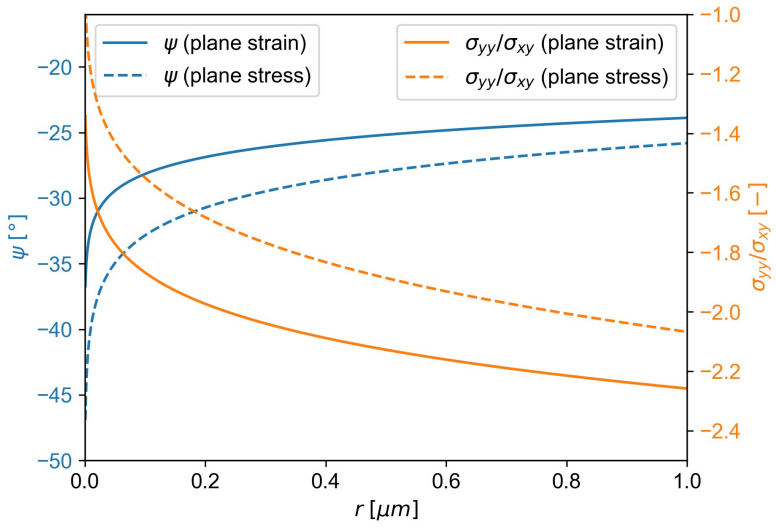

Figure 2.6: Mode mixity angle ψ and ratio between normal (mode I) and shear (mode II) stresses in front of the crack tip for a cantilever under pure bending.

2.3 Interaction of interface fracture with plasticity

In multilayered structures with at least one metallic constituent, interface fracture and dislocation plasticity are rarely exclusive, but rather simultaneous processes. While it is possible to describe experimental data using isotropic assumption and general Ramberg-Osgood type hardening [107, 119, 120], the ease and type of crack extension is very much dependent on the actual crystallographic orientations around the crack tip. Depending on the resolved shear stress on the occurring slip planes at the crack tip, nucleation and glide of dislocations is either facilitated or inhibited. Kysar [121] investigated a diffusion bonded single crystalline Cu/sapphire interface and found a strong dependence of interface fracture behaviour with respect to Cu crystal orientation. His experiments showed that whether the interface crack behaves ductile or brittle was contrary to the ease of dislocation nucleation arguments as predicted by Rice *et al.* [122] and Beltz and Rice [123]. Rather, using continuum mechanic FEM simulations, he was able to show that it is mainly driven by the opening stresses at the interface. Given that the elastic stress field of a dislocation can distort the stress field of a loaded crack, an accumulation of dislocations surrounding the crack tip can lead to a reduction of such opening stresses. This is commonly referred to as *crack tip shielding* and can be experimentally validated by *e.g.* high resolution TEM (HR-TEM) [124] or HR-EBSD [64]. While the exact distribution of

dislocations in the crack tip vicinity is usually unknown, one can calculate the distorted stress field of a crack by resultant of the presence of one single dislocation using Muskhelishvili's complex potential approach [114]. This is shown in Fig. 2.7a for a homogeneous material [125] and in Fig. 2.7b and for a heterogeneous Cu/W interface [126]. Both of these figures illustrate the opening stress σ_{yy} around a crack (red, along the negative x-axis) at a nominal load of $K_I = 1\,\mathrm{MPa}\sqrt{\mathrm{m}}$ with a dislocation positioned at an angle of 70°, 400 nm from the crack tip. While the absolute stress values should be taken with care, the distortion of the stress field is evident and the reduction of stresses given enough dislocations in the close vicinity of the crack tip seems reasonable.

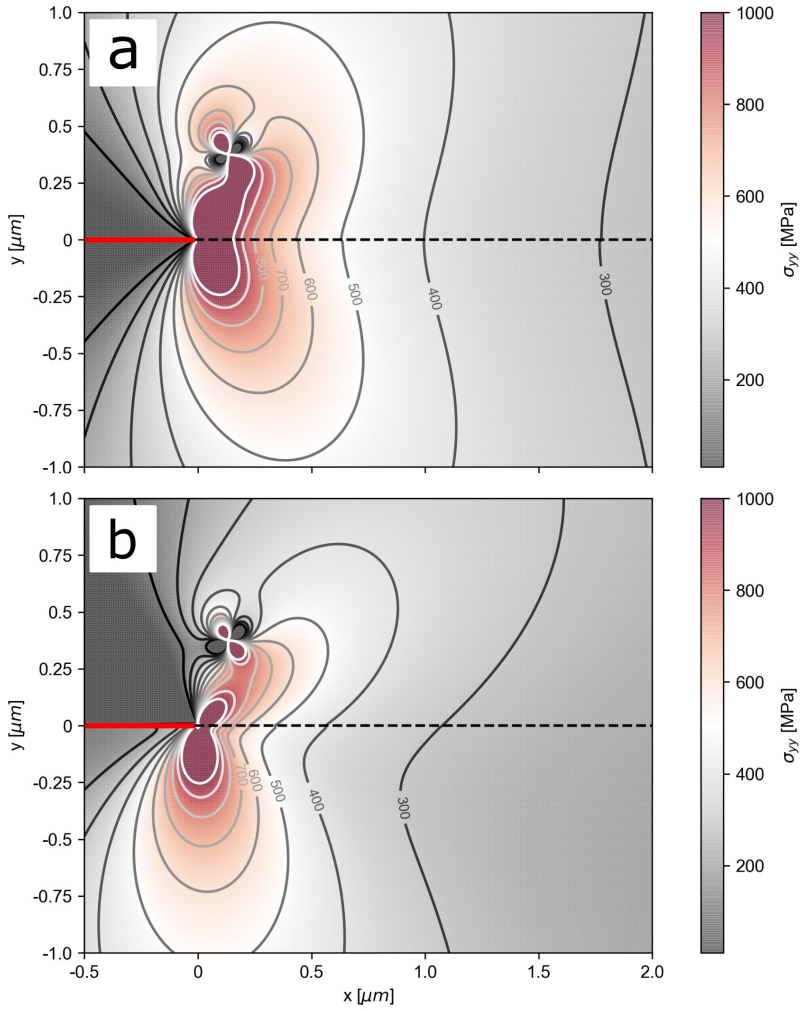

Figure 2.7: Opening stress field around a crack tip (red) in proximity to a dislocation for (a) a general homogeneous material and (b) a heterogeneous Cu/W bimaterial based on Muskhelishvili's complex potential approach [125, 126].

While some initial dislocations can be close to the crack tip prior to loading, the majority of dislocations will be newly nucleated, either from statistically occurring dislocation sources which are activated by the singular stress field or from the crack tip itself. There are various models for the nucleation of dislocations from a crack tips [127–129] which are in good agreement with the number of dislocations found in experimental TEM observations [130]. Furthermore, also the presence of a dislocation free zone, directly in front of the crack tip due to high resulting stresses has been revealed by TEM investigations [131, 132]. However this does not answer the question as to whether dislocation emission and crack extension are simultaneous processes, mutually exclusive, or at which point one changes to the other. Lin and Thomson [133] developed a framework for the interplay between cleavage and dislocation emission based on simplified isotropic energy assumptions. Whereas the detailed derivations are to excessive to be included herein, the essential message is that there are dislocation emission threshold stress intensities in each of the three modes ($k_{Ie}, k_{IIe}, k_{IIIe}$), while for crack extension only mode I (k_{Ic}) seems to be important. This leads to the fact that depending on the external loading, different regimes can be activated, from sole dislocation emission, over equal likelihood for both to mainly crack extension. However, considering that the accumulation of dislocations changes the stress field around the crack tip and thus also the local stress intensities, a transition from plasticity to crack extension can occur during loading given a specific crystallographic arrangement and dislocation activity. Thus, further raising the need for a methodology that does not only probe a scalar crack initiation value but the whole occurring fracture process.

Chapter 3

Experimental Realization

As a large fraction of this thesis focuses on developing a quantifiable methodology for interface fracture mechanical testing, the following chapter will concentrate on experimental details of the novel "*in situ* continous J-integral microcantilever testing" as well as the "*in situ* transmission push-to-pull shear testing" techniques.

3.1 *In situ* continous J-integral microcantilever testing

While in macroscopic testing a symmetric three-point bending geometry is commonly desired, microscopic fracture specimens commonly exhibit a cantilever shaped geometry due to the ease of fabrication through FIB milling. However, when testing a very local feature such as the heterogeneous WTi/Cu interface studied herein, fabrication of such a specimen still presents some challenges. In consideration with the fact that one side of the specimen needs to be accessible by an electron beam to enable SEM image formation, while a perpendicular plane is required for mechanical loading, the only region where such an interface containing specimen can be positioned is at a 90° corner of the wafer. This is shown schematically in Fig. 3.1a, where the cantilever axis, the loading axis of the wedge and the electron beam need to stand at right angles with respect to each other, forming an orthogonal system. Therefore, only one specimen can be fabricated and subsequently tested at a time, before another edge needs to be machined, which results in a rather high effort if one is to obtain statistically significant results. However, the additional information from *in situ* SEM images (see Fig.3.1b) provides rather detailed information of the deformation and fracture behaviour at the crack tip, which eliminates many unknowns and provides a high confidence in the obtained results.

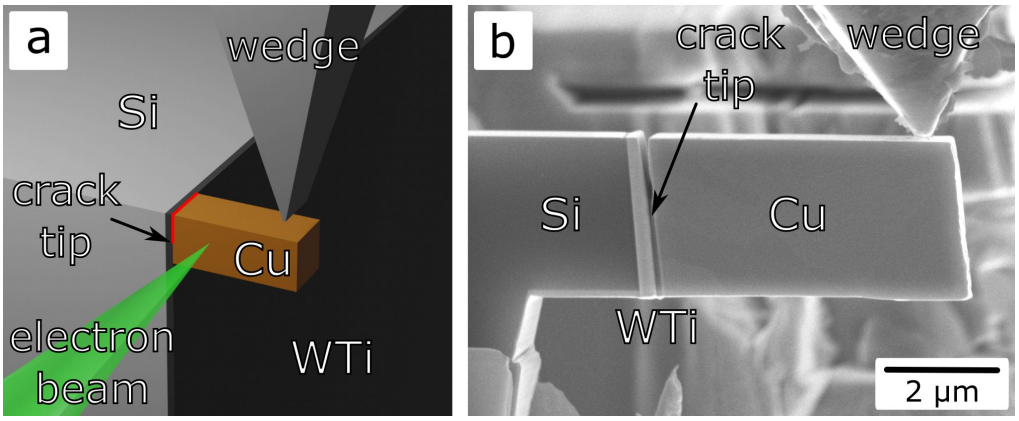

Figure 3.1: (a) Schematic of cantilever testing geometry depicting the 90° edge orientation of the specimen with respect to the electron beam and the wedge tip. (b) *In situ* SEM micrograph of a specimen before testing.

Another challenge is the fabrication of the initial notch in the specimen (see Fig. 3.1b). For an optimal notch geometry it was found that milling from the top leads to the smallest radii [134] and to circumvent major "curtaining artefacts" due to over-FIBing [135] the notches were processed with a low current of 50 pA before the final polishing steps on the cantilever side face were performed. However, with heterogeneous cantilevers it is still challenging to produce a notch that sits at the exact position to be probed, *e.g.* an interface or a single layer. Therefore, all notches were fabricated *in situ* and the positioning of the notches was adapted accordingly during the process. This led to slight differences in notch length, but all initial notch lengths were measured after testing on a 30°-tilted image of the fracture surface to obtain correct results.

To ensure pure bending without any torsional component all specimens were tested using a wedge shaped conductive diamond tip with an opening angle of 60° and an edge length of 5 µm (see Figs. 3.1). This is necessary as it simplifies the fracture mechanical assessment essentially to a two-dimensional problem, given the full wedge length is in contact with the cantilever, which was confirmed by shadows in the SEM images.

Optimal testing parameters for the used Hysitron PI 85 transducer (Bruker Corporation, Billerica, USA) were found to be load-controlled open loop with a loading rate of 10 µN/s and a sinusoidal signal with an amplitude of 5 µN and a frequency of 80 Hz. This led to a good trade off between accuracy of the continuous stiffness signal and dynamic resonance phenomena of the experimental setup, as shown in detail in **publication A**.

The crack extension measurement via stiffness was initially done using FEM simulation data and polynomial fitting (**publication A**), but a generally

applicable analytical model was developed in **publication B** and used in later works. The classical splitting of the J-integral into elastic and plastic parts [105] is only applicable in the homogeneous case (**publication A**) and was therefore exchanged by an older formulation [136, 137] in the later works (**publications C, D**).

3.2 *In situ* transmission push-to-pull shear testing

Using push-to-pull (PTP) devices is common practice in TEM investigations for standard tensile configurations. Thereby a specimen, *e.g.* a pre-processed foil [138] or a nanowire [139, 140] is intermittently attached to a movable needle and then positioned onto the PTP device using metal deposition. All of these manipulation steps need to be positioned accurately in the nm-range and therefore it needs to be done *in situ* inside an SEM/FIB workstation. However, the geometry of the PTP device does not only allow for a translation between compression and tension, but also for a translation between compression and shear. The two different positions are in close proximity to each other and in the center of the PTP device, close to the line of loading which counteracts any kinematic issues that might arise due to the symmetry of the device. These two positions are shown schematically in Fig. 3.2a. This setup allows for an investigation with different loading mode contributions (mode I, mode II) and gives an experimental approach for mode mixity investigations as outlined in **publication F**. While the processing steps for such a PTP tensile specimen are optimized rather well [138], shear specimens have not been realized on PTP devices before and therefore no fabrication routine has been developed previously. The process which lead to the first shear specimen was as follows. Initially, two plateaus were deposited to a height of $\approx 2\,\mu m$ on either side (red, blue) of the PTP device as shown in Fig. 3.2b. These were polished flat under an inclination angle of $\approx 3°$ from the top to the bottom of Fig. 3.2b. Thereafter, a pre-thinned foil ($\approx 1\,\mu m$), containing all layers of the model material was positioned on these two plateaus in such a way that the interface was aligned along the red/blue boundary in Fig. 3.2b and fixed with additional Pt deposition on top. The previous inclination angle of 3° allows for a necessary tilting degree of freedom to thin the specimen while already mounted on the chip, using decreasing FIB acceleration voltages and probe currents from 30 keV/93 pA down to 5 keV/16 pA until electron transparency was achieved. This "on-chip" thinning allowed for considerable simplification of the previous manipulation steps as a thicker foil could be used.

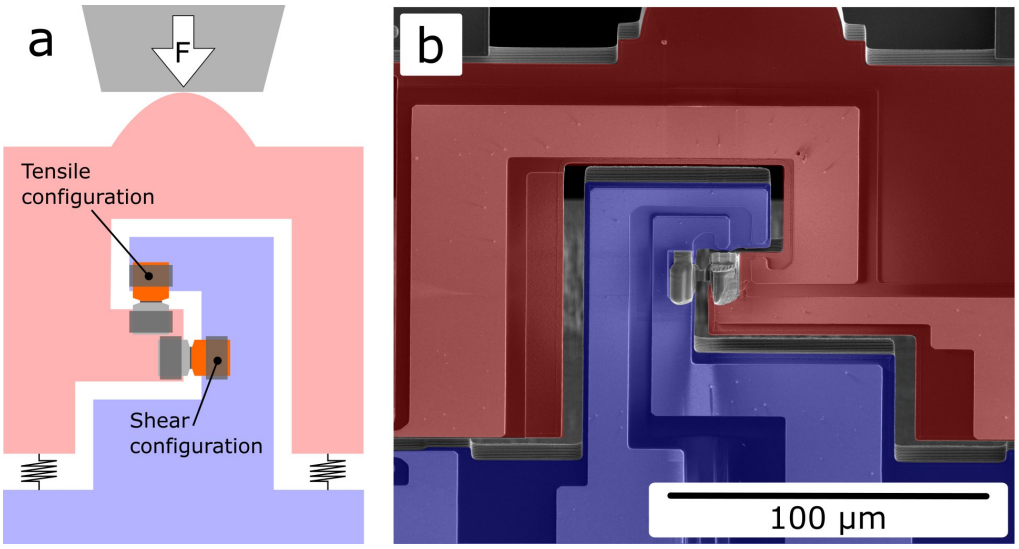

Figure 3.2: (a) Schematic PTP device depicting the standard tensile as well as the novel shear configuration and (b) SEM micrograph of an actual shear specimen with colored overlays showing the two independently moving parts.

For the experiments the PTP device was mounted inside an FT-NMT03 nanomechanical testing device (FemtoTools AG, Buchs, Switzerland), which was then inserted into an SEM equipped with an annular scanning transmission detector. The large chamber of the SEM allowed for positioning the testing device in such a way that the specimen was in the axis of the electron beam and a transmitted image was obtainable as schematically shown in Fig. 3.3. The annular detector facilitated the formation of different imaging modes as common in TEM techniques, *i.e.* bright-field (BF), annular dark-field (ADF) and high angle annular dark-field (HAADF) (see Fig. 3.3), whereby all different detector signals were obtainable simultaneously. This allowed for a detailed investigation of the occurring dislocation activity using the higher contrast of the BF images, while simultaneously studying the formation and extension of cracks using the edge sensitive ADF images. Furthermore, to obtain the best signal to noise ration on the detector and therefore the highest quality images, the PTP device was mounted such that the specimen remained on the lower side during the experiments. Thus the incoming electron beam traveled through the device before interacting with the specimen which resulted in a reduced distance between specimen and detector and therefore a shorter scattering length where signal could have been lost.

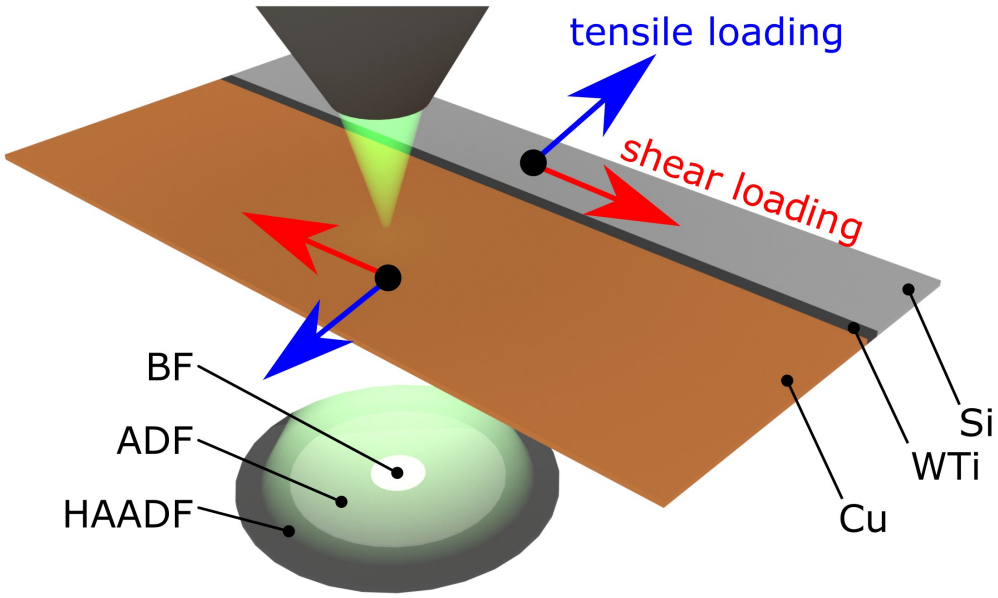

Figure 3.3: Schematic of the specimen in the transmission scanning electron microscopy setup. The annular detector underneath shows the different imaging mode regions: bright-field (BF), annular dark-field (ADF) and high angle annular dark-field (HAADF).

During the experiment the desired shear deformation was evident. However, as the gap between the two sides of the PTP device was $\approx 5\,\mu m$, which is necessary to observe the specimen, also a slight bending component was observed in the Cu phase. Nevertheless, FEM simulations revealed a mode mixity angle of 44.7°, as shown in detail in **publication F**, which suggests a mixed mode loading of roughly equal mode I and mode II contributions. Thus, it is successfully demonstrated that this novel methodology is capable of considerable shear loading and therefore a promising basis for *in situ* mixed mode investigations on the microscale.

Chapter 4

Overview of Publications

In the following an overview of all publications that originated during this thesis is given. Detailed remarks on individual co-author contributions are given prior to summaries of all appended publications. These publications are ordered as to outline the train of thought from the onset of the question of interfacial fracture behaviour in the model system to the final results. Additionally, a list of all further peer-reviewed publications that have been authored or co-authored, but do not focus on interface fracture, is given at the end of this chapter.

4.1 Remarks

The main ideas for the publications were conceived in collaboration with D. Kiener. Aside from the remarks mentioned in detail all co-authors contributed by proof-reading and constructive discussion to these publications.

Publication A: FEM simulations were conducted by D. Kozic. O. Kolednik contributed with his knowledge about fracture mechanics.

Publication B: FEM simulations were conducted by S. Kolitsch. S. Wurster contributed with his knowledge about microcantilever specimens.

Publication C: J. Zechner contributed with his knowledge about interface fracture mechanics.

Publication D: R. Bodlos conducted the DFT simulations. L. Romaner contributed with his knowledge about DFT simulations.

Publication E: G. Balbus and F. Wang operated the equipment during the experiments. D. S. Gianola contributed with his knowledge regarding general dislocation plasticity and the TSEM technique.

4.2 Publication A:

In-situ elastic-plastic fracture mechanics on the microscale by means of continuous dynamical testing

Markus Alfreider[1,2], Darjan Kozic[3], Otmar Kolednik[2], Daniel Kiener[1]

[1]Department of Materials Physics, Montanuniversität Leoben, Leoben, Austria

[2]Erich Schmid Institute for Materials Science, Austrian Academy of Science, Leoben, Austria

[3]Materials Center Leoben Forschungs GmbH, Leoben, Austria

In this publication the continous J-integral technique, initially introduced by Ast *et al.* [21], was for the first time realized *in situ* inside an SEM to obtain simultaneous mechanical and visual fracture data of a single crystalline W specimen. This methodology is based on a sinusoidal signal on top of the loading signal to obtain quasi-continuous stiffness data. While the dynamics of such a testing setup *ex situ* are easily controllable due to air damping, utilizing this technique in vacuum results in challenging experimental conditions due to the occurrence of resonance phenomena. Therefore, the publication focuses on the determination of an operational load-amplitude-frequency parameter set as well as addressing the machine compliance and obtaining a translation from stiffness change to crack extension based on experimental data of different materials. Finally, the details of J-integral evaluation in microscopic specimens, where classical macroscopic fracture mechanical assumptions are not valid, is reviewed and a new strategy is suggested, based on which the data is compared to literature values of both, macroscopic and microscopic specimens, showing good overall agreement.

4.3 Publication B:

An analytical solution for the correct determination of crack lengths via cantilever stiffness

Markus Alfreider[1], Stefan Kolitsch[2,3], Stefan Wurster[2], Daniel Kiener[1]

[1]Department of Materials Physics, Montanuniversität Leoben, Leoben, Austria

[2]Erich Schmid Institute for Materials Science, Austrian Academy of Science, Leoben, Austria

[3]Materials Center Leoben Forschungs GmbH, Leoben, Austria

This publication addresses the relationship between cantilever stiffness and crack extensions. Previously, the only analytical relationship available was based on the assumption that the whole cantilever reduces in height and not only in the cracked region [59]. This consideration was shown to be incorrect in comparison to individual finite element investigations [134], which could be explained by the fact that an extending crack reduces the stiffness only locally and not globally as the simplified assumptions in the analytical model suggest [59]. In this work, an extended analytical model is presented based on the classical Euler-Bernoulli approach with a singularity at the position of the crack tip [141], which is substituted by a rotational spring with a strength proportional to the remaining ligament length of the cantilever [142]. The result is a very compact analytical relationship, which is only dependent on the geometry of the specimen and a $1-\nu^2$ term. Given that the range of ν is 0.2-0.35 in common materials, this term varies only between 0.96 and 0.88, which suggests that it is nearly independent of the material and can be also utilized for heterogeneous systems as is the case in the present thesis. Due to the restrictions of the journal's *Express article* format, the mathematical derivations are outsourced into a supplementary document which is also appended after Publication B.

4.4 Publication C:

Addressing fracture properties of individual constituents within a Cu-WTi-SiO_x-Si multilayer

Markus Alfreider[1], Johannes Zechner[2], Daniel Kiener[1]

[1]Department of Materials Physics, Montanuniversität Leoben, Leoben, Austria

[2]KAI Kompetenzzentrum Automobil- u. Industrieelektronik GmbH, Villach, Austria

This invited publication contains the first fracture mechanical investigations on the Cu-WTi-SiO_x-Si model material system using the methodology developed in publications A and B. The focus is placed on the difference in fracture behaviour with respect to the initial notch position. Deliberately changing the notch position allowed to control the crack propagation path to change between the Cu-WTi interface and the WTi-SiO_x interface. It was found that while in the WTi-SiO_x interface the crack propagates in a purely brittle manner, other crack positions inside the WTi, or close to the WTi-Cu interface result in a major crack tip blunting and arrest of crack propagation. The mechanical data showed a step-wise crack extension for the WTi-SiO_x interface, which can be attributed to initial crack growth towards the interface. The resulting J-integral value for crack initiation is $14.2\,\mathrm{J/m^2}$, which is in good agreement with previous results, considering valid geometry factors [56]. The specimens with initial cracks inside the WTi layer and close to the WTi-Cu interface depicted a concave up J-Δa behaviour, which is invalid in classical fracture mechanic evaluations and can be attributed to the high amount of dislocation activity in comparison to crack extension. However, the specimen with the initial notch inside the WTi phase showed slight crack extension in the WTi layer before it deflected towards the WTi-Cu interface and was arrested. The initiation J-integral value was identified as $51.2\,\mathrm{J/m^2}$, which is again in excellent agreement with literature data of similar materials. The specimen with the notch in the WTi-Cu interface showed no evident crack extension in the mechanical data, which suggests that the respective initiation value in the range of $\approx$15–$23\,\mathrm{J/m^2}$ can be attributed to the onset of dislocation plasticity in the Cu phase. This work emphasizes that the developed framework for micron sized EPFM evaluation is uniquely capable of resolving and quantifying differences in fracture behaviour within this very confined volume based on the initial notch position variation of only 300 nm.

4.5 Publication D:

The influence of chemistry on the interface toughness in a WTi-Cu system

Markus Alfreider[1], Rishi Bodlos[2], Lorenz Romaner[2], Daniel Kiener[1]

[1]Department of Materials Physics, Montanuniversität Leoben, Leoben, Austria
[2]Materials Center Leoben Forschungs GmbH, Leoben, Austria

Building on the previous work, in this publication the same cantilever shaped specimens and mathematical framework are used to investigate the change in fracture behaviour upon diverging interface chemistry. To change the interface chemistry some wafers were intentionally exposed to atmosphere between the WTi deposition and the Cu seed layer deposition steps, resulting in a somewhat undefined oxygen containing interface layer. In the *in situ* SEM images it was evident that the WTi-Cu interface showed crack extension after some plastic deformation in the air exposed specimens, which was never observed for the standard vacuum processed ones. The mechanical data revealed that plastic deformation dominated up to $\approx 100\,\mathrm{J/m^2}$ before interfacial crack extension took over. To understand this change in behaviour additional density functional theory simulations where conducted on W-Cu systems with and without an oxygen interlayer. These exhibit a reduction in maximum binding energy of a factor of ≈ 8, upon air exposition. Utilizing analytical models based on the nucleation of dislocations from a crack tip as well as dislocation pile-up models, it was rendered physically plausible for fracture processes as well as dislocation plasticity to occur congruently given such a high reduction in binding energy. Furthermore, the dislocation pile-up model suggests that the accumulation of dislocations in front of the crack tip results in a change of mode mixity towards a relatively higher mode I component, which would promote the nucleation of an interface crack. This insight promotes the conclusion that interface chemistry and mode mixity might have a similar impact on the crack nucleation and extension behaviour.

4.6 Publication E:

Interface related deformation and fracture of an elastic-plastic bimaterial system resolved by *in situ* transmission scanning electron microscopy

Markus Alfreider[1,2], Glenn Balbus[2], Fulin Wang[2], Johannes Zechner[3], Daniel S. Gianola[2], Daniel Kiener[1]

[1]Department of Materials Physics, Montanuniversität Leoben, Leoben, Austria
[2]Materials Department, University of California, Santa Barbara, CA 93106, USA
[3]KAI Kompetenzzentrum Automobil- u. Industrieelektronik GmbH, Villach, Austria

In this publication a detailed investigation with respect to mode mixity is conducted on the WTi/Cu interface. As the previously introduced cantilever technique does not allow for a change in mode mixity angle, another approach based on the use of push-to-pull (PTP) devices was utilized. Thereby, electron transparent foils were produced by FIB milling and mounted on a PTP device such that either a high normal or shear component was present at the interface [138]. The specimens were tested *in situ* using a transmission configuration inside an SEM (TSEM) [143], which allowed for continuous observation of dislocation activity in the Cu phase, as well as occurring fracture processes. The opening mode tested specimen showed pronounced localization of plasticity in the Cu phase, which led to textbook-like ductile fracture by nucleation and coalescence of voids in front of the initial notches. The shear mode tested specimen on the other hand showed a wide distribution of plasticity, without any localizing dislocation paths. This absence of a pronounced ductile failure behaviour eventually led to the nucleation of an interface crack. Upon further loading plasticity and crack extension occured simultaneously and the translation of CTOD measurements (Eq. 2.16) resulted in a J-integral value of $J \approx 8.8\,\mathrm{J/m^2}$ for the initiation of crack extension. This is seemingly less than the $J \approx 15$–$23\,\mathrm{J/m^2}$ for dislocation activity. However, this discrepancy does not take into account the differences in crystallographic orientation of the Cu grains close to the interface, nor the position and amount of dislocation sources close to the crack tip. Thus, the $J \approx$15–$23\,\mathrm{J/m^2}$ are interpreted as onset

range for dislocation plasticity in the given system, as underlined by reproducible results in the cantilever experiments, where multiple Cu grains were probed. Contrarily, the $J \approx 8.8\,\mathrm{J/m^2}$ initiation value for crack extension is unique for the investigated specimen with the respective specific configuration of Cu grains in front of the crack tip. This result shows that, while fracture can in principle occur along the WTi/Cu interface, in most cases dislocation plasticity exhibits a lower threshold and is therefore more likely to occur. For interface fracture to take place, a specific configuration that inhibits dislocation plasticity is necessary. Without loss of generality by restriction to concrete slip systems, this could be achieved through either a high amount of mode II loading, which spreads dislocation plasticity and counteracts localization, or through restriction of dislocation mobility close to the crack tip, *e.g.* by grain refinement or solid solution hardening.

4.7 Further peer-reviewed Publications

Wurster, S.; Treml, R.; Fritz, R.; Kapp, M. W.; Langs, E.; Alfreider, M.; Ruhs, C.; Imrich, P.; Felber, G.; Kiener, D. Novel Methods for the Site Specific Preparation of Micromechanical Structures *Practical Metallography* **52** 131-146 (2015)

Alfreider, M.; Jeong, J.; Esterl, R.; Oh, S.; Kiener, D. Synthesis and Mechanical Characterisation of an Ultra-Fine Grained Ti-Mg Composite *Materials* **9**, 688 (2016)

Jeong, J.; Alfreider, M.; Konetschnik, R.; Kiener, D., Oh; S. H. In-situ TEM observation of $\langle 101\bar{2} \rangle$ twin-dominated deformation of Mg pillars: Twinning mechanism, size effects and rate dependency *Acta Materialia* **158** 407-421 (2018)

Kiener, D.; Fritz, R.; Alfreider, M.; Leitner, A.; Pippan, R.; Maier-Kiener, V. Rate limiting deformation mechanisms of bcc metals in confined volumes *Acta Materialia* **166** 687-701 (2019)

Wat, A.; Lee, J. I.; Ryu, C. W.; Gludovatz, B.; Kim, J.; Tomsia, A. P.; Ishikawa, T.; Schmitz, J.; Meyer, A.; Alfreider, M.; Kiener, D.; Park, E. S.; Ritchie, R. O. Bioinspired nacre-like alumina with a bulk-metallic glass-forming alloy as a compliant phase *Nature Communications* **10** (2019)

Alfreider, M.; Issa, I.; Renk, O.; Kiener, D. Probing defect relaxation in ultra-fine grained Ta using micromechanical spectroscopy *Acta Materialia* **185** 309-319 (2020)

Glechner, T.; Lang, S.; Hahn, R.; Alfreider, M.; Moraes, V.; Primetzhofer, D.; Ramm, J.; Kolozsvári, S.; Kiener, D.; Riedl, H. Correlation between

fracture characteristics and valence electron concentration of sputtered Hf-C-N based thin films *Surface and Coatings Technology* **399** 126212 (2020)

Alfreider, M.; Meindlhumer, M.; Maier-Kiener, V.; Hohenwarter, A.; Kiener, D. Extracting information from noisy data: strain mapping during dynamic in situ SEM experiments *Journal of Materials Research* **36** 2291-2304 (2021)

Burtscher, M.; Alfreider, M.; Schmuck, K.; Clemens, H.; Mayer, S.; Kiener, D. In situ fracture observations of distinct interface types within a fully lamellar intermetallic TiAl alloy *Journal of Materials Research* **36** 2465-2478 (2021)

Kiener, D.; Jeong, J.; Alfreider, M.; Konetschnik, R.; Oh, S. H. Prospects of Using Small Scale Testing to Examine Different Deformation Mechanisms in Nanoscale Single Crystals—A Case Study in Mg *Crystals* **11** 61 (2021)

Chapter 5

Summary and Conclusion

This work focuses on establishing a framework capable of the investigation of interface fracture properties of micron scaled bimaterial interfaces in the presence of a significantly plastically deforming constituent. For validation these concepts were applied to a multilayered Cu-WTi-SiO_x-Si model material system, as common in the microelectronics industry.

A novel investigation technique was developed based on microcantilever shaped specimens tested *in situ* inside an SEM, with crack extension converted from continuous stiffness measurements. This allowed the use of the J-integral concept and thus EPFM evaluation schemes in order to take considerable extents of plastic deformation into account. This technique was validated on single crystalline W specimens by comparison with literature data. However, the absence of elastic parameters (with the exception of Poisson's ratio) in the derived analytical solution for crack measurements suggests validity also for heterogeneous systems as investigated herein.

Specimens with varying initial notch positions showed evident differences in fracture behaviour, from purely brittle fracture along the SiO_x/WTi interface to pronounced crack tip blunting without crack extension for the WTi/Cu interface. This confirmed that the presented methodology is capable of resolving and quantifying changes in fracture processes within very confined spatial changes of $\approx 300\,\mathrm{nm}$. Nevertheless, the lack of crack extension along the WTi/Cu interface made precise determination of the occurring mechanisms rather challenging. Therefore, additional specimens with a deliberately induced oxygen contamination layer were tested and showed a distinct transition from pure crack tip blunting to nucleation and extension of an interfacial crack. These investigations were supported by additional density functional theory simulations and analytical models resulting in the prediction that a change in mode mixity with accumulation of dislocation plasticity is the reason for the occurence of crack extension.

To obtain a more detailed understanding of the interaction between plasticity and fracture processes along the WTi/Cu interface in the light of varying mode mixity, additional experiments were conducted using a push-to-pull (PTP) setup inside an SEM operated in transmission configuration. This allowed for simultaneous observation of dislocations in the Cu phase and crack extension along the interface. Two extreme orientations were investigated with a maximum in opening stresses (mode I) and shear stresses (mode II) at the interface, respectively. These experiments revealed that a high amount of mode I contribution results in localization of plasticity and therefore ductile failure in the Cu phase, while the shear mode tested specimens exhibited nucleation and growth of an interface crack. However, while no general quantified statement can be draw from these specimens, they clearly emphasize that mechanistically crack extension along the WTi/Cu interface is a result of local inhibition of dislocation plasticity through *e.g.* crystallographic orientation or grain size in the vicinity of the interface and/or crack tip.

In conclusion, a detailed investigation on the fracture behaviour of a WTi/Cu interface was conducted by newly developed methods and analytical concepts. The result can be summarized as follows:

- In general, the dominant dissipation mechanism is dislocation plasticity in the Cu phase, which results in pronounced crack tip blunting.
- Deliberately weakening the interface by air exposition during synthesis enables crack nucleation and propagation in conjunction with plastic deformation.
- Given the standard synthesis route, crack extension along the interface is very difficult and occurs only when dislocation nucleation and mobility in the vicinity of the interface are strongly inhibited.
- A high amount of mode II loading component, through *e.g.* thermal loading, distributes dislocation plasticity further and prevents pronounced localization. In conjunction with specific crystallographic features this can lead to a combination of hardening phenomena that enable the formation of an interface crack.

While the presented study was focused on a specific model system, the novel presented methods such as the *in situ* continous J-integral microcantilever deflection technique or the PTP shear testing configuration in conjunction with analytical frameworks can be utilized for various different systems, where heterogeneous interfaces and mixed mode loading are present, *e.g.* thermal wear-, barrier- or biofunctional coatings. Thus, the developed methodologies can find several applications within the micromechanics community as well as in general miniaturized engineering.

References

1. Mirigliano, M. & Milani, P. Electrical conduction in nanogranular cluster-assembled metallic films. *Advances in Physics: X* **6,** 1908847 (2021).
2. Tanner, C. M., Perng, Y.-C., Frewin, C., Saddow, S. E. & Chang, J. P. Electrical performance of Al2O3 gate dielectric films deposited by atomic layer deposition on 4H-SiC. *Applied Physics Letters* **91,** 203510 (2007).
3. Thakare, J. G., Pandey, C., Mahapatra, M. M. & Mulik, R. S. Thermal Barrier Coatings - A State of the Art Review. *Metals and Materials International* (2020).
4. Hoque, M. J. *et al.* Modular Heat Sinks for Enhanced Thermal Management of Electronics. *Journal of Electronic Packaging* **143** (2021).
5. Nelhiebel, M. *et al.* Effective and reliable heat management for power devices exposed to cyclic short overload pulses. *Microelectronics Reliability* **53,** 1745–1749 (2013).
6. Ilican, S., Caglar, Y., Caglar, M. & Yakuphanoglu, F. Structural, optical and electrical properties of F-doped ZnO nanorod semiconductor thin films deposited by sol–gel process. *Applied Surface Science* **255,** 2353–2359 (2008).
7. Xi, J.-Q. *et al.* Optical thin-film materials with low refractive index for broadband elimination of Fresnel reflection. *Nature Photonics* **1,** 176–179 (2007).
8. Shang, C. *et al.* Perspectives on Advances in Quantum Dot Lasers and Integration with Si Photonic Integrated Circuits. *ACS Photonics* **8,** 2555–2566 (2021).
9. Souli, I. *et al.* Effect of growth conditions on interface stability and thermophysical properties of sputtered Cu films on Si with and without WTi barrier layers. *Journal of Vacuum Science & Technology B, Nanotechnology and Microelectronics: Materials, Processing, Measurement, and Phenomena* **35,** 022201 (2017).
10. Subramanian, C. & Strafford, K. Review of multicomponent and multilayer coatings for tribological applications. *Wear* **165,** 85–95 (1993).

11. Wolf, K. V. *et al.* An investigation of adhesion in drug-eluting stent layers. *Journal of Biomedical Materials Research Part A* **87A,** 272–281 (2008).
12. Rahbar, N. *et al.* Adhesion and interfacial fracture toughness between hard and soft materials. *Journal of Applied Physics* **104,** 103533 (2008).
13. Evans, A., Mumm, D., Hutchinson, J., Meier, G. & Pettit, F. Mechanisms controlling the durability of thermal barrier coatings. *Progress in Materials Science* **46,** 505–553 (2001).
14. Begley, M. R. & Wadley, H. N. Delamination resistance of thermal barrier coatings containing embedded ductile layers. *Acta Materialia* **60,** 2497–2508 (2012).
15. Shih, H.-Y. *et al.* Ultralow threading dislocation density in GaN epilayer on near-strain-free GaN compliant buffer layer and its applications in hetero-epitaxial LEDs. *Scientific Reports* **5** (2015).
16. Gopalan, S., Krabbenborg, B., Egbers, J.-H., van Velzen, B. & Zingg, R. Reliability of power transistors against application driven temperature swings. *Microelectronics Reliability* **42,** 1623–1628 (2002).
17. Detzel, T., Glavanovics, M. & Weber, K. Analysis of wire bond and metallization degradation mechanisms in DMOS power transistors stressed under thermal overload conditions. *Microelectronics Reliability* **44,** 1485–1490 (2004).
18. Nelhiebel, M. *et al.* A reliable technology concept for active power cycling to extreme temperatures. *Microelectronics Reliability* **51,** 1927–1932 (2011).
19. Fattori, R. & Piva, T. Drug-eluting stents in vascular intervention. *The Lancet* **361,** 247–249 (2003).
20. Chichareon, P. *et al.* Mechanical properties and performances of contemporary drug-eluting stent: focus on the metallic backbone. *Expert Review of Medical Devices* **16,** 211–228 (2019).
21. Ast, J., Merle, B., Durst, K. & Göken, M. Fracture toughness evaluation of NiAl single crystals by microcantilevers-a new continuous J-integral method. *Journal of Materials Research* **31,** 3786–3794 (2016).
22. Charalambides, P. G., Lund, J., Evans, A. G. & McMeeking, R. M. A Test Specimen for Determining the Fracture Resistance of Bimaterial Interfaces. *Journal of Applied Mechanics* **56,** 77–82 (1989).
23. Klingbeil, N. & Beuth, J. Interfacial fracture testing of deposited metal layers under four-point bending. *Engineering Fracture Mechanics* **56,** 113–126 (1997).
24. Hofinger, I., Oechsner, M., Bahr, H.-A. & Swain, M. V. Modified four-point bending specimen for determining the interface fracture

energy for thin, brittle layers. *International Journal of Fracture* **92,** 213–220 (1998).

25. Eberl, C., Gianola, D. S. & Hemker, K. J. Mechanical Characterization of Coatings Using Microbeam Bending and Digital Image Correlation Techniques. *Experimental Mechanics* **50,** 85–97 (2008).
26. Völker, B. *et al.* Mechanical and chemical investigation of the interface between tungsten-based metallizations and annealed borophosphosilicate glass. *Thin Solid Films* **583,** 170–176 (2015).
27. Anderson, T. L. *Fracture Mechanics: Fundamentals and Applications, Second Edition* (CRC Press, 2005).
28. Østergaard, R. C., Sørensen, B. F. & Brøndsted, P. Measurement of Interface Fracture Toughness of Sandwich Structures under Mixed Mode Loadings. *Journal of Sandwich Structures & Materials* **9,** 445–466 (2007).
29. Sundararaman, V. & Davidson, B. D. An unsymmetric double cantilever beam test for interfacial fracture toughness determination. *International Journal of Solids and Structures* **34,** 799–817 (1997).
30. Shahverdi, M., Vassilopoulos, A. P. & Keller, T. Mixed-Mode I/II fracture behavior of asymmetric adhesively-bonded pultruded composite joints. *Engineering Fracture Mechanics* **115,** 43–59 (2014).
31. Akazawa, T. New test method for evaluating internal stress due to compression of concrete (the splitting tension test)(part 1). *Journal of Japan Society of Civil Engineers* **29,** 777–787 (1943).
32. *ASTM Standard C496-17, Standard Test Method for Splitting Tensile Strength of Cylindrical Concrete Specimens* (ASTM International, 2017).
33. Wang, J.-S. & Suo, Z. Experimental determination of interfacial toughness curves using Brazil-nut-sandwiches. *Acta Metallurgica et Materialia* **38,** 1279–1290 (1990).
34. Banks-Sills, L., Travitzky, N., Ashkenazi, D. & Eliasi, R. A methodology for measuring interface fracture properties ofcomposite material. *International Journal of Fracture* **99,** 143–161 (1999).
35. Pethica, J. B., Hutchings, R. & Oliver, W. C. Hardness measurement at penetration depths as small as 20 nm. *Philosophical Magazine A* **48,** 593–606 (1983).
36. Uchic, M. D., Dimiduk, D. M., Florado, J. N. & Nix, W. D. Sample dimensions influence strength and crystal plasticity. *Science* **305,** 986–989 (2004).
37. Kiener, D., Grosinger, W., Dehm, G. & Pippan, R. A further step towards an understanding of size-dependent crystal plasticity: In situ tension experiments of miniaturized single-crystal copper samples. *Acta Materialia* **56,** 580–592 (2008).

38. Moon, M.-W., Lee, K.-R., Oh, K. & Hutchinson, J. Buckle delamination on patterned substrates. *Acta Materialia* **52,** 3151–3159 (2004).
39. Cordill, M., Bahr, D., Moody, N. & Gerberich, W. Adhesion measurements using telephone cord buckles. *Materials Science and Engineering: A* **443,** 150–155 (2007).
40. Pundt, A., Brekerbohm, L., Niehues, J., Wilbrandt, P.-J. & Nikitin, E. Adhesion-energy measurements by means of white-light interferometry and controlled-buckling technique. *Scripta Materialia* **57,** 889–892 (2007).
41. Hutchinson, J. & Suo, Z. in *Advances in Applied Mechanics* 63–191 (Elsevier, 1991).
42. Bagchi, A., Lucas, G., Suo, Z. & Evans, A. A new procedure for measuring the decohesion energy for thin ductile films on substrates. *Journal of Materials Research* **9,** 1734–1741 (1994).
43. Bagchi, A. & Evans, A. Measurements of the debond energy for thin metallization lines on dielectrics. *Thin Solid Films* **286,** 203–212 (1996).
44. Rossington, C., Evans, A. G., Marshall, D. B. & Khuri-Yakub, B. T. Measurements of adherence of residually stressed thin films by indentation. II. Experiments with ZnO/Si. *Journal of Applied Physics* **56,** 2639–2644 (1984).
45. Kriese, M. D., Gerberich, W. W. & Moody, N. R. Quantitative adhesion measures of multilayer films: Part II. Indentation of W/Cu, W/W, Cr/W. *Journal of Materials Research* **14,** 3019–3026 (1999).
46. Steinmann, P., Tardy, Y. & Hintermann, H. Adhesion testing by the scratch test method: The influence of intrinsic and extrinsic parameters on the critical load. *Thin Solid Films* **154,** 333–349 (1987).
47. Bull, S. Failure modes in scratch adhesion testing. *Surface and Coatings Technology* **50,** 25–32 (1991).
48. Kleinbichler, A., Zechner, J. & Cordill, M. Buckle induced delamination techniques to measure the adhesion of metal dielectric interfaces. *Microelectronic Engineering* **167,** 63–68 (2017).
49. Jensen, H. M. The blister test for interface toughness measurement. *Engineering Fracture Mechanics* **40,** 475–486 (1991).
50. Hohlfelder, R. J., Luo, H., Vlassak, J. J., Chidsey, C. E. D. & Nix, W. D. Measuring Interfacial Fracture Toughness With The Blister Test. *MRS Proceedings* **436** (1996).
51. Konetschnik, R., Daniel, R., Brunner, R. & Kiener, D. Selective interface toughness measurements of layered thin films. *AIP Advances* **7,** 035307 (2017).
52. Ichikawa, Y. *et al.* Fracture Behavior of Micro-Sized Ni-P Amorphous Alloy Specimens. *MRS Proceedings* **605** (1999).

53. DiMaio, D. & Roberts, S. Measuring fracture toughness of coatings using focused-ion-beam-machined microbeams. *Journal of Materials Research* **20,** 299–302 (2005).
54. Armstrong, D., Rogers, M. & Roberts, S. Micromechanical testing of stress corrosion cracking of individual grain boundaries. *Scripta Materialia* **61,** 741–743 (2009).
55. Horowitz, H. H. Chemical studies of polythionic acid stress-corrosion cracking. *Corrosion Science* **23,** 353–362 (1983).
56. Matoy, K., Detzel, T., Müller, M., Motz, C. & Dehm, G. Interface fracture properties of thin films studied by using the micro-cantilever deflection technique. *Surface and Coatings Technology* **204,** 878–881 (2009).
57. Kupka, D. & Lilleodden, E. T. Mechanical Testing of Solid-Solid Interfaces at the Microscale. *Experimental Mechanics* **52,** 649–658 (2011).
58. Schaufler, J., Schmid, C., Durst, K. & Göken, M. Determination of the interfacial strength and fracture toughness of a-C:H coatings by in-situ microcantilever bending. *Thin Solid Films* **522,** 480–484 (2012).
59. Wurster, S., Motz, C. & Pippan, R. Characterization of the fracture toughness of micro-sized tungsten single crystal notched specimen. *Philosophical Magazine* **92,** 1–23 (2012).
60. Pippan, R., Wurster, S. & Kiener, D. Fracture mechanics of micro samples: Fundamental considerations. *Materials & Design* **159,** 252–267 (2018).
61. Mueller, M. *et al.* Fracture toughness testing of nanocrystalline alumina and fused quartz using chevron-notched microbeams. *Acta Materialia* **86,** 385–395 (2015).
62. Žagar, G., Pejchal, V., Mueller, M. G., Michelet, L. & Mortensen, A. Fracture toughness measurement in fused quartz using triangular chevron-notched micro-cantilevers. *Scripta Materialia* **112,** 132–135 (2016).
63. Li, X. & Bhushan, B. A review of nanoindentation continuous stiffness measurement technique and its applications. *Materials Characterization* **48,** 11–36 (2002).
64. Ast, J., Polyakov, M. N., Mohanty, G., Michler, J. & Maeder, X. Interplay of stresses, plasticity at crack tips and small sample dimensions revealed by in-situ microcantilever tests in tungsten. *Materials Science and Engineering: A* **710,** 400–412 (2018).
65. Mathews, N. G., Mishra, A. K. & Jaya, B. N. Mode dependent evaluation of fracture behaviour using cantilever bending. *Theoretical and Applied Fracture Mechanics* **115,** 103069 (2021).

66. Issa, I. *et al.* In-situ TEM investigation of toughening in Silicon at small scales. *Materials Today* **48,** 29–37 (2021).
67. Kalha, C. *et al.* Thermal and oxidation stability of TixW1-x diffusion barriers investigated by soft and hard x-ray photoelectron spectroscopy. *Journal of Applied Physics* **129,** 195302 (2021).
68. Brotherton, S. D., Ayres, J. R., Gill, A., van Kesteren, H. & Greidanus, F. J. A. M. Deep levels of copper in silicon. *Journal of Applied Physics* **62,** 1826–1832 (1987).
69. Wimmer, A. *et al.* Temperature dependent transition of intragranular plastic to intergranular brittle failure in electrodeposited Cu micro-tensile samples. *Materials Science and Engineering: A* **618,** 398–405 (2014).
70. Wang, Q., Fan, Z. & Liang, S. Thermal stability of nanocrystalline W-Ti diffusion barrier thin films. *Science China Technological Sciences* **53,** 1049–1055 (2010).
71. Scherrer, P. in *Kolloidchemie Ein Lehrbuch* 387–409 (Springer Berlin Heidelberg, 1912).
72. Plappert, M., Humbel, O., Koprowski, A. & Nowottnick, M. Characterization of Ti diffusion in PVD deposited WTi/AlCu metallization on monocrystalline Si by means of secondary ion mass spectroscopy. *Microelectronics Reliability* **52,** 1993–1997 (2012).
73. Fugger, M. *et al.* Comparison of WTi and WTi(N) as diffusion barriers for Al and Cu metallization on Si with respect to thermal stability and diffusion behavior of Ti. *Microelectronics Reliability* **54,** 2487–2493 (2014).
74. Volterra, V. Sur l'équilibre des corps élastiques multiplement connexes. fre. *Annales scientifiques de l'École Normale Supérieure* **24,** 401–517 (1907).
75. Griffith, A. A. The Phenomena of Rupture and Flow in Solids. *Philosophical Transactions of the Royal Society A: Mathematical, Physical and Engineering Sciences* **221,** 163–198 (1921).
76. Blum, W., Eisenlohr, P. & Breutinger, F. Understanding creep—a review. *Metallurgical and Materials Transactions A* **33,** 291–303 (2002).
77. Nabarro, F. *Theory of crystal dislocations* (Oxford University Press, 1967).
78. Hirth, J. P. & Lothe, J. *Theory of Dislocations (2nd ed.)* 857 (Wiley & Sons, 1983).
79. Hull, D. & Bacon, D. *Introduction to Dislocations* (Elsevier, 2011).
80. Kittel, C. *Introduction to Solid State Physics* (WILEY, 2004).
81. Nabarro, F. Fifty-year study of the Peierls-Nabarro stress. *Materials Science and Engineering: A* **234-236,** 67–76 (1997).
82. Schoeck, G. The Peierls dislocation: Line energy, line tension, dissociation and deviation. *Acta Materialia* **45,** 2597–2605 (1997).

83. Kamimura, Y. *et al.* Peierls stresses estimated via the Peierls-Nabarro model using ab-initio Γ -surface and their comparison with experiments. *Acta Materialia* **148,** 355–362 (2018).
84. Lee, T. C., Robertson, I. M. & Birnbaum, H. K. An in situ transmission electron microscope deformation study of the slip transfer mechanisms in metals. *Metallurgical Transactions A* **21,** 2437–2447 (1990).
85. Shen, Z., Wagoner, R. & Clark, W. Dislocation and grain boundary interactions in metals. *Acta Metallurgica* **36,** 3231–3242 (1988).
86. Werner, E. & Prantl, W. Slip transfer across grain and phase boundaries. *Acta Metallurgica et Materialia* **38,** 533–537 (1990).
87. Read, W. T. & Shockley, W. Dislocation Models of Crystal Grain Boundaries. *Physical Review* **78,** 275–289 (1950).
88. Sass, S. L., Tan, T. Y. & Balluffi, R. W. The detection of the periodic structure of high-angle twist boundaries. *The Philosophical Magazine: A Journal of Theoretical Experimental and Applied Physics* **31,** 559–573 (1975).
89. Priester, L. *Grain Boundaries - From Theory to Engineering* (Springer, 2013).
90. Hall, E. O. The deformation and ageing of mild steel: III discussion and results. *Proceedings of the Physical Society B* **64,** 747–753 (1951).
91. Petch, H. J. The cleavage strength of polycrystals. *Journal of Iron and Steel Institute* **174,** 25–28 (1953).
92. Gurrutxaga-Lerma, B., Balint, D. S., Dini, D. & Sutton, A. P. Elastodynamic image forces on dislocations. *Proceedings of the Royal Society A: Mathematical, Physical and Engineering Sciences* **471,** 20150433 (2015).
93. Irwin, G. R. Analysis of stresses and strains near the end of a crack traversing a plate. *Journal of Applied Mechanics* **24,** 361–364 (1957).
94. Zhu, X.-K. & Joyce, J. A. Review of fracture toughness (G, K, J, CTOD, CTOA) testing and standardization. *Engineering Fracture Mechanics* **85,** 1–46 (2012).
95. Rice, J. R. *A path independent integral and the approximate analysis of strain concentartion by notches and cracks* (Brown University, 1967).
96. Wells, A. A. *Unstable Crack Propagation in Metals: Cleavage and Fast Fracture* in *Proceedings of the Crack Propagation Symposium* (1961).
97. Kolednik, O. in *Encyclopedia of Composites* (Wiley, 2012).
98. Inglis, C. E. Stresses in a Plate Due to the Presence of Cracks and Sharp Corners. *SPIE Milestone Series* **137,** 3–17 (1913).

99. Orowan, E. Notch brittleness and the strength of metals. *Transactions of the Institution of Engineers and Shipbuilders Scotland* **89,** 165–215 (1945).
100. *ASTM Standard E399-09, Standard Test Method for Linear-Elastic Plane-Strain Fracture Toughness KIC of Metallic Materials* 399 (ASTM international, West Conshohocken, USA, 2009).
101. Hohenwarter, A. & Pippan, R. A comprehensive study on the damage tolerance of ultrafine-grained copper. *Materials Science and Engineering: A* **540,** 89–96 (2012).
102. Eshelby, J. D. The Force on an Elastic Singularity. *Philosophical Transactions of the Royal Society A: Mathematical, Physical and Engineering Sciences* **244,** 87–112 (1951).
103. Rice, J. R. in *Fracture: An Advanced Treatise* (ed Liebowitz, H.) 191–311 (Academic Press, N.Y., 1968).
104. *ISO 12135:2002 - Metallic materials — Unified method of test for the determination of quasistatic fracture toughness* (International Organization for Standardization, 2002).
105. *ASTM Standard E1820-13, Standard Test Method for Measurement of Fracture Toughness* 1820 (ASTM International, West Conshohocken, USA, 2013).
106. Ledbetter, H. M. & Naimon, E. R. Elastic Properties of Metals and Alloys. II. Copper. *Journal of Physical and Chemical Reference Data* **3,** 897–935 (1974).
107. Ramberg, W. & Osgood, W. *Description of stress-strain curves by three parameters* (NACA, 1943).
108. Hutchinson, J. Singular behaviour at the end of a tensile crack in a hardening material. *Journal of the Mechanics and Physics of Solids* **16,** 13–31 (1968).
109. Rice, J. & Rosengren, G. Plane strain deformation near a crack tip in a power-law hardening material. *Journal of the Mechanics and Physics of Solids* **16,** 1–12 (1968).
110. Brocks, W. *et al. Lösung der HRR-Feld-Gleichungen der elastisch-plastischen Bruchmechanik* (Wirtschaftsverl. NW, Verl. für Neue Wiss, Bremerhaven, 1990).
111. Tracey, D. M. Finite Element Solutions for Crack-Tip Behavior in Small-Scale Yielding. *Journal of Engineering Materials and Technology* **98,** 146–151 (1976).
112. Shih, C. Relationships between the J-integral and the crack opening displacement for stationary and extending cracks. *Journal of the Mechanics and Physics of Solids* **29,** 305–326 (1981).
113. Dundurs, J. in *Mathematical Theory of Dislocations* (ed Mura, T.) 70–115 (ASME, 1969).

114. Muskhelishvili, N. I. in *Some Basic Problems of the Mathematical Theory of Elasticity* 89–104 (Springer Netherlands, 1977).
115. Rice, J. R. & Sih, G. C. Plane Problems of Cracks in Dissimilar Media. *Journal of Applied Mechanics* **32,** 418–423 (1965).
116. Hutchinson, J. W., Mear, M. E. & Rice, J. R. Crack Paralleling an Interface Between Dissimilar Materials. *Journal of Applied Mechanics* **54,** 828–832 (1987).
117. Lowrie, R. & Gonas, A. M. Dynamic Elastic Properties of Polycrystalline Tungsten, 24°-1800°C. *Journal of Applied Physics* **36,** 2189–2192 (1965).
118. Suo, Z. & Hutchinson, J. W. Interface crack between two elastic layers. *International Journal of Fracture* **43,** 1–18 (1990).
119. Shih, C. Cracks on bimaterial interfaces: elasticity and plasticity aspects. *Materials Science and Engineering: A* **143,** 77–90 (1991).
120. Tvergaard, V. & Hutchinson, J. W. The influence of plasticity on mixed mode interface toughness. *Journal of the Mechanics and Physics of Solids* **41,** 1119–1135 (1993).
121. Kysar, J. W. Directional dependence of fracture in copper/sapphire bicrystal. *Acta Materialia* **48,** 3509–3524 (2000).
122. Rice, J. R., Suo, Z. & Wang, J.-S. in *Metal–Ceramic Interfaces* 269–294 (Elsevier, 1990).
123. Beltz, G. & Rice, J. Dislocation nucleation at metal-ceramic interfaces. *Acta Metallurgica et Materialia* **40,** S321–S331 (1992).
124. Adhika, D. R., Tanaka, M., Daio, T. & Higashida, K. Crack tip shielding observed with high-resolution transmission electron microscopy. *Microscopy* **64,** 335–340 (2015).
125. Pippan, R., Weinhandl, H. & Kreuzer, H. G. M. in *Multiscale Modelling of Plasticity and Fracture by Means of Dislocation Mechanics* 149–184 (Springer Vienna, 2010).
126. Zhang, T.-Y. & Li, J. C. M. Interaction of an edge dislocation with an interfacial crack. *Journal of Applied Physics* **72,** 2215–2226 (1992).
127. Rice, J. R. & Thomson, R. Ductile versus brittle behaviour of crystals. *The Philosophical Magazine: A Journal of Theoretical Experimental and Applied Physics* **29,** 73–97 (1974).
128. Schoeck, G. Dislocation emission from crack tips. **63,** 111–120 (1991).
129. Li, J. Computer simulation of dislocations emitted from a crack. *Scripta Metallurgica* **20,** 1477–1482 (1986).
130. Zielinski, W., Lii, M. & Gerberich, W. Crack-tip dislocation emission arrangements for equilibrium —I. In situ TEM observations of Fe2wt%Si. *Acta Metallurgica et Materialia* **40,** 2861–2871 (1992).
131. Ohr, S. An electron microscope study of crack tip deformation and its impact on the dislocation theory of fracture. *Materials Science and Engineering* **72,** 1–35 (1985).

132. Ohr, S. Dislocation-crack interaction. *Journal of Physics and Chemistry of Solids* **48,** 1007–1014 (1987).
133. Lin, I.-H. & Thomson, R. Cleavage, dislocation emission, and shielding for cracks under general loading. *Acta Metallurgica* **34,** 187–206 (1986).
134. Ast, J., Przybilla, T., Maier, V., Durst, K. & Göken, M. Microcantilever bending experiments in NiAl-Evaluation, size effects, and crack tip plasticity. *Journal of Materials Research* **29,** 2129–2140 (2014).
135. Brinckmann, S., Matoy, K., Kirchlechner, C. & Dehm, G. On the influence of microcantilever pre-crack geometries on the apparent fracture toughness of brittle materials. *Acta Materialia* **136,** 281–287 (2017).
136. Rice, J. R., Paris, P. C. & Merkle, J. G. in *Progress in Flaw Growth and Fracture Toughness Testing* (eds Kaufman, J. *et al.*) 231–245 (ASTM International, West Conshohocken, PA, 1973).
137. Zhu, Y. T., Liao, X. Z. & Wu, X. L. Deformation twinning in nanocrystalline materials. *Progress in Materials Science* **57,** 1–62 (2012).
138. Stinville, J. *et al.* Dislocation dynamics in a nickel-based superalloy via in-situ transmission scanning electron microscopy. *Acta Materialia* **168,** 152–166 (2019).
139. Gianola, D. S. & Eberl, C. Micro- and nanoscale tensile testing of materials. *JOM* **61,** 24–35 (2009).
140. Shin, J., Richter, G. & Gianola, D. S. Suppressing instabilities in defect-scarce nanowires by controlling the energy release rate during incipient plasticity. *Materials & Design* **189,** 108460 (2020).
141. Biondi, B. & Caddemi, S. Closed form solutions of Euler-Bernoulli beams with singularities. *International Journal of Solids and Structures* **42,** 3027–3044 (2005).
142. Alijani, A., Abadi, M. M., Darvizeh, A. & Abadi, M. K. Theoretical approaches for bending analysis of founded Euler-Bernoulli cracked beams. *Archive of Applied Mechanics* **88,** 875–895 (2018).
143. Callahan, P. G. *et al.* Transmission scanning electron microscopy: Defect observations and image simulations. *Ultramicroscopy* **186,** 49–61 (2018).

Appendix

Publication A

In-situ elastic-plastic fracture mechanics on the microscale by means of continuous dynamical testing

Materials and Design 148 (**2018**) p. 177-187
doi:10.1016/j.matdes.2018.03.051

In-situ elastic-plastic fracture mechanics on the microscale by means of continuous dynamical testing

Markus Alfreider[1,2], Darjan Kozic[3], Otmar Kolednik[2], and Daniel Kiener[1]

[1]Department of Materials Physics, Montanuniversität Leoben, Leoben, Austria
[2]Erich Schmid Institute for Materials Science, Austrian Academy of Science, Leoben, Austria
[3]Materials Center Leoben Forschungs GmbH, Leoben, Austria

Abstract

Measuring the local behaviour of a propagating crack in a quantitative manner has always been a challenge in the field of fracture mechanics. In-situ microcantilever testing inside a scanning electron microscope (SEM) is one of the most promising techniques for the investigation thereof. However, quantifying such experiments is fairly challenging. Here, for the first time we utilize a continuous measurement of the dynamic compliance in-situ to permit evaluation of the crack length. Microcantilever experiments have been performed on brittle single crystalline Si and nanocrystalline Fe to assess the stability of the setup, the applicability of the technique inside an SEM and to establish a correlation between stiffness and crack length. Subsequently, micromechanical fracture tests were performed on single crystalline, $\langle 001 \rangle \{001\}$ oriented tungsten as a model material and continuous J-Δa curves were measured. The gathered data was evaluated with close relation to standardized fracture mechanics testing and showed an overall agreement with literature data. This novel possibility to measure J-Δa curve behaviour continuously and locally while also following the crack extension through in-situ imaging inside an SEM is generally applicable and will allow new insights in the crack propagation of modern materials.

Part 1
Introduction

With the development of micro- and nanomechanical testing [1–4], also a wide new field of miniaturized fracture testing techniques [5–12] were created. These enable a very local examination of various materials that would be otherwise impossible to test, such as micron-sized hard coatings [13–15], specific microstructural features such as individual grain boundaries [16, 17] or interfaces [18–20], layers in a multilayer stack [21] or single ceramic fibres [22]. However, miniaturizing sample dimensions results in the fact that the plastic zone in front of a crack tip can extend over a considerable part of the sample, even for macroscopically brittle materials such as tungsten. Thus, the application of linear elastic fracture mechanics (LEFM) is often questionable. Furthermore, stable crack extension is often the topic of interest in various investigations [19, 23, 24]. Wurster *et al.* [25] were the first to systematically investigate elastic-plastic fracture mechanics (EPFM) on tungsten in micron-sized cantilever shaped specimen by means of J-integral and crack tip opening displacement (CTOD) evaluations. They reported good agreement between their data and literature values of macroscopically tested specimens, proposing that fracture toughness characteristics of elastic-plastic samples can generally be tested on the microscale as well. However, they also found that an evaluation of the J-integral based on sequential unloading steps results in an overestimation of the fracture toughness compared to macroscopic samples, which can be led back to only a small number of unloading cycles, due to concerns regarding low-cycle fatigue. Considering that a small crack extension of hundreds of nanometres can already be a noticeable change of ligament length in a micron-sized sample, it is necessary to take this into account upon evaluation of the J-integral. Ast *et al.* [26] resolved this issue by continuously measuring the stiffness of a cantilever with a sinusoidal signal superimposing the loading excitation, commonly known as continuous stiffness measurement (CSM) signal, and subsequently calculated the crack length as a function of that stiffness. However, these experiments were carried out ex-situ in a nanoindenter, which does not allow a detailed study of crack propagation during the experiment. The current work aims to further improve this technique by implementing such a CSM testing approach in a scanning electron microscope (SEM), allowing for in-situ imaging of the crack extension upon loading. This will permit a direct correlation between crack extension and stiffness changes on a micron scale.

Part 2
Experimental procedure

2.1 Materials and sample preparation

Three different materials were chosen for this work, namely semiconductor-industry grade single crystalline (sxx) Si and electrochemically deposited nanocrystalline (nc) Fe for calibration and evaluation reasons, as well as sxx W, as well documented semi-brittle model material for validation of the technique itself. The W single crystal was grown by the procedure described by Glebovsky [27] and is identical to the one studied by Wurster *et al.* [25] and Riedle *et al.* [28]. The sxx Si and nc Fe were prepared using conventional mechanical grinding and polishing techniques to obtain a wedge shaped specimen with an approximately 20 µm thick topside. The sxx W was prepared also by mechanical grinding, but the final polishing step was conducted electrochemically with a 2 % NaOH solution. Subsequently cantilevers were prepared by focussed ion beam (FIB) milling (Leo 1540XB, Carl Zeiss AG, Oberkochen, Germany) with currents ranging from 10 nA for coarse cuts to fine milling with 50 pA at 30 kV voltage [29]. Notches were created with 50 pA before the final polishing step. Subsequently polishing the side face after cutting the notch allows the removal of large curtaining artefacts and creates a straight crack front through the whole cantilever. The final dimensions of all cantilevers were measured from SEM images and are summarized in Table 1. The initial crack length a was measured on higher magnification images of the fracture surface. All standard deviations stem from repeated measurements.

Table 1: Final dimensions of the three tested sxx W specimens.

	B [µm]	W [µm]	L [µm]	L' [µm]	a [µm]
Sample 1	3.3 ± 0.1	3.8 ± 0.2	14.4 ± 0.1	15.8 ± 0.1	1.22 ± 0.06
Sample 2	3.0 ± 0.2	3.6 ± 0.1	19.3 ± 0.1	20.7 ± 0.1	1.03 ± 0.06
Sample 3	2.1 ± 0.4	2.7 ± 0.2	9.7 ± 0.1	11.4 ± 0.1	0.98 ± 0.07

2.2 Testing setup

All tests were conducted using a Hysitron picoindenter PI 85 (Bruker Corporation, Billerica, USA) with a nanoDMA III upgrade for CSM measurement.

Experiments without the CSM signal were conducted in closed-loop load-controlled mode with a data acquisition rate of 200 Hz, while experiments using the CSM signal were performed in open-loop load-controlled mode with a data acquisition rate of 300 Hz, a sinusoidal vibration of 80 Hz frequency and 3 microN load amplitude. All experiments were conducted with a constant loading rate of 10 µN/s. During the tests SEM images were taken continuously for later correlation at a rate of 2 images/s. Fig. 1a shows schematically the outline of the specimen, including relevant geometries: width B, height W, length to notch L, length to base L' and notch depth a. All specimens were tested using a wedge shaped indenter as indicated in Fig. 1a (red). The alignment of specimen and wedge were done manually until no projected surface was seen in the SEM images.

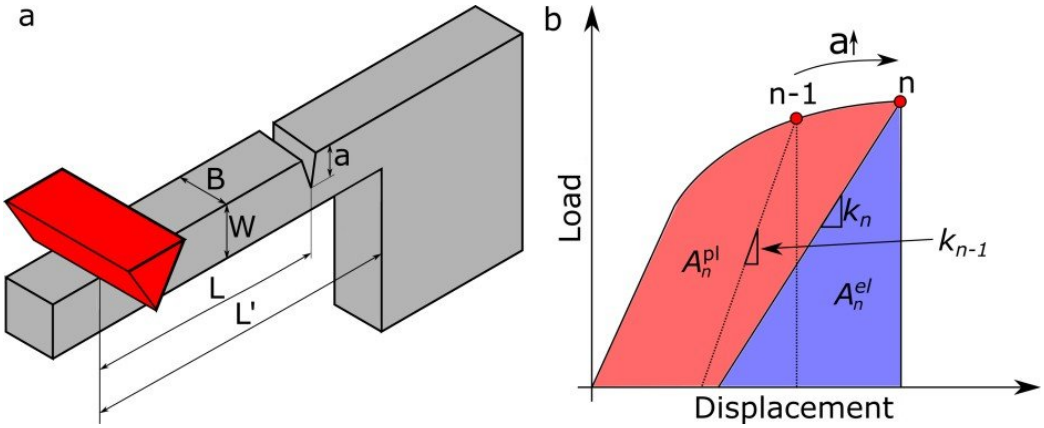

Figure 1: (a) Cantilever geometry with: width B, height W, length to notch L, length to base L' and notch depth a. The red body indicates the wedge shaped indenter. (b) Schematic load displacement curve showing the plastic and elastic parts of the mechanical work for two subsequent data points, n-1 and n, respectively.

2.3 Fracture toughness evaluation

For the evaluation of the following results only the raw data: time t, displacement u, load F and dynamic compliance c (=displacement amplitude/load amplitude) was used. Dynamic stiffness k was calculated as the inverse of the compliance k=c^{-1}. For the evaluation of the J-integral according to EPFM the iterative method described in ASTM 1820 [30] was applied:

$$J(a) = J^{el}(a) + J^{pl}(a) \tag{1}$$

$$J_n^{el} = \frac{K_{q,n}^2(1-\nu^2)}{E} \tag{2}$$

$$J_n^{pl} = \left\{ J_{n-1}^{pl} + \frac{\eta_n}{W-a_n}\frac{A_n^{pl}-A_{n-1}^{pl}}{B} \right\} \left\{ 1 - \gamma_n \frac{a_n - a_{n-1}}{W-a_n} \right\} \tag{3}$$

where $J_{el}(a)$ and $J_{pl}(a)$ are the elastic and plastic J-Integral values at specific crack lengths a. The number of iteration steps is n and the stress intensity factor K_q was evaluated following ASTM 399 [31]:

$$K_{q,n} = \frac{F_n L}{BW^{1.5}} f\left(\frac{a_n}{W}\right) \tag{4}$$

Here B, W and L are geometric dimensions as shown in Fig. 1a, F is the load and $f(a/W)$ is a geometry factor specified for the cantilever geometry. The subscript q denotes that it is a conditional value and not a geometry independent fracture toughness parameter. In this study the function proposed by Wurster *et al.* [32] was used. The plastic part of the J-integral was calculated using geometry independent prefactors η=1.9 and γ=0.9 as proposed for single edge notched bend (SENB) specimen in ASTM 1820 [30], due to the similarity in loading dynamic between this geometry and cantilever shaped beams. The plastic work A_{pl} was computed numerically from the load-displacement curves for each point n after Eq. 5, where u_n, F_n and k_n are the respective displacement, load and stiffness.

$$A_n^{pl} = A_n - A_n^{el} = \int_0 u_n F du - \frac{F_n^2}{2k_n} \tag{5}$$

Fig. 1b shows the areas of the plastic (A_{pl}) and elastic (A_{el}) parts of the work done for two subsequent data points in the schematic load-displacement curve. Considering that a crack extension results in a reduction in cantilever stiffness ($k_{n-1} \rightarrow k_n$) it is evident that A_{el} changes not only due to increase in load, but also due to increase in crack length.

2.4 Finite element simulation

For the correlation between crack length and change in stiffness two dimensional finite element (FE) simulations were conducted using the commercial software package ABAQUS (Simulia, Dassault Systèmes SE, Vélizy-Villacoublay, France). A constant load line displacement was applied and the resulting force was calculated to evaluate the cantilever stiffness. This was done for a/W-ratios varying from 0 to 0.85. The FE models were built using 2D-plane strain elements (CPE4) with the smallest element size of approximately 10 nm directly at the crack tip. The resulting stiffness k was normalized by the stiffness of an unnotched cantilever $k_0{=}k(a/W{=}0)$ to remove any influence of cantilever geometry. Three different materials were analysed using small-strain theory, namely Cu with $E{=}$ 130 GPa/ $\nu{=}$ 0.34, Si with $E{=}$ 170 GPa/ $\nu{=}$ 0.28 and W $E{=}$ 410 GPa/ ν 0.28. Furthermore, the geometries were varied from $B{=}$ 3–9 µm and $L{=}$ 16–26 µm, while $L' - L$ was kept constant, spanning a range of typical experimental dimensions.

Part 3
Results

3.1 Dynamic setup

As the application of harmonic excitation on top of a quasi-static loading is already a major point of debate in the literature regarding various dynamic effects [33–35], it is necessary to thoroughly investigate the possible influence of testing frequency on the compliance measurement. This was addressed by frequency sweep testing on sxx Si cantilevers in unnotched (Fig. 2a) and notched (Fig. 2b) condition with a preload of 50 µm and a load amplitude of 5 µN. Fig. 2c shows that the system has an inherent resonance peak at around 114 Hz (black data) in vacuum and out of contact. This peak shifts towards higher frequencies when in contact with the beam through the increase in system stiffness (red data). However, the peak shifts back towards the out of contact condition with increasing notch depth (blue data), due to the thereby reduced beam stiffness.

Fig. 3a shows representative data of a load-time sequence as used for this test, including a reference segment at the beginning, which is set to 220 Hz by default from the manufacturer. Thus, the first few seconds of every test are above the resonance frequency of the system. For each cantilever two tests

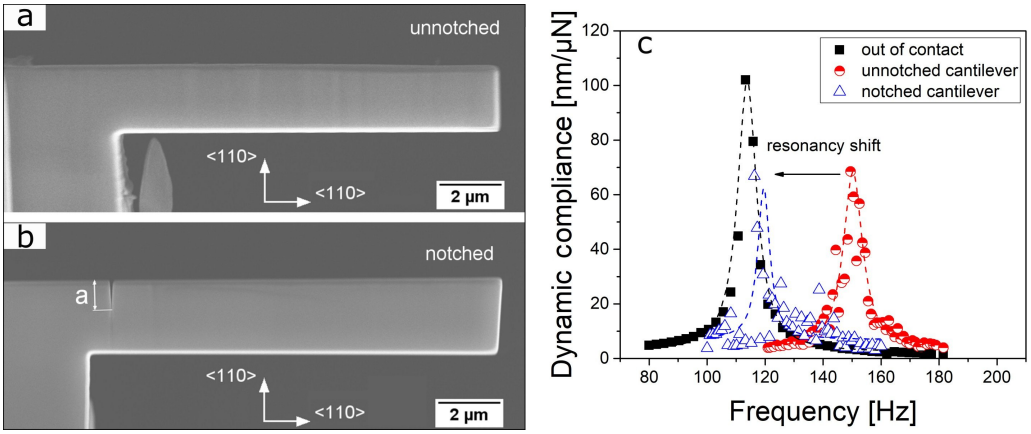

Figure 2: SEM images of (a) unnotched and (b) notched sxx Si cantilevers. (c) The dynamic compliance data as a function of frequency shows that the resonance peak shifts back to the inherent resonancy of the system with increased notch depth.

were conducted well below (80 Hz) and above (200 Hz) the resonance frequency of the system. Fig. 3b depicts the phase shift over displacement data, clearly indicating that load and displacement are in phase (phase shift=0°) for a testing frequency of 80 Hz and out of phase (phase shift=−180°) for a testing frequency of 200 Hz. It is also evident that the phase shift changes at the end of the reference segment, from out of phase to in phase condition. Fig. 3c shows the stiffness over displacement data for the unnotched and notched specimens. It is evident that for both cantilevers the measurements at 200 Hz result in a much higher noise and a different stiffness level as the measurements at 80 Hz. Since the stiffness of a notched cantilever of approximately the same geometrical dimensions should be smaller than that of an unnotched one, it is clear that the 200 Hz data is implausible.

Another aspect to consider is whether the dynamic compliance actually represents the compliance of the cantilever, or if any other unknown influence factors (*e.g.*: machine compliance, contact compliance) need to be taken into account. Therefore, an unnotched sxx Si cantilever was loaded elastically, with and without CSM signal in order to get a quasi-static and a dynamic stiffness of the cantilever. For comparison the Young's modulus was calculated, by applying classical Euler-Bernoulli beam theory [36], from the stiffness k and the radius of curvature ρ_0 gathered from in-situ SEM images, according to following equation:

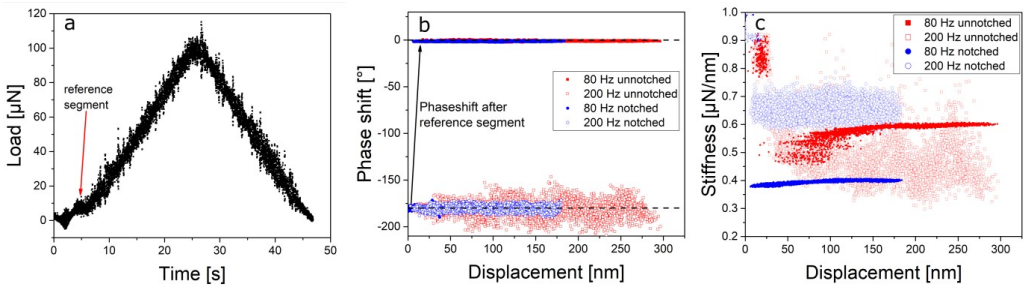

Figure 3: (a) Load-time data following the used loading sequence including a 220 Hz reference segment. (b) Phase shift over displacement data for notched/unnotched samples at 80/200 Hz. (c) Stiffness over displacement data for the same samples, indicating the increase in scatter when testing above the resonance frequency of the system.

$$E = \frac{(L')^3}{3I} k_0 = \frac{F L' \rho_0}{I} \tag{6}$$

where I denotes the area moment of inertia.

Fig. 4a shows an overlay of SEM images taken at contact (F= 0 µN) and at maximum load (F= 200 µN), from which the curvatures on the lower (compression) and upper (tension) bounds of the cantilever were measured by tracking points along the cantilever boundaries (coloured points) and subsequent fitting of a $3^r d$ order polynom as shown in Fig. 4b. The curvature at the base of the cantilever (x= 0 µm) was calculated for the outermost fibres. All error calculations were conducted using uncertainty estimations based on uncorrelated input quantities [37]. The resulting Young's moduli are: E_{dyn}= (139 ± 15) GPa for the dynamical measurement, E_{slope}= (92 ± 9) GPa for the slope of the quasi-static measurement, $E_{compression}$= (144 ± 28) GPa for the curvature measurements on the compression side and $E_{tension}$= (12 ± 19) GPa for the curvature measurements on the tension side. It is evident that the dynamically evaluated Young's modulus yields results in good accordance with the evaluated moduli from curvature, as well as literature values, which range from 169 GPa for the ⟨110⟩ direction to 130 GPa for the ⟨001⟩ direction [38]. E_{slope} underestimates the actual modulus by over 30 %, which is due to negligence of machine and contact compliance. Thus, for the following we utilize the dynamic compliance measurement taken at a frequency of 80 Hz, as it delivers valid data without requiring any major corrections.

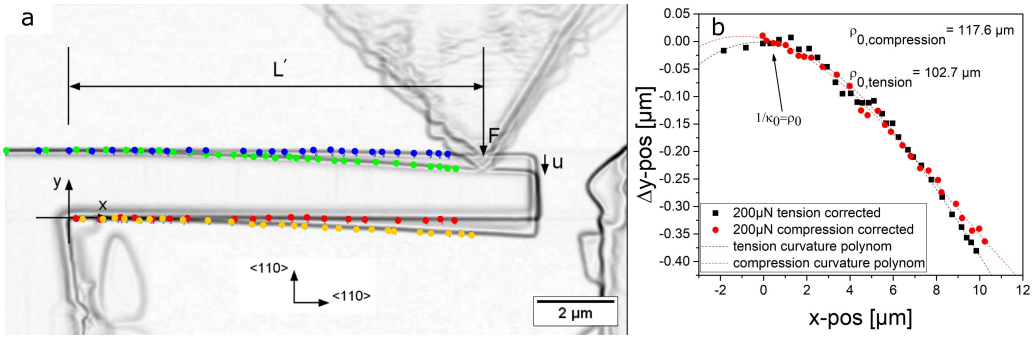

Figure 4: (a) Overlay of a sxx Si cantilever in unloaded and elastically loaded condition with differently coloured points depicting the measuring positions. (b) Deflection of the upper and lower bounds along the beam length. Dotted lines show 3^{rd} order polynomial fits for evaluation of the elastic modulus.

3.2 Relating stiffness to crack length

The calculation of crack length by compliance methods is standardized for various geometries, *e.g.* in ASTM 1820 [30]. However, the cantilever geometry as used in this study and many previous works [9, 10, 17, 32, 39] is not one of them. Wurster *et al.* [25] estimated the crack length by an analytical approach, assuming that a cracked cantilever has a stiffness similar to an unnotched beam of height W-a, which results in an underestimation of stiffness. Ast *et al.* [39] and more recently Yin *et al.* [40] resolved this issue by modelling the specimens with varying notch depths and fitting the data by a polynomial function. However, the simulations shown in said papers are specifically modelled for the chosen geometry and material and, therefore, not generally applicable. In the present study we altered loading condition, crack position and material, both numerically and experimentally, to find a universal formulation of the stiffness to crack length behaviour for microcantilever beams. The tests on nc Fe were performed on an individual cantilever, cut under 54°, as depicted in Fig. 5a,b. This specific geometry facilitates alternated FIB milling to increase the crack depth and subsequent loading for stiffness determination. Thus, there can be no influence of system compliance or cantilever geometry change, other than the increase in notch depth in this experiment. Another positive aspect of this approach is that any possible influences of other defects, *i.e.* the surface defect in the middle of the cantilever (Fig. 5a), do not play a role.

Fig. 5c-g, show the increasingly cut notch depths between each loading cycle. At each a/W ratio the cantilever was loaded three consecutive times. Although the notches are not atomically sharp as desired for fracture me-

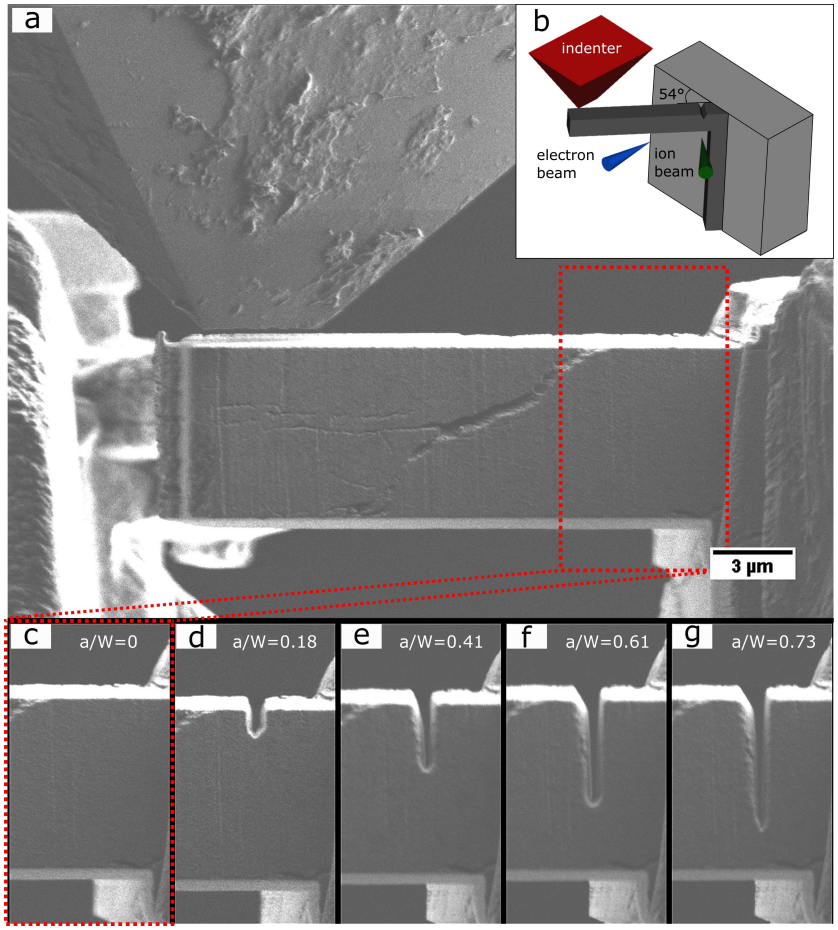

Figure 5: (a) FIB image of the 54° tilted nc Fe cantilever which allows stiffness measurements directly after step-wise increase of notch length. (b) Sketch of the testing arrangement. (c-g) Detailed outlines of a/W=0, 0.18, 0.41, 0.61, and 0.73 respectively. The micron bar is applicable to all images.

chanical evaluations, for elastic loading the wider notch radius should not make much of a difference.

Fig. 6a shows the loading-unloading curves for the different notch depths. The agreement of loading and unloading segments gives reason to assume that no major plastic deformation took place in the cantilevers, as was intended for this evaluation. Notably, the curves with a very high ratio of a/W= 0.73 show a slight hysteresis. However, since no residual displacement was measured and taking into account that the loading setup has slightly different voltage to force constants in loading versus unloading direction, it is safe to assume that this behaviour has no physical meaning, but is rather a machine measuring artefact.

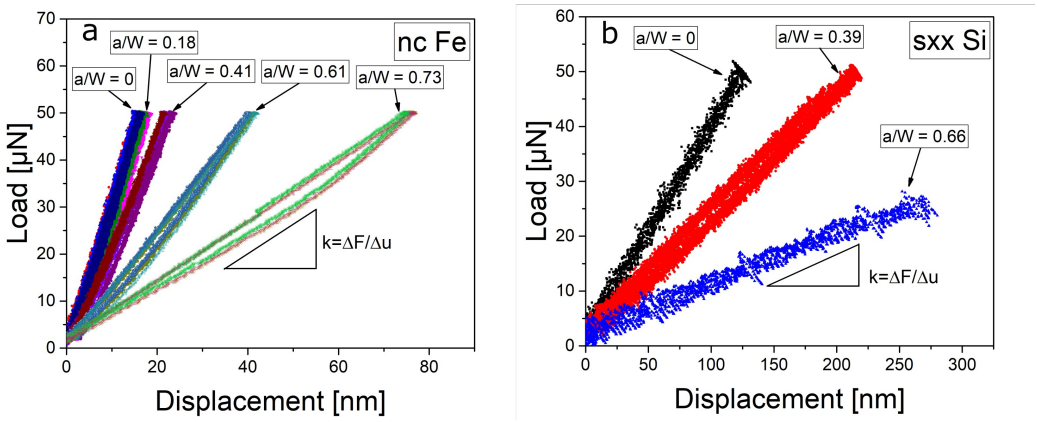

Figure 6: Elastic loading curves of (a) sxx Si and (b) nc Fe with various a/W ratios, showing the distinct reduction in stiffness with increasing notch depth.

For sxx Si, three different cantilevers (one unnotched and two with different notch lengths) were made and tested in a load controlled mode. Fig. 6b shows the elastic loading curves of the three sxx Si cantilevers. For comparability it was necessary to utilize a correction of the data based on classical beam theory [36], as the geometry of the cantilevers was not exactly identical. The detailed procedure is shown in the Appendix. Fig. 7 shows the normalized stiffness over a/W data for all experimental and simulated data. As the various changes in geometry, as well as the changes in material did not show any major deviation for the FE simulation, the stiffness data from all simulations on a given a/W-ratio were averaged (black data). It is evident that the experimental results show a fairly good agreement, as depicted in Fig. 7. Therefore, a 5^{th} order polynomial function as described in Eq. 7 was fitted through the mean of the simulated data points for each a/W-ratio and used for correlation between stiffness and crack length.

$$\frac{a}{W} = 1 - 2.897\left(\frac{k}{k_0}\right) + 10.618\left(\frac{k}{k_0}\right)^2 - 23.620\left(\frac{k}{k_0}\right)^3 + 24.497\left(\frac{k}{k_0}\right)^4 - 9.600\left(\frac{k}{k_0}\right)^5 \tag{7}$$

Additionally, the dynamical stiffness of the sxx W specimens, normalized by the apparent stiffness of the unnotched cantilevers, calculated after Euler-Bernoulli Beam theory [36] (Appendix) is also shown in Fig. 7 (pink data). For comparison the analytical model proposed by Wurster *et al.* [25] is plotted, exhibiting fairly large discrepancy to the experimental data. Given the

large dimensional variations of the FE simulations and the good agreement to the present experiments Fig. 7 suggests that the polynomial function fitted through the simulated data (red dotted curve, Eq. 7) can be used as a crack length estimation for cantilever shaped beams in the micron range.

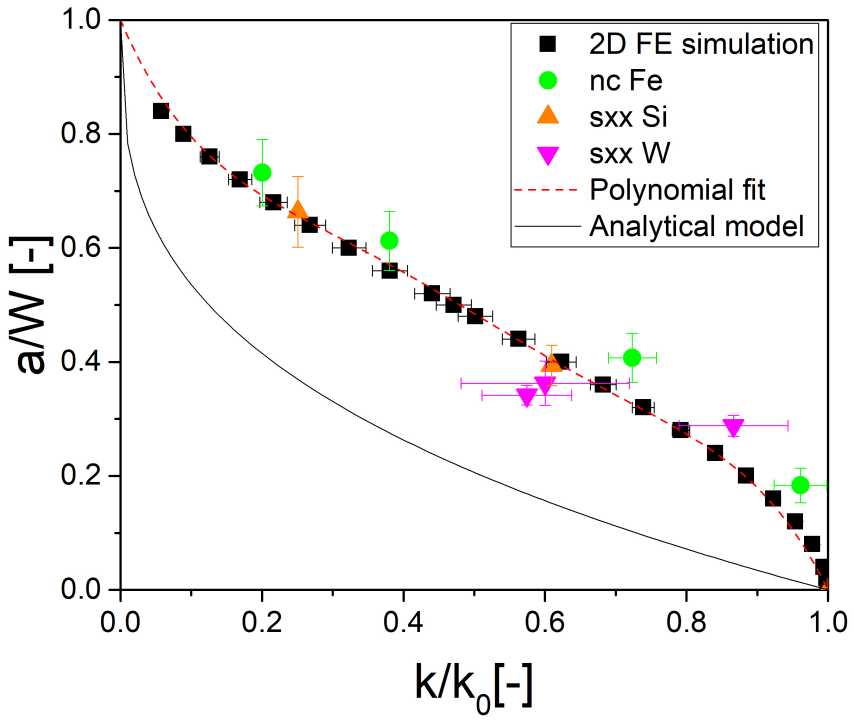

Figure 7: Ratio a/W as a function of normalized stiffness, showing the simulated FE data for different geometries (black squares), the diverse experimental data (sxx Si, orange; nc Fe, green and sxx W, pink) and the comparison with the analytical model proposed by Wurster *et al.* [25] (black line). The red dotted line is a polynomial fit through the FE data as given by Eq. 7.

3.3 Elastic-plastic fracture mechanical evaluation in sxx W

Prior to the actual experiments, machine compliance measurements were performed, by loading the sample base up to various loads at the position depicted by the white arrow in Fig. 8a. The dynamical compliance was

smoothed using a moving average technique with 500 points (1 % of all gathered data). The results are shown in Fig. 8b for all cantilevers. It is evident that the machine compliance is highly reproducible and that at a certain load a stable contact is developed, resulting in a constant machine compliance. For further evaluation a mean machine compliance was calculated by least-square fitting of the gathered data by a classical reciprocal relation $c = a_1 + \frac{a_2}{a_3+F}$, where a_1, a_2 and a_3 are fitting parameters. The result is depicted by the black curve in Fig. 8b. The dynamic compliance as well as the displacement were corrected by the mean machine compliance the following way:

$$c_{specimen} = c_{experiment} - c_{machine} \tag{8}$$

$$u_{specimen} = u_{experiment} - c_{machine}F \tag{9}$$

Here, $c_{specimen}$ and $u_{specimen}$ describe the apparent specimen quantities used for further evaluation, $c_{experiment}$ and $u_{experiment}$ describe the measured experimental values, and $c_{machine}$ labels the mean machine compliance.

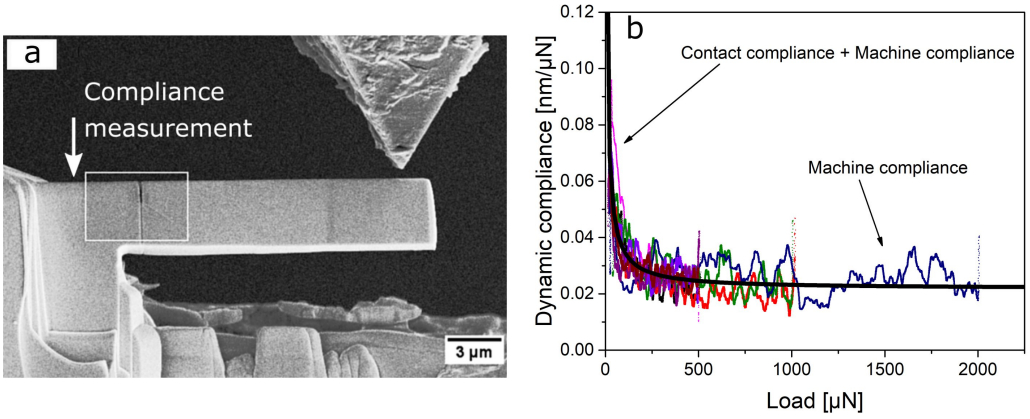

Figure 8: (a) In-situ SEM image to visualize the cantilever deformation as well as the deformation around the crack tip. The white arrow indicates the position of machine compliance measurements. (b) Machine compliance measurements of three different cantilevers to various loads, showing a good overall agreement.

Three sxx W cantilevers were tested and for evaluation an elastic modulus of E= 410 GPa and Poisson's ratio ν=0.28 were chosen [41]. Due to the similarity of the experiments, only one of will be shown in detail. The results of the other two beams can be found in the supplementary material. Fig.9a

shows the load-displacement data (black curve) as well as the crack length-displacement data (red curve) evaluated from the dynamic compliance after smoothing in the same way as previously stated. The blue points are the crack lengths deduced from the in-situ images shown in Fig. 9c-g. The discrepancy between the data can be explained from fracture surface inspections (Fig. 9b), where it is evident that the crack front is not straight. The measurement from in-situ images can only resolve the lowest crack extension, whereas the mechanical data results in an average crack length estimation over the whole thickness. This is detailed in Fig. 9b, where $a_0 = (1.22 \pm 0.06)\,\mu m$ is the mean initial notch depth, $a_1 = (1.48 \pm 0.06)\,\mu m$ is the lowest visible crack extension, when looking from the side and $a_{End} = (1.85 \pm 0.20)\,\mu m$ is the mean final crack length before unstable fracture, measured at the fracture surface. All measurements at the fracture surface are corrected for tilt (45°) and the error estimations result from measuring five times, where the measurements for a_0 and a_{End} are evenly spaced over the cantilever width. These points are also plotted in Fig. 9a, showing a good agreement with the respective crack length measurements. For the evaluation of crack growth initiation, the crack length over displacement data (red curve) is utilized, as depicted by the dashed black lines in Fig:9a. The crack length over displacement data shows still some contact compliance issues up to 120 nm, as depicted by the brighter red data points. From 120 nm up to 360 nm the crack length is constant and thereafter the crack length increases, giving an evident measure for the point of crack growth initiation. A movie showing the in-situ images and the data generation over time can be found in the supplementary material.

Following the procedure described in section 2.2, J-Δa curves were calculated for all three specimens, as depicted in Fig.10a. Two of the samples showed unstable crack growth at a certain J-value $J_{fracture}$, while one was deformed to the maximum displacement possible without any instability. However, even considering the difference in fracture behaviour the data aligns reasonably well with each other. As the crack length over displacement data can be correlated with the J-Δa curve, it is possible to evaluate a J-value J_i for crack growth initiation. To account for any measuring uncertainties, the J_i value was averaged over 200 data points (1 s). For the evaluation according to ASTM 1820 [30] a blunting line with a macroscopic effective yield strength $\sigma_y = 650\,MPa$ [25, 42] was drawn. As single crystalline specimen in the micron-sized regime are prone to show size effects [3, 43–45], a second blunting line as an upper limit was drawn with $\sigma_y = 1750\,MPa$ after data on similar sized microcompression experiments on sxx W in $\langle 001 \rangle$ direction [46]. The classical evaluation described in ASTM 1820 [30] demands a shift of the blunting line and therefore a minimal crack extension of 200 µm, which is not possible for the experiments shown here. Therefore, a different approach, as

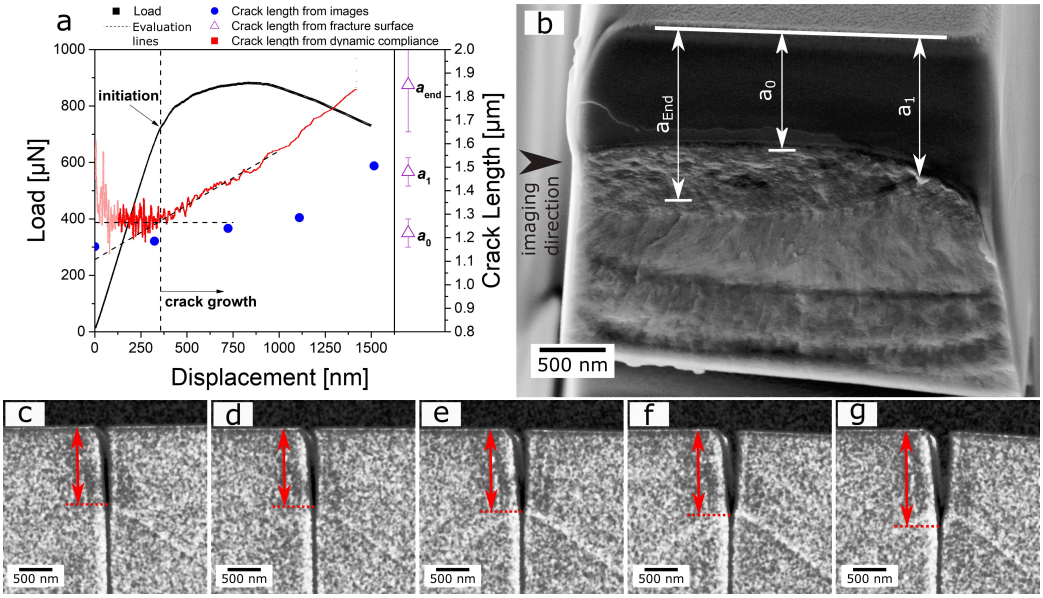

Figure 9: (a) Load-displacement curve (black) and dynamic compliance data (red curve) of a sxx W specimen, with evaluation lines (dashed line) for crack growth initiation. The blue points are crack lengths measured from images (c)-(g) as shown by the red arrows. The purple points in (a) correspond to the mean initial notch depth a_0, the lowest crack extension a_1 and the mean final crack extension a_{End} measured at the fracture surface shown in (b). The imaging direction is indicated by the black arrow in (b).

proposed by Bohnert *et al.* [47], was used where the shift of the blunting line should be half of the crack-tip opening displacement that can be accounted only to blunting of the notch δ_b. As the initiation of crack extension can be evaluated from the crack length-displacement data (Fig.9a), it is reasonable to utilize the image just before this point, Fig. 9d, for the measurement of $\delta_b = (74 \pm 21)\,\mathrm{nm}$. The crack tip opening displacement was estimated by inscribing circles in the crack notch and calculating the diameter thereof. As the resolution of the in-situ images is limited by the signal noise and a pixel size of 3 nm this process was applied multiple times and a mean δ_b was evaluated. J_Q was evaluated by averaging over all data points recorded between the dotted blue lines, which are plotted using the minimally and maximally measured δ_b. Fig.10b shows the detailed J_Q evaluation of sample 1 with both blunting lines shifted by $\delta_b/2$. The values of J_Q result in $(65.9 \pm 4.7)\,\mathrm{J/m^2}$ and $(55.4 \pm 2.8)\,\mathrm{J/m^2}$ for the macroscopic and microscopic blunting lines, respectively. Thus, it is debatable if the classical evaluation scheme is applicable to microscopic samples. To further compare the present

experiments with macroscopic fracture mechanics testing J_{Limit} as standardized in ASTM 1820 [30] is shown, indicating that the evaluated parameters lie well below the given limit. The limiting crack growth a_{Limit}= 620 nm is also far outside the achieved crack extension.

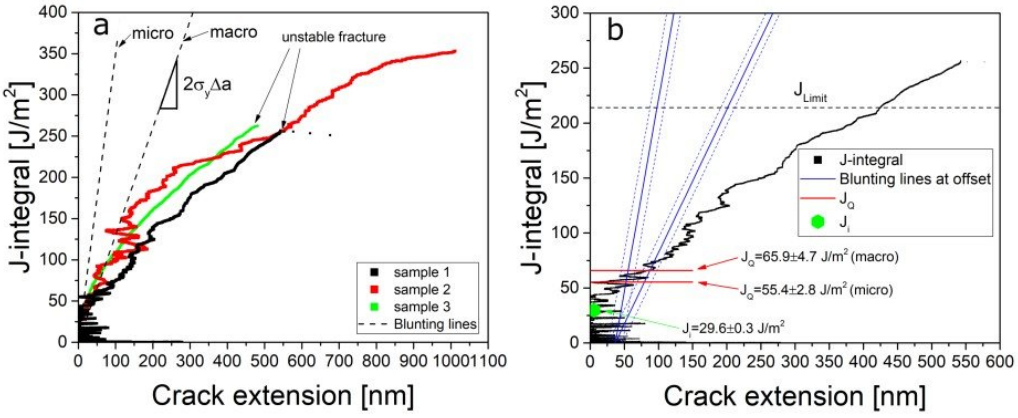

Figure 10: ((a) J-Δa curves of all three samples. Samples 1 and 3 show unstable fracture at a J-value$\approx$ 250 J/m^2, whereas sample 2 was bent to maximum displacement without any instability. The dashed lines indicate the blunting lines for macroscopic (σ_y= 650 MPa) and microscopic (σ_y= 1750 MPa) flow stress data. (b) Detailed evaluation of sample 1 showing J_i evaluated using the crack length over displacement data and J_Q evaluated using the blunting line method.

For better comparison with literature data and data from LEFM all J-values were transformed to K-values using:

$$K_J = \sqrt{\frac{JE}{1-\nu^2}} \tag{10}$$

as described in ASTM 1820 [30].

Part 4
Discussion

To facilitate the discussion and aim on the specific aspect of the work shown herein, the following is split in three parts focusing at the dynamical setup, the measurement of continuous J-Δa curves and the validity of the evaluated data, respectively.

4.1 Dynamical testing inside an SEM

Quasi-static testing in vacuum and the quantification thereof is already established quite well. The resolution of such experiments improves continuously with advances in damping technology, whether it being active damping on a hardware bases [4] or using a tuned feedback loop [48]. However, for the measurement of a dynamically excited vibration the use of damping systems can be counterproductive, as it is fairly difficult to distinguish between wanted and undesired vibrations. On the other hand, the lack of damping without any atmosphere or electronic vibration control can result in the appearance of resonance phenomena. Therefore, it is essential to assess the precise characteristics of the setup. The presented data shows that plausible results can be achieved when the excitation frequency is well below the resonance frequency of the system. Choosing an excitation frequency far above the resonance would not yield an increase in amplitude as close to the resonance frequency, however, the measurement of load and displacement would be out of phase and therefore an immense scatter as seen in Fig. 2c for the 200 Hz data arises. Regarding the quantification of compliance data, it is essential to validate the machine setup, *e.g.* with reliable determination of known moduli as shown in the present study.

4.2 In-situ continuous measurement of J-Δa curves

In-situ fracture mechanical investigations have the advantage of allowing a detailed view on crack propagation and the deformation occurring around the crack. However, as the images gathered offer only two-dimensional information, the results can be distorted as is evident by comparing crack lengths measured at the fracture surface with ones measured at the side of the specimen as detailed in Fig. 9. Therefore, applying a dynamic compliance measurement to evaluate actual average crack lengths seems very promising. One of the major problems with compliance measurements is the fact that in order to evaluate the crack length, a detailed knowledge of the tested geometry is necessary. Previous works were based on FE simulations of the specific geometries and tested materials [26, 47] or analytic approaches [25]. In this work, we tried for the first time to correlate 2D FE simulations with experimental investigations on three different materials with varying geometric dimensions. Considering the fact that all data points shown in Fig. 7 match the numerically obtained data, it is safe to assume that the proposed function, Eq. 7, allows for a reasonable crack length to

stiffness estimation for cantilever shaped beams in the micron range. However, further investigations are necessary to find the limits and constrictions for applicability of the given relation. Nevertheless, the tested specimens show a good overall agreement in the shape of the J-Δa curves, giving further assurance for the applicability of the presented approach. Still, an open question remains in the fact that the evaluation procedure of the J-integral is not necessarily geometry-independent. The pre-factors $\eta(a/W)$= 1.9 and $\gamma(a/W)$= 0.9 are usually assumed to be constant for SENB specimen in the range of a/W= 0.45-0.7 [30]. Given the fact that the initial crack lengths lie below a/W= 0.45 and the loading conditions are, albeit similar, not the same in a cantilever shaped beam as in a three-point bending setup, it would be worthwhile to address these parameters in a separate study.

4.3 Evaluation of elastic-plastic fracture mechanical parameters

As the standardized method for J_{IC} [30] is not applicable due to the fact that no crack extension of 200 µm can be reached, it is necessary to find other approaches equivalent to the macroscopic one. Ast *et al.* [26] assumed that the initial blunting of the crack is finished at an arbitrary crack extension of 0.2 µm. However, applying this criterion for the present data is rather unfitting as crack extension can already be detected in the in-situ images at that point. Therefore, we decided to utilize the approach suggested by Bohnert *et al.* [47], where a blunting line with no arbitrary offset, but half of δ_b before crack extension, is used. This approach mimics the standardized one for macroscopic samples better. However, for the data fitting in macroscopic samples, it is also necessary to evaluate exclusion lines at 0.15 and 1.5 mm, which is obviously not possible. Hence, we decided to average all the data points in between the maximal and minimal δ_b, which should lead to similar results as fitting the gathered data numerically and evaluating the intersection with the blunting line. As the slope of the blunting line is a function of σ_y, it has to be considered whether size effects need to be taken into account with evaluation of microcantilever beams. This might be a topic for further investigation. Considering for a conceptual worst case the rather large deviation from σ_y= 650 MPa for macroscopic samples to 1750 MPa for microscopic samples a deviation in J_Q of ∼16 % was found. While such procedure raises ambiguities or might fall short to the absence of strength data, our novel evaluation method based on the crack length over displacement (Fig. 9a) does not depend on any unknown material parameters. Another often dis-

cussed topic is the influence of FIB damage at the crack tip on the crack growth resistance. Considering a FIB damage depth of 70 nm in a worst case scenario of 30 kV ions under an impact angle of 90° for 15 min, as investigated by Ast *et al.* [26], it can be assumed that if a major influence on the J-value due to FIB damage would be existent, a change in slope in the J-Δa curve at around that crack extension would be evident. Furthermore, Wurster *et al.* [25] compared naturally cracked specimen with FIB notched specimen and found no distinguishable difference in fracture toughness. Thus, no or only minor influence of FIB damage on the evaluated fracture parameters can be assumed. Fig. 11 shows the comparison of all tested specimens, where K_i is the fracture initiation toughness evaluated using the crack length over displacement data as proposed herein, K_Q is the fracture toughness using the blunting line method and $K_{fracture}$ is the stress intensity at the final unstable crack extension, which was only seen for samples 1 and 3 in this work. The indices "J" and "LEFM" describe whether the K value was calculated from a J-integral value or calculated purely from a linear elastic fracture mechanics approach. When comparing the LEFM and EPFM K-values at initiation, it is obvious the linear elastic approach underestimates the apparent fracture toughness, giving a rather conservative parameter for further engineering purposes. One major criterion for LEFM to hold is that the plastic zone size $r_{pl} = \frac{1}{6\pi}(\frac{K_Q}{\sigma_y})^2$ [49] (for plane strain) has to be considerably smaller than both the crack length a as well as the ligament size b_0. Even considering the lowest measured $K_{Q,LEFM}$= 3.4 MPa$\sqrt{\text{m}}$ and highest σ_y= 1750 MPa, as well as plane strain condition, the plastic zone results in $r_{pl} \sim 0.25\,\mu$m, which is still a considerable part of the starting ligament size $b_0 \sim 2\,\mu$m, rendering LEFM inapplicable for the given experiments. On the other hand, the validation criteria for J_Q to J_{IC} ($K_{Q,J}$ to K_{JIC}) are that $b_0, B > 10J_Q/\sigma_y$. Again, considering the extreme case of a maximal J_Q= 119.3 J/m^2 and minimal σ_y= 650 MPa the validation value results in ∼1.8 µm. Not all three specimens fulfil that criterion, but the largest shortfall thereof is ∼100 nm. Thus, measuring macroscopic fracture parameters on the microscale with the present technique seems possible for the given material. For comparison the results on ⟨001⟩ {001} oriented sxx W, from macroscopic fracture mechanical investigations by Riedle *et al.* [28] and microscopic experiments on similarly shaped cantilevers by Ast *et al.* [50] is shown. Notably the data of other works is not evaluated exactly the same way as proposed herein, which should be taken into consideration. However, the literature data in Fig.11 is depicted with the closest conformity in regards to the presented data, showing an overall correspondence with $K_{Q,J}$. However, as stated previously, given the fact that there is no consent evaluation criterion for fracture mechanical testing

on the micro-scale, it is preferable to evaluate onset of fracture by physical measurements, *e.g.* dynamic compliance measurement, as proposed herein.

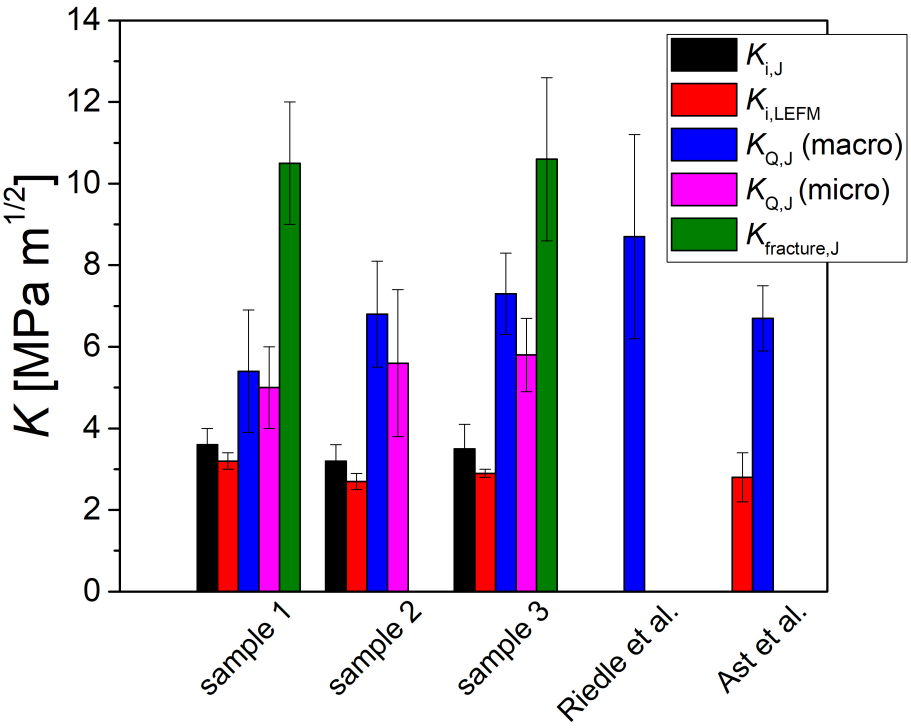

Figure 11: K-values of in comparison with literature [28, 50]. The indices "i" and "Q" describe the crack growth initiation toughness evaluated using the crack length over compliance signal and the fracture toughness evaluated using a blunting line method, respectively. The index "fracture" describes the final unstable crack growth for those samples where it occurred. The indices J and LEFM indicate whether the K value was calculated from a J-Integral value or according to linear elastic fracture mechanics.

Part 5
Summary

For the first time a dynamic measurement of compliance was used to directly determine crack extension of cantilever shaped specimens inside an SEM. A detailed assessment of the setup reveals that for a reliable compliance

measurement it is important to understand the frequency response of the equipment out of contact as well as in contact. Even more so for systems that do not rely on ambient damping mechanisms through atmospheres as in the present case. Furthermore, a general relationship between crack length and stiffness is proposed, based on numerical as well as experimental data. However, further detailed studies are necessary to find the limits for the applicability of this relationship.

It has been demonstrated that in-situ microscale measurement of J-Δa curves by means of dynamic compliance methods are possible and that it provides quantitative insight on the processes, occurring locally around a crack tip during elastic-plastic fracture.

Acknowledgments

The authors thank T. Müller, from the Erich Schmid Institute of Materials Science for providing the nc Fe material. Financial support by the Austrian Federal Government (837900) represented by Österreichische Forschungsförderungsgesellschaft mbH and the Styrian and the Tyrolean Provincial Government within the framework of the COMET Funding Programme (MPPE, A1.24), as well as partial financial support by the Austrian Science Fund FWF (project number P25325-N20) is gratefully acknowledged.

Data availability

The datasets generated during the current study are available from the corresponding author on reasonable request.

Appendix A

For the fast comparison of slightly different shaped cantilever specimens as well as the normalization of stiffness without experimental data of the unnotched geometry, it is functional to utilize an analytical approach. The simplest model to consider is a clamped unnotched beam with a square cross section $B \times W$ and a point load F at L' (Fig. 1a). The solution to this problem yields according to classical Euler-Bernoulli beam theory [36].

$$k = \frac{F}{u} = \frac{EBW^3}{4(L')^3} \tag{A1}$$

where k is the stiffness, u is the load line displacement and E is the elastic modulus. For comparison of the different sxx cantilevers the individual stiffnesses were based on the unnotched one by multiplication of the measured stiffness with the calculated factor $k_{unnotched}/k_{notched}$, respectively. However, for this approach to yield sufficiently good results it is important to make three major assumptions. First, it is important to note that this relation holds only for linear elasticity. Thus, it is sufficient as normalization parameter, but as soon as any deviation from linear elastic behaviour occurs, *i.e.* plasticity, this relation is not valid anymore. Second, it is assumed that the base is infinitely stiff, hence no deformation (elastic or plastic) can occur. In the current study the base was checked via in-situ imaging, showing no evident movement. Last, it is important that classical beam theory does not take any shear deformation or rotations into account. To address this issue, Timoshenko beam theory [36] would need to be applied. However, if the shear force term given in Eq. A2 is considerably smaller than 1, this issue can be neglected.

$$\frac{EI}{\kappa(L')^2AG} = \frac{E}{10G}(\frac{W}{L'})^2 = \frac{1+\nu}{5}(\frac{W}{L'})^2 \ll 1 \tag{A2}$$

Here, I, A and G are the second moment of area, the cross sectional area and the shear modulus respectively and κ= 5/6 is a constant for rectangular cross sections. Considering $E = 2G(1+\nu)$ and ν= 0.28 it results that the bending length of the beam L' has to be minimum 5 times as large as the height W, for the shear force term to be below 0.1.

Appendix B

The detailed data of samples 2 and 3, similar to Fig.9 can be found in the supplementary material, as well as a video showing the in-situ images of the fracture in parallel with the generated data, resolved over time. Supplementary data to this article can be found online at:
https://doi.org/10.1016/j.matdes.2018.03.051.

References

1. Pethica, J. B., Hutchings, R. & Oliver, W. C. Hardness measurement at penetration depths as small as 20 nm. *Philosophical Magazine A* **48,** 593–606 (1983).
2. Oliver, W. & Pharr, G. An improved technique for determining hardness and elastic modulus using load and displacement sensing indentation experiments. *Journal of Materials Research* **7,** 1564–1583 (1992).
3. Uchic, M. D., Dimiduk, D. M., Florado, J. N. & Nix, W. D. Sample dimensions influence strength and crystal plasticity. *Science* **305,** 986–989 (2004).
4. Kiener, D., Grosinger, W., Dehm, G. & Pippan, R. A further step towards an understanding of size-dependent crystal plasticity: In situ tension experiments of miniaturized single-crystal copper samples. *Acta Materialia* **56,** 580–592 (2008).
5. Jaya, B. N., Kirchlechner, C. & Dehm, G. Can microscale fracture tests provide reliable fracture toughness values? A case study in silicon. *Journal of Materials Research* **30,** 686–698 (2015).
6. Armstrong, D. *et al.* Small-scale characterisation of irradiated nuclear materials: Part II nanoindentation and micro-cantilever testing of ion irradiated nuclear materials. *Journal of Nuclear Materials* **462,** 374–381 (2015).
7. McLean, M. J., Wade, C. A., Watanabe, M. & Vinci, R. P. Microscale Fracture Toughness of Bismuth Doped Copper Bicrystals Using Double Edge Notched Microtensile Tests. *Experimental Mechanics* **54,** 685–688 (2013).
8. Sebastiani, M., Johanns, K., Herbert, E., Carassiti, F. & Pharr, G. A novel pillar indentation splitting test for measuring fracture toughness of thin ceramic coatings. *Philosophical Magazine* **95,** 1928–1944 (2014).
9. Cao, W. *et al.* Correlations between microstructure, fracture morphology, and fracture toughness of nanocrystalline Ni-W alloys. *Scripta Materialia* **113,** 84–88 (2016).
10. Iqbal, F., Ast, J., Göken, M. & Durst, K. In situ micro-cantilever tests to study fracture properties of NiAl single crystals. *Acta Materialia* **60,** 1193–1200 (2012).
11. Liu, S. *et al.* Measuring the fracture resistance of hard coatings. *Applied Physics Letters* **102,** 171907 (2013).

12. Žagar, G., Pejchal, V., Mueller, M. G., Michelet, L. & Mortensen, A. Fracture toughness measurement in fused quartz using triangular chevron-notched micro-cantilevers. *Scripta Materialia* **112,** 132–135 (2016).

13. Hahn, R. *et al.* Superlattice effect for enhanced fracture toughness of hard coatings. *Scripta Materialia* **124,** 67–70 (2016).

14. Riedl, A. *et al.* A novel approach for determining fracture toughness of hard coatings on the micrometer scale. *Scripta Materialia* **67,** 708–711 (2012).

15. Matoy, K. *et al.* A comparative micro-cantilever study of the mechanical behavior of silicon based passivation films. *Thin Solid Films* **518,** 247–256 (2009).

16. Armstrong, D., Rogers, M. & Roberts, S. Micromechanical testing of stress corrosion cracking of individual grain boundaries. *Scripta Materialia* **61,** 741–743 (2009).

17. Kupka, D. & Lilleodden, E. T. Mechanical Testing of Solid-Solid Interfaces at the Microscale. *Experimental Mechanics* **52,** 649–658 (2011).

18. Matoy, K., Detzel, T., Müller, M., Motz, C. & Dehm, G. Interface fracture properties of thin films studied by using the micro-cantilever deflection technique. *Surface and Coatings Technology* **204,** 878–881 (2009).

19. Sernicola, G. *et al.* In situ stable crack growth at the micron scale. *Nature Communications* **8** (2017).

20. Kelling, A. *et al.* Investigating fracture of nanoscale metal-ceramic multilayers in the transmission electron microscope. *Scripta Materialia* **115,** 42–45 (2016).

21. Treml, R. *et al.* Miniaturized fracture experiments to determine the toughness of individual films in a multilayer system. *Extreme Mechanics Letters* **8,** 235–244 (2016).

22. Mueller, M. *et al.* Fracture toughness testing of nanocrystalline alumina and fused quartz using chevron-notched microbeams. *Acta Materialia* **86,** 385–395 (2015).

23. B, N. J., Jayaram, V. & Biswas, S. K. A new method for fracture toughness determination of graded (Pt,Ni)Al bond coats by microbeam bend tests. *Philosophical Magazine* **92,** 3326–3345 (2012).

24. Hintsala, E., Kiener, D., Jackson, J. & Gerberich, W. W. In-Situ Measurements of Free-Standing, Ultra-Thin Film Cracking in Bending. *Experimental Mechanics* **55,** 1681–1690 (2015).

25. Wurster, S., Motz, C. & Pippan, R. Characterization of the fracture toughness of micro-sized tungsten single crystal notched specimen. *Philosophical Magazine* **92,** 1–23 (2012).

26. Ast, J., Merle, B., Durst, K. & Göken, M. Fracture toughness evaluation of NiAl single crystals by microcantilevers-a new continuous J-integral method. *Journal of Materials Research* **31,** 3786–3794 (2016).

27. Glebovsky, V., Semenov, V. & Lomeyko, V. Influence of the crystallization conditions on the structural perfection of molybdenum and tungsten single crystals. *Journal of Crystal Growth* **87,** 142–150 (1988).

28. Riedle, J., Gumbsch, P. & Fischmeister, H. F. Cleavage Anisotropy in Tungsten Single Crystals. *Physical Review Letters* **76,** 3594–3597 (1996).

29. Moser, G. *et al.* Sample preparation by metallography and Focused Ion Beam for nanomechanical testing. *Practical Metallography* **49,** 343–355 (2012).

30. *ASTM Standard E1820-13, Standard Test Method for Measurement of Fracture Toughness* 1820 (ASTM International, West Conshohocken, USA, 2013).

31. *ASTM Standard E399-09, Standard Test Method for Linear-Elastic Plane-Strain Fracture Toughness KIC of Metallic Materials* 399 (ASTM international, West Conshohocken, USA, 2009).

32. Wurster, S., Motz, C. & Pippan, R. Notched-Cantilever testing on the micrometer Scale - Effects of Constraints on Plasticity and Fracture Behaviour. *18th European Conference on Fracture, European Structural Integrity Society & German Association for Materials Research and Testing (DVM)* (2010).

33. Cordill, M. *et al.* The Nano-Jackhammer effect in probing near-surface mechanical properties. *International Journal of Plasticity* **25,** 2045–2058 (2009).

34. Pharr, G., Strader, J. & Oliver, W. Critical issues in making small-depth mechanical property measurements by nanoindentation with continuous stiffness measurement. *Journal of Materials Research* **24,** 653–666 (2009).

35. Merle, B., Maier-Kiener, V. & Pharr, G. M. Influence of modulus-to-hardness ratio and harmonic parameters on continuous stiffness measurement during nanoindentation. *Acta Materialia* **134,** 167–176 (2017).

36. Gere, J. M. & Timoshenko, S. P. *Mechanics of Materials* (Springer US, 1991).

37. *ISO/IEC 98-3:2008 Uncertainty of measurement — Part 3:Guide to the expression of uncertainty in measurement (GUM:1995)* (ISO, 2008).

38. Hopcroft, M. A., Nix, W. D. & Kenny, T. W. What is the Young's Modulus of Silicon? *Journal of Microelectromechanical Systems* **19,** 229–238 (2010).

39. Ast, J., Przybilla, T., Maier, V., Durst, K. & Göken, M. Microcantilever bending experiments in NiAl-Evaluation, size effects, and crack tip plasticity. *Journal of Materials Research* **29,** 2129–2140 (2014).

40. Yin, D., Marvel, C. J., Cui, F. Y., Vinci, R. P. & Harmer, M. P. Microstructure and fracture toughness of electrodeposited Ni-21 at.% W alloy thick films. *Acta Materialia* **143,** 272–280 (2018).

41. Simmons, G. & Wang, H. *Single Crystal Elastic Constants and Calculated Aggregate Properties. A Handbook* (The MIT Press, 1971).

42. Argon, A. & Maloof, S. Plastic deformation of tungsten single crystals at low temperatures. *Acta Metallurgica* **14,** 1449–1462 (1966).

43. Fleck, N., Muller, G., Ashby, M. & Hutchinson, J. Strain gradient plasticity: Theory and experiment. *Acta Metallurgica et Materialia* **42,** 475–487 (1994).

44. Schneider, A., Frick, C., Clark, B., Gruber, P. & Arzt, E. Influence of orientation on the size effect in bcc pillars with different critical temperatures. *Materials Science and Engineering: A* **528,** 1540–1547 (2011).

45. Motz, C., Schöberl, T. & Pippan, R. Mechanical properties of micro-sized copper bending beams machined by the focused ion beam technique. *Acta Materialia* **53,** 4269–4279 (2005).

46. Abad, O. T., Wheeler, J. M., Michler, J., Schneider, A. S. & Arzt, E. Temperature-dependent size effects on the strength of Ta and W micropillars. *Acta Materialia* **103,** 483–494 (2016).

47. Bohnert, C., Schmitt, N., Weygand, S., Kraft, O. & Schwaiger, R. Fracture toughness characterization of single-crystalline tungsten using notched micro-cantilever specimens. *International Journal of Plasticity* **81,** 1–17 (2016).

48. Gianola, D. S. *et al.* In situ nanomechanical testing in focused ion beam and scanning electron microscopes. *Review of Scientific Instruments* **82,** 063901 (2011).

49. Irwin, G. R. Analysis of stresses and strains near the end of a crack traversing a plate. *Journal of Applied Mechanics* **24,** 361–364 (1957).

50. Ast, J., Göken, M. & Durst, K. Size-dependent fracture toughness of tungsten. *Acta Materialia* **138,** 198–211 (2017).

Publication B

An analytical solution for the correct determination of crack lengths via cantilever stiffness

Materials and Design 194 (**2020**) 108914
doi:10.1016/j.matdes.2020.108914

An analytic solution for the correct determination of crack lengths via cantilever stiffness

Markus Alfreider[1], Stefan Kolitsch[2,3], Stefan Wurster[2], and Daniel Kiener[1]

[1]Department of Materials Physics, Montanuniversität Leoben, Leoben, Austria
[2]Erich Schmid Institute for Materials Science, Austrian Academy of Science, Leoben, Austria
[3]Materials Center Leoben Forschungs GmbH, Leoben, Austria

Abstract

The present work provides an analytic solution for the stiffness to crack length relation in microscopic cantilever shaped fracture specimens based on classical beam theory and substitution of the crack by a virtual rotational spring element. The resulting compact relationship allows for accounting of the actual beam geometry and agrees very well with accompanying finite element simulations. Compared with the only other model present in literature the proposed relationship reduces the deviation between model and data to a maximum of 1.6 % from the previous minimum of 15 %. Thus, the novel solution will help to reduce the necessity for individual simulations and aim to increase the comparability of elastic-plastic microcantilever fracture experiments in the future.

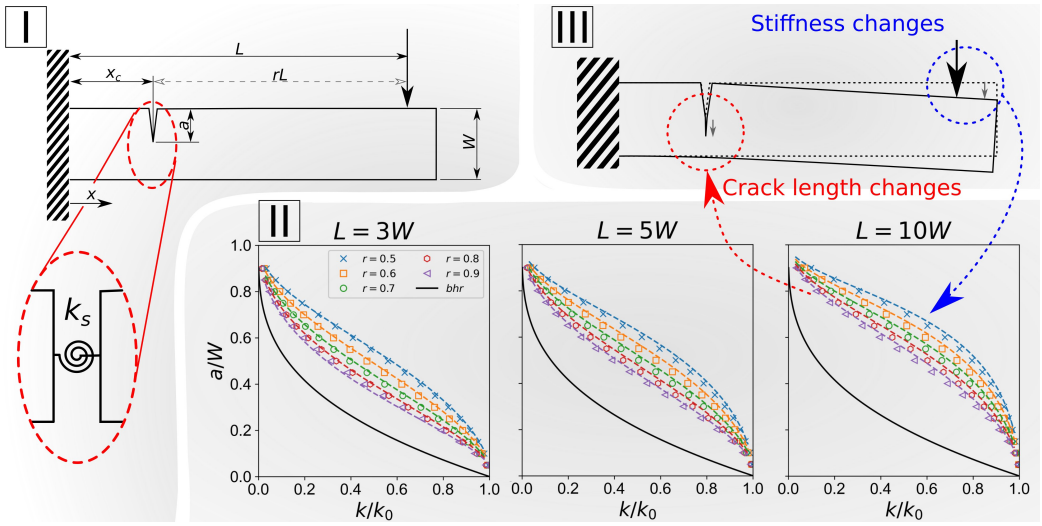

Microscale fracture testing is a rising field in materials science as it enables investigation of previously inaccessible features. A great number of different miniaturized methods has been reported in the literature, from pillar splitting to double cantilever wedging or three-point bending approaches. However, the most prominent realization is the fracture testing of a single notched cantilever geometry [1]. The experimental approach and evaluation is reasonably well understood and agreed on for the case of brittle materials, *e.g.* hard coatings or ceramics, where for a sufficiently sharp initial notch the concept of linear elastic fracture mechanics holds true. Contrarily, the area of elastic-plastic fracture mechanics is still being explored on the microscopic scale, with a lesser degree of best practices in terms of test setup and data analysis achieved to date. Once the regime of linear elasticity does not hold anymore and noticeable amounts of plasticity take place in the fracture process, elastic-plastic fracture concepts must be involved for analysis. Thereby, independent of the exact experimental testing geometry and analysis method, *i.e.* crack-tip opening displacement [2] or J-integral [3], the key challenge is always the determination of crack extension.

Most approaches quantify crack extension in an indirect way, through either sequential unloading segments [4] or by an overlaid sinusoidal signal to the applied force [5, 6] to measure the change in specimen stiffness. Thereafter, this change in stiffness is used to derive the crack extension. While this seems a trivial elasticity problem and solutions for other geometries are already present in literature [7], for cantilever shaped specimens various different ways were suggested so far. Wurster *et al.* [4] first assumed a classical Euler-Bernoulli beam with the height being reduced due to the crack exten-

sion to describe the stiffness to crack length relation in their experiments. This initial beam height reduction (*bhr*) approach (shown in detail as supplementary A) gives a straightforward mathematical formulation. However, comparing it to recent results from finite element modelling and in-situ experiments it appears to deviate rather distinct from the actual relation between stiffness and crack length, as shown in [6]. The reason for this characteristic is because this analysis results in a globally reduced bending stiffness, whereas the stiffness reduction originating from a sharp crack is of local nature and therefore less pronounced.

Ast *et al.* [5] later employed finite element modelling for their specific geometry, while Alfreider *et al.* [6] used a polynomial fit through a wide range of finite element data, validated by experiments on various different materials to ensure a certain degree of geometrical and material independence of their approach. However, the correct physical fundamental translation from experimentally determined stiffness changes to actual crack length is still unknown, therefore giving rise to ambiguity in evaluation of nominally analogous experiments in literature.

To model the realistic situation, a concept in recent works by Biondi and Caddemi [8] as well as Alijani *et al.* [9] is adopted, where such singularities are addressed analytically through Dirac's delta function $\delta(x)$ as a bending slope discontinuity at the crack position by substitution with a virtual rotational spring k_s , in a two-dimensional Euler-Bernoulli framework, as shown in feature I of the graphical abstract.

The detailed mathematical derivation of the problem can be found as supplementary material (supplementary B), but the final compact relation states:

$$\int_0^a \frac{a}{W}\left(Y\left(\frac{a}{W}\right)\right)^2 da = \frac{(k_0/k-1)L}{18\pi(1-\nu^2)r^2} \tag{1}$$

where a is the crack length, W and L are geometric parameters shown in the graphical abstract (feature II), k and k_0 are the stiffnesses of the cracked and unnotched beam respectively, ν is Poisson's ratio, $r = (L - {}_x c)/L$ (with x_c being the offset of the crack from the base) and $Y\,(a/W)$ is a geometry factor. This factor has previously been calculated for the shown cantilever geometry by various groups, with only slight deviations among each other as shown by Brinckmann *et al.* [10]. The first term of Eq. 1 cannot be solved analytically in the general case. However, with nowadays computational efficiency it is trivial to compute the integral approximately, *e.g.* trapezoidal rule, for a sensible range of a/W and find the corresponding a by interpolation.

To study the accuracy of the model, it was compared with two-dimensional linear elastic finite element simulations. They were conducted using 4-node plane-stress and plane-strain elements and an isotropic material behaviour with an elastic modulus $E_0 = 130\,\mathrm{GPa}$ and a Poisson's ratio $\nu = 0.34$. The cantilever base was considered rigid, with a displacement equal to zero, in accordance with the analytical assumptions taken herein. The calculations were conducted for three different cantilever lengths $3W$, $5W$ and $10W$ with $W = 2\,\mu\mathrm{m}$, while r ranges from 0.5 to 0.9 in increments of 0.1, and a/W spans from 0.05 to 0.95 in 0.05 increments. Thus, a total of 540 different simulations were performed. As expected, no difference in a/W over k/k_0 data was found in comparison between plane stress and plane strain state, respectively. Hence, all the results summarized in feature II of the graphical abstract are shown in plane strain condition. There, the finite element data is depicted by symbols, and the analytical model is shown by the dotted curves in colours corresponding to the given geometries. The continuous black curve depicts the *bhr* model [4]. As shown in supplementary A the *bhr* model is independent of the cantilever geometry when considered in a normalized manner.

It is evident from the presented data that the proposed analytical model is in very good agreement with the finite element data and the changes in geometry are reflected quite well. To estimate the differences between analytical model and finite element data, the root mean square deviation was calculated for all combinations of r and L, revealing the highest deviation to be 1.6 % for $r = 0.5$, $L = 10W$. In comparison, the *bhr* model would deviate by 15 % from the data for $L = 3W$, $r = 0.9$, which represents the minimum discrepancy between finite element data and *bhr* model. Notably, isotropic elasticity was used for convenience. However, due to normalization by the unnotched beam configuration Eq. 1 is independent of elastic properties and therefore, errors originating from elastic anisotropy can be neglected in the given form. In conclusion, the proposed simple and straight forward analytical model describes the observed physical behaviour very well and is recommended to address the stiffness to crack length conversion in the analysis of miniaturized elastic-plastic fracture experiments as schematically depicted in feature III of the graphical abstract.

Acknowledgement

The authors gratefully acknowledge the financial support under the scope of the COMET program within the K2 Center "Integrated Computational Material, Process and Product Engineering, IC-MPPE" (Projects A2.12 and

A1.24). This program is supported by the Austrian Federal Ministries for Transport, Innovation and Technology (BMVIT) and for Digital and Economic Affairs (BMDW), represented by the FFG (Funder ID: 10.13039/501100004955), and the federal states of Styria, Upper Austria, and Tyrol. This project has received funding from the European Research Council (ERC) under the European Union's Horizon 2020 research and innovation programme (Grant No. 771146 TOUGHIT and No. 757333 SPDTuM).

Data availability statement

The raw/processed data required to reproduce these findings cannot be shared at this time as the data also forms part of an ongoing study.

References

1. Jaya, B. N. & Jayaram, V. Fracture Testing at Small-Length Scales: From Plasticity in Si to Brittleness in Pt. *JOM* **68,** 94–108 (2015).
2. Wells, A. A. *Unstable Crack Propagation in Metals: Cleavage and Fast Fracture* in *Proceedings of the Crack Propagation Symposium* (1961).
3. Rice, J. R. *A path independent integral and the approximate analysis of strain concentartion by notches and cracks* (Brown University, 1967).
4. Wurster, S., Motz, C. & Pippan, R. Characterization of the fracture toughness of micro-sized tungsten single crystal notched specimen. *Philosophical Magazine* **92,** 1–23 (2012).
5. Ast, J., Merle, B., Durst, K. & Göken, M. Fracture toughness evaluation of NiAl single crystals by microcantilevers-a new continuous J-integral method. *Journal of Materials Research* **31,** 3786–3794 (2016).
6. Alfreider, M., Kozic, D., Kolednik, O. & Kiener, D. In-situ elastic-plastic fracture mechanics on the microscale by means of continuous dynamical testing. *Materials & Design* **148,** 177–187 (2018).
7. *ASTM Standard E1820-13, Standard Test Method for Measurement of Fracture Toughness* 1820 (ASTM International, West Conshohocken, USA, 2013).
8. Biondi, B. & Caddemi, S. Closed form solutions of Euler-Bernoulli beams with singularities. *International Journal of Solids and Structures* **42,** 3027–3044 (2005).
9. Alijani, A., Abadi, M. M., Darvizeh, A. & Abadi, M. K. Theoretical approaches for bending analysis of founded Euler-Bernoulli cracked beams. *Archive of Applied Mechanics* **88,** 875–895 (2018).
10. Brinckmann, S., Matoy, K., Kirchlechner, C. & Dehm, G. On the influence of microcantilever pre-crack geometries on the apparent fracture toughness of brittle materials. *Acta Materialia* **136,** 281–287 (2017).

Supplementary material to: An analytic solution for the correct determination of crack lengths via cantilever stiffness

Markus Alfreider[1], Stefan Kolitsch[2,3], Stefan Wurster[2], and Daniel Kiener[1]

[1]Department of Materials Physics, Montanuniversität Leoben, Leoben, Austria
[2]Erich Schmid Institute for Materials Science, Austrian Academy of Science, Leoben, Austria
[3]Materials Center Leoben Forschungs GmbH, Leoben, Austria

Supplementary A: The beam height reduction approach (*bhr*) after Wurster *et al.* [1]

The classical analytical description for the stiffness of an isotropic cantilever, neglecting transverse shear stresses, is the Euler-Bernoulli theory:

$$k = \frac{\delta P}{\delta \omega} = \frac{3E_0 I_0}{L^3} = \frac{E_0 B W^3}{4L^3} \tag{A1}$$

with B being the in-plane thickness of the beam and all other variables as defined previously. It is a reasonable first order assumption that a crack of length a reduces the initial unnotched beam height W, so that virtually a beam of height $W - a$ remains. Thus, substituting W by $W - a$ and rearranging leads to:

$$a = W - \sqrt[3]{\frac{4kL^3}{BE_0}} \tag{A2}$$

Furthermore, formulating Eq. A1 in a normalized manner, *i.e.* k/k_0 results in:

$$\frac{k}{k_0} = \frac{(W-a)^3}{W^3} \tag{A3}$$

which leads to:

$$\frac{a}{W} = 1 - \sqrt[3]{\frac{k}{k_0}} \tag{A4}$$

Thus, when normalized as shown in feature II of the graphical abstract, this approach is independent of the geometric shape of the specimen, which is contradictory to the presented finite element simulations.

Supplementary B: Detailed derivation of the correlation between crack length and cantilever stiffness

To model the realistic situation, a concept from recent works by Biondi and Caddemi [2] as well as Alijani *et al.* [3] is adopted, where such singularities are addressed analytically through Dirac's delta function $\delta(x)$ as a bending slope discontinuity at the crack position. Applying this to the depicted problem leads to an Euler-Bernoulli beam equation as follows:

$$E_0 I_0 (1 - \gamma\, \delta(x - x_c))\omega''(x) = P(L - x) \tag{B1}$$

where E_0 is the elastic modulus and I_0 the moment of inertia of the unnotched beam, x_c is the position of the crack, ω is the deflection, thus $\omega''(x)$ is the second derivative with respect to x and represents the curvature, and P is the point load acting on the cantilever. Deflection and load are positive in downward direction, as is common for these experiments. The strength of the Dirac delta singularity is described by γ and is a function of the crack

length relative to the specimen height a/W for the present problem. Laplace transformation is a well-known method to address differential mathematical problems that inhibit singularities, *e.g.* Dirac's delta or step functions, such as the initial mathematical problem of interest herein. Hence, one can start with a transformation of Eq. B1 as:

$$E_0 I_0 \, \mathcal{L}\left((1 - \gamma\delta(x - x_c)\omega''(x)\right) = P \, \mathcal{L}\left(L - x\right) \tag{B2}$$

resulting in:

$$E_0 I_0 \left[s^2 \mathbf{W}(s) - s\omega(0) - \omega'(0) - \gamma\omega''(x_c)e^{-x_c s}\right] = P\frac{Ls - 1}{s^2} \tag{B3}$$

where s is the complex variable and $[W](s) = \mathcal{L}\left(\omega(x)\right)$ is the Laplace transformation of the deflection. In the classical picture of a beam with an infinitely rigid base it is known that $\omega(0) = 0$ and $\omega'(0) = 0$. Furthermore, it is assumed that $\omega''(x_c)$ is constant. Thus, one can rearrange Eq. B3 into:

$$\mathbf{W}(s) = \frac{P}{E_0 I_0}\frac{Ls - 1}{s^4} + \gamma\omega''(x_c)\frac{e^{-x_c s}}{s^2} \tag{B4}$$

hence

$$\omega(x) = \mathcal{L}^{-1}\left(\mathbf{W}(s)\right) = \frac{P}{E_0 I_0}\frac{3Lx^2 - x^3}{6} + \gamma\omega''(x_c)(L - x_c)\sigma(L - x_c) \tag{B5}$$

where $\sigma(x)$ is the Heaviside function, which equals 1 for $L - x_c > 0$ (the only physically reasonable case). As the focus lies solely on the load line displacement, one can evaluate $\omega(L)$ from Eq. B5, resulting in:

$$\omega(L) = \frac{PL^3}{E_0 I_0} + \gamma\omega''(x_c)(L - x_c) = \omega_0 + \gamma\omega''(x_c)(L - x_c) \tag{B6}$$

It is evident that the deflection is increasing compared to the deflection of the unnotched cantilever ω_0 by a term dependent on the strength of Dirac's delta γ, the curvature at the position of the crack $\omega''(x_c)$, and the lever between load and crack position $(L - xc)$. Substituting the crack virtually by a discrete rotational spring, as shown schematically in feature I of the graphical abstract, allows a connection between spring stiffness k_s and the strength of the singularity γ [3]:

$$\gamma = \frac{E_0 I_0}{k_s + E_0 I_0 A} \tag{B7}$$

where A=2.013 is a constant value, based on the product of two Dirac delta functions at the same position [2]. The stiffness k_s of this rotational spring is known to be described by [3]:

$$k_s^{-1} = \frac{2B(1-\nu^2)}{E_0} \int_0^a \left(\frac{K_I}{M}\right)^2 da \tag{B8}$$

where B is the depth of the cantilever in plane, ν is Poisson's ratio, $M = PL$ is the bending moment, and K_I is the stress intensity factor at the notch under mode I loading condition. Given the classical formulation for stress intensity and loading geometry [4, 5], one can write:

$$K_I = \sigma\sqrt{\pi a} Y\left(\frac{a}{W}\right) = \frac{6PL}{BW^2}\sqrt{\pi a} Y\left(\frac{a}{W}\right) \tag{B9}$$

where $Y(a/W)$ is a geometry factor. This has previously been calculated for the shown cantilever geometry by various groups [1, 5–7], with only slight deviations from each other as shown by Brinckmann *et al.* [8]. All calculations shown herein are conducted using the analytical solution for $Y(a/W)$ by Riedl *et al.* [5], which takes into account only bending stresses. Substituting Eq. B9 into equation Eq. B8, and rearranging leads to:

$$k_s^{-1} = \frac{6\pi(1-\nu^2)}{E_0 I_0} \int_0^a \frac{a}{W}\left(Y\frac{a}{W}\right)^2 da = \frac{6\pi(1-\nu^2)}{E_0 I_0}\frac{1}{G(a,W)} \tag{B10}$$

where $G(a, W)$ is a function of the crack length a and the cantilever height W only, and can be easily evaluated numerically for a given configuration and a sensible range of a/W. As all of the experimental specimens have slightly different geometries depending on the fabrication route and material features, the stiffness change is commonly not used as an absolute value, but rather as a relative measure, normalized by the stiffness of the unnotched beam k_0:

$$\frac{k}{k_0} = \frac{\omega_0}{\omega(L)} \tag{B11}$$

Thus, substituting Eqs. B6, B7 and B10 into B11 and rearranging leads to:

$$G(a,W) = 6\pi(1-\nu^2)\left(\frac{3r^2}{(k_0/k-1)L} - 1\right) \tag{B12}$$

under the assumption of $E_0 I_0 \omega''(x_c) = P(L-x_c)$ and with $r = (L-x_c)/L$.

Notably, the result is a rather compact relation between the stiffness of a cracked cantilever k and the function of its crack length $G(a,W)$ which is only depending on the actual specimen geometry. Furthermore, as $A = 2.013$ is a constant value and L usually in the range of 10×10^{-4}–10×10^{-6} m for microcantilever experiments, A does not have a noticeable contribution. For a typical specimen of $L = 10\,\mu\text{m}$ and $r = 0.8$ the average deviation between Eq. B12 with and without the term A is 20 ppm. Even up to $L = 10 \times 10^{-3}$ m it is only 0.56 % for $r = 0.9$ and increases up to 1.83 % for $r = 0.5$, which is already a rather unlikely geometry, thus suggesting that A can be safely neglected for the experiments considered herein. Therefore, Eq. B12 simplifies to:

$$\int_0^a \frac{a}{W} Y\left(\frac{a}{W}\right)^2 da = \frac{1}{G(a,W)} = \frac{(k_0/k-1)L}{18\pi(1-\nu^2)r^2} \tag{B13}$$

The translation from $G(a,W)$ to the crack length a cannot be solved analytically, as the geometry functions $Y(a/W)$ turn out to be very complex or of higher order polynomial degree, which, to the best of the authors knowledge, makes finding an inverse function impossible. However, with nowadays improved computational efficiency the dependency of a over $G(a,W)$ for a sensible range of a/W can be carried out numerically, for example spanning values from 0.1–0.9, to then conveniently find the corresponding a for a given $G(a,W)$, *i.e.* a given stiffness k, by interpolation.

References

1. Wurster, S., Motz, C. & Pippan, R. Characterization of the fracture toughness of micro-sized tungsten single crystal notched specimen. *Philosophical Magazine* **92,** 1–23 (2012).
2. Biondi, B. & Caddemi, S. Closed form solutions of Euler-Bernoulli beams with singularities. *International Journal of Solids and Structures* **42,** 3027–3044 (May 2005).
3. Alijani, A., Abadi, M. M., Darvizeh, A. & Abadi, M. K. Theoretical approaches for bending analysis of founded Euler-Bernoulli cracked beams. *Archive of Applied Mechanics* **88,** 875–895 (Feb. 2018).
4. Irwin, G. R. Analysis of stresses and strains near the end of a crack traversing a plate. *Journal of Applied Mechanics* **24,** 361–364 (1957).
5. Riedl, A. *et al.* A novel approach for determining fracture toughness of hard coatings on the micrometer scale. *Scripta Materialia* **67,** 708–711 (Oct. 2012).
6. Matoy, K. *et al.* A comparative micro-cantilever study of the mechanical behavior of silicon based passivation films. *Thin Solid Films* **518,** 247–256. ISSN: 0040-6090 (2009).
7. Iqbal, F. *Fracture mechanism of y-TiAl alloys investigated by in-situ experiments in a SEM and AFM* PhD thesis (UniversitÃ¤t Erlangen-NÃ¼rnberg, 2012).
8. Brinckmann, S., Matoy, K., Kirchlechner, C. & Dehm, G. On the influence of microcantilever pre-crack geometries on the apparent fracture toughness of brittle materials. *Acta Materialia* **136,** 281–287 (Sept. 2017).

Publication C

Addressing Fracture Properties of Individual Constituents Within a Cu-WTi-SiO_x-Si Multilayer

JOM 72 (**2020**) p. 4551-4558
doi:10.1007/s11837-020-04444-6

Addressing fracture properties of individual constituents within a Cu-WTi-SiO_x-Si multilayer

Markus Alfreider[1], Johannes Zechner[2], and Daniel Kiener[1]

[1]Department Materials Science, Chair of Materials Physics, Montanuniversität Leoben, Leoben, Austria
[2]KAI Kompetenzzentrum Automobil- u. Industrieelektronik GmbH, Villach, Austria

Abstract

With modern materials applications continually decreasing in size, *e.g.* microelectronics industry, sensors, actuators or medical implants, quantifying materials parameters becomes increasingly challenging. Specifically, addressing individual constituents of a system, such as interfaces or buried layers in a multi-layered structure, emerges as a topic of great importance. In the present work we demonstrate a technique to assess fracture parameters of different interfaces of a Cu-WTi-SiO_x-Si model system based on in-situ microcantilever testing in a scanning electron microscope. Positioning the initial notch position with respect to the interface of interest enabled selection of different crack paths, while an additional overlaid sinusoidal signal permitted for continuous measurement of stiffness changes and therefore an experimental measure for the actual crack extension. Thus, we achieved continuous J-Δa-curve measurements for the interface between Cu and WTi, the bulk WTi and the interface between WTi and SiO_x, respectively. The localized nature of this novel approach makes it generally applicable to testing specific interfaces.

Part 1
Introduction

Due to the continuous drive towards more powerful devices, a wide variety of nowadays materials applications exhibit very small structural features. Based on their usage, utilizing *e.g.* structural, semiconducting or optical properties, this trend urges for an increasing amount of different constituents confined in a very limited volume such as multilayers or coatings of only a few tens to hundred nm in size. Addressing the individual properties of these constituents experimentally is rather challenging, but necessary as such nano- and microscale structures can exhibit drastically different properties compared to their bulk-like counterparts, if they even exist [1]. Specifically, interface adhesion and fracture properties of the involved materials are a concern, as these characteristics could be origins for structural failure [2]. Microscale fracture mechanics is a rather recent field, with varying approaches, such as double cantilever wedging [3], pillar splitting [4] or micro cantilever bending as the most prominent geometries. However, the majority of research in the field so far, has been directed towards measuring single phase fracture parameters of rather brittle materials with only few groups addressing interface properties. Matoy *et al.* [5] studied the interface adhesion between SiO_x and Cu, W and WTi, respectively, using the cantilever deflection technique, while Schaufler *et al.* [6] applied the same approach to study amorphous carbon coatings on steel substrates. However, due to the brittle nature of these materials, both groups were able to successfully apply linear elastic fracture mechanics concepts for evaluation [7]. Given that some components in applied systems can exhibit rather pronounced ductility, *e.g.* heat sinks or conductive layers (Cu, Al), those approaches are insufficient and it appears necessary to advance the field towards miniaturized elastic-plastic fracture mechanics concepts for interface testing. This will enable a better understanding of interface controlled fracture processes for a wider group of materials. In the present work, we utilize experiments based on the continuous J-Integral measurement concept [8, 9] in-situ inside a scanning electron microscope (SEM) and employ them on a Cu-WTi-SiO_x-Si multi-layered model system. This was chosen as it combines materials with noticeable differences in elastic and plastic properties, giving an ideal test case for our elastic-plastic fracture methodology. The cantilever shaped specimens manufactured from the layer stack are notched at different positions to address the crack extension behaviour of the interface between SiO_x and WTi, the interface between WTi and Cu and the WTi layer itself, respectively.

Part 2
Experimental procedure

The model material system was synthesized on a (001) oriented 8-inch Si wafer by first thermally growing amorphous SiO_x of about 50–70 nm height. Thereafter, a 270–300 nm thick WTi layer, as widely used in semiconductor and MEMS fabrication, and a 300 nm Cu seed layer were deposited by magnetron sputtering. By electrochemical deposition an additional Cu layer was grown onto the seed resulting in a total Cu thickness of 5 µm. Finally, the sample was annealed at 400 °C for 30 minutes to ensure a stable microstructure at room temperature, resulting in a polycrystalline Cu film with a grain size of ∼2.7 µm. Further details can be found in Wimmer *et al.* [10] and Bigl *et al.* [11] (refer to Film A therein). Thereafter, the wafers were mechanically broken into 2x2 mm^2 platelets, revealing the cross-sectional structure on a 90° edge, which enables further processing of the micron sized specimens. The cantilevers were fabricated using a focussed ion beam work station (FIB, LEO 1540XB, Carl Zeiss AG, Oberkochen, Germany) situated at the edge of these platelets, as schematically shown in Fig. 1. To ensure a precise sample geometry, the ion beam current was subsequently reduced from 10 nA for coarse cuts to 50 pA for final polishing steps. The initial notch (a_0) was introduced as a through thickness notch at the desired position (possibly close to the interfaces or within the WTi layer) before the final polishing step to minimize curtaining artefacts on the specimen surface. The experiments were conducted inside the same FIB using a Hysitron PI-85 picoindenter (Bruker Corporation, Billerica, USA) equipped with a nanoDMA III upgrade to enable sinusoidal excitation for compliance measurements and a 5 µm long conductive diamond wedge shaped tip with an opening angle of 60° (Synton-MDP AG, Nidau, Switzerland).

All tests were conducted in open-loop mode with a nominal speed of 10 µN/s, a sinusoidal amplitude of 5 µN and a frequency of 80 Hz, based on previous works [9]. The tests started from an initial contact load of 10 µN to reduce any issues with the inherently load-controlled transducer. The gathered data was evaluated similarly to the approach shown in [9], with some adjustments required due to the heterogeneous nature of the specimens as detailed below. First, the usual approach of splitting the J-integral into elastic and plastic parts and calculating iteratively, as suggested in ASTM 1820 [12], cannot be applied since no general elastic modulus E can be defined. Thus, we utilize an older form of the J-integral evaluation [13, 14]:

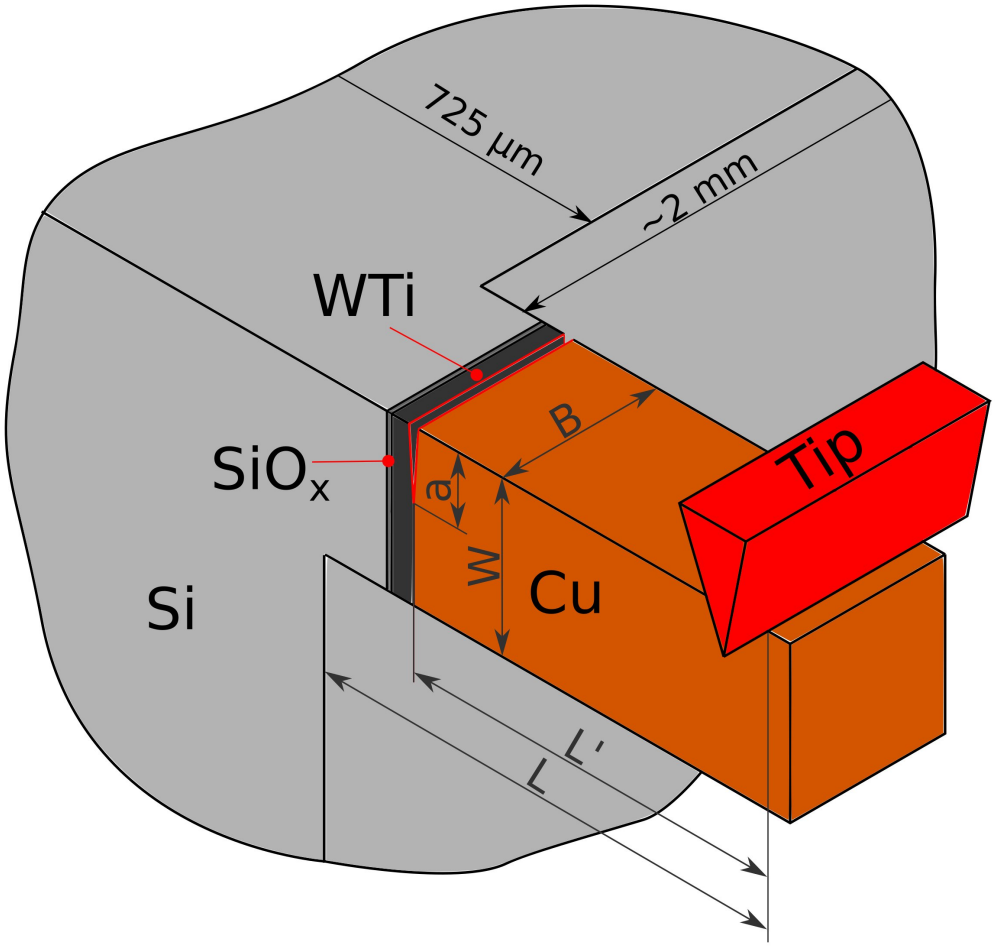

Figure 1: (Schematic of the microcantilever testing geometry on the edge of a platelet showing the individual constituents as well as the geometric parameters.

$$J_n = \frac{2A_{tot,n}}{B(W - a_n)} \tag{1}$$

where, $A_{tot,n}$ is the total area under the load-displacement curve up to point n, B is the width and W the height of the cantilever as shown in Fig. 1, and a_n is the crack length at point n. The respective crack length an was derived from the change in compliance signal following the formulation outlined in [15] as:

$$\int_0^{a_n} \frac{a}{W} Y\left(\frac{a}{W}\right)^2 da = \frac{\left(\frac{k_0}{k_n} - 1\right) L^3}{18\pi(1-\nu^2)L'^2} \tag{2}$$

where $Y(a/W)$ is a geometry factor, taken from [16], ν is Poisson's ratio (taken as 0.3), W, L and L' are geometric parameters shown in Fig. 1, k_0 is the stiffness of the unnotched beam and k_n is the stiffness at point n. The stiffness in this case is inverse to the experimentally gathered dynamic compliance data. The integral term of Eq. 2 was evaluated numerically using the trapezoidal rule, so that a_n was found by interpolation. The unnotched beam stiffness k_0 is dependent on the geometry of the specimen and the exact shape and elastic parameters of the individual constituents, making it challenging to evaluate. Therefore, we calculate k_0 from the initial stiffness of the notched cantilever $k(a_0)$ as:

$$k_0 = k(a_0)\left(1 + \frac{18\pi(1-\nu^2)L'^2}{L^3} \int_0^{a_0} \frac{a}{W} Y\left(\frac{a}{W}\right)^2 da\right) \tag{3}$$

It should be noted that Eqs. 2 and 3 are independent of specific materials parameters (with the exception of Poisson's ratio), as they consider a normalization by the stiffness of an unnotched cantilever. Thus, it is suggested that they are applicable also for heterogeneous materials systems as examined herein.

Part 3
Results

The geometry of the specimens was measured using ImageJ 1.54s before deformation and is summarized in Tab. 1 The error estimations for L, L', B and W are based on a measuring error of $\pm 5\,\mathrm{px} = \pm 40\,\mathrm{nm}$, while the error estimations for the initial crack length a_0 is based on the standard deviation of 20 individual measurements conducted on the fracture surface after the experiment.

Since the goal was to compare the cantilevers with different notch positions, it is necessary to keep the overall geometries identical, which is not always straightforward in micron sized specimens. However, as shown in Tab. 1, the ratios a_0/W, L'/L and L'/W are in very good agreement among

Table 1: Geometry of the individual cantilevers

	L [µm]	L' [µm]	B [µm]	W [µm]	a_0 [nm]	a_0/W	L'/L	L'/W
WTi-Cu Interface	6.97 ± 0.04	4.06 ± 0.04	2.26 ± 0.04	2.06 ± 0.04	1259 ± 206	0.61	0.58	1.97
inside WTi	6.79 ± 0.04	3.95 ± 0.04	1.29 ± 0.04	1.79 ± 0.04	1092 ± 76	0.61	0.58	2.01
WTi-SiO_x Interface	7.34 ± 0.04	4.95 ± 0.04	1.79 ± 0.04	2.08 ± 0.04	1328 ± 70	0.64	0.67	2.38

the different realizations, providing a strong indication that the observed behaviour will be mainly dependent on the initial notch position.

In Fig. 2 the respective raw load-displacement data is shown on the left axis in black, while the dynamic compliance data is shown on the right axis in red. Due to slight variations in the sample geometry, the absolute values of the dynamic compliance can vary. However, it should be noted that the plotted range is kept constant at 1 nm/µN for all three specimens to give a better comparability, while the distinctly different levels of load and displacement required variable scaling of the axis. The data of the WTi-Cu interface (Fig. 2a) shows a load level exceeding 150 µm when the first strong deviation from linear behaviour occurs, while these deviations are noticeable for the other two specimens at significantly lower levels, around 50–60 µm. Furthermore, the load in Fig. 2a increases up to 1 µm of deflection, suggesting material hardening, whereas the load in Fig. 2b gradually decreases after an initial load drop at 360 nm. The dynamic compliance data of the WTi-Cu interface displays a significant amount of initial contact compliance, down to a base level of 0.8 nm/µN, and only a small increase in dynamic compliance during the experiment, while the data inside the WTi (Fig. 2b) shows only a small amount of initial contact compliance and a pronounced change of compliance during the experiment. Initial changes in compliance can be attributed to the establishment of a rigid contact between indenter tip and cantilever and is a function of the individual material pairing, surface roughness, global stiffness of the specimen and indentation plasticity. However, once the contact is established during elastic loading of the beam the overall cantilever compliance overtakes the contribution, from contact compliance as is evident from the constant compliance level observed before the occurrence

of plastic deformation or crack extension. The load displacement curve of the SiO_x-WTi interface (2c) depicts a step-wise behaviour, suggesting that a crack forms at the notch tip and grows towards a feature, *i.e.* the interface, where it is stopped. This is further supported by the step-wise behaviour of the matching dynamic compliance data.

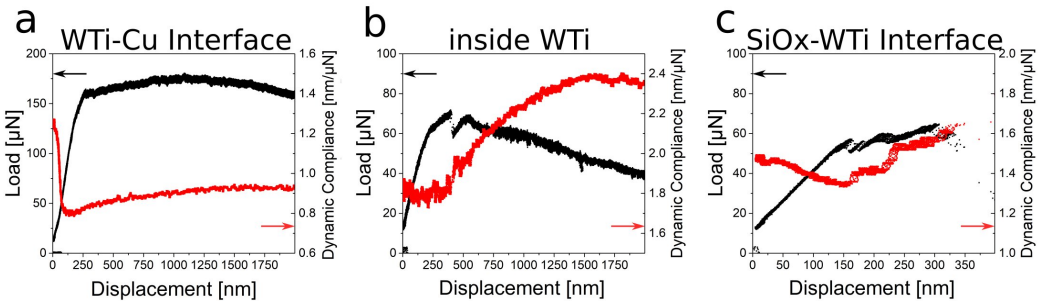

Figure 2: Raw load-displacement data (black, lefthandside) and dynamic compliance data (red, righthandside) of the individual specimens with notches at the (a) WTi-Cu interface, (b) inside the WTi and at (c) the SiO_x-WTi interface, respectively.

Fig. 3 depicts in-situ SEM images of the individual specimens before and after testing. The WTi-Cu interface shows a major amount of plastic deformation, *i.e.* crack tip blunting in the Cu (Fig. 3b) and no obvious crack extension in the in-situ images (Fig. 3c). This is in good accordance with the load and dynamic compliance data (Fig. 2a), respectively. The pore at the bottom of the cantilever in Fig. 3a as well as the hook shaped edge of the sample are FIB processing artefacts. However, the pore should not have a major influence, as its position is rather far away from the stress concentration produced by the notch, while the hook shaped edge in connection with residual material on the wedge (Fig. 3a) is the most likely explanation for the strong change in contact compliance evident in the dynamic compliance data of this specimen (Fig. 2a). The sample with the notch inside the WTi (Fig. 3d) shows initial crack extension through the WTi layer, followed by a deflection of the crack front perpendicular towards the WTi-Cu interface, where again plastic deformation in the Cu governed the mechanical behaviour and stopped further crack extension, as is evident from the decrease in dynamic compliance (Fig. 2b). The vertical feature at the interface between WTi and Cu is again a residual from FIB processing. However, as the crack grew initially inside the WTi, it is assumed to not act as a major defect influencing the fracture process. The specimen notched between WTi and SiO_x depicted in Fig. 3g exhibited the straightest crack extension without any visible plastic deformation.

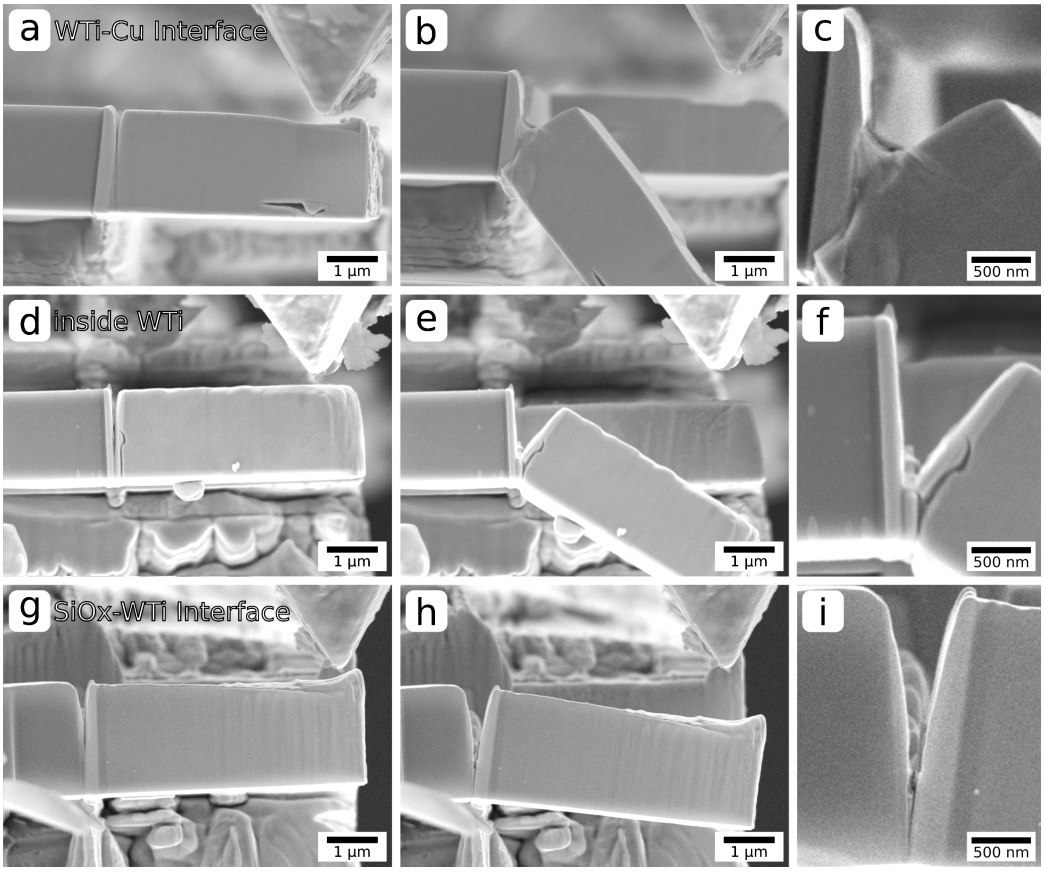

Figure 3: In-situ SEM images of the three cantilevers (a,d,g) before and (b,e,h) after deformation. The images c,f and i provide the magnified notch position after deformation for a detailed view on the fracture/deformation process of the individual specimens.

Fig. 4 shows the fracture surfaces under a tilt angle of 30° towards the base of each cantilever, respectively. From the WTi-Cu interface (Fig. 4a) it is evident that mainly plastic deformation has taken place, leading to the formation of a pore in the centre of the fracture surface. It should be noted that the cantilever was bent down further to achieve better visibility of the fracture surface after the actual experiment had ended. This resulted in a slight twist misalignment of the cantilever with respect to the crack front. In comparison, the fracture surface inside the WTi (Fig. 4b) shows short crack extension parallel to the interfaces, followed by perpendicular crack deflection towards the WTi-Cu interface. The faceted features at the origin of crack deflection suggest that it had originated at WTi grain boundaries. Finally, the fracture surface of the SiO_x-WTi interface (Fig. 4c) depicts completely

different features with perfectly straight crack extension starting from the initial notch through the connected ligament. The jagged line on the fracture surface suggests that the initial notch was not positioned perfectly at the interface, but rather in the WTi close to the interface. Thus, the crack had to grow towards the SiO_x-WTi interface before it accelerated in the interface, which is in good agreement with the step-wise load and dynamic compliance data (Fig. 2c) that was evident during the testing of this specimen.

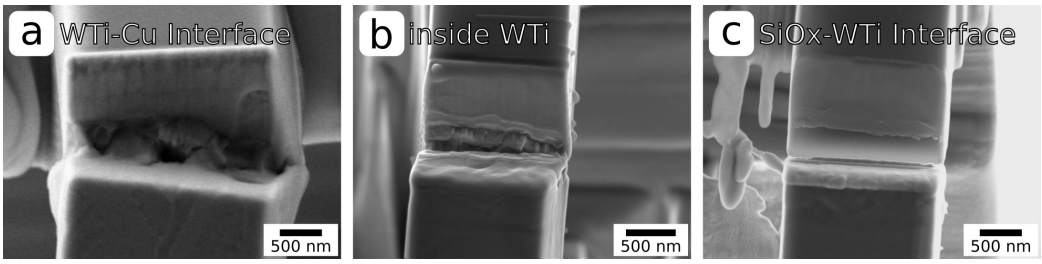

Figure 4: Fracture surfaces of (a) the WTi-Cu interface, (b) the WTi and (c) the SiOx-WTi interface, respectively. All images are taken under 30° tilt and in the direction towards the base of the cantilever.

Figs. 5a to c depict the calculated J-integral values (Eq. 1) as a function of crack extension $\Delta a = a - a_0$ (Eq. 2) for all three specimens, respectively. The data on the bottom of the graph ($<10\,\mathrm{J/m^2}$, greyed area) shows negative crack extension, which is only a measurement artefact due to the undefined increase in contact stiffness between wedge tip and specimen in the early loading stages and should not be mistaken as physical crack extension. It is evident that the data for the WTi-Cu interface (Fig. 5a), as well as the data of the WTi notch (Fig. 5b) curve in the opposite direction to the commonly observed behaviour in J-Δa analysis. Thus, they are far outside any classical evaluation scheme for elastic-plastic fracture mechanics, as plasticity governs the majority of deformation in these specimens. However, considering the detailed data shown in Figs. 5d and e, one can observe that the first point of virtual crack extension exceeding 10 nm is around $23.6\,\mathrm{J/m^2}$ for the WTi-Cu interface , while it is at about $51.2\,\mathrm{J/m^2}$ for WTi, respectively. The J-Δa curve of the SiO_x-WTi interface (Figs. 5c and f) shows two steps of rapid crack extension at $12.1\,\mathrm{J/m^2}$ and $18.2\,\mathrm{J/m^2}$ before the final unstable crack extension at $32.4\,\mathrm{J/m^2}$, after which J increases approximately linearly with Δa.

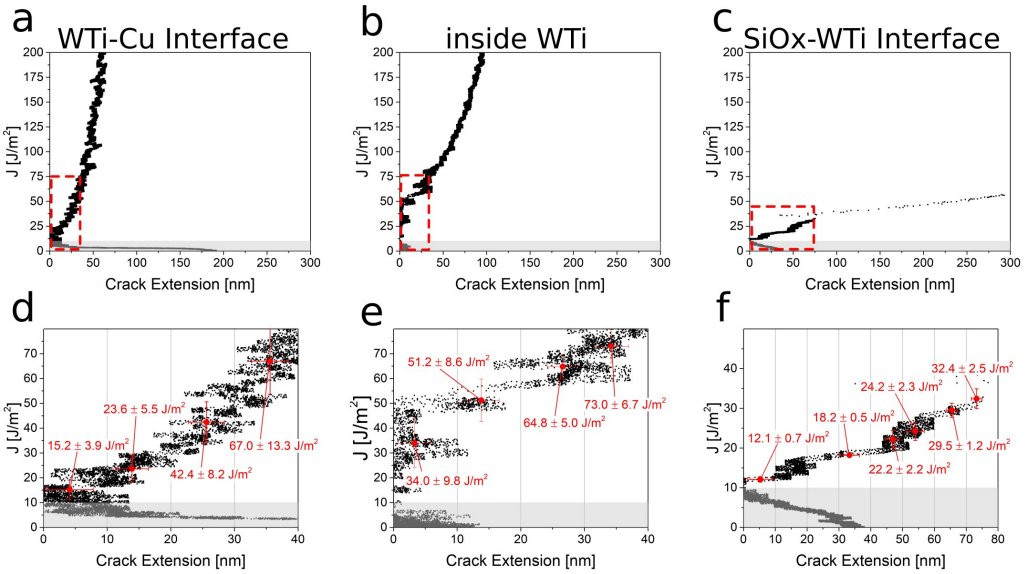

Figure 5: J-Δa curves of the individual specimens: (a) WTi-Cu interface, (b) WTi and (c) SiO_x-WTi interface. The details marked with red boxes are shown below (d,e,f) with the red marks being averaged data in the respective 10 nm wide windows.

Part 4
Discussion

It is clearly evident from the in-situ images as well as the J-Δa data that all three specimens show distinctly different behaviour with regards to the interplay between crack extension and plastic deformation. The WTi-Cu interface specimen shows no resemblance with classical fracture mechanics, where the initial crack tip blunting, visible as an increasing J-integral at an approximately constant initial crack length a_0 would be followed by evident crack extension, resulting in a concave down shape (negative second derivative) of the J-Δa curve. Instead, the measured compliance increases nearly instantly (Fig. 2a) resulting in an immediate increase in calculated crack extension (Figs. 5a,d) and a concave up shape of the J-Δa curve. However, as evident from the in situ images (Figs. 3b,c) this only corresponds to a major amount of plastic deformation, resulting in crack tip blunting right from the start of the experiment. On the other hand, the specimen with the notch inside the WTi exhibits a more classical behaviour with loading up to 51.2 J/m^2 (Fig. 5e) before a crack extension higher than 20 nm is detected.

This suggests that the initial behaviour is driven to a larger extent by fracture through the WTi layer, before plasticity finally takes over once the crack deviates into the WTi-Cu interface. Considering an elastic modulus for WTi of E= 324 GPa [5], a J-integral value of 51.2 J/m^2 corresponds to a stress intensity factor $K = \sqrt{JE}$ of 4.1 MPam$^{1/2}$ (in plane stress loading condition). Studies on single crystalline W of similar size and with elastic-plastic considerations in mind showed stress intensities between 3 and 16 MPam$^{1/2}$ [9, 17, 18], depending on orientation, size and exact evaluation criterion. However, considering that the WTi layer is synthesized by sputter deposition, which commonly results in grain sizes of tens of nm [19], the contribution of grain boundaries and their respective interface toughness cannot be neglected. Therefore, the observed value of 4.1 MPam$^{1/2}$ is on the lower end of the spectrum in comparison to single crystalline W. Treml *et al.* [20] studied a multilayer stack consisting of sputtered W and Cu, with a similar film thickness to the WTi in the present experiments and found a fracture toughness of 3.3 MPam$^{1/2}$. Taking into account that their experimental setup allowed for a crack propagation along the columnar grain boundaries obtained by sputter deposition, while the geometry shown herein constrains the crack to grow perpendicular to the columns, a slightly higher fracture toughness is expected [21]. Furthermore, one has to mention that the creation of the notch through FIB processing can lead to an undefined higher defect density at the notch ground [22], which could promote the initial crack extension through the WTi layer. Since the crack deflects along the weaker columnar boundaries as shown in Fig. 4b it is not possible to distinguish if the initial crack growth is a result of the local position of the initial notch (inside the grains) or the FIB damage. However, in comparison with literature the obtained value seems reasonable and gives us confidence that the calculated initiation of crack extension is mainly due to material fracture processes. The SiO_x-WTi specimen shows the most resemblance with classical fracture mechanics, as it is the only specimen with unstable crack growth. However, the initial two steps in the J-Δa data (Fig. 5f) suggest that a crack nucleus was forming at the interface prior to final failure. Therefore, the interface toughness should not be taken as the maximum J, but rather as the difference between the maximum J before final failure and the last plateau which suggests crack initiation, such that $J_{interface}$= 32.4-18.2= 14.2 J/m^2. Matoy *et al.* [5] reported an interface toughness for their SiO_x-WTi interface of G= 4.8 J/m^2, with G=J in the linear elastic case. This value seems to be quite low in comparison to our elastic-plastic result, especially as no strong evidence of plastic deformation is present in the SiO_x-WTi specimen (Figs. 3h,i and Fig. 4c). Calculating the linear elastic energy release rate for the given specimen as presented in [5], with a maximum load of F= 64.7 µN

(Fig. 2c) results in G= 2.9 J/m^2, which is in the same range as their results. However, Matoy *et al.* took a constant geometry factor of 1.12, which is known to be only valid for very deep notches in a semi-infinite plate, loaded in pure tension (mode I) [23]. Considering that the geometry factor shows a rather different dependence in the used cantilever shaped geometry, as shown by Brinkmann *et al.* [24], one can recalculate the linear elastic energy release rate from Matoy *et al.* [5] to be G= 11.0 J/m^2, when using the more appropriate geometry factor taken from [16]. This appears to be in good agreement with the observed amount of J= 14.2 J/m^2, in particular when taking into account differences in chemistry and some minor contribution of plasticity. While the distinctive difference between all three samples is evident, it should be noted that the quantitative values should be taken with care, as the measurements are in a regime where the classical criterions for size independent fracture properties are not valid anymore. Furthermore, as only 3-4 Cu grains are in contact with the WTi interface, the specific crystallographic orientation of the individual Cu grains could have a distinct influence. However, a full tomographical analysis of each specimen would be necessary to address the individual orientational dependencies, which is outside the scope of this work. Furthermore, the experiments as conducted herein (based on load-displacement data) measure the global change of J-integral and are not capable of resolving the fluctuations in the near field surrounding the crack tip, which are governed by elastic and plastic incompatibilities of the individual constituents. Nevertheless, as the size of features in microelectronic components is in the dimensional range shown herein, the obtained values can be considered valid as the experiments were conducted at the native scale of the features of interest. Thus, the shown experimental approach can act as a method to generate input for further analysis of microelectronic components or other miniaturized features.

Part 5
Conclusion

Different interfaces of a Si-SiO_x-WTi-Cu multilayer were successfully measured by the micro cantilever deflection technique. The WTi-Cu interface showed no resemblance with classical fracture mechanics concepts, but rather a distinct contribution of plastic deformation. However, as the geometry allowed for a very local probing of this interface, no other interface reached a critical stress intensity, which is very promising in the context of probing

individual features with higher toughness close to others with lower toughness. On the SiO_x-WTi interface we demonstrated the possibility to nucleate a natural crack from a FIB notch prior to final failure. This again is very promising for specimens that are known to be influenced by FIB processing. Furthermore, the resulting interface toughness of $14.2\,\mathrm{J/m^2}$ is in excellent agreement with previously conducted experiments when properly analyzing the experiments. Beyond interface toughness experiments, it was also shown that with careful positioning of the initial notch, even the only 300 nm thick WTi-layer could be investigated, resulting in a fracture toughness of $J = 51.2\,\mathrm{J/m^2}$ ($K = 4.1\,\mathrm{MPa}^{1/2}$), which is again in good agreement with literature values of sputtered W. Therefore, these results give confidence that carefully executed micro cantilever deflection experiments in conjunction with proper elastic-plastic fracture mechanics considerations can be utilized to address quantitative, if not always size-independent, local fracture properties of specific phases and interfaces.

Acknowledgments

The authors gratefully acknowledge the financial support under the scope of the COMET program within the K2 Center "Integrated Computational Material, Process and Product Engineering, IC-MPPE" (Project A2.12). This program is supported by the Austrian Federal Ministries for Transport, Innovation and Technology (BMVIT) and for Digital and Economic Affairs (BMDW), represented by the Österreichische Forschungsförderungsgesellschaft (Funder ID: 10.13039/501100004955), and the federal states of Styria, Upper Austria, and Tyrol. This project has received funding from the European Research Council (ERC) under the European Union's Horizon 2020 research and innovation programme (Grant No. 771146 TOUGHIT).

Conflict of interest

On behalf of all authors, the corresponding author states that there is no conflict of interest.

References

1. Uchic, M. D., Dimiduk, D. M., Florado, J. N. & Nix, W. D. Sample dimensions influence strength and crystal plasticity. *Science* **305,** 986–989 (2004).
2. Berger, J., Glushko, O., Marx, V. M., Kirchlechner, C. & Cordill, M. J. Effect of Microstructure on the Electro-Mechanical Behaviour of Cu Films on Polyimide. *JOM* **68,** 1640–1646 (2016).
3. Sernicola, G. *et al.* In situ stable crack growth at the micron scale. *Nature Communications* **8** (2017).
4. Sebastiani, M., Johanns, K., Herbert, E. & Pharr, G. Measurement of fracture toughness by nanoindentation methods: Recent advances and future challenges. *Current Opinion in Solid State and Materials Science* **19,** 324–333 (2015).
5. Matoy, K., Detzel, T., Müller, M., Motz, C. & Dehm, G. Interface fracture properties of thin films studied by using the micro-cantilever deflection technique. *Surface and Coatings Technology* **204,** 878–881 (2009).
6. Schaufler, J., Schmid, C., Durst, K. & Göken, M. Determination of the interfacial strength and fracture toughness of a-C:H coatings by in-situ microcantilever bending. *Thin Solid Films* **522,** 480–484 (2012).
7. Pippan, R., Wurster, S. & Kiener, D. Fracture mechanics of micro samples: Fundamental considerations. *Materials & Design* **159,** 252–267 (2018).
8. Ast, J., Merle, B., Durst, K. & Göken, M. Fracture toughness evaluation of NiAl single crystals by microcantilevers-a new continuous J-integral method. *Journal of Materials Research* **31,** 3786–3794 (2016).
9. Alfreider, M., Kozic, D., Kolednik, O. & Kiener, D. In-situ elastic-plastic fracture mechanics on the microscale by means of continuous dynamical testing. *Materials & Design* **148,** 177–187 (2018).
10. Wimmer, A. *et al.* Temperature dependent transition of intragranular plastic to intergranular brittle failure in electrodeposited Cu microtensile samples. *Materials Science and Engineering: A* **618,** 398–405 (2014).
11. Bigl, S., Wurster, S., Cordill, M. J. & Kiener, D. Advanced characterisation of thermo-mechanical fatigue mechanisms of different copper film systems for wafer metallizations. *Thin Solid Films* **612,** 153–164 (2016).

12. *ASTM Standard E1820-13, Standard Test Method for Measurement of Fracture Toughness* 1820 (ASTM International, West Conshohocken, USA, 2013).

13. Rice, J. R. Elastic-plastic fracture mechanics. *Engineering Fracture Mechanics* **5,** 1019–1022 (1973).

14. Zhu, Y. T., Liao, X. Z. & Wu, X. L. Deformation twinning in nanocrystalline materials. *Progress in Materials Science* **57,** 1–62 (2012).

15. Alfreider, M., Kolitsch, S., Wurster, S. & Kiener, D. An analytical solution for the correct determination of crack lengths via cantilever stiffness. *Materials & Design* **194,** 108914 (2020).

16. Riedl, A. *et al.* A novel approach for determining fracture toughness of hard coatings on the micrometer scale. *Scripta Materialia* **67,** 708–711 (2012).

17. Ast, J., Göken, M. & Durst, K. Size-dependent fracture toughness of tungsten. *Acta Materialia* **138,** 198–211 (2017).

18. Wurster, S., Motz, C. & Pippan, R. Characterization of the fracture toughness of micro-sized tungsten single crystal notched specimen. *Philosophical Magazine* **92,** 1–23 (2012).

19. Saghaeian, F. *et al.* Microstructure and stress gradients in TiW thin films characterized by 40 nm X-ray diffraction and transmission electron microscopy. *Thin Solid Films* **691,** 137576 (2019).

20. Treml, R. *et al.* Miniaturized fracture experiments to determine the toughness of individual films in a multilayer system. *Extreme Mechanics Letters* **8,** 235–244 (2016).

21. Daniel, R. *et al.* Anisotropy of fracture toughness in nanostructured ceramics controlled by grain boundary design. *Materials & Design* **161,** 80–85 (2019).

22. Kiener, D., Motz, C., Rester, M., Jenko, M. & Dehm, G. FIB damage of Cu and possible consequences for miniaturized mechanical tests. *Materials Science and Engineering A* **459,** 262–272 (2007).

23. Anderson, T. L. *Fracture Mechanics: Fundamentals and Applications, Second Edition* (CRC Press, 2005).

24. Brinckmann, S., Matoy, K., Kirchlechner, C. & Dehm, G. On the influence of microcantilever pre-crack geometries on the apparent fracture toughness of brittle materials. *Acta Materialia* **136,** 281–287 (2017).

Publication D

The influence of chemistry on the interface toughness in a WTi-Cu system

Acta Materialia
under review

The influence of chemistry on the interface toughness in a WTi-Cu system

Markus Alfreider[1], Rishi Bodlos[2], Lorenz Romaner[2], and Daniel Kiener[1]

[1]Department Materials Science, Chair of Materials Physics Montanuniversität Leoben, 8700 Leoben, Austria
[2]Materials Center Leoben Forschungs GmbH, 8700 Leoben, Austria

Abstract

With a considerable amount of commonly used material systems consisting of individual, rather confined layers, the question for mechanical behaviour of their individual interfaces arises. Especially, when considering varying interfacial structures as a result of the processing environment. Furthermore, the interaction between pronounced plasticity and fracture processes can lead to challenges with regards to separation between sole interface- or bulk properties. The present work investigates the interfacial fracture characteristic of a WTi-Cu sytem commonly found in the microelectronics industry as a heterogeneous model material with pronounced plasticity in the Cu phase. To study this behaviour on a rather limited scale ($< 6\,\mu m$), microcantilever experiments were conducted and evaluated using a continuous J-Δa curve evaluation scheme with classical elastic plastic considerations in mind. A change in interface chemistry, resulting from air exposure between processing steps was probed and found to show distinct crack propagation along the interface opposed to crack tip blunting as found in the vacuum processed sample. Complementary density functional theory calculations also showed a strong reduction of interface cohesion upon oxygen accumulation and a model framework based on classical dislocation plasticity considerations revealed the transition from plasticity to fracture processes to be a result of shielding and following change in mode mixity.

Part 1
Introduction

A considerable amount of technologically relevant material systems consists of multi-layered structures, where individual constituents meet different demands with regards to, *e.g.* electrical [1, 2] or thermal [3–5] insulation/conduction, wear protection [6], semi-conducting [7] or optical properties [8]. These systems are often confined to only a few hundred nm up to tens of um, which gives rise to significant challenges with regards to evaluation of structural properties. However, as the resulting stresses during service, arising due to thermal conditions and/or external loading, are commonly non-negligible, it is necessary to investigate mechanical threshold values, *e.g.* yield onset or critical fracture parameters. First steps to meet these challenges were made in recent years, facilitated by the development of various small scale testing techniques, such as nanoindentation [9, 10], micropillar compression [11, 12] or microtensile testing [13–15] for plasticity values and notched microcantilever bending [16, 17], double cantilever wedging [18] or pillar splitting [19] for fracture toughness values. Especially, microcantilever bending has been successfully applied to a wide field of systems with either spatially limited geometries, *i.e.* thin films [20] or very confined local features of interest, such as grain boundaries [21, 22] or interfaces [23–25], to address fracture properties of confined material conditions. However, while most of the recent literature addresses the experimental evaluation within the framework of linear-elastic fracture mechanics (LEFM) [16, 26, 27], the application of elastic-plastic fracture mechanics (EPFM) [28–30] is only rarely found due to more challenging experimental conditions. Given that a high failure tolerance is generally desired, and many application relevant systems already show pronounced plastic deformation around the fracture process zone, it is necessary to incorporate EPFM into small scale testing, especially if subtle changes of mechanical response due to local fluctuations in chemistry or structure are to be probed. In the present work, we focus on the fracture characteristics of a WTi-Cu interface in a thin ($< 6\,\mu m$) multilayer system as a universal model system for a heterogeneous interface with significant differences in elastic properties amongst the phases and pronounced plasticity in one of them. The interface was deliberately altered by air exposition between processing steps to induce chemical changes due to oxide formation, leading to a comparative set of samples with and without an interfacial oxide layer, while leaving everything else unaltered. Microcantilever experiments and EPFM evaluation schemes were conducted to investigate the interface frac-

ture properties, and pronounced changes with respect to air exposition were evidenced. In conjunction with density functional theory (DFT) simulations and classical dislocation plasticity considerations, we present a reasoning for the observed behaviour, which we suggest as an explanatory foundation for the general behaviour of elastic-plastic bi-layer materials systems at the micron scale.

Part 2
Experimental procedure

2.1 Materials and sample preparation

The multi-layered material system studied herein is based on common wafer processing technologies and consists of the following constituents: (001) oriented single crystalline Si substrate, 50–70 nm thermally grown SiO_x, 270–300 nm WTi layer ($\approx$ 100 nm grain size) and 5 µm electrodeposited Cu film ($\approx$ 2.7 µm grain size). This material combination is a common base structure in the microelectronics industry and was studied previously, *e.g.* by Wimmer *et al.* [31], Bigl *et al.* [32] (Film A) and Alfreider *et al.* [33], where further information can be found. Usually, such specimens are entirely processed in vacuum. However, to obtain a different chemical environment at the interface between WTi and Cu, the specimens were deliberately exposed to atmosphere after the WTi deposition step for a short amount of time ($\approx$ 10 min]), which resulted in the formation of an undefined surface oxide layer before Cu deposition was continued. Thus, this layer stack allows the investigation of mechanical differences at the WTi-Cu interface as a consequence of oxygen exposition. To probe the interface fracture properties of the standard vacuum processed as well as the air-exposed specimens, micron sized cantilever shaped specimens were fabricated by focussed ion beam milling (FIB, LEO 1540XB, Carl Zeiss AG, Oberkochen, Germany) on mechanically broken platelets of the multilayer stack as shown in Fig. 1a. First, a smooth 90° corner was fabricated using higher FIB milling currents (10 nA) as shown in Fig. 1b, followed by subsequently decreasing currents down to 50 pA for polishing the final shape as depicted in Fig. 1c. An initial notch a_0 was produced also with 50 pA and positioned manually between the Cu and the WTi layer before the final polishing step to reduce curtaining artefacts.

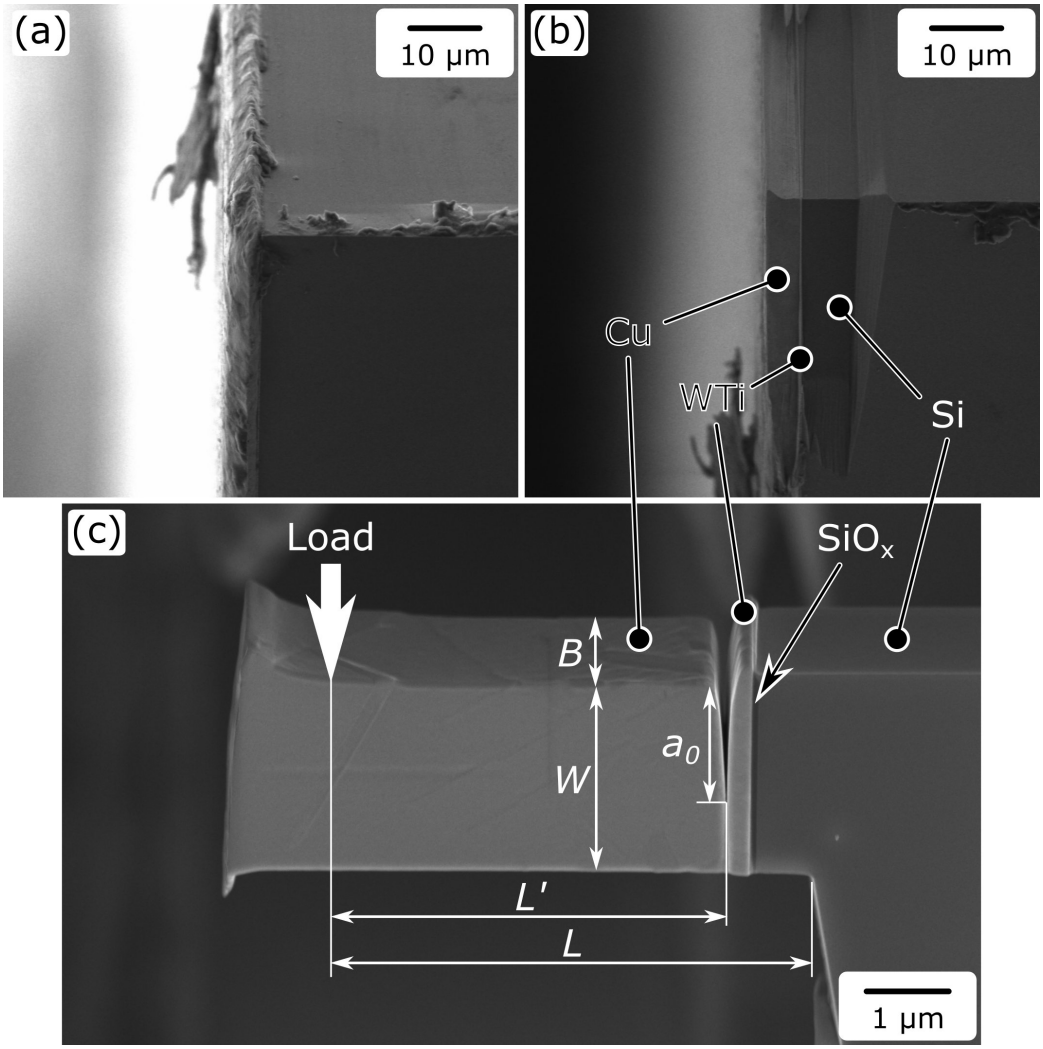

Figure 1: (a) The 90° corner of an as-broken wafer platelet. (b) The same 90° corner after coarse FIB processing reveals the individual constituents of the multilayer stack. (c) The final shape of a microcantilever specimen on the same corner before testing, with indication of all necessary geometric dimensions for further evaluation.

2.2 Microcantilever fracture experiments and evaluation

All microcantilever deflection experiments were conducted in the same FIB, utilizing a Hysitron PI-85 system (Bruker Corporation, Billerica, USA) equipped with the nanoDMA III upgrade to allow for continuous measurement of stiff-

ness changes during testing. To achieve a line contact between transducer and specimen, a 5 µm wide conductive diamond wedge tip with an opening angle of 60° (Synton-MDP AG, Nidau, Switzerland) was used. The specimens were loaded in open-loop, load-controlled mode with a superimposed sinusoidal amplitude of 5 µN at a frequency of 80 Hz and a nominal loading speed of 10 µN/s, based on previous investigations [30]. To reduce any contact issue with the inherently load-controlled transducer, the specimens were elastically pre-loaded to 10 µN before the start of each experiment. As the Cu part of the fracture specimen is prone to a major amount of plastic deformation, it is necessary to conduct an elastic-plastic fracture mechanical evaluation based on the J-Integral concept, as described in detail previous works [30, 33]. Due to the heterogeneous nature of the specimens it is not possible to apply the common splitting of elastic and plastic components of the J-integral [34, 35], as the Young's modulus of the multilayer stack is not properly defined. Therefore, we consider an older calculation for the J-integral evaluation as [36, 37]:

$$J_n = \frac{2A_{tot,n}}{B(W - a_n)} \tag{1}$$

where J_n is the J-integral at point n, $A_{tot,n} = \int_0^{u_n} F du$ is the total area under the measured load-displacement (F-u) curve up to point n, a_n is the current crack length at point n and B, W are geometric parameters as defined in Fig. 1c. The current crack length a_n is calculated from the experimentally gathered compliance signal [30] as:

$$\int_0^{a_n} \frac{a}{W}\ Y\left(\frac{a}{W}\right)^2 da = \frac{(c_n/c_0 - 1)L^3}{18\pi(1-\nu^2)L'^2} \tag{2}$$

where $Y(a/W)$ is a geometry factor [16], $\nu = 0.3$ is Poisson's ratio, c_n is the measured compliance of the cantilever at point n and c_0 is the compliance of the unnotched cantilever. The detailed derivation of Eq. 2 is provided in [38]. The compliance of the unnotched beam is initially unknown, but can be evaluated from the stable compliance level $c(a_0)$ after initial contact is established [30] and before crack extension occurs as [33]:

$$c_0 = \frac{c(a_0)}{1 + \left(18\pi(1-\nu^2)\frac{L'^2}{L^3}\right)\int_0^{a_0} \frac{a}{W}\ Y\left(\frac{a}{W}\right)^2 da} \tag{3}$$

All integration was done numerically using the trapezoidal rule and the crack length a_n was found by interpolation. Furthermore, as both Eqs. 2 and

3 are independent of any material parameters with the exception of Poisson's ratio, they can be considered applicable for the given heterogeneous material system.

2.3 Density functional theory simulations

As the aim of the DFT calculations was to study the difference of interface cohesion, with and without air exposure it was feasible to simplify the investigated system and reduce computational effort by considering single phase body centred cubic (bcc) W instead of WTi and considering a single layer of O instead of varying air compositions. This is supported by the findings of Kalha *et al.* [39] who found that these are the major surface components of the present film in as-deposited condition without any annealing treatment. The simulation system consisted of 48 W atoms (valence electron configuration: 5p6 5d4 6s2) on top of 60 Cu atoms (valence electron configuration: 3d10 4s1) in a Nishiyama-Wassermann [40, 41] configuration (Fig. 2). In the case of the air exposed system a single layer, consisting of 8 O atoms (valence electron configuration: s2 p4) was inserted between the Cu and W. The DFT calculation were done for various interface separation distances d, using the Vienna Ab-Initio Simulation Package (VASP) [42–44] using Perdew–Burke-Ernzerhof (PBE) functionals [45, 46] and the projector augmented wave method (PAW) [47, 48]. The KPOINT mesh was $3 \times 8 \times 1$ and periodic boundary conditions were applied in x and y direction (Fig. 2). The binding energy E_b as a function of d was calculated as:

$$E_b(d) = \frac{E_{sys}(d) - E'_{sys}}{A} \tag{4}$$

With $E_{sys}(d)$ being the energy of the whole system at separation d and E'_{sys} denoting a system with sufficient amount of vacuum between the Cu fcc and W bcc slab to have no remaining interaction ($E_{sys}(d \to \infty)$). In order to probe only the cohesive properties of the interface excluding any elastic contributions from the individual slabs, the individual Cu and W atom positions remained fixed in z direction, while the O atoms were allowed to relax freely after each separation increment. Plotting the binding energy over a large separation range gives us a traction separation curve. A similar, more in depth calculation of traction separation curves with focus on the effect of C impurities on Mo grain boundaries can be found in Ref. [49].

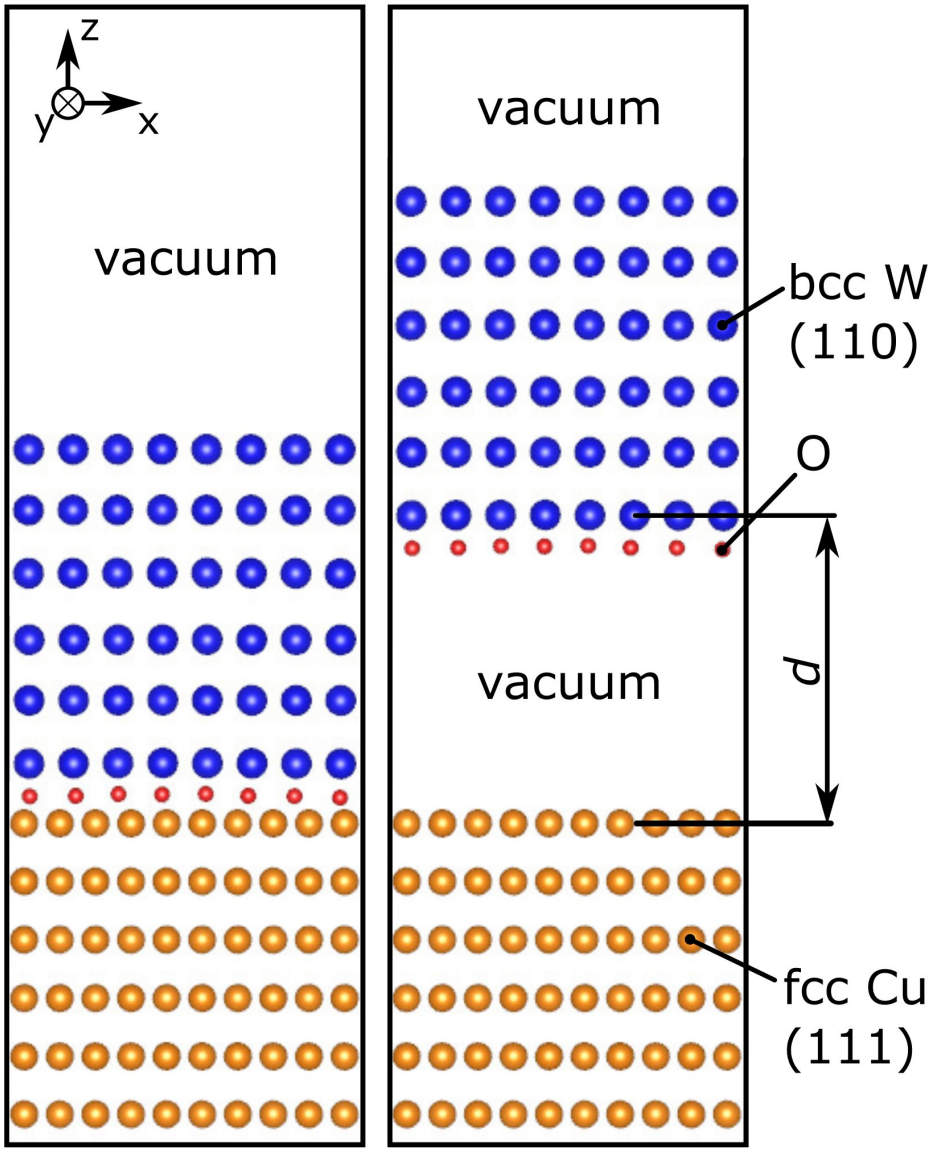

Figure 2: Simulation system in initial and separated positions. Blue spheres correspond to bcc W atoms, yellow spheres to fcc Cu atoms and the smaller red spheres to O atoms.

Part 3
Results

The challenging nature of the individual sample preparation on the edges of such platelets does not allow for a large statistical assessment, but rather

serves an in depth evaluation of each specimen specifically. Therefore, two specimens of each processing route (full vacuum processing or air exposure) are shown in detail in the following. All geometric parameters were measured before testing using ImageJ 1.54s, with the exception of a_0, which was measured after failure at the fracture surface. Error estimates for all non-specified measurements can be considered as ±30 nm, which corresponds to ±30 px. The error estimates of a_0 are based on the standard deviation of 10 evenly spaced measurements over the whole width of the fracture surface. All data is summarized in Tab. 1.

Table 1: Geometries of all cantilevers used for evaluation

	L [µm]	L' [µm]	a_0 [nm]	B [µm]	W [µm]	L'/L	a_0/W	L'/W
vacuum 1	6.79	4.20	1120 ± 252	2.02	1.14	0.62	0.55	2.08
vacuum 2	5.08	4.73	1540 ± 115	2.36	2.22	0.73	0.65	2.00
air 1	4.42	3.67	1410 ± 150	2.31	1.87	0.83	0.61	1.59
air 2	5.81	3.98	900 ± 76	2.19	1.66	0.68	0.41	1.82

3.1 Fracture experiments

The raw load and dynamic compliance data with respect to load-line displacement is shown in Fig. 3 for all specimens. Evidently, the vacuum processed specimens (Figs. 3a,b) show only minor decrease in load after the linear elastic regime, while the air exposed specimens (Fig. 3c,d) depict a distinct decrease of load with increasing displacement. This is also represented in the dynamic compliance data (red), where the vacuum processed specimens exhibit a very minor increase in dynamic compliance, which settles after roughly 1000 nm of displacement (Fig. 3a,b), while the dynamic compliance of the air exposed specimens continuously increases with displacement. This difference is specifically apparent as the plotted range of dynamic compliance is 2 nm/µN for the air exposed specimens, whereas it is only 1 nm/µN for the vacuum processed ones. To address whether a systematic influence of difference in sample geometry is present, Fig. 3e shows the conditional stress intensity K [16] of all specimens up to a deformation of 1000 nm. As K is based only on linear elastic fracture mechanics considerations, it is definitely not valid beyond the elastic loading regime. However, the deviation from the linear elastic slope (onset of plastic deformation or fracture processes) is between 0.7 and 1.4 MPa$\sqrt{\text{m}}$, without any distinct trend between vacuum

processed or air exposed specimens. Furthermore, also the stress intensity values after onset of plasticity do not show any specific trend with regards to specimen type, which emphasizes again that no systematic error with respect to specimen geometry is present and that linear elastic concepts are definitely not sufficient to evaluate the given experiments.

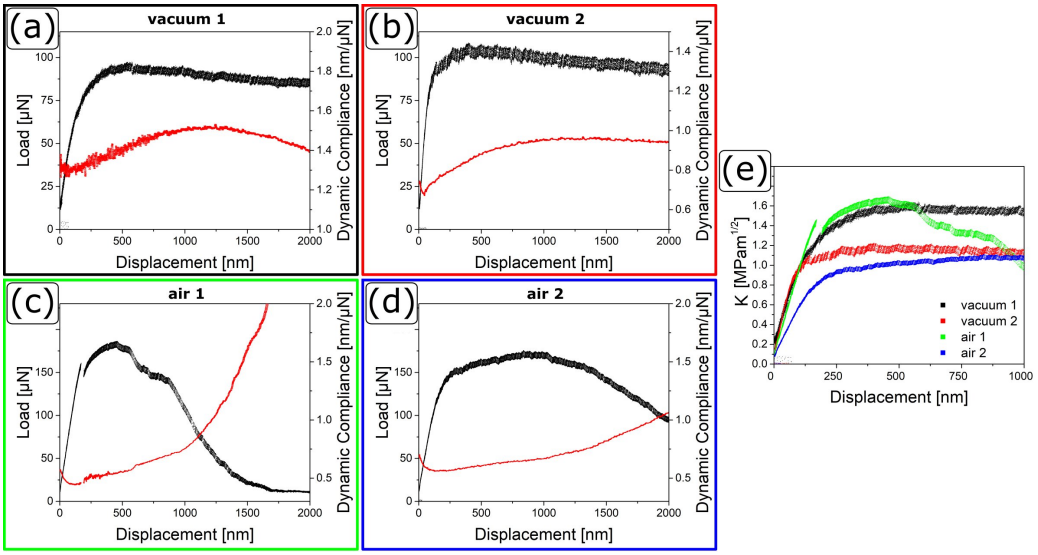

Figure 3: Raw load-displacement (black) and dynamic compliance-displacement (red) data of (a,b) the two vacuum processed specimens and (c,d) the two air exposed specimens. (e) The conditional stress intensity of all specimens shows a deviation from the linear elastic regime between 0.7 and 1.4 MPa$\sqrt{\text{m}}$, without any trend with respect to processing conditions.

The calculated J over crack extension Δa data for all specimen is summarized in Fig. 4a, where the difference between the air exposed and vacuum processed specimens is clearly evident. While the vacuum processed specimens resemble no comparability to the classical concave-down "R"-curve behaviour as observed commonly in fracture mechanical evaluation [50, 51], the air exposed specimens depict an evident transition from a similar blunting regime to a nearly linear increase of J with Δa. Fig. 4b,c show the *in situ* SEM micrographs of the initial and final shape of the second air exposed specimen, respectively. There it is evident that no pronounced crack extension took place. Instead the whole deformation was governed by plasticity in the Cu phase, which is in agreement with the corresponding J-Δa data, where no major crack extension was detected. The initial notch in the first air exposed specimen was fabricated quite far in the Cu phase (≈ 100 nm away from the interface) as seen in Fig. 4d. Nevertheless, after some major amount of plas-

tic deformation a small detachment of the Cu phase from the WTi layer was observed in the *in situ* images (Fig. 4e) up to a final full crack extension in the interface as evident in Fig. 4f. However, correlating the images with the data, one finds that the first occurrence of this detachment is already far into the linear regime of the J-Δa curve, while the transition between blunting and linear regime is considerably earlier at $J = 103.1 \pm 1.8\,\mathrm{J/m^2}$ (errors are based on the standard deviation of ± 100 data points). This leads to the conclusion that the crack did extend in the specimen interior before it was visible on the outer specimen surface. This is also reasonable considering the initial two faster crack extensions($J = 11.5 \pm 0.1\,\mathrm{J/m^2}$ and $J = 58.4 \pm 2.8\,\mathrm{J/m^2}$) in this specimen as evident in the blunting part of the data (Fig. 4a), as the crack needed to grow towards the interface in the specimen interior before it could grow towards the visible surface. The notch in the second air exposed sample was positioned precisely at the interface (Fig. 4g). However, the transition from blunting to crack extension at $J = 74.3 \pm 0.6\,\mathrm{J/m^2}$ as depicted in Fig. 4h is again not evident. Even far in the linear regime the *in situ* images still show a major amount of crack tip blunting without any evident surface crack extension (Fig. 4i). Only at a crack extension of 526 nm did it grow large enough to create a visible interface detachment (Fig. 4j) up to a nearly complete detachment of the Cu phase from the WTi layer (Fig. 4k), while still a lot of plastic deformation in the Cu was evident.

To visualize the difference between the two interface states in more detail, Fig. 5 shows the post mortem fracture surface of a vacuum processed and an air exposed specimen in comparison. The specimens were bent down further after the experiments to better expose the fracture surfaces, and the images are taken under an angle of 30°. The vacuum processed specimen (Fig. 5a) shows no distinct extension of the crack from the initial notch, while the air exposed specimen (Fig. 5b) clearly depicts a surface pattern on the WTi side which appears imprinted as a negative on the Cu side. These surface patterns are resultant of the faceted WTi layer, as shown for comparison in Fig. 5c in pristine condition before any further deposition took place. Taken together, these observations are a strong evidence that the crack grew explicitly at the interface between the layers, as this very detailed pattern still remains intact on both sides of the cantilever (Fig. 5b).

3.2 Atomistic interface binding energy

The results of the DFT simulations are summarized in Fig. 6a, where the binding energy E_b as a function of interface separation d of the W/Cu system and the W/O/Cu system are depicted as blue filled circles and orange open

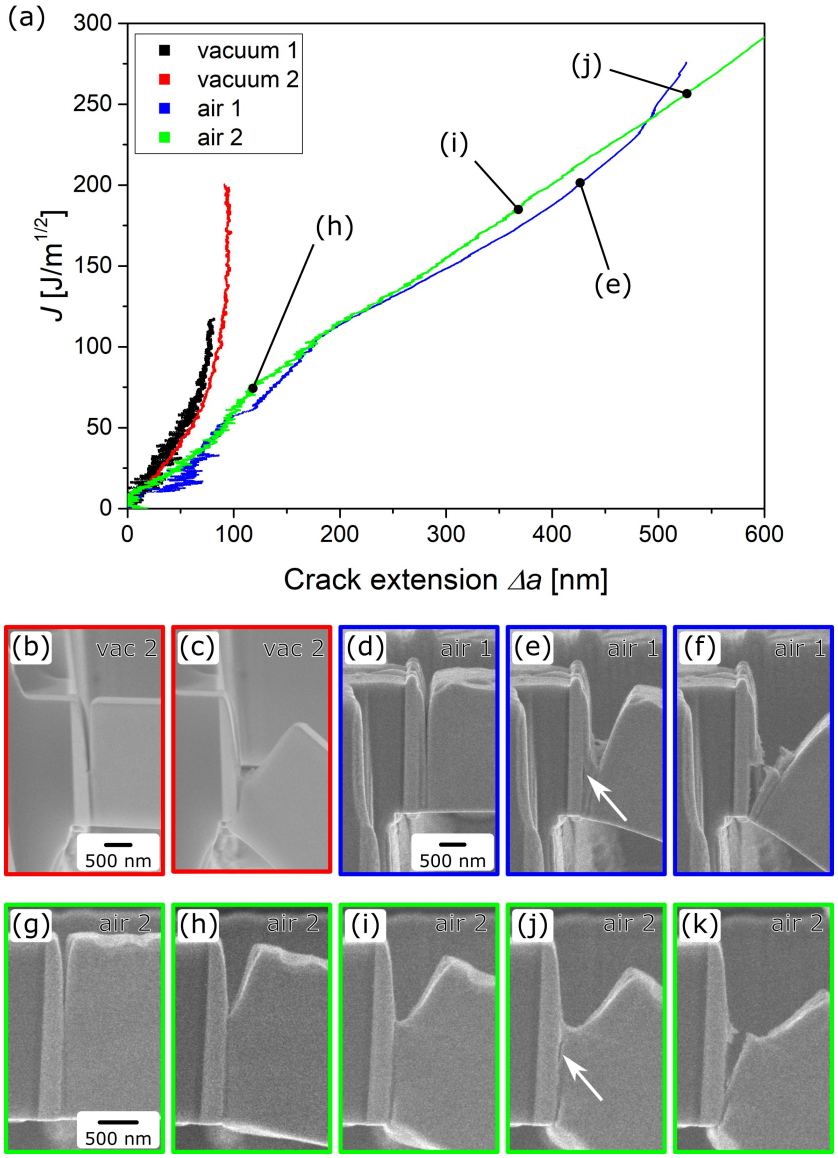

Figure 4: (a) J-Δa curves of all specimen, showing a distinct difference between the vacuum processed and air exposed versions. *In situ* SEM images showing the (b) initial and (c) final shape of a vacuum processed specimen and the evolution of crack geometry of the (d-f) first and (g-k) second air exposed specimen with notches close to and exactly at the interface, respectively.

squares, respectively. To investigate the traction-separation behaviour of the two interface states the universal binding energy relation (UBER) fit,

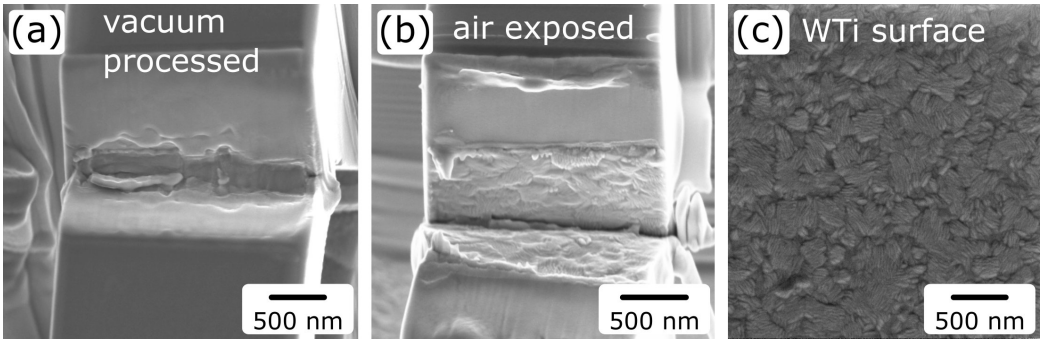

Figure 5: SEM micrographs of the fracture surfaces of (a) a vacuum processed and (b) an air exposed specimen. (c) The plain WTi surface without any further deposited layers.

proposed by Rose *et al.* [52] was utilized as:

$$E_b = -E_{b,max}\left(1+\frac{d}{l}\right)e^{\frac{-d}{l}} \tag{5}$$

where $E_{b,max}$ is the largest absolute value of the potential well, commonly also referred to as "Work Of Separation" (WOS), and l is a fitting parameter, commonly correlated with the Thomas-Fermi screening length [52, 53]. The non-linear least-square fitting procedure was conducted using the lmfit package (version 1.0.0) within the Python programming environment (version 3.7.7). The derivation of E_b with respect to d gives the traction σ perpendicular to the interface, necessary to pull it a distance d apart, as shown in Fig. 6b. It is evident from the peak heights that an approximately 6 times higher normal stress would be necessary in the pure W/Cu system compared to the W/O/Cu system to pull the interface apart. Furthermore, the respective peak positions δ show that the point at which the separation becomes unstable for a given stress is reached earlier ($\delta_{W/O/Cu} = 42.5\,\mathrm{pm}$) in the oxygen containing system than in the pristine system ($\delta_{W/Cu} = 56.5\,\mathrm{pm}$). All calculated values are summarized in Tab. 2.

Table 2: Calculated parameters based on the DFT simulations for the W/Cu and W/O/Cu system, respectively.

	$E_{b,max}$ (WOS) [J/m^2]	σ [GPa]	δ [pm]
W/Cu	3.471	22.67	56.5
W/O/Cu	0.429	3.72	42.5

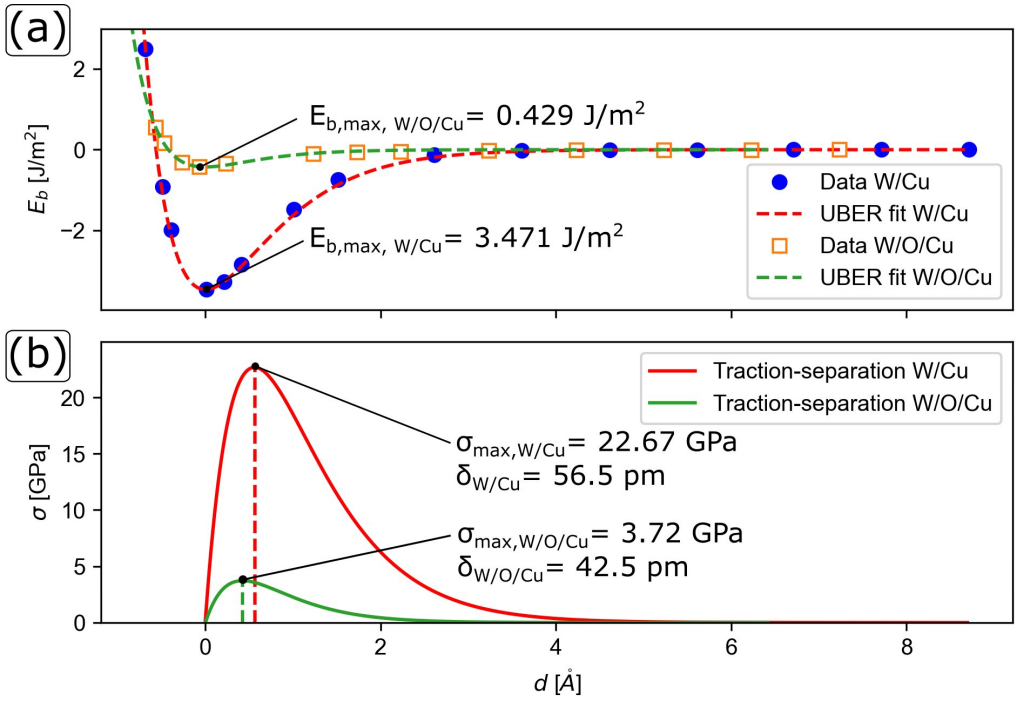

Figure 6: (a) Binding energy as a function of interface separation for the W/Cu interface (blue dots) and the W/O/Cu interface (orange squares) with the corresponding UBER-fits as dotted lines (red, green). (b) The traction-separation relations for both interfaces.

Part 4
Discussion

Based on the experimental data there is little doubt that the air exposure has a very strong influence on the fracture behaviour of the WTi-Cu interface. While both processing states show a major amount of plastic deformation in the initial loading, the air exposed specimens failed by nucleating and extending a crack at the interface, which was not observable in the vacuum processed specimens. This suggests a different threshold for the accumulation of crack tip plasticity before fracture processes occur. To rationalize the observed behaviour, we will on the one hand take a detailed look at the crack tip-dislocation nucleation interaction model proposed by Jokl *et al.* [54]. On the other hand, we will regard the change in local stress fields due to piling-up of dislocations (as a substitute for the global accumulation of plasticity) and conclude that both models are in reasonable agreement.

4.1 Crack extension vs. dislocation nucleation

The commonly applied Orowan modification [55] to the classical Griffith criterion [56] states that:

$$G_c = 2\gamma + \gamma_p \tag{6}$$

where G_c is the critical energy release rate to extend a crack, γ is the surface energy and γ_p is the dissipated work during the process, *e.g.* plasticity or phase transformation. Usually γ_p is considered a scalar material specific parameter. However, in 1980 Jokl *et al.* [54] argued that instead of a scalar value, γ_p should be considered as a function of γ as well, due to the fact that generally observed embrittling phenomena based on segregation, *e.g.* P in steels [57], S in Cu [58], would not affect dislocation mobility but rather cohesion and therefore γ. Their basic assumption is that dislocation emission and crack extension are simultaneous events, which leads to the mechanistic second order differential equation of motion as:

$$m\ddot{x} = -\frac{4\gamma b^2}{\delta^2}x + b^2\tau(v_0, n, G, k, t) \tag{7}$$

where m is the mass of a single atom, x is the displacement perpendicular to the crack plane, b is the magnitude of the Burger's vector, δ is the critical separation distance (see Tab. 2) and τ is the shear stress along the crack plane as a function of terminal dislocation velocity v_0, velocity exponent n, shear modulus G, local stress intensity k and time t. A schematic of the crack tip structure for this model is shown in Fig. 7a. Solving Eq. 7 for different values of k and searching for the first time at which $x > \delta$ leads to a function of the bond breaking time $t_B(k)$. From this, one can calculate the resulting work of dislocation emission $w_p(\gamma, k)$ up to time $t_B(k)$, and with that and the thermodynamic criterion:

$$-\frac{k^2}{2G}(1-\nu) + 2\gamma + w_p(\gamma, k) \leq 0 \tag{8}$$

find the local stress intensity upon fracture k_G. The plastically dissipated energy as a function of surface energy is then $\gamma_p(\gamma) = w_p(\gamma, k_G)$. The detailed derivation of all given formulae is not focus of this investigation and would

exceed the present manuscript, but the interested reader is encouraged to read Jokl *et al.*'s original work [54].

The given mathematical framework was solved numerically for Cu considering a full $\langle 110 \rangle \{111\}$ dislocation ($b = 256\,\mathrm{pm}$) instead of partials, with a terminal dislocation velocity $v_0 = 1600\,\mathrm{m/s}$ [59, 60] and a velocity exponent $n = 1.8$ [61]. The calculations were conducted using the LSODA algorithm [62] within the scipy library (version 1.2.1) using Python 3.7.7, with the boundary conditions of the differential Eq. 7 (initial position x_0, initial velocity $\dot{x}_0$) set to 0. The k_G (half symbols) and resulting γ_p (filled/open symbols) values were calculated as functions of the work of separation in $0.1\,\mathrm{J/m^2}$ steps for both critical separation distances $\delta_{W/Cu} = 54.5\,\mathrm{pm}$ and $\delta_{W/O/Cu} = 42.5\,\mathrm{pm}$, respectively, and are shown in Fig. 7b. There, it is evident that the W/Cu system has a steeper increase in plastic dissipation and an earlier point at which no bond breaking can be detected ($2.7\,\mathrm{J/m^2}$), in comparison to the W/O/Cu system where the bond breaking becomes undetectable at $4.3\,\mathrm{J/m^2}$. This occurs due to the fact that the thermodynamic criterion becomes non-negative over the whole k-range, which means that dissipated energy by dislocation emission dominates over the released energy by crack extension. Comparing this with the work of separation (WOS) from the DFT calculations (dotted lines), one finds that for the pure W/Cu system the point at which no bond breaking can be detected is far below $\mathrm{WOS_{W/Cu}}$, suggesting that only dislocation plasticity and no crack extension would take place, while in the W/O/Cu system the point at which bond breaking terminates is far above $\mathrm{WOS_{W/O/Cu}}$, which means that both plasticity and fracture processes are occurring.

However, the quantitative values should be taken with care, as in this model the amount of plastic dissipation would only be roughly $0.4\,\mathrm{J/m^2}$, which results in a critical J-integral value for crack initiation of $J_i \approx 0.8\,\mathrm{J/m^2}$ for the air exposed specimens, while we find values of up to $J_i = 103.1\,\mathrm{J/m^2}$ (Fig. 4a). This discrepancy of over two orders of magnitude is a result of considering only the very near crack tip region with rather simplified assumptions, *e.g.* neglecting crystallography, thermal activation, dislocation splitting or cross slipping. Nevertheless, although we only consider the Cu phase for the calculation of plasticity-fracture process interactions, the model gives an astonishing qualitative agreement with the experimental data, where again the vacuum processed specimens (correlate to W/Cu) show only plastic deformation, while the air exposed specimens (correlate to W/O/Cu) show both, plasticity and crack extension.

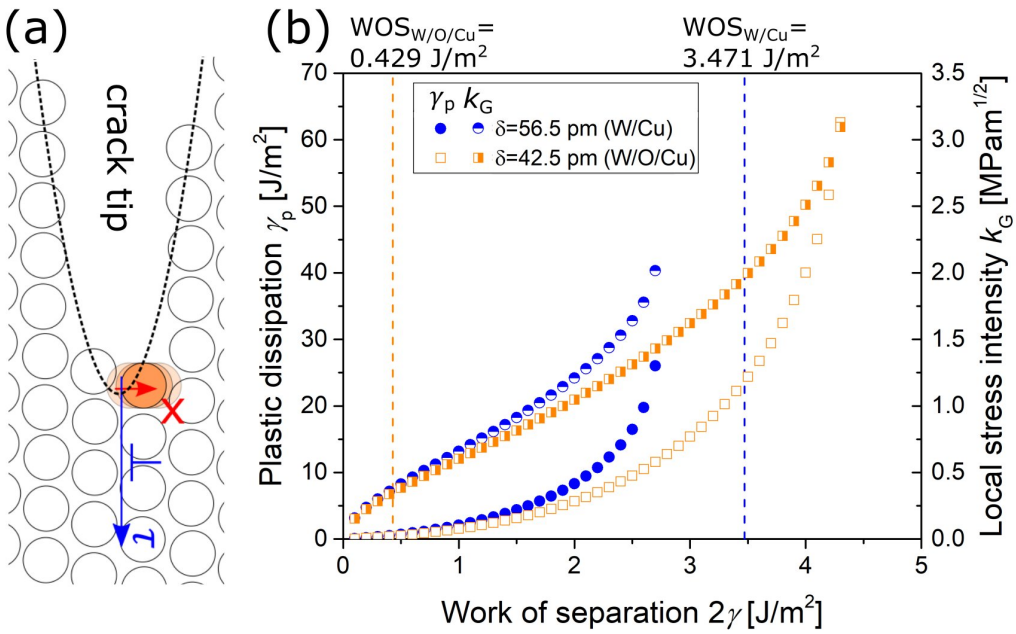

Figure 7: (a) Schematic of the atomistic crack tip model depicting the perpendicular deflection x and the direction in which the dislocation emitting shear stress τ is acting. (b) Calculated plastic dissipation γ_p and local stress intensity for unstable fracture k_G over work of separation 2γ for the W/Cu and W/O/Cu system, respectively.

4.2 Dislocation activity prior to crack extension

As the air exposed specimens do not show an initially brittle behaviour, but rather a distinct transition from plastic deformation to crack extension, it can be argued that this initial accumulation of plasticity creates an essential change to the specimen structure, which subsequently enables the fracture process. The most straightforward explanation is that continuous dislocation nucleation would lead to classical forest hardening which inhibits subsequent nucleation and leads to an increased threshold for plasticity. However, in specimens as small as the present ones, the necessary dislocation entanglements would be limited to a very confined volume, which means they need to remain in the near vicinity of the crack tip ($< 1\,\mu$m). Independent on how these dislocations arrange, such a high density of dislocations close to the crack tip would lead to a shielding effect on the crack tip and further to a reduced local stress intensity [63, 64]. Given that such an accumulation

would reduce both, the driving force for dislocation plasticity as well as for crack extension, it is difficult to understand at which point one overtakes the other (in the case of the air exposed specimens) if such a point even exists (considering the vacuum processed specimens). Thus, in the following we will present a 2-dimensional model based on piling up of edge dislocations in front of the crack tip and investigate the resulting local shielding behaviour. All geometric arguments will be presented in a r, θ-polar coordinate system as common in fracture studies, with $r = 0$ at the crack tip and $\theta = 0$ along the WTi-Cu interface (Fig. 8a, shown representatively for the 8^{th} dislocation). Consider a single slip plane in the Cu phase under an angle θ that passes through the crack tip. Neglecting the actual nucleation process at the crack tip and any subsequent cross-slip or climb mechanisms, the force equilibrium along the slip plane of the i-th dislocation in a pile-up of n dislocations is [65, 66]:

$$b\tau_i = F_{image} + F_{crack} + \sum_{m=1, m\neq i}^{n} F_d^m \tag{9}$$

where τ_i is the total shear stress acting on the i-th dislocation (classical Peach-Koehler force $F_i = b\tau_i$ [67]), F_{image} is the image force, F_{crack} is the force resulting from the stress field of the loaded crack and F_d^m is the force resulting from the stress field of the m-th dislocation acting on the i-th dislocation. Finding these force components is rather challenging due to the fact that the present study focuses on a heterogeneous material system. This leads to the fact that the local stress fields are not static, but a function of the elastic mismatches between the constituents and are changing with respect to the point of investigation as the point-specific mode I (k_I) or mode II (k_{II}) components change. This is known as an oscillatory singularity and the detailed derivation is beyond the scope of this work, but the interested reader is referred to a very thorough review by Hutchinson and Suo [68]. For the sake of conciseness, we will be taking the fact that the mode mixity angle ψ is a measure for the ratio between local mode I and mode II loading ($\tan\psi = k_{II}/k_I$) and that it is given by:

$$\psi = \arctan\left(\frac{Im\left(Kl^{i\epsilon}\right)}{Re\left(Kl^{i\epsilon}\right)}\right) \tag{10}$$

where $K = K_1 + iK_2$ is the complex loading stress intensity factor, $\epsilon = \frac{1}{2\pi} ln\left(\frac{1-\beta}{1+\beta}\right)$ is a function of the second Dundurs' parameter β [69] and therefore the individual shear moduli and Poisson's ratios $G_W = 157\,\text{GPa}$,

$\nu_W = 0.28$ [70] and $G_{Cu} = 45\,\mathrm{GPa}$, $\nu_{Cu} = 0.35$ [71], and l is an arbitrary reference length. The elastic parameters are taken for W instead of WTi for a better comparison with the DFT results. For simplification it is further assumed that the applied loading is purely mode I, *i.e.* has only a real component $K_{applied} = K_1$. With these assumptions and the radial shear stress solutions for mode I $\tau_{r\theta,I}$ and mode II $\tau_{r\theta,II}$ [51, 72, 73], F_{crack} equates to:

$$\begin{aligned} F_{crack} &= b(\tau_{r\theta,I} + \tau_{r\theta,II}) \\ &= b\frac{K_{applied}}{\sqrt{2\pi r}}\cos(\theta/2)\ \left[\cos(\epsilon ln(l))\sin(\theta/2)\cos(\theta/2)\right. \\ &\qquad \left. + \sin(\epsilon ln(l))(1 - 3\sin^2(\theta/2))\right] \end{aligned} \quad (11)$$

As the full generalized treatment of the following will lead to a very exhausting and incomprehensible set of interactions, we will at this point specify the characteristic reference length as $l = 820\,\mathrm{nm}$ (the ligament length of the second air exposed specimen), which leads to a maximum of F_{crack} at $\theta \approx 22°$ (Fig. 8a) and further consider only this slip plane. The image forces on a dislocation in the vicinity of a crack are also more complicated when an interface is involved, as an additional term perpendicular to the interface is introduced. Zhang and Li [74] have derived a full framework for the stress field of an edge dislocation in the vicinity of a crack tip at a bimaterial interface based on Muskhelishvili's complex potential treatment [75]. They found that considering an edge dislocation within the Cu phase and a Burger's vector parallel to the slip plane the image force F_{image} is:

$$\begin{aligned} F_{image} = &\left[\left(\frac{\alpha + \beta^2}{(1 - \beta^2)}\frac{G_{Cu}}{4\pi(1 - \nu_C u}\right)\right. \\ &\left. -\frac{G_{Cu}G_W}{2\pi}\left(\frac{1}{G_{Cu} + G_W(3 - 4\nu_{Cu})} + \frac{1}{G_W + G_{Cu}(3 - 4\nu_W)}\right)\right]\frac{b^2}{r} \end{aligned} \quad (12)$$

where α is Dundurs' first parameter [69]. Furthermore, the individual dislocation interaction forces F_d^m can be calculated using the same potential method [74]. The detailed derivation can be found in appendix A, to continue with the argument from this point onwards. With all terms known in Eq. 9 it is now possible to calculate the acting shear stress τ_i of any i-th dislocation in a pile-up in front of the crack tip. This enables the calculation of the actual distribution of dislocations by iteratively moving the individual dislocations along the slip plane until the resolved shear stress drops below the lattice friction, which is taken to be the Peierls-Nabarro stress [76], $\tau_p = 0.28\,\mathrm{MPa}$ for

Cu [77]. One can now argue that at some point the interaction of dislocations with each other or with occurring grain boundaries leads to a pinning of these dislocations, which creates a barrier for further dislocation motion. To obtain a lower bound estimate for the resulting pile-up behaviour, we kept the furthest dislocation sessile at a maximum distance of $820\,\mathrm{nm}/\cos\theta = 880\,\mathrm{nm}$ (as if the pinning point would be as close to the lower free Cu surface as possible), while all other dislocations where allowed to move, starting from an evenly spaced distribution of dislocations.

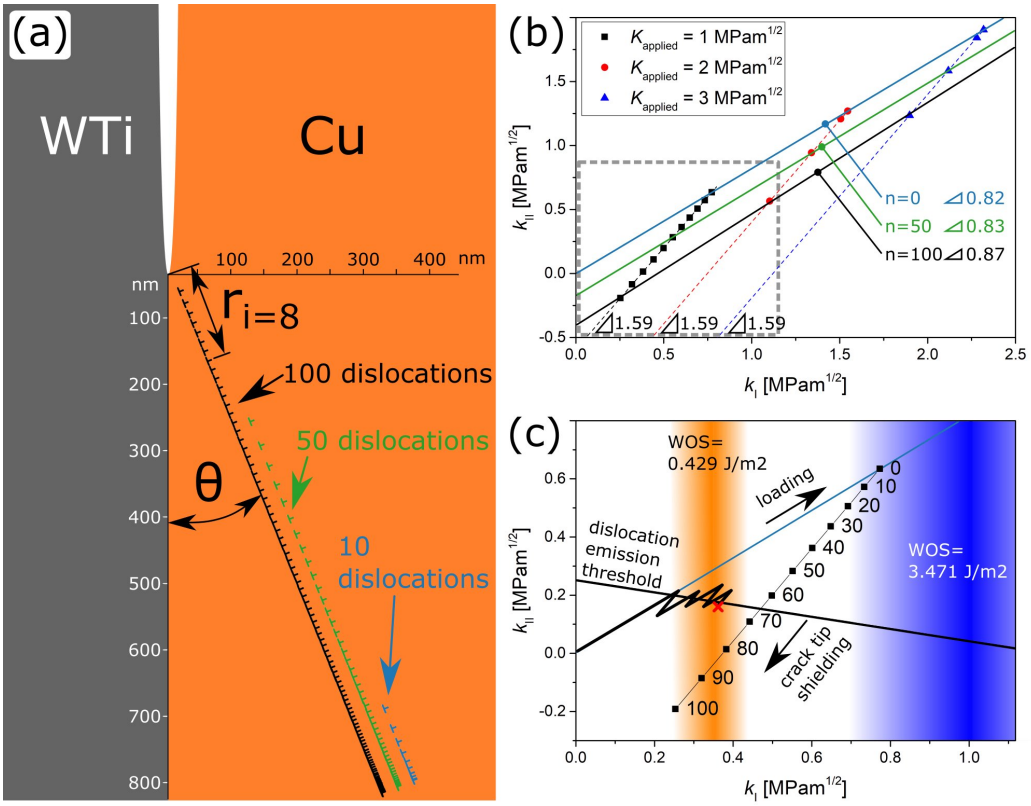

Figure 8: (a) Schematic interface crack tip showing the dislocation distribution for $n = 10$, 50, 100 dislocations on a slip plane at $\theta = 22°$, where the last dislocation is pinned at $r = 880\,\mathrm{nm}$. (b) Local k_I and k_{II} stress intensities for a shielded crack with varying applied stress intensities $K_{applied} = 1$, 2, $3\,\mathrm{MPa}\sqrt{\mathrm{m}}$ and for varying amounts of dislocations ($n = 0$-100) in the pile-up. (c) Detail of grey region in (b) showing the loading slope, dislocation emission threshold and respective crack growth thresholds after Lin and Thomson [78].

The equilibrium positions of the individual dislocations are shown in Fig. 8a for $K_{applied} = 1\,\mathrm{MPa}\sqrt{\mathrm{m}}$ and for $n = 10$, 50 and 100 dislocations

respectively. It is evident from the fact that the shortest pile-up ($n = 10$) is condensed at the furthest possible position that without any pinning the driving force from the loaded crack would move them even further away from the tip. However, with a pinning point a number of $n = 100$ dislocations leads to a nearly completely filled slip-plane up to the crack tip. With the actual equilibrium positions of the dislocations now known, one can estimate the local shielded crack tip stress intensities $k_{I,shield}$, $k_{II,shield}$, as [78]:

$$k_{j,shield} = k_j - \sum_{i=0}^{n} k^i_{j,dislocation} \tag{13}$$

where j = I,II and $k^i_{j,dislocation}$ are defined in appendix B. The shielded stress intensity is depicted in Fig.8b in k_I-k_{II} space for varying applied stress intensities $K_{applied}$ = 1,2,3 MPa$\sqrt{\text{m}}$ and various numbers of dislocations, respectively. From there it is evident that the shielding effect is stronger for mode II than for mode I and independent of $K_{applied}$, as the slopes of all points for a given $K_{applied}$ are equally 1.59. Similarly, the slopes for a given number of dislocations are nearly constant with only a very minor increase from 0.82 ($n = 0$) to 0.87 ($n = 100$). This means that, while constant loading increases k_I faster than k_{II}, constant dislocation emission on the other hand decreases k_{II} faster than it decreases k_I. Lin and Thomson developed a framework for comparison of dislocation emission with cleavage under general loading [78] and from there one finds a threshold for dislocation emission as a line intersection between k_{Ie} and k_{IIe} (neglecting k_{III}), with:

$$\begin{aligned} k_{Ie} =& \frac{G_{Cu} b}{(1-\nu_{Cu})\sqrt{2\pi r_0}} \left(\sin(\theta) \cos\left(\frac{\theta}{2}\right) \right)^{-1} \\ k_{IIe} =& \frac{G_{Cu} b}{(1-\nu_{Cu})\sqrt{2\pi r_0}} \left(2\cos\left(\frac{3\theta}{2}\right) + \sin(\theta)\sin\left(\frac{\theta}{2}\right) \right)^{-1} \end{aligned} \tag{14}$$

There, r_0 is the dislocation core cut-off radius commonly approximated by $r_0 = b$ [79, 80], which leads to $k_{Ie} = 1.204\,\text{MPa}\sqrt{\text{m}}$ and $k_{IIe} = 0.253\,\text{MPa}\sqrt{\text{m}}$ for the given system, respectively. Lin and Thomson furthermore argued that based on the differences in theoretical strengths of materials in tension and shear, the major contribution to cleavage should be due to mode I loading, which leads to the simple approximation:

$$k_{Ic} = \sqrt{\frac{2E\gamma}{1-\nu^2}} \tag{15}$$

for a threshold to crack extension. Given that our crack is in the interface, it is not entirely clear whether to use $E = E_{Cu} = 124\,\mathrm{GPa}$, $\nu = \nu_{Cu} = 0.35$ [71] or to use $E = E_W = 403\,\mathrm{GPa}$, $\nu = \nu_W = 0.28$ [70] for evaluation. Therefore, it is reasonable to consider a range, rather than a single value, which leads to $k_{Ic,W/O/Cu} = 0.242$–$0.436\,\mathrm{MPa}\sqrt{\mathrm{m}}$ for the oxygen containing system and $k_{Ic,W/Cu} = 0.688$–$1.240\,\mathrm{MPa}\sqrt{\mathrm{m}}$ for the pristine system.

Fig. 8c depicts the dislocation emission threshold (black line), the two crack extension threshold regimes (orange-W/O/Cu, blue-W/Cu) and the pure elastic loading without any shielding (pale blue line) in conjunction with the shielded values for $K_{applied} = 1\,\mathrm{MPa}\sqrt{\mathrm{m}}$ (black squares, numbers correspond to n). To elaborate on what happened in the experiment one can now artificially increase $K_{applied}$ in the graph as follows. The specimen is initially loaded along the pale blue line (slope 0.82), until it reaches the dislocation emission threshold, where dislocations nucleate and start shielding the crack tip (slope 1.59) until it drops below the emission threshold again. This process does not have to be regular, but can be stochastic due to dynamic dislocation emission effects [81]. However, with continued loading it will repeat and move the local stress intensity in close proximity to the dislocation emission line up to a point where it drops below the emission threshold, but is above the threshold for crack extension (Fig. 8c, black zig-zag line to red cross). Thus, changing the behaviour from pure dislocation plasticity, through an intermediate regime where both processes can occur, as indicated by the interplay between crack extension and plasticity in the blunting regime of the first air exposed specimen (Fig. 4), to crack extension. To establish a link to the J-integral evaluations, one can calculate the plastically dissipated work during the process by summing up the work of each individual moving dislocation. However, this would lead to a full simulation type approach with regards to time and amount of dislocation nucleation. Nevertheless, we can estimate the magnitude of the plastically dissipated work from the given static data by considering that geometrically adding all of the individual loading segments followed by all the unloading segments leads to a triangle with an endpoint above the crack extension threshold, but below the dislocation emission threshold, similar to the triangle in Fig. 8c drawn by the loading slope and the shielding data for $K_{applied} = 1\,\mathrm{MPa}\sqrt{\mathrm{m}}$. There, the first point below the dislocation emission line is $n = 70$, and the sum of the dissipated work of all 70 dislocations moving from the crack tip to their respective positions normalized by their distance from the crack tip is:

$$J_diss = \sum_{i=0}^{n=70} \frac{b}{r_i} \int_0^{r_i} \tau_i(r) dr \tag{16}$$

where τ_i is the shear stress calculated by Eq. 9, but taking only into account the dislocations which were emitted before the i-th dislocations (from i+1 to n). Calculating this quantity for $n = 70$ equals $J_{diss,n=70} = 6.14\,\mathrm{J/m^2}$ when considering only a single slip plane with a pile-up that begins with the first emitted dislocation, which is an order of magnitude larger than obtained with Jokl *et al.*'s model [54], while still lower than the experimentally observed $J = 74.3\,\mathrm{J/m^2}$. However, such a single pile-up is very unlikely to occur, as many dislocations would move out of the free surface at the bottom of the Cu phase [82] before an event occurs that would lead to dislocation entanglement, *e.g.* jog formation, to initiate a pile-up behaviour. Furthermore, as differently oriented grains are in the Cu phase, the actual crystallographic orientation of individual slip planes could lead to different behaviour, inhibiting the change in mode mixity (position in k_I-k_{II} space) necessary to initiate crack extension. All of these very likely processes would add to the dissipated work, which means that $J_{diss,n=70} = 6.14\,\mathrm{J/m^2}$ is only a lower bound estimate. Comparing the air exposed with the vacuum processed specimen in the light of this argument one could think that even the vacuum processed specimen should show crack extension given enough dislocation accumulation. Therefore, one can use the same geometric consideration as before, *i.e.* shifting the loading line and the crack tip shielding line parallel to intersect with the first point at which crack extension should occur for the W/Cu specimen ($k_I = 0.688\,\mathrm{MPa}\sqrt{\mathrm{m}}$; $k_{II} = 0.108\,\mathrm{MPa}\sqrt{\mathrm{m}}$). The intersection points of these shifted lines with the original ones allow to read out the necessary applied stress intensity $K_{applied} = 1.66\,\mathrm{MPa}\sqrt{\mathrm{m}}$ and amount of dislocations $n \approx 118$ for fracture to occur in the W/Cu specimen. However, when taking a detailed look at the equilibrium dislocation spacing after iterative relaxation for these values, one finds that the distance between the last two dislocations drops below the magnitude of the Burger's vector b, which is physically impossible and suggests that the model breaks down at that point. As a matter of fact, this behaviour starts already with $K_{applied} = 1\,\mathrm{MPa}\sqrt{\mathrm{m}}$ and $n = 80$, which gives reason to assume that the W/O/Cu system is at the very brink of physically possible crack extension, resultant of accumulation of dislocation plasticity. Nevertheless, this simplified model mimics the observed behaviour very closely and suggests that the accumulation of plasticity in these specimens leads to a change in mode mixity towards a relatively higher mode I component, which facilitates crack extension over dislocation nucleation.

Part 5
Summary and Conclusion

Micromechanical cantilever fracture experiments have been conducted on a Cu-WTi-SiO_x-Si multilayer stack with the focus on analysing the interface between the plastically deforming Cu phase and the quasi-elastic WTi layer. To address the influence of interface chemistry, one set of specimens was deliberately exposed to air between the deposition steps of the two constituents, which led to the formation of an undefined interface oxide layer. While the standard vacuum processed specimens showed only plastic deformation in the Cu phase without any crack extension along the interface, the air exposed specimens exhibited evident crack extension after an extended plastic regime. Continuous $J - \Delta a$ curves depict a very distinct transition from a concave upwards crack tip blunting to a linear crack extension behaviour, with an onset J-integral value of $J = 74.3 \pm 0.6\,\mathrm{J/m^2}$ and $J = 103.1 \pm 1.8\,\mathrm{J/m^2}$ for the two air exposed specimens, respectively. Complementary DFT simulations of a W/Cu interface revealed that upon introduction of a single layer of oxygen the work of separation of the interface drops by a factor of eight from $\mathrm{WOS_{W/Cu}} = 3.471\,\mathrm{J/m^2}$ to $\mathrm{WOS_{W/O/Cu}} = 0.429\,\mathrm{J/m^2}$. Independent of whether the nucleation of dislocations opposed to crack extension or the change in local mode mixity as a result of dislocation pile-ups is considered, the higher work of separation in the pristine interface suggests that static crack extension is impossible in this system. However, the reduced work of separation through oxygen exposition leads to physically plausible results in both model assumptions. Given that the crack extension in the air exposed specimens is preceded by a non-negligible amount of plastic deformation, the argument based on accumulation of dislocation plasticity, leading to a change in local mode mixity towards a relatively higher mode I component (opening mode) seems to be the more probable case for the change from dislocation mediated plasticity to crack extension along the interface. To conclude, the presented experimental approach on elastic-plastic fracture mechanics on spatially limited structures, *i.e.* thin films, was able to resolve changes in interface toughness in a heterogeneous system due to chemical differences. While one constituent showed a major amount of plastic deformation, the technique was still able to detect crack extension even before it was evident in the *in situ* SEM images. In conjunction with the DFT results and analytical arguments, this provides a quite complete picture of the occurring plasticity-fracture process interactions in the given system, which can act as a starting point for further investigations on similar elastic-plastic material

combinations, *e.g.* thermal barrier-, wear- or bio-functional coatings.

Acknowledgments

The authors gratefully acknowledge the financial support under the scope of the COMET program within the K2 Center "Integrated Computational Material, Process and Product Engineering, IC-MPPE" (Projects A2.12). This program is supported by the Austrian Federal Ministries for Transport, Innovation and Technology (BMVIT) and for Digital and Economic Affairs (BMDW), represented by the Österreichische Forschungsförderungsgesellschaft (Funder ID: 10.13039/501100004955), and the federal states of Styria, Upper Austria, and Tyrol. This project has received funding from the European Research Council (ERC) under the European Union's Horizon 2020 research and innovation programme (Grant No. 771146 TOUGHIT).

Appendix A

The force acting on the i-th dislocation by the m-th dislocation on a glide plane F_d^m is a result of the magnitude of the stress field of the m-th dislocation at the position of the i-th dislocation, as $F_d^m = \sigma_{r\theta}(z_i, z_m)/b$. There, $\sigma_{r\theta}(z_i, z_m)$ is the resulting shear stress along the glide plane in polar coordinates as a function of the positions of the individual dislocations z_i,z_m. In a two dimensional model these positions can be addressed by complex numbers ($z = x+iy$), which enables the use of Muskhelishvili's complex potential approach [75], leading to:

$$\begin{aligned} \sigma_{rr} + \sigma_{\theta\theta} &= 2\left[\phi'(z_i, z_m) + \overline{\phi'(z_i, z_m)}\right] \\ \sigma_{\theta\theta} + i\sigma_{r\theta} &= \phi'(z_i, z_m) + \phi'(\bar{z_i}, z_m) + \left[\overline{z_i}\phi''(z_i, z_m) + \psi'(z_i, z_m)\right] e^{i2\theta} \end{aligned} \tag{A1}$$

where ϕ and ψ are two complex potentials, the prime denotes differentiation by z_i and the bar denotes complex conjugation. The potentials for dislocations in the vicinity of an interface have been developed by Zhang and Li [74] and the respective derivations for the given system and both dislocations inside the Cu phase are:

$$\phi'_{Cu} = \frac{1}{1-\beta^2}\left[(1-\beta^2)\frac{\gamma_{Cu}}{z_i - z_m} + (\alpha-\beta)(1-\beta)\left[\frac{\gamma_{Cu}}{z_i - \overline{z_m}} - \overline{\gamma_{Cu}}\frac{z_m - \overline{z_m}}{(z_i - z_m)^2}\right]\right] \tag{A2}$$

$$\phi''_{Cu} = \frac{1}{1-\beta^2}\left[(1-\beta^2)\frac{-\gamma_{Cu}}{(z_i - z_m)^2} + (\alpha-\beta)(1-\beta)\left[\frac{-\gamma_{Cu}}{(z_i - \overline{z_m})^2} + 2\overline{\gamma_{Cu}}\frac{z_m - \overline{z_m}}{(z_i - z_m)^3}\right]\right] \tag{A3}$$

$$\begin{aligned}\psi'_{Cu} = \frac{1}{1-\beta^2}\Bigg[&(1-\beta^2)\left(\frac{\overline{\gamma_{Cu}}}{z_i - z_m} + \frac{\gamma_{Cu}\overline{z_m}}{(z_i - z_m)^2}\right) \\ &+(\alpha+\beta^2)\left(\frac{\overline{\gamma_{Cu}}}{z_i - \overline{z_m}} + \frac{\gamma_{Cu} z_m}{(z_i - \overline{z_m})^2}\right) \\ &+(1+\alpha)\beta\left(\frac{\overline{\gamma_{Cu}}}{z_i - \overline{z_m}} - \frac{\gamma_{Cu} z_m}{(z_i - \overline{z_m})^2}\right) \\ &(\alpha-\beta)(1-\beta)\Bigg((\overline{\gamma_{Cu}} - \gamma_{Cu})\frac{\overline{z_m} - z_m}{(z_i - \overline{z_m})^2} \\ &+2\overline{\gamma_{Cu} z_m}\frac{\overline{z_m} - z_m}{(z_i - z_m)^3}\Bigg)\Bigg]\end{aligned} \tag{A4}$$

whereby α,β are again Dundurs' first and second parameter [69] and:

$$\gamma_{Cu} = \frac{G_{Cu} b_{Cu} e^{i\theta}}{2i\pi(1 - 2\nu_{Cu})} \tag{A5}$$

Appendix B

Lin and Thomson [78] derived their framework for dislocation shielding in a 2D model with dislocations being able to lie on any slip plane, *i.e.* varying contributions of the Burger's vector on the real and imaginary axis. As in the present model the emitted dislocations lie on a crack tip intersecting slip plane in the Cu phase, we can simplify the shielding terms for the i-the dislocations for both modes $k^i_{I,dislocation}$, $k^i_{II,dislocation}$ as:

$$k^i_{I,dislocation} = \frac{G_{Cu}b_{Cu}}{2(1-\nu_{Cu})\sqrt{2\pi r_i}}\left[\sin(\theta)\cos(\theta)\cos\left(\frac{3\theta}{2}\right) + 2\sin(\theta)\cos\left(\frac{\theta}{2}\right) + \sin^2(\theta)\sin\left(\frac{3\theta}{2}\right)\right] \tag{B1}$$

$$k^i_{II,dislocation} = \frac{G_{Cu}b_{Cu}}{2(1-\nu_{Cu})\sqrt{2\pi r_i}}\left[2\cos(\theta)\cos\left(\frac{\theta}{2}\right) - \sin(\theta)\cos(\theta)\sin\left(\frac{3\theta}{2}\right) + \sin^2(\theta)\cos\left(\frac{3\theta}{2}\right)\right] \tag{B2}$$

References

1. Mirigliano, M. & Milani, P. Electrical conduction in nanogranular cluster-assembled metallic films. *Advances in Physics: X* **6,** 1908847 (2021).
2. Tanner, C. M., Perng, Y.-C., Frewin, C., Saddow, S. E. & Chang, J. P. Electrical performance of Al2O3 gate dielectric films deposited by atomic layer deposition on 4H-SiC. *Applied Physics Letters* **91,** 203510 (2007).
3. Thakare, J. G., Pandey, C., Mahapatra, M. M. & Mulik, R. S. Thermal Barrier Coatings - A State of the Art Review. *Metals and Materials International* (2020).
4. Hoque, M. J. *et al.* Modular Heat Sinks for Enhanced Thermal Management of Electronics. *Journal of Electronic Packaging* **143** (2021).
5. Nelhiebel, M. *et al.* Effective and reliable heat management for power devices exposed to cyclic short overload pulses. *Microelectronics Reliability* **53,** 1745–1749 (2013).
6. Subramanian, C. & Strafford, K. Review of multicomponent and multilayer coatings for tribological applications. *Wear* **165,** 85–95 (1993).
7. Ilican, S., Caglar, Y., Caglar, M. & Yakuphanoglu, F. Structural, optical and electrical properties of F-doped ZnO nanorod semiconductor thin films deposited by sol–gel process. *Applied Surface Science* **255,** 2353–2359 (2008).
8. Xi, J.-Q. *et al.* Optical thin-film materials with low refractive index for broadband elimination of Fresnel reflection. *Nature Photonics* **1,** 176–179 (2007).
9. Pethica, J. B., Hutchings, R. & Oliver, W. C. Hardness measurement at penetration depths as small as 20 nm. *Philosophical Magazine A* **48,** 593–606 (1983).
10. Oliver, W. & Pharr, G. An improved technique for determining hardness and elastic modulus using load and displacement sensing indentation experiments. *Journal of Materials Research* **7,** 1564–1583 (1992).
11. Uchic, M. D., Dimiduk, D. M., Florado, J. N. & Nix, W. D. Sample dimensions influence strength and crystal plasticity. *Science* **305,** 986–989 (2004).
12. Frick, C., Clark, B., Orso, S., Schneider, A. & Arzt, E. Size effect on strength and strain hardening of small-scale 111 nickel compression pillars. *Materials Science and Engineering: A* **489,** 319–329 (2008).

13. Kiener, D., Grosinger, W., Dehm, G. & Pippan, R. A further step towards an understanding of size-dependent crystal plasticity: In situ tension experiments of miniaturized single-crystal copper samples. *Acta Materialia* **56,** 580–592 (2008).

14. Murphy, K. F., Chen, L. Y. & Gianola, D. S. Effect of organometallic clamp properties on the apparent diversity of tensile response of nanowires. *Nanotechnology* **24.** Cited By (since 1996):2 (2013).

15. Alfreider, M., Meindlhumer, M., Maier-Kiener, V., Hohenwarter, A. & Kiener, D. Extracting information from noisy data: strain mapping during dynamic in situ SEM experiments. *Journal of Materials Research* **36,** 2291–2304 (2021).

16. Riedl, A. *et al.* A novel approach for determining fracture toughness of hard coatings on the micrometer scale. *Scripta Materialia* **67,** 708–711 (2012).

17. Ast, J., Przybilla, T., Maier, V., Durst, K. & Göken, M. Microcantilever bending experiments in NiAl-Evaluation, size effects, and crack tip plasticity. *Journal of Materials Research* **29,** 2129–2140 (2014).

18. Sernicola, G. *et al.* In situ stable crack growth at the micron scale. *Nature Communications* **8** (2017).

19. Sebastiani, M., Johanns, K., Herbert, E. & Pharr, G. Measurement of fracture toughness by nanoindentation methods: Recent advances and future challenges. *Current Opinion in Solid State and Materials Science* **19,** 324–333 (2015).

20. Meindlhumer, M. *et al.* Biomimetic hard and tough nanoceramic Ti–Al–N film with self-assembled six-level hierarchy. *Nanoscale* **11,** 7986–7995 (2019).

21. Armstrong, D. E., Wilkinson, A. J. & Roberts, S. G. Measuring anisotropy in Young's modulus of copper using microcantilever testing. *Journal of Materials Research* **24,** 3268–3276 (2009).

22. Kupka, D. & Lilleodden, E. T. Mechanical Testing of Solid-Solid Interfaces at the Microscale. *Experimental Mechanics* **52,** 649–658 (2011).

23. Matoy, K., Detzel, T., Müller, M., Motz, C. & Dehm, G. Interface fracture properties of thin films studied by using the micro-cantilever deflection technique. *Surface and Coatings Technology* **204,** 878–881 (2009).

24. Schaufler, J., Schmid, C., Durst, K. & Göken, M. Determination of the interfacial strength and fracture toughness of a-C:H coatings by in-situ microcantilever bending. *Thin Solid Films* **522,** 480–484 (2012).

25. Konetschnik, R., Daniel, R., Brunner, R. & Kiener, D. Selective interface toughness measurements of layered thin films. *AIP Advances* **7,** 035307 (2017).

26. Žagar, G., Pejchal, V., Mueller, M. G., Michelet, L. & Mortensen, A. Fracture toughness measurement in fused quartz using triangular chevron-notched micro-cantilevers. *Scripta Materialia* **112,** 132–135 (2016).

27. Glechner, T. *et al.* Correlation between fracture characteristics and valence electron concentration of sputtered Hf-C-N based thin films. *Surface and Coatings Technology* **399,** 126212 (2020).

28. Wurster, S., Motz, C. & Pippan, R. Characterization of the fracture toughness of micro-sized tungsten single crystal notched specimen. *Philosophical Magazine* **92,** 1–23 (2012).

29. Ast, J. *Untersuchung der lokalen Bruchzähigkeit und des elastisch-plastischen Bruchverhaltens von NiAl und Wolfram mittels Mikrobiegebalkenversuchen* PhD thesis (FAU Erlangen, 2016).

30. Alfreider, M., Kozic, D., Kolednik, O. & Kiener, D. In-situ elastic-plastic fracture mechanics on the microscale by means of continuous dynamical testing. *Materials & Design* **148,** 177–187 (2018).

31. Wimmer, A. *et al.* Temperature dependent transition of intragranular plastic to intergranular brittle failure in electrodeposited Cu microtensile samples. *Materials Science and Engineering: A* **618,** 398–405 (2014).

32. Bigl, S., Wurster, S., Cordill, M. J. & Kiener, D. Advanced characterisation of thermo-mechanical fatigue mechanisms of different copper film systems for wafer metallizations. *Thin Solid Films* **612,** 153–164 (2016).

33. Alfreider, M., Zechner, J. & Kiener, D. Addressing Fracture Properties of Individual Constituents Within a Cu-WTi-SiOx-Si Multilayer. *JOM* (2020).

34. *ASTM Standard E1820-13, Standard Test Method for Measurement of Fracture Toughness* 1820 (ASTM International, West Conshohocken, USA, 2013).

35. *ISO 12135:2002 - Metallic materials — Unified method of test for the determination of quasistatic fracture toughness* (International Organization for Standardization, 2002).

36. Rice, J. R., Paris, P. C. & Merkle, J. G. in *Progress in Flaw Growth and Fracture Toughness Testing* (eds Kaufman, J. *et al.*) 231–245 (ASTM International, West Conshohocken, PA, 1973).

37. Zhu, Y. T., Liao, X. Z. & Wu, X. L. Deformation twinning in nanocrystalline materials. *Progress in Materials Science* **57,** 1–62 (2012).

38. Alfreider, M., Kolitsch, S., Wurster, S. & Kiener, D. An analytical solution for the correct determination of crack lengths via cantilever stiffness. *Materials & Design* **194,** 108914 (2020).

39. Kalha, C. *et al.* Thermal and oxidation stability of TixW1-x diffusion barriers investigated by soft and hard x-ray photoelectron spectroscopy. *Journal of Applied Physics* **129,** 195302 (2021).

40. Nishiyama, Z. X-ray investigation of the mechanism of the transformation from face centered cubic lattice to body centered cubic. *Sci. Rep. Tohoku Univ.* **23,** 637 (1934).

41. Wassermann, G. *Ueber den Mechanismus der [alpha]-[gamma]-Umwandlung des Eisens* (Verlag Stahleisen, 1935).

42. Kresse, G. & Hafner, J. Ab initiomolecular dynamics for liquid metals. *Physical Review B* **47,** 558–561 (1993).

43. Kresse, G. & Hafner, J. Ab initiomolecular-dynamics simulation of the liquid-metal–amorphous-semiconductor transition in germanium. *Physical Review B* **49,** 14251–14269 (1994).

44. Kresse, G. & Furthmüller, J. Efficiency of ab-initio total energy calculations for metals and semiconductors using a plane-wave basis set. *Computational Materials Science* **6,** 15–50 (1996).

45. Perdew, J. P., Burke, K. & Ernzerhof, M. Generalized Gradient Approximation Made Simple. *Physical Review Letters* **77,** 3865–3868 (1996).

46. Perdew, J. P., Burke, K. & Ernzerhof, M. Generalized Gradient Approximation Made Simple [Phys. Rev. Lett. 77, 3865 (1996)]. *Physical Review Letters* **78,** 1396–1396 (1997).

47. Blöchl, P. E. Projector augmented-wave method. *Physical Review B* **50,** 17953–17979 (1994).

48. Kresse, G. & Joubert, D. From ultrasoft pseudopotentials to the projector augmented-wave method. *Physical Review B* **59,** 1758–1775 (1999).

49. Tahir, A. M., Janisch, R. & Hartmaier, A. Ab initiocalculation of traction separation laws for a grain boundary in molybdenum with segregated C impurites. *Modelling and Simulation in Materials Science and Engineering* **21,** 075005 (2013).

50. Tvergaard, V. & Hutchinson, J. W. The relation between crack growth resistance and fracture process parameters in elastic-plastic solids. *Journal of the Mechanics and Physics of Solids* **40,** 1377–1397 (1992).

51. Anderson, T. L. *Fracture Mechanics: Fundamentals and Applications, Second Edition* (CRC Press, 2005).

52. Rose, J. H., Smith, J. R. & Ferrante, J. Universal features of bonding in metals. *Physical Review B* **28,** 1835–1845 (1983).

53. Ashcroft, N. W. & Mermin, N. D. *Solid State Physics* (ed Crane, D. G.) (Harcourt College Publishers, 1976).

54. Jokl, M., Vitek, V. & McMahon, C. A microscopic theory of brittle fracture in deformable solids: A relation between ideal work to fracture and plastic work. *Acta Metallurgica* **28,** 1479–1488 (1980).

55. Orowan, E. Notch brittleness and the strength of metals. *Transactions of the Institution of Engineers and Shipbuilders Scotland* **89,** 165–215 (1945).

56. Griffith, A. A. The Phenomena of Rupture and Flow in Solids. *Philosophical Transactions of the Royal Society A: Mathematical, Physical and Engineering Sciences* **221,** 163–198 (1921).

57. Mulford, R. A., Mcmahon, C. J., Pope, D. P. & Feng, H. C. Temper embrittlement of Ni-Cr Steels by phosphorus. *Metallurgical Transactions A* **7,** 1183–1195 (1976).

58. Meiners, T., Peng, Z., Gault, B., Liebscher, C. H. & Dehm, G. Sulfur – induced embrittlement in high-purity, polycrystalline copper. *Acta Materialia* **156,** 64–75 (2018).

59. Mordehai, D., Ashkenazy, Y., Kelson, I. & Makov, G. Dynamic properties of screw dislocations in Cu: A molecular dynamics study. *Physical Review B* **67** (2003).

60. Oren, E., Yahel, E. & Makov, G. Dislocation kinematics: a molecular dynamics study in Cu. *Modelling and Simulation in Materials Science and Engineering* **25,** 025002 (2016).

61. Marukawa, K. Dislocation Motion in Copper Single Crystals. *Journal of the Physical Society of Japan* **22,** 499–510 (1967).

62. Hindmarsh, A. C. & Petzold, L. R. Algorithms and software for ordinary differential equations and differential- algebraic equations, Part II: Higher-order methods and software packages. *Computers in Physics* **9,** 148 (1995).

63. Zielinski, W., Lii, M. & Gerberich, W. Crack-tip dislocation emission arrangements for equilibrium —I. In situ TEM observations of Fe2wt%Si. *Acta Metallurgica et Materialia* **40,** 2861–2871 (1992).

64. Ohr, S. An electron microscope study of crack tip deformation and its impact on the dislocation theory of fracture. *Materials Science and Engineering* **72,** 1–35 (1985).

65. Pande, C., Masumura, R. & Chou, Y. Shielding of crack tips by inclined pileups of dislocations. *Acta Metallurgica* **36,** 49–54 (1988).

66. Goswami, R. & Pande, C. S. in *Handbook of Mechanics of Materials* 1–21 (Springer Singapore, 2018).

67. Peach, M. & Koehler, J. S. The Forces Exerted on Dislocations and the Stress Fields Produced by Them. *Physical Review* **80,** 436–439 (1950).

68. Hutchinson, J. & Suo, Z. in *Advances in Applied Mechanics* 63–191 (Elsevier, 1991).

69. Dundurs, J. in *Mathematical Theory of Dislocations* (ed Mura, T.) 70–115 (ASME, 1969).

70. Lowrie, R. & Gonas, A. M. Dynamic Elastic Properties of Polycrystalline Tungsten, 24°-1800°C. *Journal of Applied Physics* **36,** 2189–2192 (1965).

71. Ledbetter, H. M. & Naimon, E. R. Elastic Properties of Metals and Alloys. II. Copper. *Journal of Physical and Chemical Reference Data* **3,** 897–935 (1974).

72. Weertman, J. *Dislocation Based Fracture Mechanics* 524 pp. (WORLD SCIENTIFIC PUB CO INC, 1996).

73. Wang, Y., Wang, W., Zhang, B. & Li, C.-Q. A review on mixed mode fracture of metals. *Engineering Fracture Mechanics* **235,** 107126 (2020).

74. Zhang, T.-Y. & Li, J. C. M. Interaction of an edge dislocation with an interfacial crack. *Journal of Applied Physics* **72,** 2215–2226 (1992).

75. Muskhelishvili, N. I. in *Some Basic Problems of the Mathematical Theory of Elasticity* 89–104 (Springer Netherlands, 1977).

76. Nabarro, F. Fifty-year study of the Peierls-Nabarro stress. *Materials Science and Engineering: A* **234-236,** 67–76 (1997).

77. Kamimura, Y., Edagawa, K. & Takeuchi, S. Experimental evaluation of the Peierls stresses in a variety of crystals and their relation to the crystal structure. *Acta Materialia* **61,** 294–309 (2013).

78. Lin, I.-H. & Thomson, R. Cleavage, dislocation emission, and shielding for cracks under general loading. *Acta Metallurgica* **34,** 187–206 (1986).

79. Argon, A. S. *Strenghtening mechanisms in crystal plasticity* (Oxford University Press, 2011).

80. Messerschmidt, U. *Dislocation Dynamics During Plastic Deformation* (Springer, 2010).

81. Maaß, R. & Derlet, P. Micro-plasticity and recent insights from intermittent and small-scale plasticity. *Acta Materialia* **143,** 338–363 (2018).

82. Motz, C., Schöberl, T. & Pippan, R. Mechanical properties of micro-sized copper bending beams machined by the focused ion beam technique. *Acta Materialia* **53,** 4269–4279 (2005).

Publication E

Interface related deformation and fracture of an elastic-plastic bimaterial system resolved by in-situ transmission scanning electron microscopy

Acta Materialia
under review

Interface mediated deformation and fracture of an elastic-plastic bimaterial system resolved by *in situ* transmission scanning electron microscopy

Markus Alfreider[1,2], Glenn Balbus[3], Fulin Wang[2], Johannes Zechner[3], Daniel S. Gianola[2], and Daniel Kiener[1]

[1]Department Materials Science, Chair of Materials Physics Montanuniversität Leoben, 8700 Leoben, Austria
[2]Materials Department, University of California, Santa Barbara, CA 93106, USA
[3]KAI Kompetenzzentrum Automobil- und Industrieelektronik GmbH, Villach, Austria

Abstract

A wide variety of today's engineering material systems consist of multiple layered constituents to satisfy varying demands, *e.g.* thermal barrier- or hard coatings, thermal- or electrical conduction or insulation layers, or diffusion barriers. However, these layers are commonly only of the order of a few hundred nanometers to microns thick, which renders conventional mechanical investigation of interfacial failure quite challenging, especially if plastically deforming constituents are involved. Herein, we present an *in situ* study of the mechanical deformation of a WTi-Cu model interface, commonly encountered in the microelectronics industry, utilizing transmission scanning electron microscopy. This approach elucidated the interplay between plastic deformation and fracture processes, while loading either perpendicular to the interface (mode I) or parallel to the interface (mode II). While a purely ductile failure in the Cu phase, exhibiting classical void nucleation and coalescence, was observed under tensile loading (mode I), the shear loading (mode II) exhibited nucleation and propagation

of an interface crack. The results are discussed with respect to the frameworks of classical fracture mechanics and dislocation plasticity, providing fundamental insight into the failure behaviour of elastic-plastic interfaces with respect to loading orientation.

Part 1
Introduction

The heterogeneous structure of multilayer materials systems allows for a wide variety of tailorable properties, allowing their utilization in a wide field of different engineering systems, *e.g.* thermal barrier coatings [1], microelectronic devices [2], hard coatings [3] to name a few. However, most of these applications exhibit constituents with micrometer to sub micrometer thicknesses, making the investigation of mechanical response considerably challenging. With the rise of *in situ* micro- and nanomechanical testing techniques, *e.g.* nanoindentation [4, 5], microcompression/tension [6, 7] or microcantilever bending [8, 9], many groups were successful in investigating previously unachievable mechanical parameters of these individual phases. Nevertheless, quantifying interfacial fracture in heterogeneous systems remains a challenge, particular in elastic-plastic systems, where the interplay between plasticity and fracture processes is difficult to distinguish. While fracture mechanical testing techniques in microscopic systems have been established for linear elastic fracture mechanics (LEFM) in homogeneous materials, *e.g.* pillar splitting [10], cantilever bending [11], double cantilever wedging [12], push to pull translation [13] or symmetric double notch testing [14], similar techniques addressing elastic-plastic fracture mechanics (EPFM) have received much less attention [15–17], despite their importance in real engineering systems. Investigations of linear elastic [18, 19] or elastic-plastic [20, 21] interface failure are even rarer. This is governed by the complex and inseparable relationship between the length scales of multilayer geometries and the prevailing elastic- and plastic deformation fields, which leads to failure modes not otherwise predicted in their homogeneous counterparts. Even in the linear elastic case, the mismatch of elastic properties can lead to, *e.g.* crack deflection [22], acceleration or retardation [23]. Hence, considering the additional contribution of varying plastic deformation [24, 25] and the influence of loading modes [26, 27] results in an even much more intricate problem. However, understanding the local interfacial fracture properties of such systems becomes highly relevant in perspective to macroscopic failure. For example in nacre-like structures the macroscopic fracture toughness is governed by crack

deflection along interfaces [28, 29]. In blood vessel related medical applications, drug-eluting stents (polymer-coated steels) [30, 31] exhibit an extreme amount of plastic deformation through *in vivo* balloon expansion, which can lead to interfacial failure. Aircraft turbines are shielded against high cyclic thermal loadings during their lifetime by thermal barrier coatings, which often start to fail through local debonding at the interface, leading to buckling or full spallation of the coating [32, 33]. Finally, microelectronic components can exhibit rather large interfacial stresses through thermal mismatch, either during the deposition process [34, 35] or through their lifecycle [36, 37], which can lead to failure and consequently a full breakdown of functional properties. While seemingly from vastly different fields of applications, all of these cases have in common that their respective failure characteristics originate from a bimaterial interface combination, with at least one plastically deforming component. The present work aims to establish a better understanding of this generalized kind of problem, focussing on the deformation and fracture along a Cu-WTi interface in a multilayer stack as a model material for microelectronics applications. We utilize in situ testing inside a scanning electron microscope (SEM) of electron-transparent specimens using transmission scanning electron microscopy (TSEM). The specimens are loaded either in a tensile orientation perpendicular to the interface with predefined notches to obtain a dominant mode I contribution (opening mode), or in a shear orientation parallel to the interface to obtain a dominant mode II contribution (shearing mode). The automated and continuous collection of images during the experiments allows for a correlation of the sequence of fracture events and accompanying dislocation processes, ultimately providing fundamental insight into the different loading mode-dependent failure mechanisms of elastic-plastic bimaterial interfaces.

Part 2
Experimental procedure

2.1 Materials

The multilayer system studied herein consists of an galvanically deposited 5 µm thick Cu layer on top of a 270–300 nm thick single-phase body centred cubic WTi layer (nominally 22 % Ti [38]) with a columnar grain size of approximately 100 nm. These layers are deposited on a single crystalline (001) Si substrate with a 70 nm thermally grown amorphous SiO_x interlayer, as

shown in Fig. 1a. The interface between the ductile Cu and the stiff WTi layer exhibits corrugations, while the interfaces between WTi and SiO_x as well as those between SiO_x and Si are almost perfectly flat, as depicted by the red traces in Fig. 1a. For further details on the fabrication of the present material system, the reader is referred to previous works [21, 39, 40].

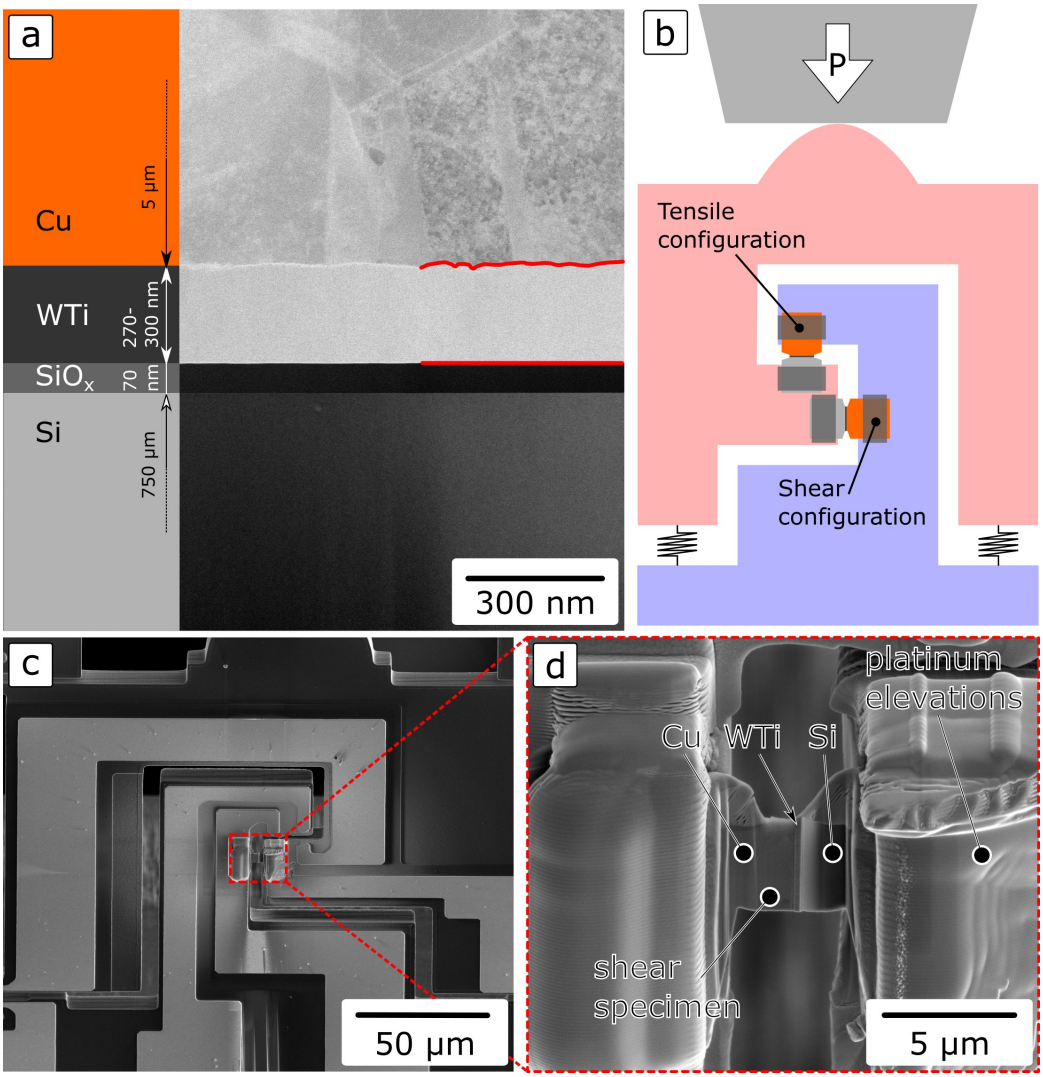

Figure 1: (a) STEM micrograph of the multi-layered material system showing the individual layers. (b) Schematic of the push to pull device configuration for both, shear and tensile loading. (c,d) SEM images of the shear specimen mounted on the push-to pull device.

2.2 Specimen fabrication

The TSEM deformation experiments were conducted using the experimental approach as described in detail by Stinville *et al.* [41], whereby two $10 \times 12\,\mu m^2$ foils with a thickness of 1 µm were processed by focused ion beam milling (FIB, Helios, Thermo Fisher Scientific, Waltham, USA) and lifted onto a pre-processed electronic push-to-pull device (ePTP, Bruker, Billerica, USA) using a micromanipulator needle (OmniProbe, Oxford Instruments, Abington, UK). The specimens were mounted on the device to promote either tensile or shear loading of the interface between Cu and WTi, as shown schematically in Fig. 1b. After manipulating the specimens onto platinum deposited elevations and fixing them with a thick Pt layer to reduce contact compliance [42], subsequent shaping and thinning steps were conducted on the chip with decreasing acceleration voltage and currents down to a minimum of 16 pA at 5 keV. The final shape of the shear specimen before mechanical testing is shown in Figs. 1c and d.

2.3 *In situ* testing setup

The experiments were conducted *in situ* in a scanning electron microscope (SEM) (Apreo S, Thermo Fisher Scientific, Waltham, USA) operated at 30 kV and equipped with an annular scanning electron transmission microscopy (STEM) detector, which allows the gathering of bright field (BF), annular dark field (ADF) and high angle annular dark field (HAADF) signals through adjustable circular regions of the detector [43]. The ePTP device with the specimen was mounted onto a specifically designed printed circuit board (PCB) adapter piece to fit into a FT-NMT03 nanomechanical testing device (FemtoTools AG, Buchs, Switzerland). This testing device is equipped with a micro electro-mechanical system (MEMS) based load cell with a maximum load of 20 mN and a resolution of ≈ 0.1 µN [41]. The experiments were conducted in a closed-loop displacement-controlled manner with a displacement rate of 3 nm/s and a mechanical data acquisition frequency of 100 Hz up to a pre-set maximum load, which was subsequently increased until failure. Lower resolution (LR, 1536×1024 px, 3.26 nm/px) images of all types (BF, ADF, HAADF) were taken continuously with an image acquisition time of 4 s, while higher resolution images (HR, 3072×2048 px, 1.14 nm/px) with image acquisition times of 22 s were taken at consecutive holding segments every 20 s or when load drops larger than 10 µN occurred. The load-displacement data was corrected by the ePTP stiffness k_{ePTP}, as:

$$F_{specimen} = F - k_{ePTP} \cdot u \tag{1}$$

where F and u are the total measured load and displacement and $F_{specimen}$ is the load on the specimen. The ePTP stiffness was measured as the linear slope of the load-displacement data after the specimens were broken.

Part 3
Results

3.1 Tensile loading

To promote failure at the interface of interest (between the Cu and WTi), the specimen was notched prior to thinning by a perpendicular FIB cut as evident in Figs. 2b-f (right-hand side notch). Through the thinning procedure another notch on the left-hand side was introduced, resulting in a double edge notch tension (DENT) geometry with the highest stress concentration at the interface. The collected load-displacement data is depicted in Fig. 2a, where the first three loading steps show only a small extent of plasticity. In loading step 4, the first slip traces are evident in the HR images (from Figs. 2b to c) under an angle of about 60° to the notch plane. These slip traces are not confined to a single plane, but fill the Cu grain below the notch, which suggests that either initial dislocations nucleated at the notch tip and cross-slipped within the grain, or the nucleation took place simultaneously at various positions within the FIB induced free surface notch. Subsequent loading (5^{th} loading) leads to obvious crack tip blunting on the left-hand side notch (Figs. 2d to f), as well as nucleation of a crack tip from the right-hand side notch, as shown from Figs. 2d to e. Furthermore, the highly stressed state in front of the right-hand side crack tip is evident by the brighter region in front of it while the contrast and brightness imaging parameters were kept constant, which is a result of local thinning of the specimen through plasticity. Additional loading (Figs. 2e to f) resulted in a significant load drop in conjunction with sudden and massive plastic deformation events in front of both notches, as depicted by the bright regions in Fig. 2f (see supplementary movie). These regions grow together on the Cu side of the specimen, without any crack extension along the WTi-Cu interface, which suggests a lower barrier for plastic deformation in the Cu phase than for interfacial crack extension.

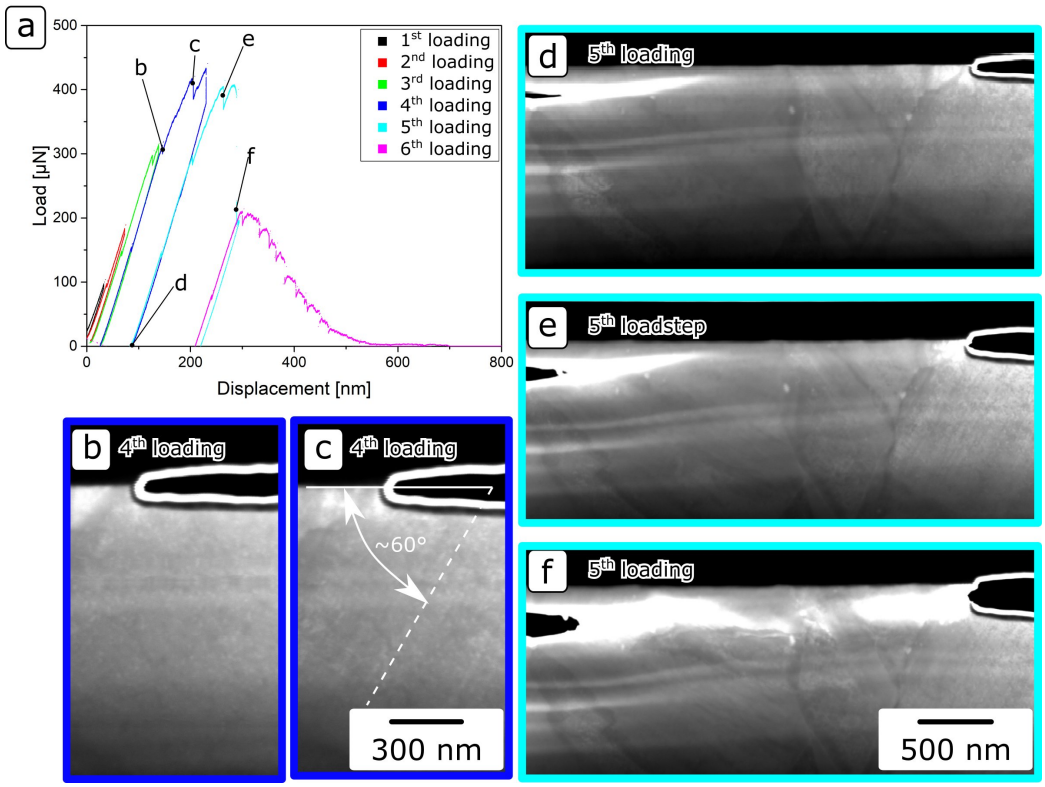

Figure 2: (a) Tensile specimen load-displacement data of six consecutive loading segments up to final failure. (b) ADF images of the 4$^{\text{th}}$ loading step (b) before and (c) after slip traces occur at the predefined notch. ADF images of the 5$^{\text{th}}$ loading step (d) in unloaded condition, (e) at the onset of crack tip blunting in the left-hand side notch and (f) after the abrupt load drop showing evident plasticity in front of both notches (bright regions).

In the 6$^{\text{th}}$ loading step, final failure occurred by plastic deformation and crack extension through the Cu phase (see supplementary movie). However, not only the cracks extended, but also separate regions in the interior of the specimen detached before any crack could reach them. For the sake of simplicity, these regions will be called voids in the following, although they are not three dimensionally closed objects as commonly assumed in macroscopic fracture analysis [44]. To visualize this process, Fig. 3 depicts multiple LR ADF images of the specimen deformation during 6$^{\text{th}}$ loading.

Utilizing an image binarization at a threshold greyscale value of 100 out of 255, the areas corresponding to the two cracks as well as the expanding voids were measured and are visualized on the right-hand side of the corresponding ADF images in Fig. 3. There, it is evident that initial crack tip blunting on

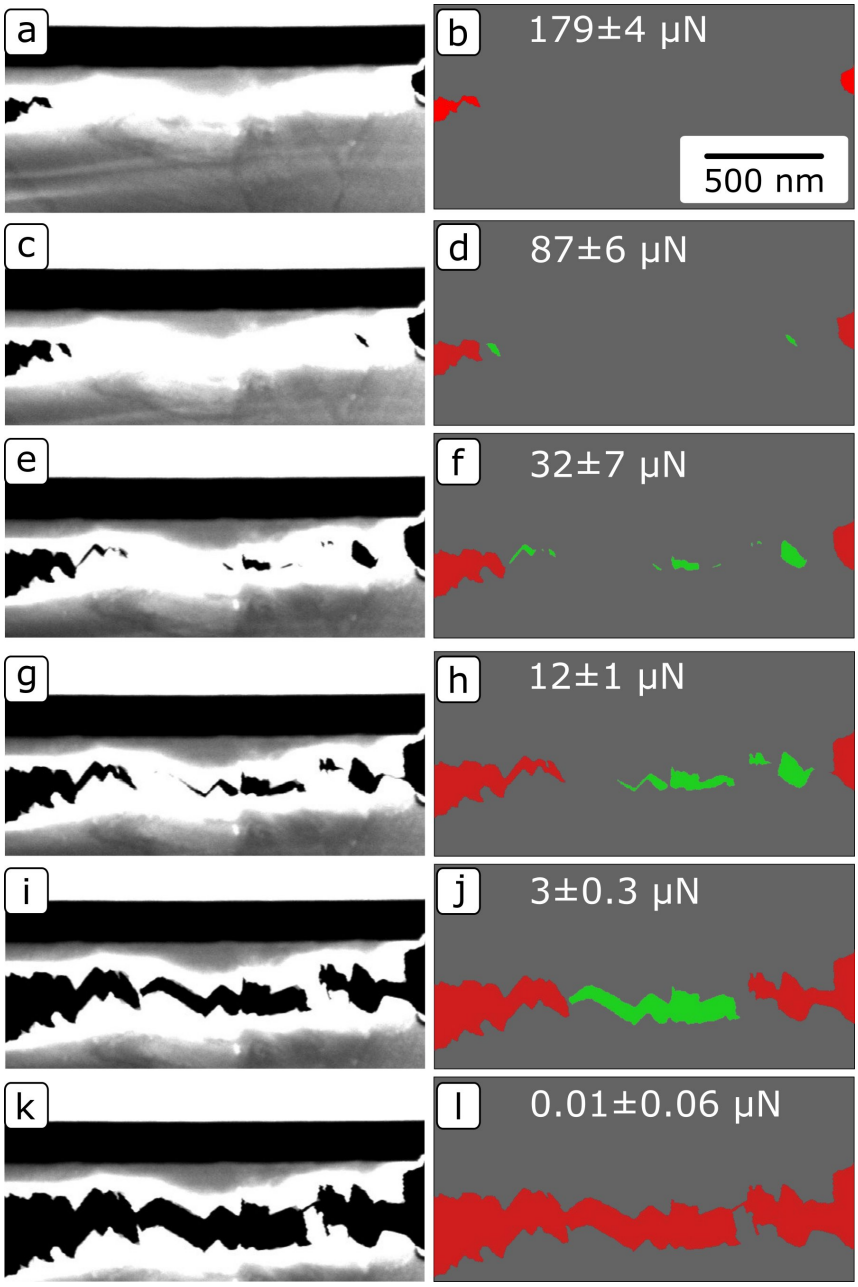

Figure 3: (a,c,e,g,I,k) Zoomed ADF LR images of loading step 6, showing the growth of the crack by nucleation and coalescence of voids, as well as (b,d,f,h,j,l) the corresponding evaluated crack extension areas and loads, where red areas depict the two crack fronts and green areas refer to not yet connected voids. The micron bar is applicable to all images.

both sides is followed by nucleation of voids in the vicinity of the crack tips (Figs. 3b,d). Upon further loading, the left void coalesces with the crack while the right void grows and multiple additional voids nucleate in the specimen interior (Figs. 3e,f). The left-hand side crack continues to grow through void coalescence, while the right-hand side crack exhibits larger crack tip blunting and the interior voids start growing together (Figs. 3g,h). Before all of the voids are connected to one of the two cracks, the remaining interior voids coalesce to one large region (Figs. 3i,j), followed by final failure as both cracks grow together (Figs. 3k,l).

Fig. 4 shows the combined load-displacement and crack analysis data from the final loading step. The black squares correspond to the average load for each image during the acquisition time with the error bars as standard deviation. The number of voids unconnected to any of the two cracks is shown as blue open squares with the corresponding second axis.

When taking into account the increase of region of interest (ROI) around the two cracks as a function of progressively increasing displacement, one can normalize the measured area of cracks and voids, as:

$$A_{cracks,voids}[-] = \frac{A_{cracks,voids}[\mathrm{px}]}{w \cdot h(u)} \tag{2}$$

where $A_{cracks,voids}$ is the normalized area or area in pixels, w is the constant width of the ROI and h is the increasing height of the ROI as a function of displacement. This increase in height was measured on distinct, non-deforming positions on the LR image away from both cracks and was found to be linear with displacement, which suggests that the full amount of plastic deformation was covered within the ROI . The relative area increase of both cracks (filled triangular symbols) as well as voids (green filled triangular symbols) is shown in Fig. 4 as red triangles.

From Fig. 4, five distinct regions are evident. Initially elastic loading took place without any plastic deformation (white region), followed by crack tip blunting on both sides, as shown by the continual increase in crack area (bright grey region). Further loading resulted in void nucleation and growth, as evident in the increase in number of individual voids (pale green region), followed by coalescence of these voids with one of the cracks or with each other, as evident by the decrease of number of voids in conjunction with increase of the void area (pale blue region). Finally, all voids coalesced with one of the cracks up to the complete detachment of both sides of the specimen (dark grey region).

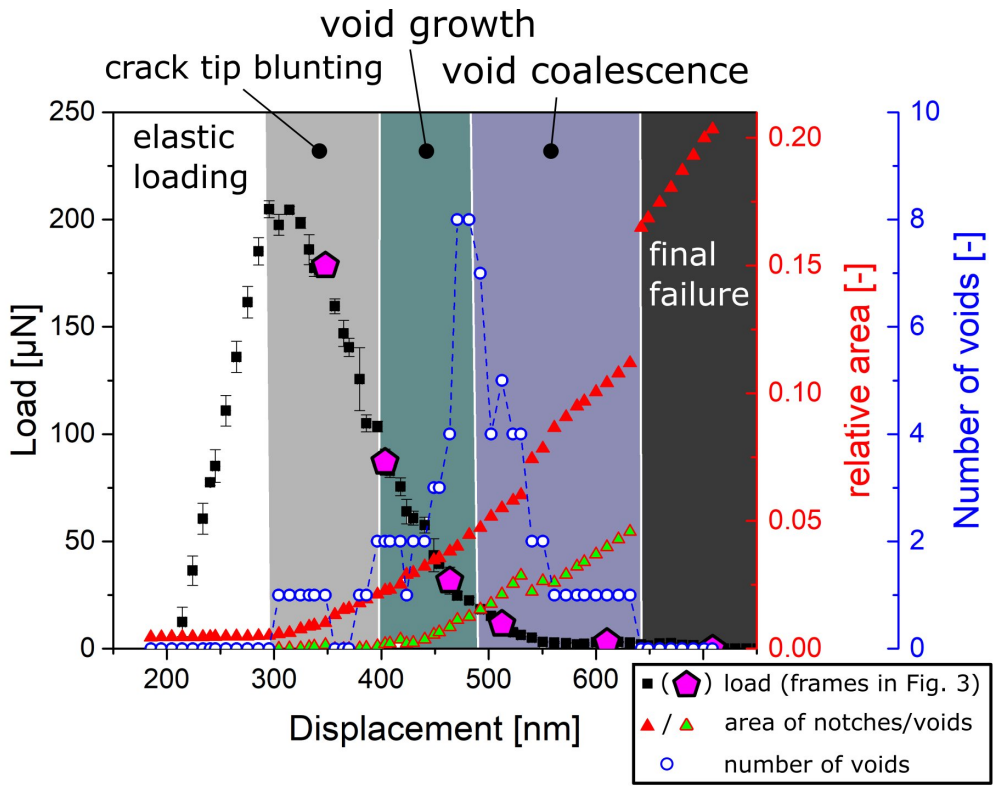

Figure 4: Load-displacement data (black squares) of the 6th loading step as well as number of interior voids (open blue squares) and relative area of cracks (red triangles) and voids (green filled triangles), respectively. The purple pentagons depict the load level of the ADF LR images as shown in detail in Fig. 3.

3.2 Shear loading

3.2.1 Plastic deformation

The second specimen was loaded in a shear configuration (Fig. 1b), to maximize the mode II loading component on the WTi-Cu interface. Fig. 5a shows the load-displacement data of subsequent loading cycles on the specimen and Fig. 5b depicts a BF image of the specimen before loading. The specimen tilt and imaging conditions have been adjusted with a focus on the largest centre grain (grain I), which is bordered by two twinned grains (grain II and V), evident by the straight boundaries between them, two non-twin oriented grains (grain III and IV) and the WTi layer. The first two loading steps showed no evident changes in the images. The first discernible features were evident in loading step 3 between 75 µN and 109 µN (Figs. 5c,d), where parallel straight

slip traces occured from the boundary between grains I and II. These slip traces cover the majority of grain I, suggesting a high density of dislocation sources at the boundary. Furthermore, these slip traces are parallel to the interface between Cu and WTi, which suggests a pure shear loading condition up to this point. The white lines in Fig. 5d depict the projection of all ⟨110⟩-directions in grain I as calculated from single spot transmission-Kikuchi diffraction measurements, with the red lines depicting the two directions in closest agreement with the observed slip traces. At the next loading step 4 additional slip traces occurred in a direction that deviates from the initial traces (Fig. 5e), suggesting that instead of a pure shear loading, some amount of mixed mode loading with a bending component, is present. The 5^{th} loading step shows a distinctive load drop (Fig. 5a), without any evident changes in the images, which was identified to be the result of breaking of residual platinum, stuck between the two moving parts of the ePTP. Subsequent loading to the maximum of the 5^{th} loading step is shown in Fig. 5f, where both of the previously observed slip trace directions became more prominent, suggesting additional dislocation activity. Furthermore, entangling and piling-up of dislocations in front of the boundary with grain V started to occur. During the 6^{th} loading step, dislocation activity continued, resulting in the formation of two entangled dislocation regions (Fig. 5g), which partially disappeared again upon unloading (see supplementary movie). With increasing deformation and the accompanied crystal rotation, the diffraction condition of grain I became unfavourable to a point where no dislocation activity could be observed (Fig. 5h). However, a contrast changing feature nucleated from the boundary between grains I and II (Fig. 5h), which is most likely a result of local bending of the specimen. Furthermore, during the 7^{th} loading step the Cu detached from the rigid WTi on the right-hand side, leaving a starting crack for the last loading step, which will be analyzed in detail in the next section.

In the beginning of the last (8^{th}) loading step it is evident that the bend contour has not fully vanished (Fig. 5i), even as the ePTP is fully unloaded, which results in a negative loading of the specimen ($-175\,\mu\text{N}$). This suggests that the accumulated plastic deformation and resulting residual stresses are high enough to keep the specimen bent locally. Subsequent loading resulted in continuing changes in imaging conditions. However, the two entangled dislocation regions continued to sharpen and form stable sub-grain boundaries (Fig. 5j), as is evident by the different imaging conditions on the right- and left-hand side of the rightmost sub-grain boundary in Fig. 5k. Final failure occurred by sudden nucleation and growth of a second crack from the left-hand side, which resulted in an area of localized plasticity oriented approximately 45° between the two crack tips (Fig. 5k).

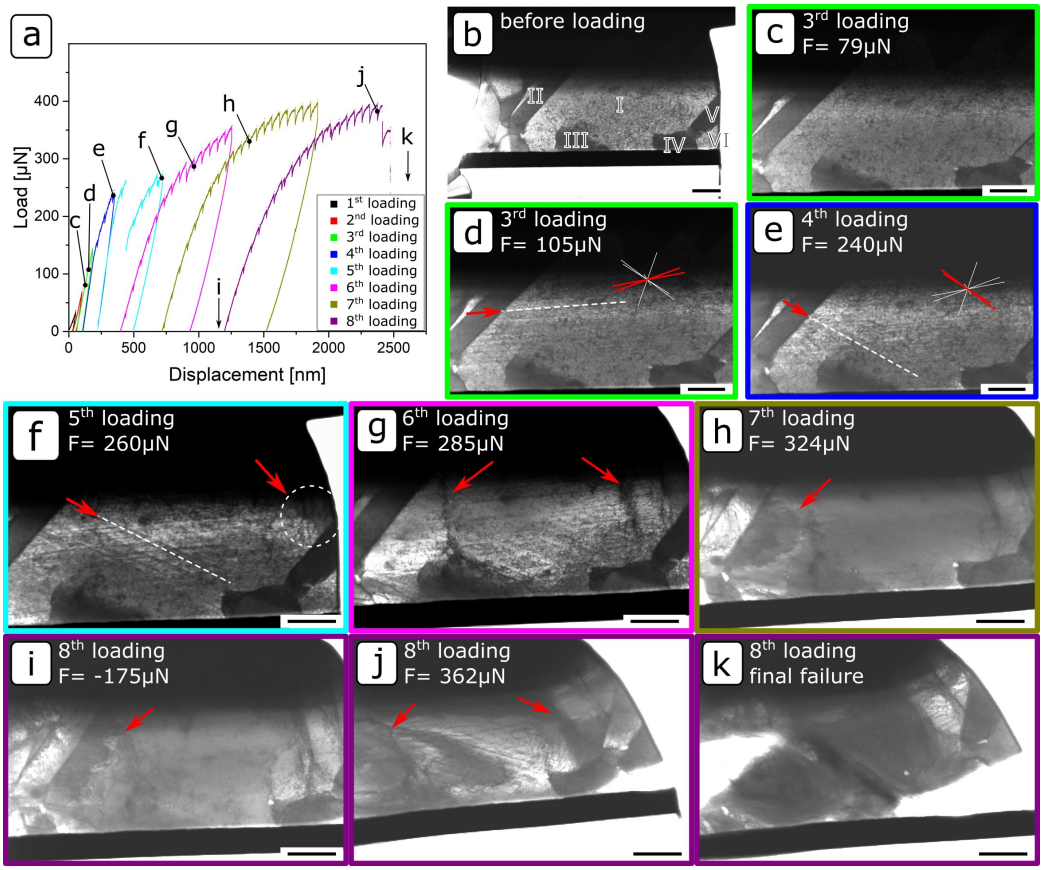

Figure 5: (a) Shear specimen load-displacement data of eight consecutive loading steps up to final failure. (b) BF image of the specimen before loading with roman numerals (I – VI) depicting individual grains. (c-k) HR BF images of subsequent steps during the experiment. The red arrows depict individual features as described in the text and all micron bars are 500 nm.

With increasing plastic deformation (5^{th} to 8^{th} loading step), a major amount of reversible plasticity is evident between the loading steps by the deviations between loading and unloading slope (Fig. 5a), as well as the formation and collapse of the local dislocation entanglements (Figs. 5g,h, see supplementary movie).

To assess the local stress situation, we focus on a single dislocation bowing event with respect to increasing load as detailed in Fig. 6. There, sections of the initial five HR BF images during the 6^{th} loading step are shown, zoomed in on a single bowed dislocation. The images were Fourier-filtered to reduce evident mechanical vibration features (see Fig. 6j). Based on the local dislocation radius of curvature R one can estimate the perpendicular

shear stress τ acting on the dislocation using the following equation [45–47]

$$\tau \approx \frac{T}{bR} \approx \frac{Gb^2}{2R} \tag{3}$$

with $T = Gb^2/2$ as the line tension of the dislocation, $G = 45\,\mathrm{GPa}$ [48] as the shear modulus and $b = 256\,\mathrm{pm}$ as the Burger's vector (assuming a full $\{111\}\langle 110\rangle$ dislocation). The radius R was calculated as the inverse of the local curvature and the detailed mathematical procedure can be found in appendix A.

It is evident that the curvature of the bowing dislocation decreases with increasing load (Figs. 6a,c,e) to a nearly straight configuration (Fig. 6g) and finally the dislocation unpins and slips away (Fig. 6i). This is also evident in the decreased calculated average shear stress on the dislocation (Figs. 6b,d,f,h). However, some details, such as the direction of the shear stress as well as the actual in-plane position of the dislocation pinning points remain unknown. Two limiting cases can be considered with regards to the pinning point position, namely: (I) a dislocation configuration where the whole dislocation line lies perfectly flat in the image plane and is pinned by *e.g.* jogs or other sessile defect configurations or (II) a dislocation configuration where one of the pinning points lies on (or very close to) the bottom side of the foil, while the other one lies on the top side of the foil. To address the second case, it is necessary to know the actual foil thickness, which would be only obtainable with additional experiments, *e.g.* electron energy loss spectroscopy or convergent beam electron diffraction. However, based on the fact that the WTi layer is not electron transparent while both the Cu as well as the Si layer are electron transparent, one can estimate an upper bound of the foil thickness based on the inelastic mean free path concept [49–51] as $t = 116\,\mathrm{nm}$. The detailed derivation can be found in appendix B.

The shear stress as a function of load is summarized for either of the two extreme cases in Fig. 6k, where the upward pointing, blue triangles correspond to the perfectly flat dislocation and the downward pointing, orange triangles correspond to a 'through-foil' dislocation for a maximum foil thickness of 116 nm. The symbols and error bars correspond to the mean value and standard deviation of the center 60 % of the dislocation line, to reduce any artefacts from straight dislocation segments at the pinning points.

3.2.2 Crack extension

During the end of the 7th loading step, at a load of 343 µN, the Cu detached on the right-hand side of the specimen from the WTi layer, initiating an in-

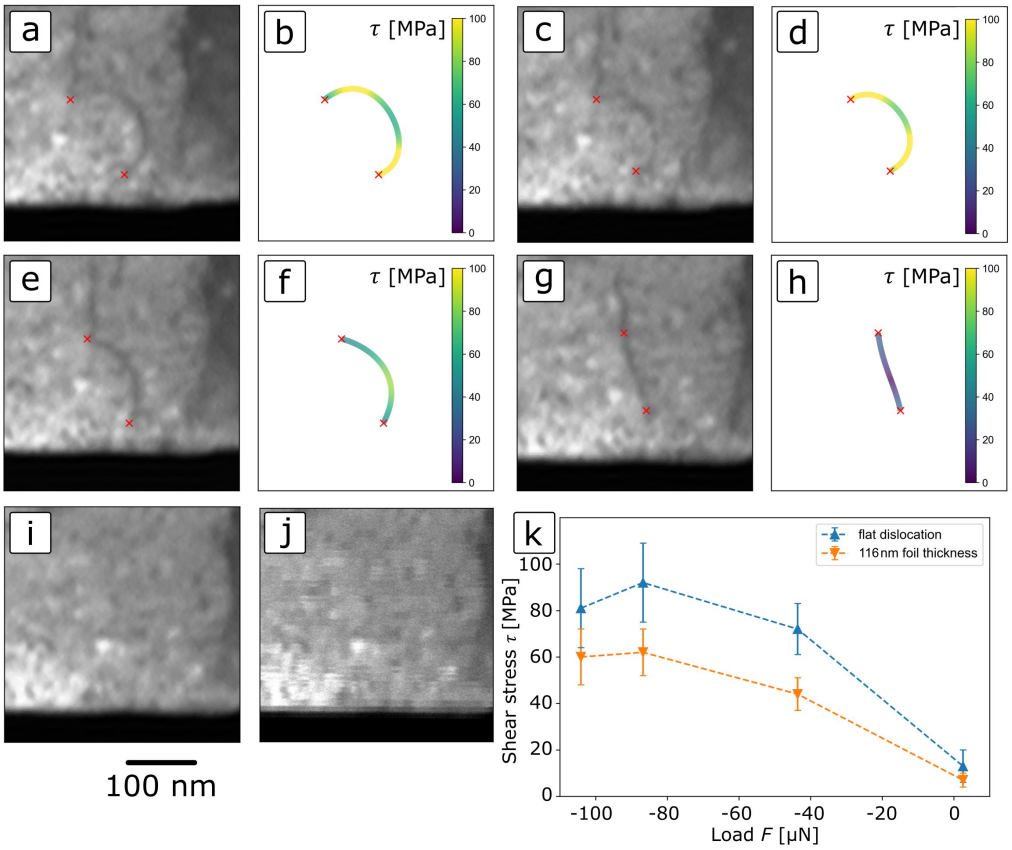

Figure 6: Fourier-filtered HR BF images and local shear stress as a function of curvature of a single dislocation bow-out at increasing loads: (a,b) −104 µN, (c,d) −87 µN, (e,f) −44 µN, (g,h) 3 µN and (i,j) 49 µN, whereby (j) is the corresponding unfiltered image revealing mechanical vibrations. (k) The calculated shear stress over load for the dislocation being parallel to the image plane (blue, upward pointing triangles) or for an inclined dislocation through a 116 nm thick foil (orange, downward pointing triangles). The micron bar is applicable to images (a-j) and the colorbar depicts shear stress in MPa.

terface crack origin as depicted in Fig. 7a (red arrow), which grew to a final shape as shown in Fig. 7b at maximum load. Even after unloading to a negative specimen load of −123 µN the interface crack flanks remained separated (Fig. 7c), which suggests a substantial amount of plastic deformation and is in agreement with the details described in the previous section. This allows for a fracture mechanics investigation during the final loading step based on the extension and opening of the initial crack tip, following the well-known

45° construction for the crack tip opening displacement δ [52, 53]. However, as the WTi part of the specimen is not subject to plastic deformation the construction is only sensible in one direction. This is shown in Fig. 7e, where the crack length a is measured from the rigid WTi edge perpendicular to the interface to the crack tip, while δ is measured as the perpendicular length between the interface and the intersection of the Cu layer with a 45° construction line. The crack extension during the 8^{th} loading step propagated as follows. Up to quasi-elastic loading (200 µN) the crack remained stable and no change in crack tip geometry was observed (Fig. 7d). Upon further loading the crack opened up considerably, while no major crack extension is evident (Fig. 7e), followed by a faster crack extension regime and a decrease in δ (Fig. 7f, red arrow) as the back part of the Cu layer (presumably a different grain) detached. Thereafter, the crack extension slowed down again, while δ increased up to the final crack tip shape shown in Fig. 7g, which is the last image before final failure.

The resulting δ over a measurements are summarized in Fig. 8, where the positions d-g correspond to the HR ADF images in Fig. 8. The error bars depict a deviation of ±3 px (±9.8 nm), under the reasonable assumption that the edges can be detected within a 6 px wide margin of error. The dotted line shows a slope of 1.4, which is the suggested value for the construction line in a standardized δ-Δa evaluation following ASTM 1820 [54]. Although deviating from macroscopic standard geometries and ratios, which are boundary conditions for standard evaluation schemes but rather indicates that reasonable agreement with macroscopic fracture mechanics is still present. The data shows a linear increase of δ with crack extension up to the aforementioned faster crack extension regime (e-f), followed by another linear regime with the same slope up to final failure. Before any of the major failure events occurred δ was in the range of 100 nm, suggesting that the critical crack tip opening displacement δ_c for the interface under the given loading conditions lies in that range.

Part 4
Discussion

The following discussion will highlight the novel insights gained by the present experiments with respect to fracture mechanical considerations, as well as the influence of loading orientation.

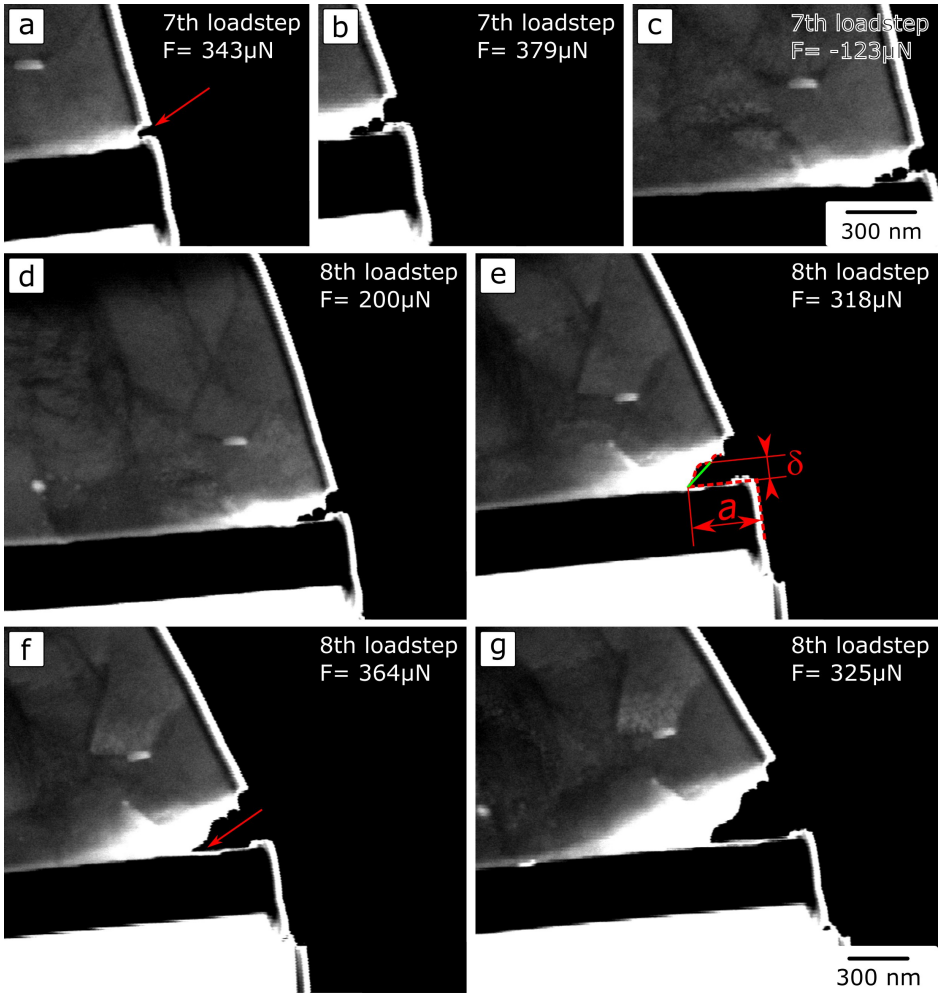

Figure 7: HR ADF images of (a-c) the 7th loading step showing the initial crack nucleation at the Cu-WTi interface and (d-g) the evolution of the crack during 8th loading step up to final failure. The micron bar in (c) is applicable to all 7th step images, while the micron bar in (g) is applicable to all 8th loading step images.

4.1 Influence of loading orientation on failure behaviour

The difference in failure mode between the two specimens is evidenced from the fact that, whereas shear loading promotes crack nucleation at the interface between WTi and Cu, tensile loading led to purely ductile failure in the Cu phase. This could have multiple reasons, such as the well-established fact

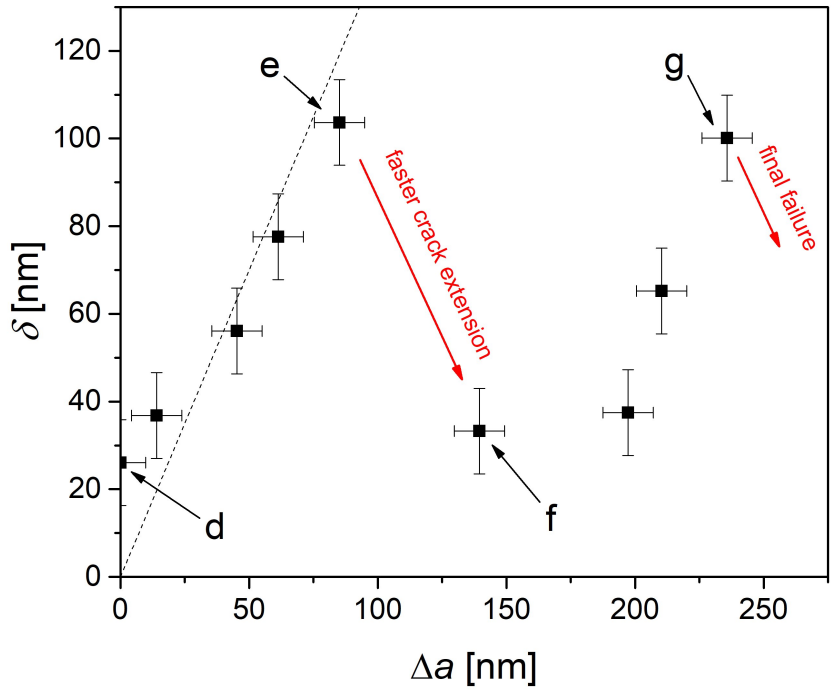

Figure 8: Crack tip opening displacement δ over crack extension Δa. The positions d-g correspond to the HR ADF images in Fig 7 and the dotted line represents a slope of 1.4 as suggested by ASTM 1820 [54].

that for bimaterial interfaces the external loading mode is not the same as the actual local loading mode at the crack tip [55]. Locally, it is governed by the stresses in front of the crack tip and can be described by the mode mixity angle ψ, as:

$$\psi(r) = tan^{-1}\left(\frac{\sigma_{xy}(r)}{\sigma_{yy}(r)}\right) \tag{4}$$

for a specific distance r, where σ_{xy} is the shear stress component parallel (corresponding to mode II) and σ_{yy} is the stress component perpendicular (corresponding to mode I) in front of the respective crack tip. However, describing ψ analytically is only possible for perfectly linear elastic material behaviour and very specific loading configurations, while still resulting in an oscillatory singularity at the crack tip. In an effort to estimate the mode mixities present in the experiments, finite element simulations (FEM) were

conducted based on the actual specimen geometries before the final loading cycle using the freely available CalculiX 2.17 Solver [56], with the assumption of a constant foil thickness of 116 nm and isotropic linear elastic behaviour in the WTi and Si phases. The Cu phase was modelled as elastic-perfectly plastic with a 0.2 % yield onset of 150 MPa [39]. The modelling parameters employed as well as the respective references are summarized in Tab. 1.

Table 1: Parameters for the finite element models.

	E [GPa]	ν [-]	σ_y [MPa]
Si	160 [57]	0.22 [57]	-
WTi	324 [18]	0.29 [58]	-
Cu	124 [48]	0.35 [48]	150 [39]

It is emphasized that the results of the given simulations should be taken as qualitative only, as crystallography and three-dimensional specimen thickness were not accounted for and simplified assumptions with regards to deformation were made. Nevertheless, in comparison to each other they provide insight into the differences between the two loading configurations. Specifically, when comparing the average mode mixity straight in front of the cracks, in a regime between 200 nm and 1000 nm to circumvent any influence of the crack tip singularity, one finds that $\psi_{tensile,left} = 5.9 \pm 3.2°$ and $\psi_{tensile,right} = 5.8 \pm 3.6°$ for the left and right crack tip in the tensile specimen, while $\psi_{shear} = 44.7 \pm 10.5°$ for the shear specimen crack tip. This suggests that the tensile specimen is indeed loaded very close to a pure mode I condition ($\psi_{Mode\ I} = 0°$), whereas the shear specimen is not loaded in a pure mode II ($\psi_{Mode\ I} = 90°$) condition, but rather in a mixed mode with equal mode I and mode II contributions. This is further supported by the actual deformed shape of the shear specimen (Fig. 7), where the crack mouth opening displacement (CMOD) evidently increases, which would not be the case for a pure mode II loading. However, the pronounced difference in failure characteristics between the two specimens can be explained when investigating the maximum shear stresses in the FEM simulations as shown in Fig. 9. There, the shape of both specimens before the final loading step is shown in conjunction with the maximum shear stress maps in 1:1 matching scale and color schemes for the individual simulations. It is evident that the maximum shear stress is distributed over the majority of the Cu phase in the shear specimen (Fig. 9b), while the tensile specimen only shows very localized maximum shear stress (Fig. 9d). Considering that the shear stress is the main component in driving dislocations, which in turn mediates plasticity, the extent of the maximum shear stress regions can be seen as areas

where the majority of non-reversible deformation occurs. While the highest shear stresses arise in the Si and WTi phases of the shear specimen, it is very unlikely to activate any dislocation movement there, as the inherent resistances are considerably higher than in the Cu part. This seems to be in excellent agreement with the previous observations of the shear specimen, where strong dislocation activity was observed in the interior of the Cu grains rather than in the vicinity of the interface (Fig. 5). Even after crack nucleation there was still only very little dislocation movement near the crack tip, while the majority of plastic deformation continued in the specimen interior (Fig. 7). This is again in very good agreement with the FEM simulation, as the maximum shear stress near the crack tip is lower than in the Cu phase (Fig. 9b). The tensile specimen on the other hand shows very localized deformation, and with the exception of some initial slip steps (Fig. 2c), no dislocation activity outside of this region, which again closely resembles the simulation (Fig. 2d), as the maximum shear stress is very localized in this area, suggesting no driving force for any dislocation plasticity outside of it.

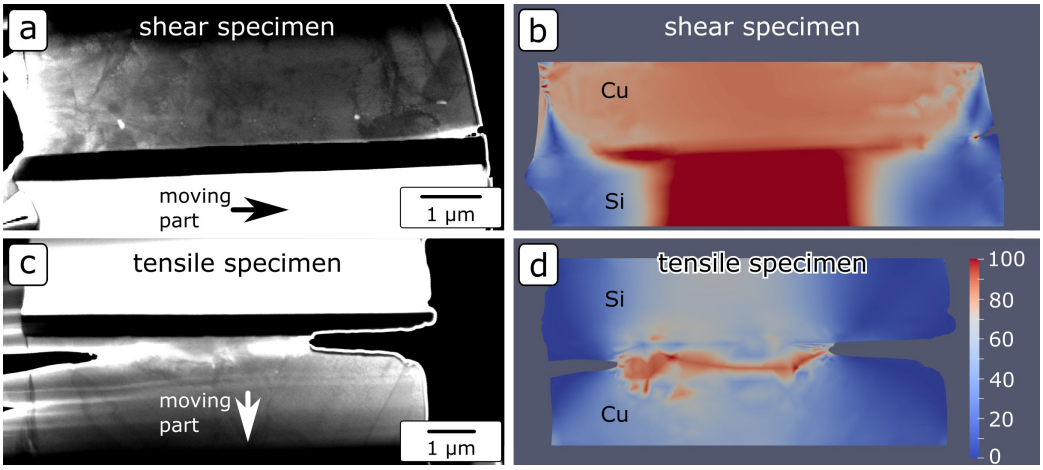

Figure 9: ADF LR images and maximum shear stress maps from the FEM simulation for (a,b) the shear specimen and (c,d) the tensile specimen. The simulations are scaled 1:1 with the respective images and the colorbar is the same for both of them.

4.2 Non-reversible accumulation of plasticity in the shear specimen (Bauschinger effect)

Due to the multiple loading cycles in the plastic regime, not all dislocation activity was completely reversible, as is evident by the formation of dislocation entanglements (Fig. 5g) which remained partially visible even in the unloaded (negative specimen load) state. This, in conjunction with the lower onset of yield in the load displacement data (Fig. 5a) in subsequent cycles, suggests that some of the stored dislocations are pinned only in one direction while being able to move under load reversal. This is commonly referred to as 'Bauschinger effect' [59–61], where initial accumulation of plasticity in one direction lowers the yield onset of subsequent loading in the other direction. This effect is illustrated by the bowed out dislocation in Fig. 6, which was pinned upon unloading at the end of loading step 6. There, the continuous loading during loading step 7 did lead to a decrease of dislocation curvature, which suggests a local shear stress in the opposite direction. Upon reaching positive specimen loads the dislocation did not bow out in the opposite direction, which would be expected if it was fully pinned by, *e.g.* sessile jogs, but it rather slipped away, vanishing out of view. This evident movement of the dislocation happened just on the first occurrence of a positive specimen load, which is usually still considered the elastic regime. However, due to the previous loading step, non-reversible dislocation mobility was possible. Comparing this 'Bauschinger effect' between the shear and the tensile specimen, one finds that it is far less pronounced in the latter. This is evident in the load displacement data, which shows no major hysteresis upon reloading for the tensile specimen (Fig. 2a), while pronounced hysteresis effects are visible in the shear specimen from loading step 6 to final failure (Fig. 5a). In conjunction with the FEM simulations this seems reasonable, as the shear stress (Fig. 9d) and resulting plasticity (Fig. 3) are very localized in the tensile specimen, whereas the shear specimen has a quite constant shear stress over a wide area (Fig. 9b), which promotes a larger spatial extent of plastic deformation (Fig. 5). Based on this observation one can argue that cyclic loading conditions with a considerable mode II component, *e.g.* sliding contact in bearings or thermal loading of heterogeneous layered structures, can accommodate a larger amount of defined dislocation structures, *e.g.* persistent slip bands [62–64], than any mode I type experiment would suggest.

4.3 Initial crack nucleation at the interface of the shear specimen

As the deformation of the specimen is governed primarily by plastic slip, the question arises why the interface crack in the shear specimen did nucleate in the first place? In a classical fracture mechanical sense, for such a crack to nucleate the local stress state at the interface needs to be high enough to overcome the interfacial adhesion, which is only possible if little to no dissipating mechanisms, *e.g.* dislocation plasticity, are present. One reason for this to occur could be the fact that the detaching grain VI (Fig. 5b) has smaller geometric dimensions than grain I, which shows the most prominent amount of dislocation activity. It is known that smaller dimensions give rise to increased resistance to dislocation glide as:

$$\Delta\tau \sim d^{-m} \tag{5}$$

where Δa is the increase in necessary shear stress, d is the relevant geometric dimension (most commonly the grain size) and m is a scaling exponent in the range of 0.5-0.66 for fcc materials, depending on whether classical Hall-Petch constraint [65–67] or free standing single crystal investigations [6, 68] are considered. Based on the *in situ* observations we observed that the first dislocation activity commenced in two different slip orientations in grain I (Fig. 5d,e), leading to a maximum distance $d_{grainI,max} = 3183\,\mathrm{nm}$ (from grain II to the right-hand side of grain I) along the first slip trace orientation and $dgrainI, min = 1671$ nm (from grain II to the triple point between grain I, grain IV and the WTi layer) along the second slip trace orientation. Grain VI on the other hand does not show pronounced slip traces, resulting in the absence of a predetermined direction. However, the largest distance in the whole grain is between the lower left triple junction (grain IV, grain VI and WTi) and the upper right triple junction (grain V, grain VI and vacuum) as $d_{grainVI,max} = 573\,\mathrm{nm}$. Thus, utilizing Eq. 5, we can estimate that the necessary shear stress to promote dislocation mobility in grain VI is between 1.7 (minimum d_{grainI}; $m = 0.5$) and 3.1 (maximum d_{grainI}; $m = 0.66$) times higher than in grain I, where the majority of dislocation activity was evident. In conjunction with the fact that the local maximum shear stress is considerably less in the vicinity of grain VI than in the specimen interior, as shown in Fig. 9a,b, dislocation activity is considerably hampered in grain VI. This is evident in Fig. 10, where a zoomed section of the specimen is shown focussed on grain VI during the 7^{th} loading step ($F = 271\,\mu\mathrm{N}$), but before the grain rotated out of a favourable imaging condition and the crack nucle-

ated. While dislocation activity in grain I at such loads occurs via multiple sources of dislocation emission and the build-up of dislocation entanglements (Fig. 5g), the only evident dislocation in the interior of grain VI bows out very slowly and no movement or multiplication of this dislocation is evident up to this point. The average shear stresses (Eq. 3, Appendix A) for the given bow-out equates to 51.5 ± 10.6 MPa for a perfectly flat dislocation in the image plane or 39.9 ± 6.1 MPa for a dislocation extending through a 116 nm foil. While there seem to be multiple dislocations in the bottom left triple junction of this grain, no further dislocation mobility was evidenced in the images, which strengthens the argument regarding Hall-Petch [67] hardening. These points underline that there is only very weak energy dissipation possible via dislocation plasticity in the vicinity of the interface where the crack originated, which results in the energetically favourable opening of the interface and hence a crack originated.

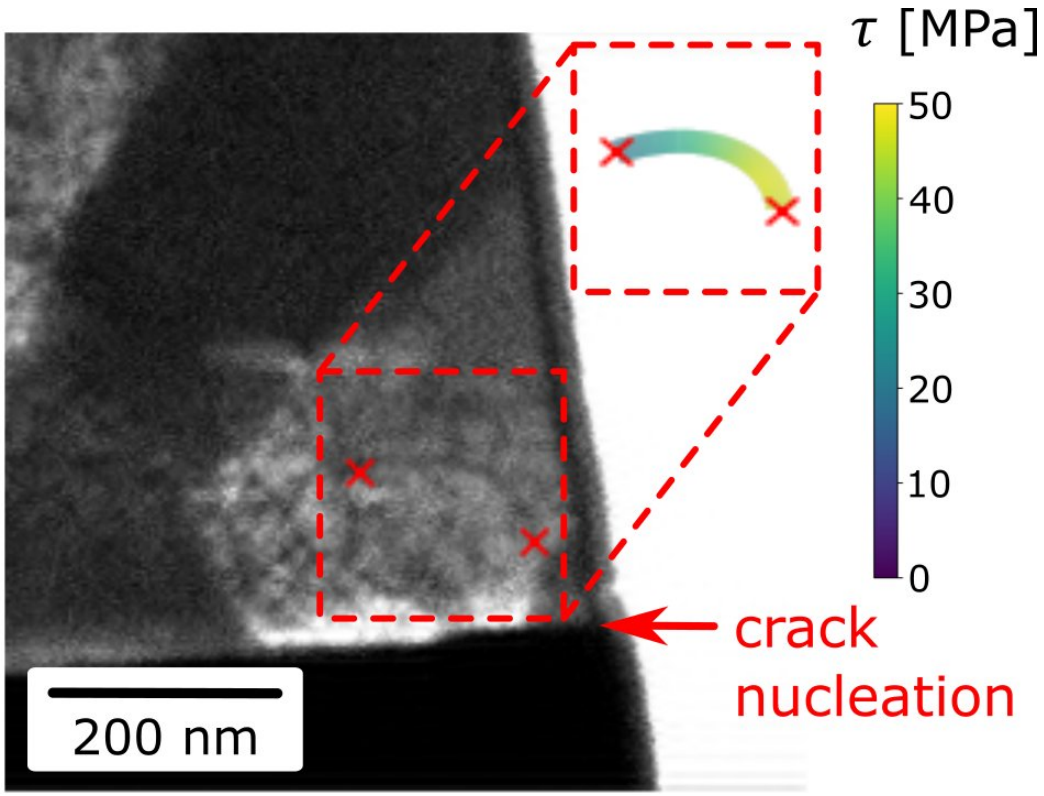

Figure 10: Zoomed LR BF image focussing on grain VI at the 7th loading step before crack nucleation ($F = 271$ µN) showing a single dislocation bow-out and quantification of local shear stresses.

4.4 Details regarding fracture mechanical parameters

Whereas the WTi part of the specimens remains rigid and does not show any evidence of irreversible deformation, the Cu part displays pronounced dislocation activity already before any crack nucleation or crack tip blunting is evident (Fig. 2c, Fig. 5d), regardless of whether the specimens are loaded in shear or tensile direction. As a consequence, a classical fracture mechanics quantification of the fracture resistance of the Cu-WTi interface is not viable. However, considering the onset of dislocation activity one can estimate a lower bound for the interface fracture resistance. Based on the work of Rice and Thomson [69], Ohr [70] derived an expression for the stress intensity necessary to nucleate an edge dislocation from a crack tip under an angle Φ for mode I loading condition, as:

$$K_{Ie} = \frac{2}{\sin\Phi\cos\left(\Phi/2\right)}\left(\frac{Gb}{(1-\nu)\sqrt{8\pi r_c}} + \sqrt{2\pi r_c}\left(\sigma_y + \frac{4\gamma b\sin\Phi}{\pi r_c^2(2+e^3)}\right)\right) \quad (6)$$

where $r_c \approx b$ [45–47] is the dislocation core radius, $\gamma = 1635\,\mathrm{mJ/m^2}$ [71, 72] (extrapolated to 25 °C) is the surface energy of Cu and e is Euler's constant. All other variables have been defined previously. Using $\Phi = 60°$ as observed in the tensile specimen (Fig. 2c) and $\sigma_y = 150\,\mathrm{MPa}$ (see Tab. 1) the resulting emission stress intensity is estimated as $K_{Ie} = 0.75\,\mathrm{MPa}\sqrt{\mathrm{m}}$. Notably, σ_y has only minor influence on this as the difference between $K_{Ie}(\sigma_y = 1\,\mathrm{MPa})$ $=0.74\,\mathrm{MPa}\sqrt{\mathrm{m}}$ and $K_{Ie}(\sigma_y = 400\,\mathrm{MPa}) = 0.78\,\mathrm{MPa}\sqrt{\mathrm{m}}$ is only 5.5 %. Ohr [70] also discussed the emission of screw dislocations under mode II and mode III loading conditions, which exhibit a lower stress intensity threshold for nucleation, but the necessary plane for dislocation glide would have to be in front of the crack tip parallel to the WTi-Cu interface. As this is clearly not the case and the tensile specimen has a significant mode I component, an argument based on the nucleation of an edge dislocation under mode seems more sensible. Furthermore, one can evaluate the tensile experiment as a classical DENT specimen using [73]:

$$K_{DENT} = \frac{F}{Bt}\sqrt{\pi a_0}\quad Y\left(\frac{a_0}{B/2}\right) \quad (7)$$

where $B = 4995\,\mathrm{nm}$ is the specimen width, $a_0 = 1119\,\mathrm{nm}$ is the (average) initial crack length from one side and $Y(2a0/B) = 1.163$ is a geometry factor [73]. With the load corresponding to the first slip trace emerging in the

tensile specimen (Fig. 2c) as $F = 373\,\mu\text{N}$ and the specimen thickness again as $t = 116\,\text{nm}$ (aiming for a lower bound), the stress intensity equates to $K_{DENT} = 1.40\,\text{MPa}\sqrt{\text{m}}$, which is about twice as high as the previously calculated K_{Ie}. However, the emission stress intensity calculations consider an atomically sharp crack tip, whereas the actual crack tip has a comparatively large radius of $\rho \approx 45\,\text{nm}$ (Fig. 2b). Fischer and Beltz [74] have developed a framework for the influence of crack tip radius on the emission stress intensity based, based on Muskhelishvili's complex potential approach [75]. While the full derivation of the equations for the present system is outside the scope of this work, linearly interpolating their data to $\rho/b \approx 175$ at $a/b \approx 4000$ as for the given system leads to a K-value between 2 and 3 times higher than for a sharp notch. This explains the observed discrepancy between K_{Ie} and K_{DENT} and leads to a fairly good agreement. Hence, one can calculate the J-integral $J_{DENT} = K_{DENT}^2/E_{Cu} = 15.8\,\text{J/m}^2$ under the assumption of a plane-stress condition, which is reasonable given the thin specimen. This value is in very good agreement with the J-integral for the onset of plastic crack tip blunting (between 15.2 and $23.6\,\text{J/m}^2$), measured by the cantilever deflection technique [76]. Furthermore, to investigate the dissipated energy not at first dislocation emission but upon final failure of the tensile specimen, we can the utilize the cohesive zone model [77, 78], where a traction separation relationship is evaluated through the whole fracture process. The area under this traction-separation curve is equivalent to the non-reversible energy [77] of deformation during the process, which we will denote as $J_{fracture}$, and given the fact that the plastic deformation is rather confined in the ligament between the two cracks (Fig. 3) it can be estimated for the present experiment as [78]:

$$J_{fracture} = \frac{1}{(B - 2a_0)t} \int_{200\,\text{nm}}^{800\,\text{nm}} F du \tag{8}$$

which amounts in $J_{fracture} = 98\,\text{J/m}^2$ ($K_{fracture} = 3.49\,\text{MPa}\sqrt{\text{m}}$). This value has to be taken with some caution as it describes the whole fracture process instead of the onset of fracture. Nevertheless, in comparison with the critical fracture toughness of coarse grained ($K_{IC} = 88.5\,\text{MPa}\sqrt{\text{m}}$), or even ultra-fine grained Cu ($K_{IC} = 33.4\,\text{MPa}\sqrt{\text{m}}$) in macroscopic experiments [79] our final fracture toughness is still considerably lower. Hirakata *et al.* [80] studied free standing electron beam deposited copper films in the range from 800 nm to 100 nm and found a pronounced size effect in fracture toughness from $7.81\,\text{MPa}\sqrt{\text{m}}$ down to $2.34\,\text{MPa}\sqrt{\text{m}}$. While their films had a smaller in-plane grain size (369 to 170 nm) than present in the tensile specimen, our fracture toughness values agree rather well, which suggests a major influence

of the volumetric constraint on fracture toughness in such thin specimens. Therefore, it has to be emphasized that comparison to similar sized specimens is desirable, as association with macroscopic data can lead to incorrect conclusions.

Similar considerations can be outlined for the shear specimen, where the critical crack tip opening displacement at crack extension is estimated to be $\delta_c \approx 100\,\mathrm{nm}$ (Fig. 8). The relationship between J-integral and crack tip opening displacement in the framework of a Hutchinson-Rice-Rosengreen (HRR) field [81, 82] is linear with the proportionality as [53]:

$$J = \frac{\delta\sigma_y}{d(n,\psi)} \tag{9}$$

where $d(n,\psi)$ is a function of the Ramberg-Osgood strain hardening exponent n [83], the mode mixity and of whether a plane strain or plane stress state dominates. Assuming again a majority of plane stress state and aiming for a lower bound ($n \to \infty$), the function $d(n)$ would equal unity without taking the bimaterial nature of the specimen into account (neglecting ψ). Shih *et al.* [84, 85] established that $d(n)$ is even higher for a bilayered structure than for a homogenous material. However, they reported only values for distinct mode mixities and plane strain condition. Pirondi and Dalla Donne [86] derived $d(n,\psi)$ based on the HRR field for a homogeneous material, but as a function of mode mixity, and found good agreement with experimental data as well as FE-simulations. Utilizing their data at a mode mixity angle of $\psi = 45°$ results at $d(n,\psi) \approx 1.7$, which equates to $J_{shear} = 8.8\,\mathrm{J/m^2}$ for the shear specimen. This is reasonable given the fact that mode II loading results in a lower threshold for crack nucleation given the far field stresses (T-stresses) have a positive contribution to mode I opening [87, 88], which is clearly the case considering the large opening angle of the crack tip (Fig. 7g). While all of the previous considerations are based on simplified assumptions, all arguments were considered towards a lower bound J-integral value, which gives estimates for dislocation nucleation $J_{dislocation} \approx 15\,\mathrm{J/m^2}$ and crack extension $J_{crack} \approx 8.8\,\mathrm{J/m^2}$. However, while the threshold for fracture seems to be lower, it has to be emphasized that the actual occurrence of crack extension can be strongly influenced by the local crystallographic orientation relationship. Kysar [89] showed that that the crack along a diffusion bonded single crystal copper-sapphire interface exhibits a slower (ductile) or faster (brittle) crack extension in opposite directions. He found that whether brittle or ductile behaviour occurred was a result of the normal stresses that are able arise in front of the crack tip [90]. Thus, in conjunction with the fact that the dislocation activity in the shear specimen is suppressed by the local stress

state (see Fig. 10), this explains the crack extension at a lower J-value, as the local opening stresses overtake the energy dissipation by plasticity. Moving forward from understanding the elastic-plastic fracture processes at bimaterial interfaces towards designing more failure resistant composite materials, there are some general aspects or countermeasures to take along from the present work. Admittedly, the fracture behaviour is strongly influenced by the local stress state and the resulting suppression or enhancement of dislocation plasticity. However, while the local stress state will always depend on external conditions, the suppression of dislocation plasticity is majorly governed by the microstructure, which can be adjusted in certain bounds. Hence, for damage tolerant applications it is recommended to avoid microstructural features that impede dislocation mobility in the vicinity of the interface, *e.g.* high defect densities or small grain sizes, as this will decrease the tendency towards interfacial fracture in such systems.

Part 5
Conclusion

In situ TSEM experiments where conducted on a Cu-WTi-Si-SiO_x multilayer stack with the aim of studying the fracture behaviour of the Cu-WTi interface. Two different loading orientations where investigated to examine the difference between mode I (tensile specimen) and mode II loading (shear specimen) on the failure behaviour of the interface. To the authors' knowledge, this was the first time that a shear configuration was successfully realized on a push-to-pull device in transmission configuration, thereby opening up the field of *in situ* mixed mode fracture investigations in such very confined scales. While the tensile specimen failed purely by localization of plastic deformation in the Cu phase, the shear specimen exhibited nucleation and further extension of an interface crack after significant plastic deformation in the specimen interior. This can be connected to the local suppression of dislocation activity at the crack tip in shear configuration, both by the local stress state as well as the microstructure in front of the crack tip. Furthermore, it was established that the lower bound for the activation of dislocation plasticity is $J_{dislocation} \approx 150\,\mathrm{J/m^2}$, which is in good agreement with previously conducted experiments on the same material system. The threshold for crack extension in the shear specimen was found to be $J_{dislocation} \approx 8.8\,\mathrm{J/m^2}$, with the caveat that interfacial crack propagation is only possible with a significant mode II component and a local inhibition of dislocation nucleation

or propagation. In a broader context, such kind of experiments hold the premise to reveal details regarding plasticity governed fracture processes in systems with a dedicated mixed mode component or common loading conditions with a significant mode II component, as encountered for example in gliding contact in bearings or thermal loading in material systems with different thermal expansion coefficients. In fact, our present work suggests that interfacial failure through crack extension would be inherently localized along the interface, given similar elastic and plastic properties of the constituents. Specifically, for the situation of dislocation plasticity governed metallic materials, this failure could be counteracted by, *e.g.* locally reducing the defect density or increasing the grain size in the vicinity of the interface to reduce dislocation confinement in front of the crack tip. Overall, this paves a strategy towards more damage resistant multiphase structures by topologically optimized microstructures.

Acknowledgments

This study was conducted during a research stay at UCSB financed by an Austrian Marshall Plan Scholarship, which is gratefully acknowledged. Further financial support under the scope of the COMET program within the K2 Center "Integrated Computational Material, Process and Product Engineering, IC-MPPE" (Project 859480, A2.12) is also acknowledged. This program is supported by the Austrian Federal Ministries for Transport, Innovation and Technology (BMVIT) and for Digital and Economic Affairs (BMDW), represented by the Österreichische Forschungsförderungsgesellschaft (Funder ID: 10.13039/501100004955), and the federal states of Styria, Upper Austria, and Tyrol. This project has received funding from the European Research Council (ERC) under the European Union's Horizon 2020 research and innovation programme (Grant No. 771146 TOUGHIT). The authors also acknowledge partial support from the NSF MRSEC Program through DMR 1720256 (IRG-1). The research reported here made use of shared facilities of the UCSB MRSEC (NSF DMR 1720256), a member of the Materials Research Facilities Network (www.mrfn.org). GHB acknowledges support from the National Science Foundation Graduate Research Fellowship under Grant No. 1650114. The authors would also like to thank Aidan Taylor, Eric Yao, Jungho (Paul) Shin and Jean-Charles (JC) Stinvillle for support with the experimental setup as well as fruitful discussions.

Appendix A

To determine the stress of a dislocation line segment in three dimensions one needs to calculate the local curvature of the given segment. This can be done by parametrizing the whole dislocation as:

$$\vec{r}(l) = (f(l), g(l), h(l)) \tag{A1}$$

where $f(l)$, $g(l)$ and $h(l)$ are functions of the x, y and z positions of the dislocation in the interval $0 \leq l \leq 1$ (from the beginning to the end of the dislocation line). The functions $f(l)$ and $g(l)$ are 3^{rd} order polynomials fitted to individual points along the dislocation line, while the function $h(t)$ is either 0 (for the case of a flat dislocation) or assumed to be linear through the foil thickness. Utilizing this parametrized form one can calculate a unit tangent $\vec{T}(l)$ as:

$$\vec{T}(l) = \frac{\vec{r'}(l)}{\|\vec{r'}(l)\|} = \left(\frac{f'(l)}{\|\vec{r'}(l)\|}, \frac{g'(l)}{\|\vec{r'}(l)\|}, \frac{h'(l)}{\|\vec{r'}(l)\|} \right) \tag{A2}$$

where $\vec{r'}$ is the first derivative with respect to l and the double bars refer to the Euclidian norm. From this unit tangent $\vec{T}(l)$ the local curvature $\kappa(l)$ is calculated as:

$$\kappa(l) = \frac{1}{R} = \frac{\|\vec{T'}(l)\|}{\|\vec{r'}(l)\|} \tag{A3}$$

which serves as input for our shear stress estimates (Eq. 3).

Appendix B

The thickness of the foil can be estimated based on the fact that the intensity of the incoming electron beam is reduced by inelastic processes in the material, following a Lambert-Beer type law, as [49, 50]:

$$I = I_0 e^{\frac{-t}{\lambda_{inelastic}}} \tag{B1}$$

where I_0 and I are the incoming and outgoing beam intensities, t is the foil thickness and $\lambda_{inelastic}$ is the inelastic mean free path of an electron in a specific material. The actual transmitted intensity to initial intensity ratio is unknown due to the brightness and contrast adjustments, which lead to a fully saturated detector in vacuum. However, assuming in a worst case scenario that only 1 % of the transmitted intensity is enough to form the

gathered images and the fact that the Cu phase is still transparent while the WTi is not, one could argue that the thickness is between 116 nm and 93 nm, as summarized in Tab. B1. Considering that it is likely that a higher transmitted intensity is necessary for the observed features to be as evident as they are, the foil is probably closer to a thickness of 50 nm, as would be the case for a 10 % transmitted intensity. However, to obtain lower bound values for all mechanical parameters, the higher bound of the foil thickness $t = 116$ nm was used for calculation.

Table B1: Calculated foil thickness t for occurring species in the specimen and transmission intensities of 1 % and 10 %

	$\lambda_{inelastic}$ (E=29.7 keV) [nm] [51]	t (I/I_0=1 %) [nm]	t (I/I_0=10 %) [nm]
Cu	25.2	116	58
W	20.27	93	47
Ti	28.03	129	65
Si	39.93	184	92

References

1. Thakare, J. G., Pandey, C., Mahapatra, M. M. & Mulik, R. S. Thermal Barrier Coatings - A State of the Art Review. *Metals and Materials International* (2020).
2. Chen, Y. Nanofabrication by electron beam lithography and its applications: A review. *Microelectronic Engineering* **135,** 57–72 (2015).
3. Subramanian, C. & Strafford, K. Review of multicomponent and multilayer coatings for tribological applications. *Wear* **165,** 85–95 (1993).
4. Pethica, J. B., Hutchings, R. & Oliver, W. C. Hardness measurement at penetration depths as small as 20 nm. *Philosophical Magazine A* **48,** 593–606 (1983).
5. Oliver, W. & Pharr, G. An improved technique for determining hardness and elastic modulus using load and displacement sensing indentation experiments. *Journal of Materials Research* **7,** 1564–1583 (1992).
6. Uchic, M. D., Dimiduk, D. M., Florado, J. N. & Nix, W. D. Sample dimensions influence strength and crystal plasticity. *Science* **305,** 986–989 (2004).
7. Kiener, D., Grosinger, W., Dehm, G. & Pippan, R. A further step towards an understanding of size-dependent crystal plasticity: In situ tension experiments of miniaturized single-crystal copper samples. *Acta Materialia* **56,** 580–592 (2008).
8. Armstrong, D., Rogers, M. & Roberts, S. Micromechanical testing of stress corrosion cracking of individual grain boundaries. *Scripta Materialia* **61,** 741–743 (2009).
9. Motz, C., Schöberl, T. & Pippan, R. Mechanical properties of micro-sized copper bending beams machined by the focused ion beam technique. *Acta Materialia* **53,** 4269–4279 (2005).
10. Sebastiani, M., Johanns, K., Herbert, E. & Pharr, G. Measurement of fracture toughness by nanoindentation methods: Recent advances and future challenges. *Current Opinion in Solid State and Materials Science* **19,** 324–333 (2015).
11. Riedl, A. *et al.* A novel approach for determining fracture toughness of hard coatings on the micrometer scale. *Scripta Materialia* **67,** 708–711 (2012).
12. Sernicola, G. *et al.* In situ stable crack growth at the micron scale. *Nature Communications* **8** (2017).

13. Schwiedrzik, J., Ast, J., Pethö, L., Maeder, X. & Michler, J. A new push-pull sample design for microscale mode 1 fracture toughness measurements under uniaxial tension. *Fatigue & Fracture of Engineering Materials & Structures* **41,** 991–1001 (2017).

14. Ast, J., Schwiedrzik, J., Rohbeck, N., Maeder, X. & Michler, J. Novel micro-scale specimens for mode-dependent fracture testing of brittle materials: A case study on GaAs single crystals. *Materials & Design* **193,** 108765 (2020).

15. Wurster, S., Motz, C. & Pippan, R. Characterization of the fracture toughness of micro-sized tungsten single crystal notched specimen. *Philosophical Magazine* **92,** 1–23 (2012).

16. Ast, J. *Untersuchung der lokalen Bruchzähigkeit und des elastisch-plastischen Bruchverhaltens von NiAl und Wolfram mittels Mikrobiegebalkenversuchen* PhD thesis (FAU Erlangen, 2016).

17. Alfreider, M., Kozic, D., Kolednik, O. & Kiener, D. In-situ elastic-plastic fracture mechanics on the microscale by means of continuous dynamical testing. *Materials & Design* **148,** 177–187 (2018).

18. Matoy, K., Detzel, T., Müller, M., Motz, C. & Dehm, G. Interface fracture properties of thin films studied by using the micro-cantilever deflection technique. *Surface and Coatings Technology* **204,** 878–881 (2009).

19. Schaufler, J., Schmid, C., Durst, K. & Göken, M. Determination of the interfacial strength and fracture toughness of a-C:H coatings by in-situ microcantilever bending. *Thin Solid Films* **522,** 480–484 (2012).

20. Konetschnik, R., Daniel, R., Brunner, R. & Kiener, D. Selective interface toughness measurements of layered thin films. *AIP Advances* **7,** 035307 (2017).

21. Alfreider, M., Issa, I., Renk, O. & Kiener, D. Probing defect relaxation in ultra-fine grained Ta using micromechanical spectroscopy. *Acta Materialia* **185,** 309–319 (2020).

22. Shi, F. *et al.* Failure mechanisms of single-crystal silicon electrodes in lithium-ion batteries. *Nature Communications* **7** (2016).

23. Kolednik, O., Predan, J., Shan, G., Simha, N. & Fischer, F. On the fracture behavior of inhomogeneous materials—A case study for elastically inhomogeneous bimaterials. *International Journal of Solids and Structures* **42,** 605–620 (2005).

24. Sugimura, Y., Lim, P., Shih, C. & Suresh, S. Fracture normal to a bimaterial interface: Effects of plasticity on crack-tip shielding and amplification. *Acta Metallurgica et Materialia* **43,** 1157–1169 (1995).

25. Kolednik, O. The yield stress gradient effect in inhomogeneous materials. *International Journal of Solids and Structures* **37,** 781–808 (2000).

26. Liechti, K. M. & Chai, Y. S. Asymmetric Shielding in Interfacial Fracture Under In-Plane Shear. *Journal of Applied Mechanics* **59,** 295–304 (1992).

27. Mathews, N. G., Mishra, A. K. & Jaya, B. N. Mode dependent evaluation of fracture behaviour using cantilever bending. *Theoretical and Applied Fracture Mechanics* **115,** 103069 (2021).

28. Wegst, U. G. K., Bai, H., Saiz, E., Tomsia, A. P. & Ritchie, R. O. Bioinspired structural materials. *Nature Materials* **14,** 23–36 (2014).

29. Wat, A. *et al.* Bioinspired nacre-like alumina with a bulk-metallic glass-forming alloy as a compliant phase. *Nature Communications* **10** (2019).

30. Wolf, K. V. *et al.* An investigation of adhesion in drug-eluting stent layers. *Journal of Biomedical Materials Research Part A* **87A,** 272–281 (2008).

31. Rahbar, N. *et al.* Adhesion and interfacial fracture toughness between hard and soft materials. *Journal of Applied Physics* **104,** 103533 (2008).

32. Evans, A., Mumm, D., Hutchinson, J., Meier, G. & Pettit, F. Mechanisms controlling the durability of thermal barrier coatings. *Progress in Materials Science* **46,** 505–553 (2001).

33. Begley, M. R. & Wadley, H. N. Delamination resistance of thermal barrier coatings containing embedded ductile layers. *Acta Materialia* **60,** 2497–2508 (2012).

34. Ni, L., Pocratsky, R. M. & de Boer, M. P. Origins of thin film delamination induced by electrodeposition and processing methods to overcome it. *Thin Solid Films* **697,** 137796 (2020).

35. Shang, C. *et al.* Perspectives on Advances in Quantum Dot Lasers and Integration with Si Photonic Integrated Circuits. *ACS Photonics* **8,** 2555–2566 (2021).

36. Nelhiebel, M. *et al.* A reliable technology concept for active power cycling to extreme temperatures. *Microelectronics Reliability* **51,** 1927–1932 (2011).

37. Darveaux, R., Reichman, C. & Islam, N. *Interface Failure in Lead Free Solder Joints* in *56th Electronic Components and Technology Conference 2006* (IEEE, 2006).

38. Kalha, C. *et al.* Thermal and oxidation stability of TixW1-x diffusion barriers investigated by soft and hard x-ray photoelectron spectroscopy. *Journal of Applied Physics* **129,** 195302 (2021).

39. Wimmer, A. *et al.* Temperature dependent transition of intragranular plastic to intergranular brittle failure in electrodeposited Cu microtensile samples. *Materials Science and Engineering: A* **618,** 398–405 (2014).

40. Bigl, S., Wurster, S., Cordill, M. J. & Kiener, D. Advanced characterisation of thermo-mechanical fatigue mechanisms of different copper film systems for wafer metallizations. *Thin Solid Films* **612,** 153–164 (2016).

41. Stinville, J. *et al.* Dislocation dynamics in a nickel-based superalloy via in-situ transmission scanning electron microscopy. *Acta Materialia* **168,** 152–166 (2019).

42. Murphy, K. F., Chen, L. Y. & Gianola, D. S. Effect of organometallic clamp properties on the apparent diversity of tensile response of nanowires. *Nanotechnology* **24.** Cited By (since 1996):2 (2013).

43. Callahan, P. G. *et al.* Transmission scanning electron microscopy: Defect observations and image simulations. *Ultramicroscopy* **186,** 49–61 (2018).

44. Rice, J. & Tracey, D. On the ductile enlargement of voids in triaxial stress fields. *Journal of the Mechanics and Physics of Solids* **17,** 201–217 (1969).

45. Argon, A. S. *Strenghtening mechanisms in crystal plasticity* (Oxford University Press, 2011).

46. Hull, D. & Bacon, D. *Introduction to Dislocations* (Elsevier, 2011).

47. Hirth, J. P. & Lothe, J. *Theory of Dislocations (2nd ed.)* 857 (Wiley & Sons, 1983).

48. Ledbetter, H. M. & Naimon, E. R. Elastic Properties of Metals and Alloys. II. Copper. *Journal of Physical and Chemical Reference Data* **3,** 897–935 (1974).

49. Williams, D. B. & Carter, C. B. *Transmission Electron Microscopy* (Springer, 2009).

50. Fox, M. *Optical Properties of Solids* (Oxford University Press, 2010).

51. Shinotsuka, H., Tanuma, S., Powell, C. J. & Penn, D. R. Calculations of electron inelastic mean free paths. X. Data for 41 elemental solids over the 50 eV to 200 keV range with the relativistic full Penn algorithm. *Surface and Interface Analysis* **47,** 1132–1132 (2015).

52. Tracey, D. M. Finite Element Solutions for Crack-Tip Behavior in Small-Scale Yielding. *Journal of Engineering Materials and Technology* **98,** 146–151 (1976).

53. Shih, C. Relationships between the J-integral and the crack opening displacement for stationary and extending cracks. *Journal of the Mechanics and Physics of Solids* **29,** 305–326 (1981).

54. *ASTM Standard E1820-13, Standard Test Method for Measurement of Fracture Toughness* 1820 (ASTM International, West Conshohocken, USA, 2013).

55. Hutchinson, J. & Suo, Z. in *Advances in Applied Mechanics* 63–191 (Elsevier, 1991).

56. Dhondt, G. *The Finite Element Method for Three-Dimensional Thermomechanical Applications* (John Wiley & Sons, Ltd, 2004).

57. Hopcroft, M. A., Nix, W. D. & Kenny, T. W. What is the Young's Modulus of Silicon? *Journal of Microelectromechanical Systems* **19,** 229–238 (2010).

58. Kleinbichler, A., Zechner, J. & Cordill, M. Buckle induced delamination techniques to measure the adhesion of metal dielectric interfaces. *Microelectronic Engineering* **167,** 63–68 (2017).

59. Demir, E. & Raabe, D. Mechanical and microstructural single-crystal Bauschinger effects: Observation of reversible plasticity in copper during bending. *Acta Materialia* **58,** 6055–6063 (2010).

60. Kapp, M., Kirchlechner, C., Pippan, R. & Dehm, G. Importance of dislocation pile-ups on the mechanical properties and the Bauschinger effect in microcantilevers. *Journal of Materials Research* **30,** 791–797 (2015).

61. Rajagopalan, J., Rentenberger, C., Karnthaler, H. P., Dehm, G. & Saif, M. T. A. In situ TEM study of microplasticity and Bauschinger effect in nanocrystalline metals. *Acta Materialia* **58,** 4772–4782 (2010).

62. Laufer, E. E. & Roberts, W. N. Dislocations and persistent slip bands in fatigued copper. *The Philosophical Magazine: A Journal of Theoretical Experimental and Applied Physics* **14,** 65–78 (1966).

63. Lukas, P., Klesnil, M. & Krejci, J. Dislocations and Persistent Slip Bands in Copper Single Crystals Fatigued at Low Stress Amplitude. *Physica Status Solidi (b)* **27,** 545–558 (1968).

64. Kuhlmann-Wilsdorf, D. & Laird, C. Dislocation behavior in fatigue. *Materials Science and Engineering* **27,** 137–156 (1977).

65. Hall, E. O. The deformation and ageing of mild steel: III discussion and results. *Proceedings of the Physical Society B* **64,** 747–753 (1951).

66. Petch, H. J. The cleavage strength of polycrystals. *Journal of Iron and Steel Institute* **174,** 25–28 (1953).

67. Arzt, E. Size effects in materials due to microstructural and dimensional constraints: a comparative review. *Acta Materialia* **46,** 5611–5626 (1998).

68. Dou, R. & Derby, B. A universal scaling law for the strength of metal micropillars and nanowires. *Scripta Materialia* **61,** 524–527 (2009).

69. Rice, J. R. & Thomson, R. Ductile versus brittle behaviour of crystals. *The Philosophical Magazine: A Journal of Theoretical Experimental and Applied Physics* **29,** 73–97 (1974).

70. Ohr, S. An electron microscope study of crack tip deformation and its impact on the dislocation theory of fracture. *Materials Science and Engineering* **72,** 1–35 (1985).

71. Kumykov, V. K., Sergeev, I. N., Sozaev, V. A. & Gedgagova, M. V. Surface tension of copper in solid phase. *Bulletin of the Russian Academy of Sciences: Physics* **81,** 357–359 (2017).

72. Kumykov, V. K., Sozaev, V. A., Abazova, Z. K. & Gedgagova, M. V. Measuring the Temperature Coefficient of the Surface Tension of Metals in the Solid State. *Bulletin of the Russian Academy of Sciences: Physics* **82,** 817–819 (2018).

73. Tada, H., Press, A. & Paris, P. C. *Stress Analysis of Cracks Handbook* (ASME Press, 2000).

74. Fischer, L. L. & Beltz, G. E. The effect of crack blunting on the competition between dislocation nucleation and cleavage. *Journal of the Mechanics and Physics of Solids* **49,** 635–654 (2001).

75. Muskhelishvili, N. I. in *Some Basic Problems of the Mathematical Theory of Elasticity* 89–104 (Springer Netherlands, 1977).

76. Alfreider, M., Zechner, J. & Kiener, D. Addressing Fracture Properties of Individual Constituents Within a Cu-WTi-SiOx-Si Multilayer. *JOM* (2020).

77. Elices, M., Guinea, G., Gómez, J. & Planas, J. The cohesive zone model: advantages, limitations and challenges. *Engineering Fracture Mechanics* **69,** 137–163 (2002).

78. Zechner, J., Janko, M. & Kolednik, O. Determining the fracture resistance of thin sheet fiber composites – Paper as a model material. *Composites Science and Technology* **74,** 43–51 (2013).

79. Hohenwarter, A. & Pippan, R. A comprehensive study on the damage tolerance of ultrafine-grained copper. *Materials Science and Engineering: A* **540,** 89–96 (2012).

80. Hirakata, H. *et al.* Size effect on fracture toughness of freestanding copper nano-films. *Materials Science and Engineering: A* **528,** 8120–8127 (2011).

81. Hutchinson, J. Singular behaviour at the end of a tensile crack in a hardening material. *Journal of the Mechanics and Physics of Solids* **16,** 13–31 (1968).

82. Rice, J. & Rosengren, G. Plane strain deformation near a crack tip in a power-law hardening material. *Journal of the Mechanics and Physics of Solids* **16,** 1–12 (1968).

83. Ramberg, W. & Osgood, W. *Description of stress-strain curves by three parameters* (NACA, 1943).

84. Shih, C. Cracks on bimaterial interfaces: elasticity and plasticity aspects. *Materials Science and Engineering: A* **143,** 77–90 (1991).

85. Shih, C. F., Asaro, R. J. & O'Dowd, N. P. Elastic-Plastic Analysis of Cracks on Bimaterial Interfaces: Part III—Large-Scale Yielding. *Journal of Applied Mechanics* **58,** 450–463 (1991).

86. Pirondi, A. & Donne, C. D. Characterisation of ductile mixed-mode fracture with the crack-tip displacement vector. *Engineering Fracture Mechanics* **68,** 1385–1402 (2001).

87. Smith, D., Ayatollahi, M. & Pavier, M. On the consequences of T-stress in elastic brittle fracture. *Proceedings of the Royal Society A: Mathematical, Physical and Engineering Sciences* **462,** 2415–2437 (2006).

88. Ayatollahi, M. & Aliha, M. On determination of mode II fracture toughness using semi-circular bend specimen. *International Journal of Solids and Structures* **43,** 5217–5227 (2006).

89. Kysar, J. W. Directional dependence of fracture in copper/sapphire bicrystal. *Acta Materialia* **48,** 3509–3524 (2000).

90. Kysar, J. W. Continuum simulations of directional dependence of crack growth along a copper/sapphire bicrystal interface. Part II: crack tip stress/deformation analysis. *Journal of the Mechanics and Physics of Solids* **49,** 1129–1153 (2001).